

**FLUID DYNAMICS OF GAS-LIQUID BUBBLE  
COLUMNS  
A THEORETICAL AND EXPERIMENTAL STUDY**

**PROEFSCHRIFT**

ter verkrijging van  
de graad van doctor aan de Universiteit Twente,  
op gezag van de rector magnificus,  
prof. dr. F. A. van Vught,  
volgens besluit van het College voor Promoties  
in het openbaar te verdedigen  
op vrijdag 22 januari 1999 te 16.45 uur

door

**Erik Delnoij**  
geboren op 29 november 1969  
te Geleen.

Dit proefschrift is goedgekeurd door de promotor

**Prof. Dr. Ir. W. P. M. van Swaaij**

en de assistant promotor

**Dr. Ir. J. A. M. Kuipers**



**Referent:** Dr. Ir. J. Westerweel

DSM Research and the J. M. Burgers Center funded parts of the work outlined in this Thesis.

© 1998, 2001. E. Delnoij, Enschede, The Netherlands

---

No part of this book may be reproduced in any form by print, photoprint, microfilm or any other means without written permission from the author / publisher.

Niets uit deze uitgave mag worden verveelvoudigd en/of openbaar gemaakt door middel van druk, fotokopie, microfilm of op welke andere wijze dan ook zonder voorafgaande schriftelijke toestemming van de schrijver / uitgever.

---

**CIP-data Koninklijke Bibliotheek, Den Haag**

Delnoij, Erik

Fluid dynamics of gas-liquid bubble columns – A theoretical and experimental study –

Thesis Twente University – With index, references and summary in Dutch

ISBN 90 – 36512085

Key words: multiphase flow, bubble dynamics, gas-liquid bubble columns, CFD, PIV.

---

# Contents

<b>Summary</b>		<b>11</b>
<b>Samenvatting</b>		<b>15</b>
<b>1:</b>	<b>Introduction</b>	<b>19</b>
	1. Introduction	20
	2. The flow regimes	20
	3. Hierarchy of models	22
	4. Experimental validation	24
	5. This Thesis	25
	6. Notation	27
	7. References	27
<b>2:</b>	<b>Numerical simulation of individual bubbles using a Volume-Of-Fluid (VOF) model</b>	<b>29</b>
	0. Abstract	29
	1. Introduction	30
	2. Interface tracking methods	31
	3. The volume tracking model	34
	3.1 Tracking the gas-liquid interface	34
	3.2 Governing equations	37
	3.3 Boundary conditions and numerical solution	39
	4. Results and discussion	40
	4.1 The skirted bubble	40
	4.2 The spherical cap bubble	43
	4.3 Co-axial coalescence of two gas bubbles	45
	4.4 Adjacent bubbles	49
	5. Conclusions	50
	6. Notation	51
	7. References	52
<b>3:</b>	<b>Dynamic simulation of dispersed gas-liquid two-phase flow using a discrete bubble model</b>	<b>55</b>
	0. Abstract	55
	1. Introduction	56
	2. Bubble dynamics	57
	2.1 Bubble tracking	58
	2.2 Gravity and far field pressure contribution	59
	2.3 The drag force	59

2.4	The lift force	60
2.5	The virtual mass force	61
2.6	The hydrodynamic interaction force	61
2.7	Direct bubble-bubble interaction	64
2.8	Bubble diameter distribution	66
3.	Liquid phase hydrodynamics	66
3.1	Governing equations	66
3.2	Constitutive equations	67
3.3	Coupling between bubble and liquid and vice versa	67
3.4	Boundary conditions	70
4.	Numerical solution	71
5.	Results and discussion	71
5.1	Terminal rise velocity of a single bubble	71
5.2	Comparison with experimental data reported by Becker <i>et al.</i> (1995)	72
5.2.1	Comparison between model and experiment for large superficial gas velocity	74
5.2.2	Comparison between model and experiment for small superficial gas velocity	78
5.3	The forces acting on the bubbles	82
5.3.1	The added mass force	85
5.3.2	The lift force	86
5.3.3	The drag force	88
5.3.4	Hydrodynamic interaction	89
6.	Conclusions	92
7.	Notation	93
8.	References	95

#### **4: Dynamic simulation of gas-liquid two-phase flow: effect of column aspect ratio on the flow structure 99**

0.	Abstract	99
1.	Introduction	100
2.	CFD model	101
2.1	Bubble dynamics	102
2.2	Direct bubble-bubble interaction	103
2.3	Liquid phase hydrodynamics	103
2.4	Coupling between the phases	104
2.4.1	The liquid volume fraction	105
2.4.2	Momentum transfer term $\mathbf{F}$	106
2.4.3	Local liquid phase properties	107
2.5	Boundary conditions and numerical solution	107
3.	Experimental set-up	108
4.	Results	110
4.1	Effect of column aspect ratio: experiments by Chen <i>et al.</i> (1989)	110
4.2	Effect of column aspect ratio: comparison with experimental observations	118
5.	Conclusions	122

6.	Notation	123
7.	References	124
<b>5:</b>	<b>A three-dimensional CFD model for gas-liquid bubble columns</b>	<b>127</b>
0.	Abstract	127
1.	Introduction	128
2.	Model equations	130
	2.1 Bubble dynamics	130
	2.2 Liquid phase hydrodynamics	131
3.	Coupling between the phases	132
	3.1 The liquid volume fraction	132
	3.2 Momentum transfer from bubbles to liquid	133
	3.3 Local liquid phase properties	134
	3.4 Numerical solution	135
4.	Results	136
5.	Discussion and conclusions	142
6.	Notation	144
7.	References	146
<b>6:</b>	<b>Measurement of gas-liquid two-phase flow in bubble columns using ensemble correlation PIV</b>	<b>149</b>
0.	Abstract	149
1.	Introduction	150
2.	Theory	152
	2.1 Single-phase flow PIV	152
	2.2 Two-phase flow PIV	155
3.	Two-phase flow PIV: performance	157
	3.1 Monte-Carlo simulations	157
	3.2 Performance: number of realizations	158
	3.3 Performance: effect of bubble image displacement	160
	3.4 Performance: parallel shift	162
4.	Experimental	163
	4.1 Experimental set-up	163
	4.2 Results	165
5.	Discussion and conclusions	168
6.	Acknowledgement	171
7.	Notation	171
8.	References	172
<b>7:</b>	<b>Ensemble correlation PIV applied to bubble plumes rising in a bubble column</b>	<b>175</b>
0.	Abstract	175
1.	Introduction	176

2.	Theory of two-phase PIV	177
2.1	Directional ambiguity and image shifting	179
2.2	Window offset	182
2.3	From single-phase to two-phase PIV	183
2.4	Ensemble correlation to improve SNR	185
2.5	Discriminating between gas and liquid	187
3.	Experimental set-up	188
4.	Results	190
4.1	Instantaneous liquid flow field	192
4.2	Size of the ensemble correlation set	195
4.3	Bubble velocity and local void fraction	201
5.	Conclusions	203
6.	Acknowledgement	204
7.	Notation	204
8.	References	205
	<b>Publications</b>	<b>209</b>
	<b>Dankwoord (Acknowledgements)</b>	<b>211</b>
	<b>Levensloop</b>	<b>215</b>



## Summary

Gas-liquid bubble columns are used extensively in the process industries. The gas-liquid two-phase flow prevailing in this type of process equipment is extremely complex, inherently unsteady and dominated by phenomena with widely varying time- and length-scales. It is for this reason that many important fluid dynamical aspects of gas-liquid bubble columns are still poorly understood and difficult to predict *a priori*. This thesis aims to contribute to our understanding of the fluid dynamics of gas-liquid bubble columns by developing Computational Fluid Dynamics (CFD) models and an advanced experimental technique called Particle Image Velocimetry (PIV).

Due to the complex nature of the gas-liquid two-phase flow prevailing in a bubble column, we concluded that an attempt to develop a generalized (one-for-all) CFD model would be futile. We therefore introduced the 'hierarchy of models' concept. This 'hierarchy of models' is basically a set of three CFD models, with each model tailored to the study of specific hydrodynamic phenomena encountered in a bubble column. These three models are a Volume-Of-Fluid (VOF) model, an Euler-Lagrange discrete bubble model and an Euler-Euler Two-Fluid model. The VOF model and the discrete bubble model have been discussed in this thesis.

The Volume-Of-Fluid (VOF) model is the most detailed model in our 'hierarchy of models'. This VOF model has been developed with the specific objective of studying the time-dependent behavior of multiple (<10) 'large' gas bubbles rising in a liquid. A crucial part of any VOF model is the method used to advance the gas-liquid interface, which is embedded in the overall motion of the flow field, through the Eulerian mesh. A review of existing volume-tracking methods revealed that Youngs' VOF method is to be preferred. The model solves the instantaneous Navier-Stokes equations to obtain the flow field of both the gas and the liquid phase. Four different test cases have been studied: the formation and rise of a skirted bubble and of a spherical cap bubble, the coalescence of two identical gas bubbles and the behavior of two gas bubbles emanating from adjacent orifices. From the computational results, it could be concluded that our volume-tracking model is able to accurately resolve the motion of a

deforming gas bubble in a liquid. Additionally, the VOF model also resolves the gas- and liquid flow field induced by the rising bubble with a high spatial and temporal resolution.

The intermediate level of our ‘hierarchy of models’ consists of an Euler-Lagrange discrete bubble model. This model, which is available in a two-dimensional as well as a three-dimensional version, resolves the time-dependent motion of small, spherical gas bubbles in a liquid. The model incorporates all relevant forces (far-field pressure, drag, lift, virtual mass, hydrodynamic interaction between neighboring bubbles) acting on the bubbles, and accounts for two-way coupling between the gas and the liquid phase. The two-dimensional version of the model also accounts for direct bubble-bubble interactions (i.e. collisions). The liquid phase hydrodynamics are described using the volume-averaged Navier-Stokes equations. The two- and three-dimensional versions of the CFD model have both been validated using experimental results reported in literature.

The two-dimensional version of the discrete bubble model has been used to study the effect of the various forces acting on the bubbles on the prevailing flow pattern. It could be concluded that the virtual mass force is of particular importance near the gas distributor. The lift force acting on the bubbles disperses these bubbles over the cross-section of the bubble column, and it was shown that without lift forces acting on the bubbles, the experimentally observed wall peaking of the void fraction could not be predicted. This wall peaking of the void fraction could however, be predicted by the discrete bubble model when lift forces were accounted for. It was also found that the expression for the drag coefficient acting on the bubbles, used in the model simulations, did not markedly affect the flow pattern predicted by our model. Finally, it could be concluded from simulations with the two-dimensional version of our discrete bubble model that the force due to hydrodynamic interaction between bubbles does not significantly affect the macroscopic flow pattern prevailing in a bubble column.

The two- and three-dimensional versions of the discrete bubble model have also been used to study the effect of the aspect ratio of a bubble column on the structure of the prevailing gas-liquid two-phase flow. The aspect ratio used in this study varied from 1.0 to 11.4. Both models predicted a distinct transition in the gas-liquid flow pattern. At aspect ratios of 1.0 and 2.0, the classical ‘cooling tower’ mode of circulation prevailed whereas at aspect ratios exceeding 4.8 a highly complex and dynamic flow pattern with multiple staggered vortices was found. These computational results resemble the experimental observations reported

previously in literature. It could also be concluded that the flow structure predicted by the three-dimensional version of the discrete bubble model was considerably more complex than the flow structure inferred from the computations conducted with the two-dimensional version of the model.

Experimental validation of CFD results is a prerequisite for widespread acceptance of CFD results in the engineering community. Therefore, an advanced experimental technique called ensemble correlation multiphase flow Particle Image Velocimetry (PIV) has been developed to study the time-dependent behavior of a bubble plume rising in a liquid. This PIV technique is a straightforward extension of single-phase PIV and one of its main advantages over existing multiphase flow PIV techniques is that it employs a single CCD camera. The velocimeter estimates the motion of the liquid phase as well as the motion of the bubbles using the ensemble mean correlation function of successive PIV images.

In a first study, the performance of our ensemble correlation PIV technique was assessed using synthetic PIV recordings containing images of both tracer particles and bubbles. The performance of the velocimeter was gauged in terms of the amplitude of the displacement correlation peak pertaining to the bubbles and the valid detection probability of that same peak. It was concluded that a valid detection probability of at least 90 % could be assured if the number of PIV images that constitute the ensemble correlation set exceeds 16, whereas the mean effective number of bubble image pairs should exceed 2.5. Moreover, Monte-Carlo simulations revealed that at sufficiently large sizes of the ensemble correlation set, the strength of the bubble displacement correlation peak is proportional to the bubble image density. This finding enables us to estimate the local void fraction from the amplitude of the bubble displacement correlation peak.

Finally, an experimental setup has been constructed to demonstrate the capabilities of our newly developed PIV technique. It was concluded that the double-exposure single-frame mode of operation of the PIV technique was to be preferred due to the small exposure time-delay imposed by the mean flow velocity. Several important aspects concerning the implementation of the technique have been discussed. The PIV technique was subsequently used to study the liquid flow field induced by a bubble plume rising in a bubble column. The complex and time-dependent nature of the liquid flow field could clearly be inferred from the experimental results. The effect of the size of the ensemble correlation set and the size of the

interrogation window on the results eventually obtained with our velocimeter, was also studied. It could clearly be seen that an increased size of the ensemble correlation set increased the detectability of the displacement correlation peak but also decreased the temporal resolution of the velocimeter. Finally, we discussed sample results depicting the local gas velocity and the local void fraction.

## Samenvatting

Gas-vloeistof bellenkolommen worden veelvuldig toegepast in de procesindustrie. De gas-vloeistof twee fasen stroming in deze bellenkolommen is uitermate complex, inherent niet stationair en wordt gedomineerd door zogenaamde coherente stromingsstructuren. Door deze complexiteit is ons begrip van de gas-vloeistof stroming in bellenkolommen beperkt. Dit maakt *a priori* voorspelling van het dynamisch gedrag van een bellenkolom moeilijk. Door middel van dit proefschrift wil de auteur een bijdrage leveren aan ons begrip van de gas-vloeistof twee fasen stroming in een bellenkolom. Concreet zullen om dit doel te bereiken een tweetal Computational Fluid Dynamics (CFD) modellen voor gas-vloeistof stromingen worden ontwikkeld als mede een geavanceerde experimentele techniek die de naam Particle Image Velocimetry (PIV) draagt.

In de eerste plaats dienen we ons te realiseren dat het waarschijnlijk onmogelijk is om één enkel generiek CFD model te ontwikkelen dat in staat is alle in bellenkolommen voorkomende hydrodynamische fenomenen te beschrijven. Dit wordt veroorzaakt door de al eerder besproken complexe aard van de gas-vloeistof twee fasen stroming in een bellenkolom. Het is daarom dat wij het concept van de 'hiërarchie van modellen' hebben geïntroduceerd. Deze 'hiërarchie van modellen' is in wezen een set van drie modellen. Ieder model uit deze hiërarchie is toegesneden op de analyse van één specifiek hydrodynamisch verschijnsel in een bellenkolom. Deze drie modellen zijn een Volume-Of-Fluid model, een Euler-Lagrange discreet bellenmodel en een Euler-Euler Two-Fluid model. De eerste twee modellen worden in dit proefschrift besproken.

Het Volume-Of-Fluid model is het meest gedetailleerde model in onze 'hiërarchie van modellen'. Het model heeft de hoogste ruimtelijke resolutie, en is primair ontwikkeld voor het bestuderen van het gedrag van enkele ( $<10$ ) relatief 'grote' gasbellen in een vloeistof. Een essentieel onderdeel van een VOF model is het algoritme dat gebruikt wordt om het gas-vloeistof grensvlak te advecteren door het Euleriaans grid. Een literatuur studie leerde ons dat een modern Piecewise Linear Interface Construction (PLIC) algoritme zoals dat ontwikkeld door Youngs in alle opzichten het best voldoet. Dit algoritme is dan ook geïmplementeerd in een computercode die tevens de instantane Navier-Stokes vergelijkingen oplost om het stromingsveld van het gas en de vloeistof te verkrijgen. Dit model is gevalideerd aan de hand

van vier verschillende test cases: de vorming en het opstijgen van een ‘skirted’ bel en een ‘spherical cap’ bel, de coalescentie van twee identieke bellen en het gedrag van twee bellen die aan naast elkaar liggende orifices worden gevormd. Aan de hand van de modelresultaten kon worden geconcludeerd dat het VOF model in staat is om het gedrag van een deformerende gas bel in een vloeistof te beschrijven. Bovendien lost het model met grote ruimtelijk en temporele resolutie het bijbehorende stromingsveld van gas- en vloeistoffase op.

Het Euler-Lagrange discreet bellenmodel vormt het middelste niveau in de ‘hiërarchie van modellen’. Dit model, waarvan zowel een twee- als een drie-dimensionale versie is ontwikkeld, beschrijft het tijdsafhankelijk gedrag van kleine, bolvormige gasbellen in een vloeistof. Het model houdt rekening met alle belangrijke krachten op een bel (drukveld, wrijving, lift, toegevoegde massa, hydrodynamische interactie tussen nabijgelegen bellen) en modelleert de koppeling tussen gas en vloeistof en *vice versa*. De twee-dimensionale versie van het model beschrijft bovendien directe bel-bel interacties, zeg maar botsing tussen bellen. De vloeistof hydrodynamica wordt in het discreet bellenmodel gemodelleerd door middel van de volume gemiddelde Navier-Stokes vergelijkingen. Beide versies van het model zijn gevalideerd aan de hand van experimentele resultaten uit de literatuur.

Wij hebben de twee-dimensionale versie van ons discreet bellenmodel in de eerste plaats gebruikt voor een onderzoek naar het relatieve belang van de verschillende krachten die op een belletje werken in een gedispergeerde gas-vloeistof stroming. Het blijkt dat de kracht als gevolg van toegevoegde massa vooral in de buurt van de gasverdeler belangrijk is en zeker niet verwaarloosd mag worden. De lift kracht heeft tot gevolg dat een bellenpluim sterk uitwaaiert en de bellen zich verspreiden over de gehele dwarsdoorsnede van de kolom. Wij waren in staat aan te tonen dat als de lift kracht verwaarloosd wordt de experimenteel waargenomen verhoging van de gasfractie nabij de wand van de bellenkolom niet kan worden voorspeld door het discrete bellenmodel. Het discreet bellenmodel kan deze ‘wall peaking’ wel voorspellen als de lift kracht op een bel in beschouwing wordt genomen. Verschillende uitdrukkingen voor de frictiefactor van een bolvormig belletje bleken geen significante verschillen in het uiteindelijk voorspelde macroscopische stromingspatroon op te leveren. Dit geldt ook voor de kracht als gevolg van hydrodynamische interactie tussen naburige bellen; het meenemen van deze kracht heeft geen merkbare verandering in het macroscopisch stromingspatroon tot gevolg.

Zowel het twee- als het drie-dimensionaal discreet bellenmodel zijn gebruikt om het effect van de lengte-diameter verhouding van een bellenkolom op de gas-vloeistof stroming in die kolom te bestuderen. De lengte-diameter verhouding werd gevarieerd van 1.0 tot 11.4. Beide modellen voorspellen een opmerkelijke verandering in het stromingregiem. Als de lengte-diameter verhouding 1.0 en 2.0 is, prevaleert de klassieke ‘cooling tower’ circulatie. Wordt de lengte-diameter verhouding echter verhoogd tot 4.8 of meer dan ontstaat een complex, dynamisch stromingspatroon dat gedomineerd wordt door zogenaamde ‘staggered vortices’. Deze numerieke resultaten komen in kwalitatieve zin overeen met experimentele observaties uit de literatuur. Tenslotte blijkt dat de stromingsstructuur zoals die door de drie-dimensionale versie van het model wordt berekend aanzienlijk complexer is dan de structuur die het twee-dimensionale model voorspelt.

In de optiek van de auteur is experimentele validatie van numerieke resultaten een absolute voorwaarde voor toepassing van CFD modellen in de praktijk van het procesontwerp. Daarom is een geavanceerde meerfasen meettechniek ontwikkeld gebaseerd op het uit de één fase stromingen bekende Particle Image Velocimetry (PIV). Deze non-intrusive, twee-dimensionale meettechniek maakt het mogelijk het tijdsafhankelijk gedrag van een bellenpluim in een vloeistof te bestuderen. De PIV methode schat de lokale snelheden van zowel de vloeistof als de bellen door middel van een ensemble gemiddelde correlatie van opeenvolgende PIV beelden.

In eerste instantie zijn de prestaties van de ensemble correlatie PIV techniek onderzocht door middel van kunstmatig gegenereerde PIV beelden die afbeeldingen van zowel tracers als bellen bevatten. Met name de amplitude van de verplaatsingspiek geassocieerd met de beweging van de bellen en de valid detection probability van diezelfde piek zijn als maatstaf voor de prestaties van de snelheidsmeter gebruikt. Op basis van deze studie is geconcludeerd dat een valid detection probability van 90 % haalbaar is als bij de bepaling van de ensemble correlatie tenminste 16 PIV beelden worden betrokken en als de effectieve dichtheid van de bellen in een interrogatie gebied 2.5 of meer bedraagt. Ook bleek uit Monte-Carlo simulaties dat de amplitude van de ‘bellenpiek’ rechtevenredig is met de hoeveelheid bellen in een interrogatie gebiedje (mits voldoende PIV beelden aan de ensemble correlatie ten grondslag hebben gelegen). Dit maakt het mogelijk om de lokale gas fractie uit de amplitude van de betrokken verplaatsingspiek te schatten.

Tenslotte hebben wij een experimentele opstelling geconstrueerd om de nieuwe PIV techniek te demonstreren. Er werd geconcludeerd dat de ‘double-exposure single-frame PIV mode of operation’ de voorkeur verdiend; dit vanwege de relatief hoge snelheden in de bellenkolom die ons noodzaken om met een kleine belichtingstijd te werken. Enkele belangrijke aspecten van de implementatie van deze specifieke ‘mode of operation’ zijn besproken. Vervolgens hebben we de snelheidsmeter gebruikt om de vloeistofstroming geïnduceerd door een bellenpluim die opstijgt in een bellenkolom te bestuderen. De resultaten van de PIV metingen lieten de complexe en tijdsafhankelijke aard van de vloeistofstroming in een bellenkolom duidelijk zien. Het effect van het aantal PIV beelden gebruikt bij het bepalen van de ensemble gemiddelde correlatie functie is ook onderzocht. Het blijkt dat als meer beelden bij de ensemble correlatie worden betrokken, de detectability van de gas en vloeistof pieken sterk toeneemt, maar dat de temporele resolutie afneemt. Tenslotte hebben wij een voorbeeld van een lokaal gas snelheidsveld en een lokaal gas volumefractie veld besproken.



# **Chapter 1:**

## **Introduction**

## 1. Introduction

A number of important industrial processes require a reaction between a gas and a liquid to produce a particular product or to absorb a gaseous component in a liquid. In some of these processes, a large liquid bulk is required because the chemical reaction between the dissolved component and a component of the liquid phase is slow with respect to gas-liquid mass transfer. In these cases, an elementary gas-liquid bubble column (a vessel filled with liquid equipped with a sparger at the base for dispersing gas) is a suitable reactor, which is therefore extensively used in the process industries. Gas-liquid bubble columns offer some distinct advantages among which their relatively simple construction, low operating costs, excellent heat transfer characteristics to immersed surfaces and the ease with which the liquid residence time can be varied should be mentioned (Shah *et al.* (1982)). However, many important fluid dynamical aspects of the gas-liquid two-phase flow prevailing in bubble columns are still poorly understood and difficult to predict *a priori*. This unsatisfactory state of the art has led to an increased interest in recent years in detailed modeling of bubble columns and in the development of advanced experimental tools. This thesis aims to contribute to our understanding of the fluid dynamics of gas-liquid bubble columns. It discusses two different CFD (Computational Fluid Dynamics) models for gas-liquid two-phase flows and an advanced experimental technique that can be used to study dispersed gas-liquid and gas-liquid-solid flows.

## 2. The flow regimes

Before discussing these models and the experimental technique in more detail, let us first consider the various flow regimes encountered in bubble column operation. These flow regimes strongly affect hydrodynamic, transport and mixing properties such as pressure drop, gas holdup, interfacial area and mass and heat transfer coefficients. Generally, three different flow regimes are reported in literature (Becker, 1997). At low superficial gas velocities (up to 5 [cm s<sup>-1</sup>]) the *bubbly flow* or *homogeneous flow regime* prevails (see Figure 1). Small, spherical and equally sized gas bubbles that are distributed more or less uniformly over the columns' cross section characterize this flow regime. The rise velocities of the bubbles in the homogeneous flow regime are approximately 0.18 – 0.30 [m s<sup>-1</sup>] (Levich, 1962). Liquid up flow is observed in the wake of the bubbles whereas liquid down flow is observed in between the bubbles and near the column wall. Time-averaged measurements of the liquid velocity in

the bubble column reveal the classical ‘cooling tower’ mode of operation with liquid upflow in the column center and liquid down flow along both walls of the column.

At higher superficial gas velocities, a transition to the *heterogeneous flow regime* can be observed. In this flow regime, bubbles of widely varying size and shape can be observed as well as bubble coalescence and breakup. The larger bubbles tend to rise through the column center with the smaller bubbles trailing in their wakes and moving along the walls of the column. The liquid flow field is characterized by inherent unsteadiness and dominated by a rich variety of vortical and turbulent structures.

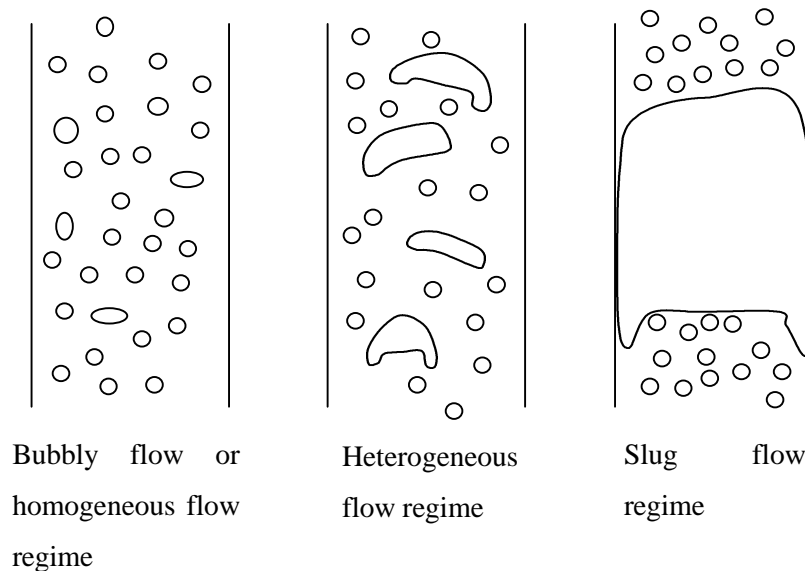


**Figure 1.** The flow regimes observed in a gas-liquid bubble column.

Chen *et al.* (1994) subdivided the heterogeneous regime into the *vortical spiral flow regime* and the *turbulent flow regime*. The vortical spiral flow regime prevails at superficial gas velocities between 1.7 and 4.9 [ $\text{cm s}^{-1}$ ]. A bubble plume (containing the larger gas bubbles) that spirals around the column’s axis characterizes this flow regime. As the superficial gas velocity increases and the bubble size increases accordingly, the vortical spiral flow regime is ultimately replaced by the turbulent flow regime. Liquid circulation in this flow regime is in general more vigorous and the flow structure is inherently unsteady.

Finally, at high superficial gas velocities and in bubble columns with a diameter smaller than approximately 0.15 [m] the *slug flow regime* can be observed. This regime is typified by bubbles that span the entire cross section of the bubble column: the so-called slug (see also Figure 1). In practical bubble column operation, the slug flow regime is undesirable due to its excessive gas by-pass. This regime can however, be encountered in pipelines used to transport mixtures of oil and gas from offshore oilrigs to coastal processing facilities.

### 3. Hierarchy of models

In the preceding section, we have discussed the various flow regimes detected in gas-liquid bubble columns. These flow regimes encompass a wide range of hydrodynamic phenomena (liquid circulation, bubble dynamics, coalescence, breakup etc.) and their associated lengthscales. These lengthscales typically range from several meters (the overall liquid circulation) down to the Kolmogorov scales of turbulence. In a bubble column, bubble diameters typically range from  $O(10^{-3} \text{ m})$  to  $O(10^{-1} \text{ m})$ , and bubble shapes range from spherical to spherical cap, depending on the flow regime prevailing in the column and the physical properties of the liquid (see for instance Grace, 1973 and Grace *et al.*, 1976). And finally, bubble columns encountered in industry differ substantially in size and geometry. Shah *et al.* (1982) for instance, distinguish nine basic types of bubble column reactors such as the single stage and multistage bubble column, the internal and external loop reactor and the down flow bubble column.

It is evident that the gas-liquid two-phase flow prevailing in bubble columns is extremely complex, and that it will be very difficult (if not impossible) to develop a generalized CFD model that accounts for all the hydrodynamic phenomena described previously. We therefore think that it is appropriate to employ a ‘hierarchy of models’<sup>1</sup> to study the dynamic behavior of gas-liquid bubble columns. This ‘hierarchy of models’ is basically a set of CFD models; each tailored to the study of specific hydrodynamic phenomena encountered in a bubble column.

Table 1 lists the three CFD models that make up our ‘hierarchy of models’: an Euler-Euler two-fluid model, an Euler-Lagrange discrete bubble model (or bubble tracking model) and a

---

<sup>1</sup> The ‘hierarchy of models’ concept is also used by Tomiyama (1998).

volume-tracking model. Briefly: an Euler-Euler two fluid model employs the volume-averaged mass and momentum conservation equations to describe the time-dependent motion of both phases. A two fluid model requires additional equations, so called constitutive equations for the closure of the model. These constitutive equations (who's proper formulation is still being debated) model the interfacial transport of mass, momentum and heat. An Euler-Lagrange discrete bubble model tracks each individual bubble or a cluster of bubbles by solving a Newtonian equation of motion. Additionally, the model employs the volume-averaged Navier-Stokes equations to obtain the liquid flow field. This discrete bubble model also requires constitutive equations for the forces acting on a bubble. Again, there is considerable debate among scientists about the correct equations for these forces. A discrete bubble model also requires an algorithm mapping the Lagrangian data (those data pertaining to the bubbles) on to the Eulerian mesh (employed to solve the Navier-Stokes equations). Finally, a volume-tracking model solves the instantaneous Navier-Stokes equations to obtain the gas and liquid flow field with an extremely high spatial resolution. The evolution of the gas-liquid interface is tracked using a volume-tracking scheme. This volume-tracking scheme has to be extremely accurate to avoid numerical diffusion of the gas-liquid interface and to account for the substantial changes in interface geometry. In the last decade, there has been considerable progress in this field and advanced high order volume-tracking schemes are becoming more widely available. Finally, it should be mentioned that a volume-tracking model requires no empirical constitutive equations.

As indicated in Table 1, the spatial resolution increases dramatically from the two-fluid model to the volume-tracking model whereas the applicability of these models to problems of genuine practical importance decreases. Key to the 'hierarchy of models' concept is exchange of information between the three levels that constitute our hierarchy. For example: the detailed volume-tracking model requires no empirical closure laws at all, but it does provide us with extremely detailed information on the flow in and around a deforming gas bubble. This knowledge can subsequently be used to derive constitutive equations for the closure of the discrete bubble model or the two fluid model. In this thesis, a two- and three-dimensional discrete bubble model and a two-dimensional volume-tracking model will be discussed and used to study various aspects of the two-phase flow prevailing in a bubble column.

**Table 1.** The hierarchy of models concept, and the different CFD models comprising this concept.

Model:	Equations:	Spatial Resolution:	Applicability:
Two Fluid model	Volume averaged mass- and momentum conservation equations for both phases.	Low $\delta x \gg D_b$	Practical problems.
Discrete Bubble Model (DBM)	Equation of motion for each bubble; volume averaged mass- and momentum conservation equations for liquid phase.	Intermediate $\delta x > D_b$	Lab-scale bubble columns, bubble plumes.
Volume Tracking Model	Instantaneous Navier-Stokes equations for both phases; advanced Volume Tracking scheme.	High $\delta x \ll D_b$	Small systems: 1-10 bubbles.

#### 4. Experimental validation

Experimental validation of CFD results is a prerequisite for the widespread acceptance of CFD as a design tool in the engineering community, as well as for the development of more sophisticated and refined CFD models. To accurately assess the validity of CFD models, quantitative data are required on the instantaneous, whole field characteristics of the two-phase flow prevailing in a bubble column. I.e. there is a need for accurate data on the instantaneous velocity field of both phases and on the time-dependent evolution of the local void fraction in the bubble column. In recent years, two different techniques have emerged with the potential to yield these data: Particle Tracking Velocimetry (PTV) and Particle Image Velocimetry (PIV)<sup>2</sup>.

In single-phase flow applications, PTV and PIV visualize fluid motion by adding small tracer particles to the fluid and infer the velocity field from the position of the tracer particles at two

---

<sup>2</sup> It should be noted that these two experimental techniques also serve a purpose in their own right. Quantitative experimental data on the two-phase flow prevailing in a bubble column can be used regardless of any possible model validation.

instances of time, from the particle displacement. PTV refers to the mode of operation where the number density of the tracer particles is low and the velocity field is obtained from the displacement of individual tracer particles. This implies that the measured velocities are sparse and irregularly spaced. PIV on the other hand, determines the velocity field by estimating the mean displacement of groups of tracer particles. The number density of the tracer particles in the PIV mode of operation exceeds that employed in the PTV mode. In the PIV mode of operation, the velocity field is obtained on a uniform grid. The spatial resolution obtained in the PIV mode of operation is generally (though not always) higher than the resolution attained in the PTV mode.

In dispersed gas-liquid two-phase flows the Lagrangian trajectories of the dispersed gas bubbles are of fundamental interest (especially in connection with experimental validation of the discrete bubble model). For this reason, a velocimeter that combines a PIV approach to resolve the liquid flow field and a PTV technique to track the motion of the individual bubbles would be ideal. Such a combined system is however complex and requires additional software or hardware to distinguish bubbles from tracers. In this thesis, we will therefore present a simpler, single camera, ensemble correlation PIV technique. This technique can be used to measure the pseudo-instantaneous velocities of both the gas and the liquid phase in a planar cross section of a small-scale gas-liquid (and possibly gas-liquid-solid) bubble column.

## **5. This thesis**

The objective of the Ph.D. work discussed in the thesis is to develop *and* validate CFD models that describe the time-dependent characteristics of the gas-liquid two-phase flow observed in bubble columns. To this end, the ‘hierarchy of models’ concept has been introduced. Within the framework of this concept two different CFD models will be discussed in this thesis: a volume-tracking model and a discrete bubble model. A Particle Image Velocimeter has been constructed to validate the discrete bubble model. This velocimeter will also be discussed extensively.

*Chapter 2* discusses the volume-tracking model that has been developed with the specific objective to study the time-dependent characteristics of multiple, ‘large’ gas bubbles rising in an initially quiescent liquid. This volume-tracking model is the most detailed model in our ‘hierarchy of models’ concept. The model does not require any adjustable or empirical

parameters. Chapter 2 will discuss the fundamentals of the model and the numerical techniques used to obtain an accurate and reliable solution for the flow field and for the topology of the gas-liquid interface. Results obtained with our volume-tracking model for various cases discussed in literature will be presented.

*Chapter 3, Chapter 4 and Chapter 5* discuss in detail the model comprising the intermediate level of our ‘hierarchy of models’: the Euler-Lagrange discrete bubble model. In Chapter 3, the basics of the two-dimensional version of this model are highlighted. The governing equations, the forces acting on the bubbles and the various numerical aspects of this CFD model will be discussed. A preliminary model validation using literature data and a study of the effect of the various forces acting on a bubble on the overall macroscopic flow pattern will be presented. Chapter 4 applies the two-dimensional discrete bubble model to assess in what way the aspect ratio of a bubble column affects the flow field prevailing in that bubble column. And finally, Chapter 5 extends the two-dimensional discrete bubble model to three dimensions. Certain technicalities associated with the extension of the model to three dimensions will be described.

*Chapter 6 and Chapter 7* will subsequently discuss an ensemble correlation Particle Image Velocimetry (PIV) technique that can be used to study the two-phase flow prevailing in a bubble column. The ensemble correlation PIV technique enables the simultaneous measurement of the velocity and hold up of both the gas and liquid phases. These results can, in turn, be used to validate the three-dimensional discrete bubble model. In Chapter 6, the fundamentals underlying the PIV technique will be introduced and the performance of the velocimeter will be assessed using synthetic PIV images. Results obtained with this particular PIV implementation in a pseudo two-dimensional bubble column will also be shown. Chapter 7 highlights experimental data on the structure of the two-phase flow prevailing in a small-scale, three-dimensional, bubble column as obtained with our newly developed PIV technique. These results clearly demonstrate the capabilities of our ensemble correlation, multiphase flow PIV implementation.



## 6. Notation

$\delta x$	Grid spacing [m]
$D_b$	Bubble diameter [m]

## 7. References

Becker, S., 1997, "Experimentelle Untersuchungen von Blasensäulen als Basis für detaillierte Modellrechnungen", *Fortschrittberichte VDI, Reihe 3: Verfahrenstechnik (In German)*, VDI Verlag GmbH., Düsseldorf.

Chen, R. C., Reese, J. and Fan, L. -S., 1994, "Flow structure in a three-dimensional bubble column and three-phase fluidized bed", *AIChE J.* **40** (7), 1093.

Grace, J.R., 1973, "Shapes and velocities of bubbles rising in infinite liquids", *Trans. Inst. Chem. Eng.* **51**, 116.

Grace, J.R., Wairegi, T. and Nguyen, T.H., 1976, "Shapes and velocities of single drops and bubbles moving freely through immiscible liquids", *Trans. Inst. Chem. Eng.* **54**, 167.

Levich, V. G, 1962, "Physicochemical hydrodynamics", Prentice Hall, Englewood Cliff, NJ.

Shah, Y. T., Kelkar, B. G., Godbole, S. P. and Deckwer, W. -D., 1982, "Design parameter estimations for bubble column reactors", *AIChE Journal* **28** (3), 353.

Tomiyama, A., 1998, "Struggle with computational bubble dynamics", *Third Int. Conf. Multiphase Flow 1998*, 8-12 June, Lyon, France.



## Chapter 2:

### Numerical simulation of individual bubbles using a Volume-Of-Fluid (VOF) model<sup>1</sup>

#### 0. Abstract

This paper presents a CFD (Computational Fluid Dynamics) model developed with the specific objective of studying the time-dependent behavior of multiple, “large” gas bubbles rising in an initially quiescent liquid. The model, based on the Volume-Of-Fluid concept, employs an advanced interface tracking scheme known as Youngs’ VOF to advance the gas-liquid interface through the Eulerian mesh. Additionally, the model solves the incompressible Navier-Stokes equations to obtain the flow field. Results obtained for four different cases will be discussed: the formation and rise of a skirted bubble and of a spherical cap bubble, the coalescence of two identical gas bubbles and the behavior of two gas bubbles emanating from two adjacent orifices. It could be concluded that the volume tracking model is able to track the motion of a gas-liquid interface embedded in a flow field with significant vorticity.

---

<sup>1</sup> Parts of this chapter have been published at the third international conference on multiphase flow, ICMF’98: Delnoij, E., Kuipers, J. A. M. and van Swaaij, W. P. M., 1998, “Numerical simulation of bubble coalescence using a Volume-Of-Fluid (VOF) model”, *Int. Conf. Multiphase Flow 1998*, 8-12 June, Lyon, France

## 1. Introduction

Gas-liquid bubble columns are employed throughout the biological, chemical and petrochemical industries. Many applications involve gas-liquid mass transfer with accompanying (exothermal) chemical reactions. The widespread industrial application stems from the fact that bubble columns offer some distinct advantages over other gas-liquid reactors, among which its excellent heat transfer characteristics, its simple construction and its low operating costs should be mentioned (Shah *et al.*, 1982). However, despite their industrial relevance, many important hydrodynamic phenomena associated with the gas-liquid two-phase flow prevailing in bubble columns are still poorly understood. These phenomena include bubble formation, bubble coalescence and breakup and the transition between the various flow regimes observed in bubble columns.

This deficiency of fundamental knowledge regarding bubble column hydrodynamics is especially apparent in the design and scale up of bubble columns operating in the heterogeneous or churn-turbulent regime. This regime, arguably the most important in industrial operation, is characterized by intermediate gas velocities, a fierce liquid circulation and the co-existence of “large” and “small” bubbles that differ considerably in shape (see for instance Grace, 1973, Grace *et al.*, 1976 and Deckwer and Schumpe, 1993). The larger bubbles observed in this regime are of particular importance because of their significant impact on gas-liquid contacting, and consequently on the overall performance of the bubble column as a chemical reactor. It is also in this regime that many of the aforementioned phenomena are of considerable importance and traditional semi-empirical approaches often fail to provide adequate explanations for experimental observations.

To study the time-dependent behavior of these “large” gas bubbles in a more fundamental way, we have developed a CFD model based on the Volume-Of-Fluid (VOF) concept (Hirt and Nichols, 1981). This two-dimensional, finite difference volume tracking model resolves the time-dependent motion of the gas and liquid phases, and of the interface separating the two phases. Due to its advanced interface tracking scheme, referred to as Youngs’ VOF (Youngs, 1982), the model is able to account for substantial changes in the topology of the gas-liquid interface induced by the relative liquid motion. This particular capability allows a detailed study of bubble formation, coalescence and breakup.

This paper reviews the existing numerical approaches to interface tracking, it discusses in detail the Youngs' VOF model developed at Twente University and it highlights and discusses results obtained with this model.

## 2. Interface tracking methods

Let us first review the most popular interface tracking methods: front tracking methods, shock capturing methods, level set methods, marker particle methods and SLIC and PLIC VOF methods (see also Rider and Kothe, 1995). See also Table 1, which summarizes the advantages and disadvantages of these techniques.

Front tracking methods describe the interface (for example the gas-liquid interface between the bubble and the surrounding liquid) by additional computational elements, usually a connected set of points or a separate unstructured grid that forms a moving boundary (Unverdi and Tryggvason, 1992). Front tracking methods therefore describe and track the time-dependent behavior of the interface itself. These front tracking methods are extremely accurate but also very complex. This complexity arises from the interaction between the moving boundary and the Eulerian mesh employed to solve the flow field. Major difficulties also arise when multiple interfaces interact with each other as in bubble coalescence or breakup. These cases require a separate algorithm governing the merger or breakup of interfaces.

Shock capturing methods, level set methods, marker particle methods and VOF methods all employ a scalar quantity carrying material (or fluid) information. This scalar quantity is tied to the fluid it represents and advected using equation (1). The essential difference between the methods based on a scalar quantity and the front tracking methods is that the methods discussed here track the motion of the both fluids; not the motion of the interface itself. The motion of the interface is tracked indirectly through the motion of the fluids separated by the interface.

Shock capturing methods discretize equation (1) using a high order (usually second order) shock-capturing scheme. Although novel shock capturing methods are quite sophisticated, they work less well for the sharp discontinuities generally encountered in multiphase flows (density ratios up to 1000 are not uncommon). Moreover, they require relatively fine grids to

obtain accurate solutions. Rider and Kothe (1995) used a high order Godunov method and conducted several numerical tests; they concluded that: “In all cases the use of shock-capturing methods was inadequate”.

**Table 1.** Summary of the characteristics of the different interface tracking methods discussed in section 2.

Method:	Advantages:	Disadvantages:
Front Tracking	<ul style="list-style-type: none"> <li>• Extremely accurate</li> <li>• Robust</li> <li>• Account for substantial topology changes interface</li> </ul>	<ul style="list-style-type: none"> <li>• Mapping interface grid onto the Eulerian mesh</li> <li>• Re-meshing required</li> <li>• Merging of interfaces requires additional algorithm</li> </ul>
Shock Capturing	<ul style="list-style-type: none"> <li>• Straightforward implementation</li> <li>• Abundance of advection schemes</li> </ul>	<ul style="list-style-type: none"> <li>• Numerical diffusion</li> <li>• Require fine grids</li> <li>• Limited to small discontinuities</li> </ul>
Level Set	<ul style="list-style-type: none"> <li>• Conceptually simple</li> <li>• Easy to implement</li> </ul>	<ul style="list-style-type: none"> <li>• Limited accuracy</li> <li>• Loss of mass (or volume)</li> </ul>
Marker Particle	<ul style="list-style-type: none"> <li>• Extremely accurate</li> <li>• Robust</li> <li>• Track substantial topology changes interface</li> </ul>	<ul style="list-style-type: none"> <li>• Computationally expensive</li> <li>• Re-distribution of particles required</li> <li>• Merging of interfaces requires additional algorithm</li> </ul>
SLIC VOF	<ul style="list-style-type: none"> <li>• Conceptually simple</li> <li>• Can be extended to 3D</li> </ul>	<ul style="list-style-type: none"> <li>• Numerical diffusion</li> <li>• Limited accuracy</li> <li>• Problems with deforming interfaces</li> </ul>
PLIC VOF	<ul style="list-style-type: none"> <li>• Relatively simple</li> <li>• Accurate</li> <li>• Track substantial topology changes interface</li> <li>• Merging of interfaces is implicitly accounted for</li> </ul>	<ul style="list-style-type: none"> <li>• Numerical surface tension</li> <li>• Difficult to implement in 3D</li> </ul>

Level set methods are designed to minimize the numerical diffusion hampering shock-capturing methods. Level set methods define the interface as the zero level set of a distance function from that interface. The advection of this distance function evolves through the solution of equation (1). Level set methods are conceptually simple and relatively easy to implement. These methods yield accurate results when the flow is simple and the interface is advected parallel to one of the coordinate axis. In flow fields with appreciable vorticity or in cases where the interface is significantly deformed, level set methods suffer from severe loss of mass and thus loss of accuracy.

Marker particle methods use marker particles that are assigned a color based on the fluid in which they reside. These marker particles are pegged to this particular fluid and their motion is tracked in time. The instantaneous positions of the marker particles are used to derive the relevant Eulerian fluid properties (required to solve the Navier-Stokes equations) and the position of the (gas-liquid) interface. Marker particle methods are extremely accurate and robust and can be used with confidence to predict the topology of an interface subjected to shear or vorticity in the carrier phase. Marker particle methods are however complex and expensive (in terms of CPU time). The complexities arise when the interface stretches considerably; this requires additional marker particles, which have to be generated during the computation. A similar problem occurs when the interface shrinks. Also merging or breakup of interfaces represents a problem; this is not automatically accounted for.

VOF methods employ a marker function  $F(\mathbf{x}, t)$  that uniquely identifies the fluid under consideration. This marker function is advected by the flow. The position of the (gas-liquid) interface is inferred from the marker function. Because the marker function  $F(\mathbf{x}, t)$  does not uniquely identify the interface (several different interface configurations might correspond to a field of  $F$ -values), we have to assume an interface orientation. Over the years, a number of different techniques have been proposed that differ in their assumptions about this interface geometry. Earlier work is generally typified by the SLIC (simple line interface calculation) algorithm due to Noh and Woodward (1976) and the Donor-Acceptor algorithm published by Hirt and Nichols (1981). Modern VOF methods include the PLIC method (piecewise linear interface calculation) due to Youngs (1982) and its extensions (Pilliod, 1992). The accuracy and capability of these modern PLIC VOF algorithms greatly exceeds that of the older VOF algorithms such as the Hirt and Nichols VOF method (Kothe and Rider, 1995a and 1995b, Rider *et al.*, 1995, Rider and Kothe, 1995 and Rudman, 1997).

### 3. The volume tracking model

The VOF model presented in this paper consists of two intimately coupled parts: a part that tracks the gas-liquid interface through the Eulerian mesh and maintains an accurate and sharp representation of this interface, and a part that solves for the gas and liquid phase flow field. Both parts will subsequently be discussed in more detail.

#### 3.1 Tracking the gas-liquid interface

The essential feature of the first part of the model is that it tracks the motion of the gas-liquid interface embedded in the overall motion of the flow field, while maintaining a compact interface thickness (one cell width). This requires a capability, on the part of the model, to uniquely identify the gas-liquid interface. The VOF concept achieves this by defining a fractional volume or ‘color’ function  $F(\mathbf{x}, t)$  which specifies the fraction of a computational cell filled with liquid. More specific, a unit value of  $F$  indicates a computational cell completely filled with liquid, whereas a zero value of  $F$  indicates a cell containing only gas. Obviously, cells with intermediate  $F$  values contain a gas-liquid interface. The motion of the liquid and thus that of the interface can now be tracked through the solution of the  $F$  transport equation, given by:

$$\frac{DF}{Dt} = \frac{\partial F}{\partial t} + (\mathbf{u} \cdot \nabla)F = 0 \quad 1$$

The finite difference approximation of this equation relates the new time level value of  $F$  to its previous time level value and to the fluxes of  $F$  through the four cell faces. When calculating these convective fluxes, computational smearing of the gas-liquid interface has to be avoided because this causes considerable inaccuracy in the interface representation. Several VOF algorithms have been developed that address this problem (see also section 2 of this chapter). Probably the most popular among these methods is the VOF algorithm originally developed by Hirt and Nichols (1981), also used to study gas bubbles rising in liquids by Tomiyama *et al.* (1993), Lin *et al.* (1996) and Delnoij *et al.* (1997). This algorithm uses an approximate interface reconstruction that forces the interface to align with one of the coordinate axis depending on the prevailing direction of the interface normal; meaning that an interface can only be horizontal or vertical (see Figure 1). For fluxes in a direction parallel to the reconstructed interface, upwind fluxes are used. Fluxes in a direction perpendicular to the reconstructed interface are estimated using a Donor-Acceptor method.



In this study however, the PLIC VOF method due to Youngs (1982) is used because of its superior accuracy and rigorous volume (mass) conservation, especially in flow fields with considerable spatial and temporal variations (see also section 2 of this chapter). The method is robust, is able to account for significant changes in the topology of the gas-liquid interface, and implicitly accounts for mergers between different interfaces or between different parts of the same interface. The particular Youngs' VOF<sup>2</sup> implementation discussed in this paper is derived from the method published by Rudman (1997) and is in most respects very similar to this method.

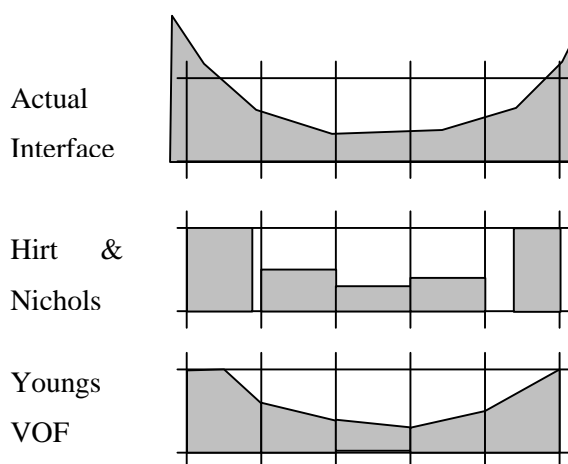
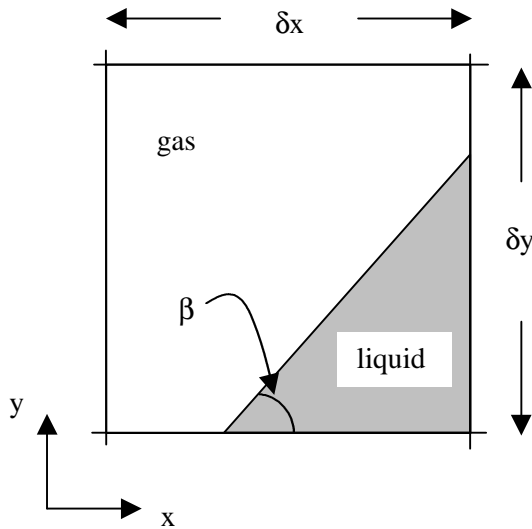


**Figure 1.** Youngs' VOF interface reconstruction compared to the Hirt and Nichols' VOF interface reconstruction and the actual interface.

Youngs' VOF method approximates the interface within a cell by a straight-line segment with a slope determined from the interface normal (see also Figure 1). This normal, in turn, is calculated from the gradient of the volume fraction using a nine-point stencil (in the two-dimensional case). The line segment cuts the computational cell under consideration in such a way that the fractional fluid volume is equal to  $F_{i,j}$ . The resulting fluid polygon is then used to determine the fluxes through any cell face with an *outwards* directed velocity. Figure 2 graphically depicts the methodology used to calculate the fluxes through the cell faces for a specific interface configuration.

---

<sup>2</sup> In this paper the terms PLIC VOF and Youngs' VOF will be used to refer to our implementation of the PLIC VOF method introduced by Youngs (1982) and Rudman (1997).



Side fractions:

$$S_{top} = 0$$

$$S_{right} = \sqrt{F(i, j) \cdot 2 \cdot \tan \mathbf{a}}$$

$$S_{left} = 0$$

$$S_{bottom} = \sqrt{F(i, j) \cdot 2 \cdot \cot \mathbf{a}}$$

$$\mathbf{b} = \tan^{-1} \left( \frac{-n^x}{n^y} \right)$$

Fluxes through the four cell faces:

If  $u_{top} > 0$ if  $u_{top} \cdot \mathbf{dt} \leq (1 - S_{right}) \cdot \mathbf{dy}$ 

$$F_{top} = 0$$

else

$$F_{top} = \frac{1}{2} [u_{top} \cdot \mathbf{dt} - (1 - S_{right}) \cdot \mathbf{dy}]^2 \cot \mathbf{b}$$

If  $u_{right} > 0$ if  $u_{right} \cdot \mathbf{dt} \geq S_{bottom} \cdot \mathbf{dx}$ 

$$F_{right} = F(i, j) \cdot \mathbf{dx} \cdot \mathbf{dy}$$

else

$$F_{right} = \frac{1}{2} u_{right} \cdot \mathbf{dt} \left[ 2 - \frac{u_{right} \cdot \mathbf{dt}}{S_{bottom} \cdot \mathbf{dx}} \right] S_{right} \cdot \mathbf{dy}$$

If  $u_{bottom} > 0$ if  $u_{bottom} \cdot \mathbf{dt} \geq S_{right} \cdot \mathbf{dy}$ 

$$F_{bottom} = F(i, j) \cdot \mathbf{dx} \cdot \mathbf{dy}$$

else

$$F_{bottom} = \frac{1}{2} u_{bottom} \cdot \mathbf{dt} \left[ 2 - \frac{u_{bottom} \cdot \mathbf{dt}}{S_{right} \cdot \mathbf{dy}} \right] S_{bottom} \cdot \mathbf{dx}$$

If  $u_{left} > 0$ if  $u_{left} \cdot \mathbf{dt} \leq (1 - S_{bottom}) \cdot \mathbf{dx}$ 

$$F_{left} = 0$$

else

$$F_{left} = \frac{1}{2} [u_{left} \cdot \mathbf{dt} - (1 - S_{bottom}) \cdot \mathbf{dx}]^2 \tan \mathbf{b}$$

**Figure 2.** Summary of Youngs' VOF method to determine the F-fluxes through the four cell faces of a computational cell containing a gas-liquid interface. This Figure depicts a single case. The entire algorithm distinguishes between 16 different cases.

Initially, the Youngs' VOF algorithm presented in this paper classifies the interface orientation as one of 16 possible interface configurations. This classification is based on the orientation of the interface normal with respect to the coordinate axis. Once this configuration is determined, the four side fractions are calculated. These side fractions are the fractions of the top, right, bottom and left sides of the cell that lie within the liquid. Once these side fractions are known, the fluxes through the four cell faces can be calculated with relative ease. The fluxes through cell faces of computational cells that do not contain a gas-liquid interface are determined using conventional first order upwind approximations.

### 3.2 Governing equations

The part of the volume tracking model that describes the gas and liquid phase flow fields employs the conservation equations for mass and momentum for an incompressible fluid:

$$\nabla \cdot \mathbf{u} = 0 \quad 2$$

$$\frac{\partial \mathbf{r}\mathbf{u}}{\partial t} + \nabla \cdot \mathbf{r}\mathbf{u}\mathbf{u} = -\nabla P + \nabla \cdot \mathbf{m}((\nabla \mathbf{u}) + (\nabla \mathbf{u})^T) + \mathbf{r}\mathbf{g} + \mathbf{F}_{SF} \quad 3$$

Where the density and viscosity in equation (3) are defined as:

$$\mathbf{r} = F(\mathbf{x}, t) \cdot \mathbf{r}_l + (1 - F(\mathbf{x}, t)) \cdot \mathbf{r}_g \quad 4$$

$$\mathbf{m} = F(\mathbf{x}, t) \cdot \mathbf{m}_l + (1 - F(\mathbf{x}, t)) \cdot \mathbf{m}_g \quad 5$$

The model presented in this paper uses the Continuum Surface Force (CSF) model, originally developed by Brackbill *et al.* (1992), to describe interfacial surface tension. This CSF model replaces the interfacial force due to surface tension by a smoothly varying volumetric force ( $\mathbf{F}_{SF}$ ) acting on all fluid elements in the interface transition region. The computer implementation of the CSF model, including wall adhesion, is similar to the approach followed by Kothe *et al.* in their RIPPLE code (Kothe *et al.*, 1991). The volumetric force due to surface tension is therefore represented as:

$$\mathbf{F}_{SF} = 2 \cdot F(\mathbf{x}, t) \cdot \mathbf{s} \cdot \mathbf{k}(\mathbf{x}, t) \cdot \mathbf{n}(\mathbf{x}, t) \quad 6$$

With the normal vector  $\mathbf{n}$  given by:

$$\mathbf{n}(\mathbf{x}, t) = \nabla F(\mathbf{x}, t) \quad 7$$

In equation (6),  $F(\mathbf{x}, t)$  represents the fractional amount of liquid and  $\kappa$  represents the local surface curvature.

This local surface curvature  $\kappa$  can be calculated from the *unit* normal at the gas-liquid interface ( $\tilde{\mathbf{n}}(\mathbf{x}, t)$ ):

$$\mathbf{k}(\mathbf{x}, t) = -(\nabla \cdot \tilde{\mathbf{n}}) = \frac{1}{|\mathbf{n}|} \left[ \left( \frac{\mathbf{n}}{|\mathbf{n}|} \cdot \nabla \right) |\mathbf{n}| - (\nabla \cdot \mathbf{n}) \right] \quad 8$$

The volumetric force  $\mathbf{F}_{\text{SF}}$  due to surface tension, as specified by equation (6), is located at (scalar) cell centers with face centered values (needed in the finite difference approximation to equation (3)) obtained by interpolating from the two nearest cell centered values. Kothe *et al.* (1991) found that a co-located force representation, having both components at the same location, has favorable properties over a component separated representation that is found to misrepresent free surface geometries somewhat. In the RIPPLE implementation of surface tension, and in our code, the surface curvature  $\kappa$  is located at cell centers and the normal vector  $\mathbf{n}$  is located at cell vertices. This normal vector  $\mathbf{n}$  is obtained by differentiating the color function  $F$  in the four cells surrounding the vertex under consideration (see Figure 3)<sup>3</sup>.

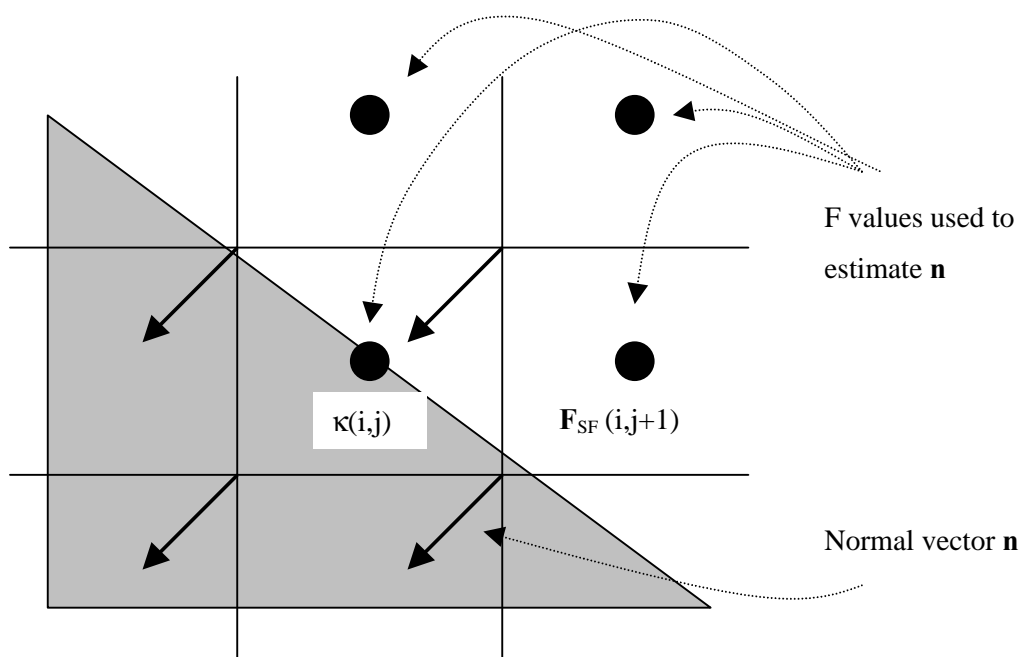


**Figure 3.** In the Continuum Surface Force (CSF) model, the force due to surface tension  $\mathbf{F}_{\text{SF}}$  and the surface curvature  $\kappa$  are located at cell centers. The normal vectors  $\mathbf{n}$  however are calculated using a four cell stencil and they are located at cell vertices.

<sup>3</sup> The stencil employed to estimate the surface normal vector  $\mathbf{n}$  that is used to calculate the force due to surface tension (four-cell stencil) differs from the stencil used to approximate the surface normal used to derive the interface orientation (a nine-cell stencil).

This procedure effectively yields a nine-point stencil for the cell-centered value of  $\mathbf{F}_{SF}$  and a twelve-point stencil for the face centered value of  $\mathbf{F}_{SF}$ . This rather large stencil leads to a better estimate of surface curvature because the stencil incorporates more information regarding the gas-liquid interface (Kothe *et al.*, 1991). This is achieved at the expense of reduced locality of the volumetric surface tension force ( $O(2\delta x)$ ). Clearly, to enhance the accuracy of the CSF model, the volume tracking model has to maintain as compact and sharp an interface as possible (preferably  $O(\delta x)$ ).

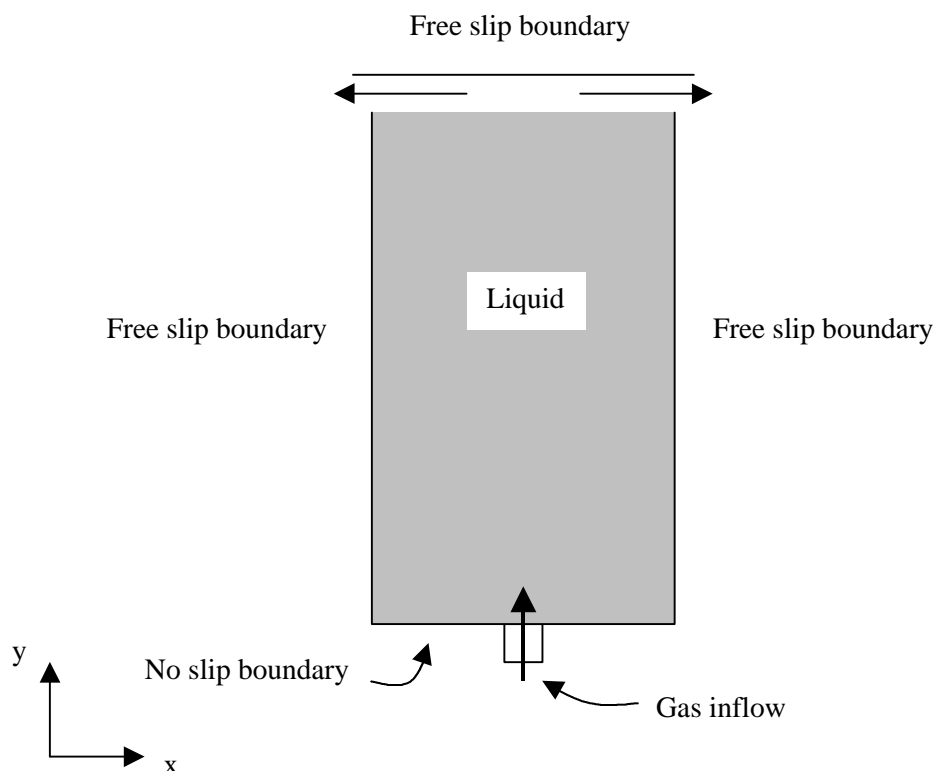


**Figure 4.** Schematic representation of a typical system used to study the time dependent behavior of “large” gas bubbles rising in an initially quiescent liquid. The boundary conditions applied are also shown. The top of this two-dimensional bubble column contains a “splash plate” that allows outflow of liquid during bubble formation.

### 3.3 Boundary conditions and numerical solution

The VOF model discussed in this chapter has been developed with the specific objective of studying the formation and rise of multiple, “large” gas bubbles in liquids. A typical system used for these purposes is depicted in Figure 4. The bubble column depicted in this Figure is initially filled with a quiescent liquid; at  $t = 0.0$  [s] gas is fed (with a fixed axial gas velocity)

to one or more orifices mounted in the bottom of the column. The boundary conditions required to solve the system of partial differential equations (equations (2) and (3)) are imposed using the flag matrix concept also used by Kuipers *et al.* (1993). The boundary conditions employed in the simulations presented in this paper are also shown in Figure 4.

The PLIC VOF algorithm outlined in the previous sections has been implemented in a computer code written in C. The code solves the incompressible Navier-Stokes equations in two dimensions, and tracks the motion of the gas-liquid interface in time. The system of linear equations arising from the finite difference approximation of the pressure-poisson equation (PPE) is solved using an Incomplete Choleski Conjugate Gradient method. A typical problem involving a single gas bubble rising during 1.0 [s] in a liquid, using a computational mesh of 100 x 150 cells and a time step of  $1.0 \times 10^{-4}$  [s], requires 16 hours dedicated CPU time on a Silicon Graphics Indigo<sup>2</sup> workstation. Approximately 50% of the CPU time used by the volume tracking code is required to solve the system of linear equations, whereas about 30% of the CPU time is used to track the interface.

#### **4. Results and discussion**

Key features of the volume tracking model outlined in the previous sections, are its capability to resolve the shape of a bubble under the prevailing flow conditions and physical properties of the liquid, and its capability to resolve the gas and liquid flow field associated with the rising bubble. In this section, four typical results obtained with this model will be discussed. The first two case studies will explore the capability of the volume tracking model to accurately predict the formation and rise of a skirted bubble and of a spherical capped bubble. The third case study focuses on the co-axial rise, and eventual coalescence, of two gas bubbles emanating from the same orifice. Finally, the formation and rise of two identical gas bubbles emanating from two adjacent orifices will be investigated.

##### **4.1 The skirted bubble**

Grace (1973) and Grace *et al.* (1976) presented a diagram that reflects the (experimentally determined) effect of fluid properties and equivalent bubble diameter on the shape and terminal rise velocity of an isolated bubble. This diagram is depicted in Figure 5 for reference purposes. In the following discussion about the theoretically predicted behavior of individual bubbles, it should be noted that the diagram presented in Figure 5 reflects the behavior of real

(viz. three-dimensional) bubbles in liquids, whereas the PLIC VOF model presented in this paper is a two-dimensional model.

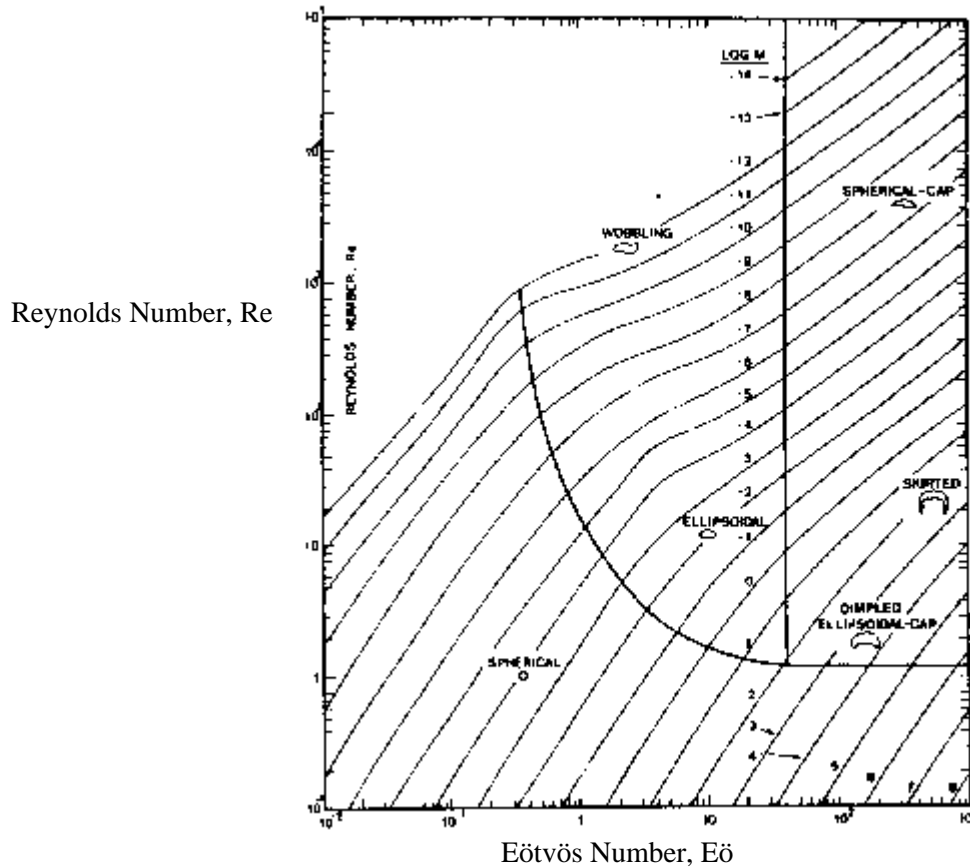


**Figure 5.** Graphical correlation by Grace (1973) and Grace *et al.* (1976) that shows the effect of fluid properties and equivalent bubble diameter on the shape and terminal rise velocity of bubbles in a quiescent Newtonian liquid.

According to this diagram, at  $E\ddot{o} \approx 4.0 \times 10^2$  and  $Mo = 1.0 \times 10^2$  a so-called skirted bubble should be obtained. Figure 6 shows the formation and rise of a single gas bubble emanating from a central orifice at  $E\ddot{o} \approx 4.0 \times 10^2$  and  $Mo = 1.0 \times 10^2$ , as calculated with our volume tracking code. Figure 6 depicts the gas-liquid interface in precisely the same orientation as used by the Youngs' VOF algorithm to calculate the F fluxes; no interface smoothing has been applied. The Youngs' VOF algorithm resolves the bubble formation in detail: at  $t = 0.2$  [s] the bubble is still attached to the nozzle and necking can be observed. The bubble eventually detaches from the nozzle, causing the neck to break into smaller gas bubbles. At  $t = 0.4$  [s] the remnants of the neck (the small bubble trailing the skirted bubble) are about to

coalesce with the main body of gas. Finally, a skirted bubble emerges, as is expected on basis of the aforementioned diagram. The rise velocity of this skirted bubble, as can be derived from the results obtained with the Youngs' VOF model, is approximately  $32 \text{ [cm s}^{-1}\text{]}$ . Given an equivalent bubble diameter<sup>4</sup> of  $5.5 \text{ [cm]}$ , the Reynolds number corresponding to this rising skirted bubble is 12, which is in accordance with the diagram presented in Figure 5.

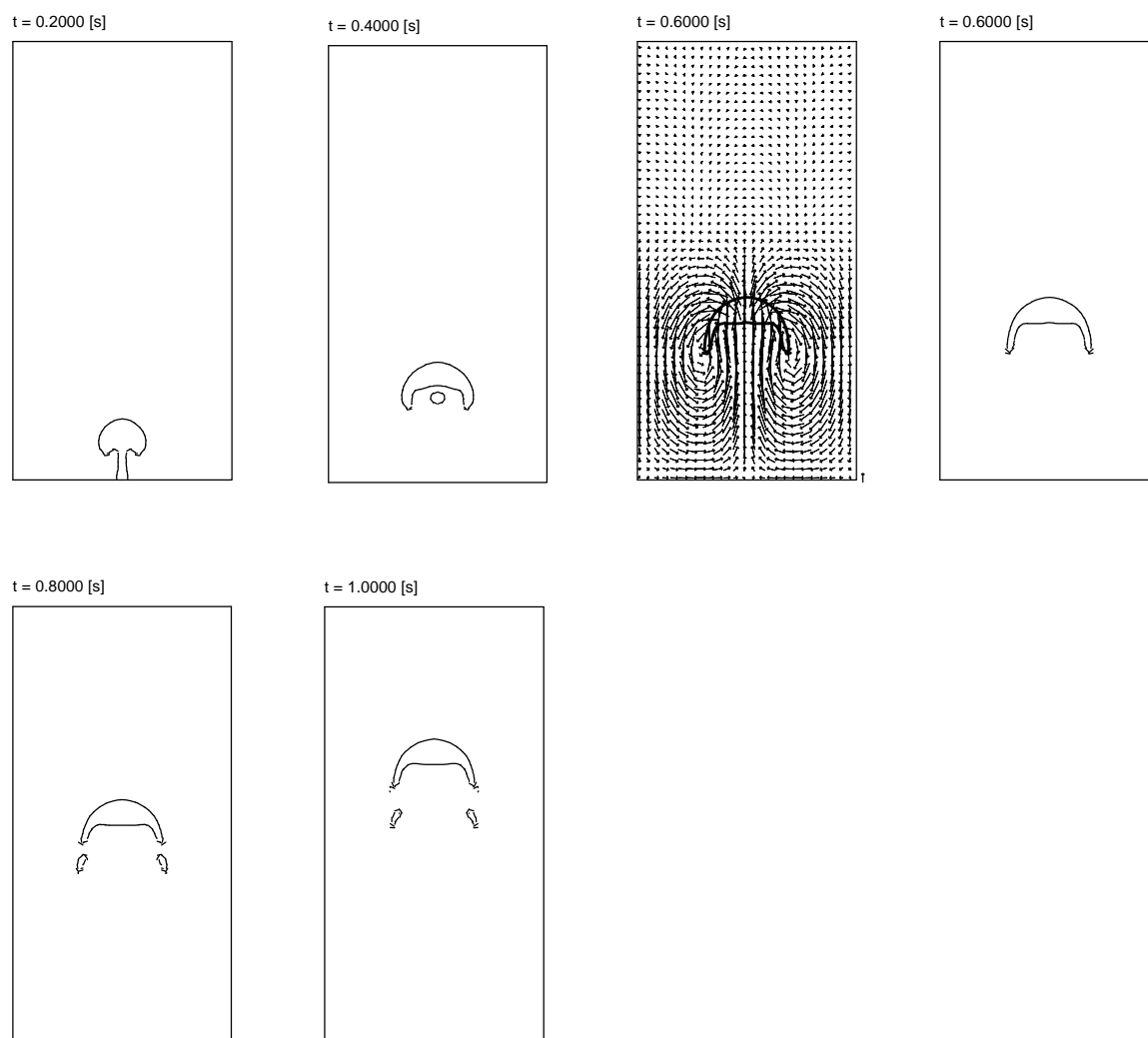


**Figure 6.** Bubble emanating from a central orifice at  $E\ddot{o} \approx 4.0 \times 10^2$  and  $Mo = 1.0 \times 10^2$ . Results obtained with Youngs' VOF model. Height = 0.50 m, width = 0.25 m,  $NX = 50$ ,  $NY = 100$ ,  $DT = 1.0 \times 10^{-5} \text{ s}$ , liquid density =  $1000 \text{ kg m}^{-3}$ , gas density =  $1.2 \text{ kg m}^{-3}$ , liquid viscosity =  $1.41 \text{ kg m}^{-1} \text{ s}^{-1}$ . The reference vector provided with the flow field corresponds to a velocity of  $10 \text{ cm s}^{-1}$ .

<sup>4</sup> The equivalent bubble diameter is the diameter of a spherical bubble with the same volume as the skirted bubble.



The skirts of the bubble are especially pronounced at  $t = 0.6$  [s], they stretch considerably as the bubble continues its ascent through the liquid and eventually break into smaller skirts and two small trailing bubbles ( $t = 1.0$  [s]). This breakup is most likely due to the limited resolution of the finite difference mesh. Figure 6 also shows the gas-liquid flow pattern at  $t = 0.6$  [s], clearly revealing the structure of the wake trailing the skirted bubble. The skirts can be seen to extend into the eye of the vortices that make up the bubble wake.

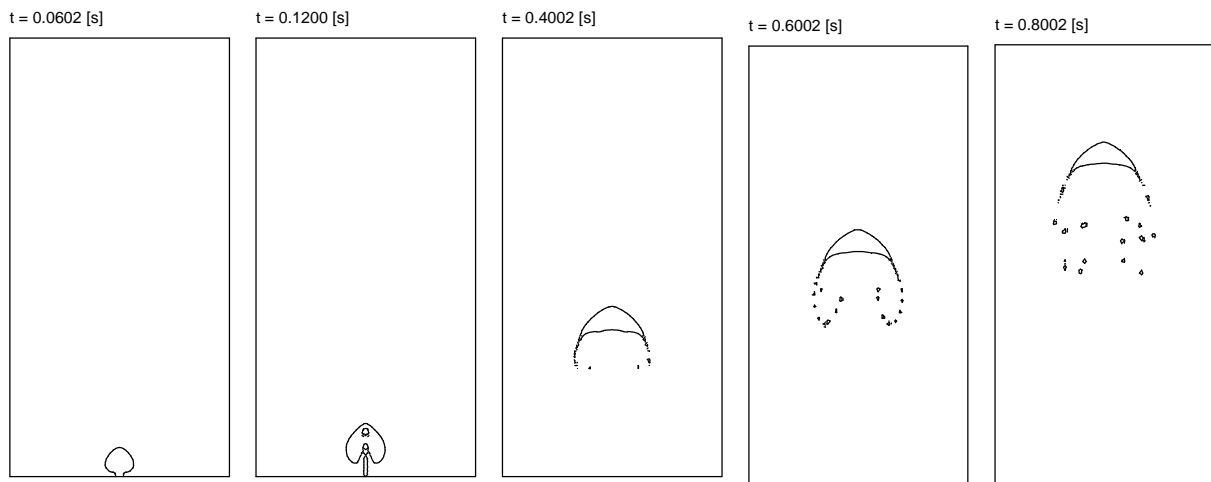


**Figure 7a.** Bubble emanating from orifice at  $E\ddot{o} \approx 1.0 \times 10^2$  and  $Mo = 1.0 \times 10^{-12}$ . Results obtained with Youngs' VOF model. Height = 0.20 m, width = 0.10 m,  $NX = 100$ ,  $NY = 150$ ,  $DT = 2.0 \times 10^{-4}$  s, liquid density =  $1000 \text{ kg m}^{-3}$ , gas density =  $1.0 \text{ kg m}^{-3}$ , liquid viscosity =  $1.0 \times 10^{-3} \text{ kg m}^{-1} \text{ s}^{-1}$ .

## 4.2 The spherical cap bubble

At  $E\ddot{o} \approx 1.0 \times 10^2$  and  $Mo = 1.0 \times 10^{-12}$  a spherical cap bubble should emerge, according to the diagram presented by Grace (1973) and Grace *et al.* (1976). Figure 7a shows a sequence of snapshots depicting the instantaneous position of the gas-liquid interface of a gas bubble emanating from an orifice at (approximately) these  $E\ddot{o}$  and  $Mo$  numbers. As can be seen from this Figure, a spherical cap bubble eventually emerges. The formation of this cap shaped bubble is worth discussing in more detail. At  $t = 0.06$  [s] a bubble has formed that possesses sufficient buoyancy to start its ascent through the liquid. The liquid motion induced by this forming bubble causes severe necking. The neck, eventually detaches from the primary bubble to form a second, elongated bubble ( $t = 0.12$  [s]). This secondary bubble subsequently coalesces with the first bubble causing small pockets of liquid to be included in the main

bubble. Figure 7b, depicts this stage of the bubble formation in more detail, clearly revealing the encapsulated liquid pockets.

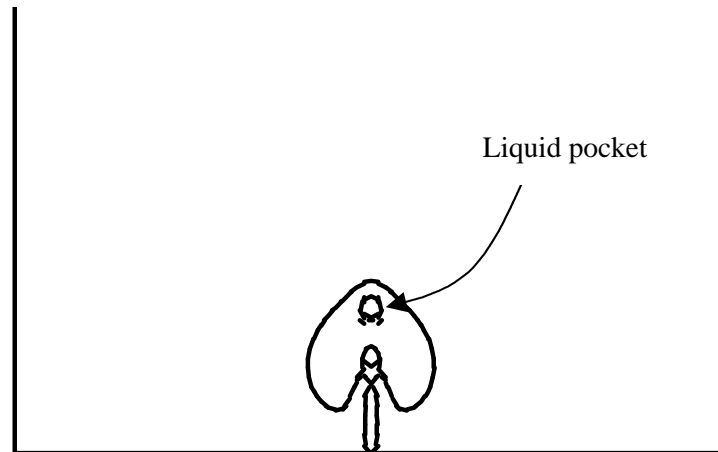


**Figure 7b.** Details of the formation of a spherical cap bubble at  $t = 0.1200$  [s]. During this formation process, the gas bubble encapsulates pockets of liquid. The caption of Figure 7a lists the relevant physical properties and numerical parameters.

At  $t = 0.6$  [s] the distinctly spherical cap shaped bubble can be seen to shed small satellite bubbles from its rear edges. These satellite bubbles, whose motion is also tracked by the volume tracking code, tend to accumulate in the wake of the cap shaped bubble. Figure 7c enlarges the flow field immediately surrounding the spherical cap shaped bubble. The small satellite bubbles can clearly be seen. The structure of the wake trailing the bubble can also be inferred from Figure 7c. Clearly, the wake is of the closed laminar type and stretches over several bubble diameters. The shedding of satellite bubbles is frequently observed in experiments, but (numerically) it might be exacerbated by a locally (at the edges) under-resolved interface curvature, despite the considerable spatial resolution of the Eulerian mesh.

The results depicted in Figure 7a have been used to estimate the rise velocity of the spherical cap bubble. In this case, the rise velocity is approximately  $20$  [ $\text{cm s}^{-1}$ ] corresponding to a bubble Reynolds number of  $3300$  ( $d_b \approx 1.7$  [cm]). This result is in accordance with the diagram presented by Grace and Grace *et al.*, which is shown in Figure 5. Clearly, the Youngs' VOF model is able to predict (with considerable accuracy!) the rise velocity of both a skirted bubble and a spherical cap bubble, despite the two-dimensional nature of our model.

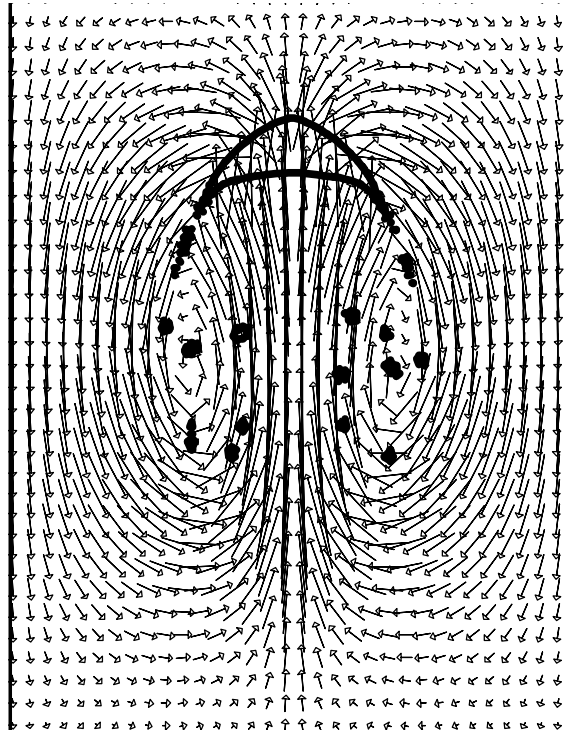


**Figure 7c.** Spherical cap bubble at  $t = 0.8002$  [s] and the associated gas and liquid flow field.

Relevant physical properties and numerical parameters are listed in the caption of Figure 7a. Note that one in every three velocity vectors is depicted in this Figure.

### 4.3 Co-axial coalescence of two gas bubbles

Brereton and Korotney (1991) presented experimental observations of the co-axial coalescence of two gas bubbles rising in an initially quiescent liquid. Using flash photography, they were able to analyze the coalescence process, and reveal the remarkable difference in shape between the leading and trailing bubble. The VOF model presented in this paper has also been used to study the co-axial coalescence of two identical gas bubbles at  $E\ddot{o} \approx 16$  and  $Mo = 2.0 \times 10^{-4}$ , conditions identical to those employed by Brereton and Korotney (1991). Snapshots depicting the instantaneous position of both the leading and the trailing bubble are shown in Figure 8a. At  $t = 0.3$  [s] the effect of the wake of the leading bubble on the shape of the trailing bubble can clearly be seen. The base of the trailing bubble is severely indented owing to the greater velocity of the liquid behind the trailing bubble compared to the velocity of the liquid preceding that bubble. At  $t = 0.40$  [s] the base of the leading bubble deforms inward, due to interaction with the trailing bubble and the liquid immediately behind the leading bubble. Coalescence is imminent. At  $t = 0.42$  [s] the inertia of the liquid behind

the trailing bubble drives the coalescence of that bubble with the leading bubble. Figure 8b shows the coalescence and the velocities of the gas and liquid phases in more detail. The gas-liquid interface of the coalesced bubble initially assumes a very complex shape, but eventually a spherical cap bubble emerges. It can also be seen that, during the coalescence of both bubbles, the coalesced bubble encapsulates a small drop of liquid that leaves the newly formed bubble through its base. These results agree remarkably well with the experimental observations reported by Brereton and Korotney (depicted in Figure 8c), especially in view of the complexity of the coalescence process and the fundamental nature of our model.

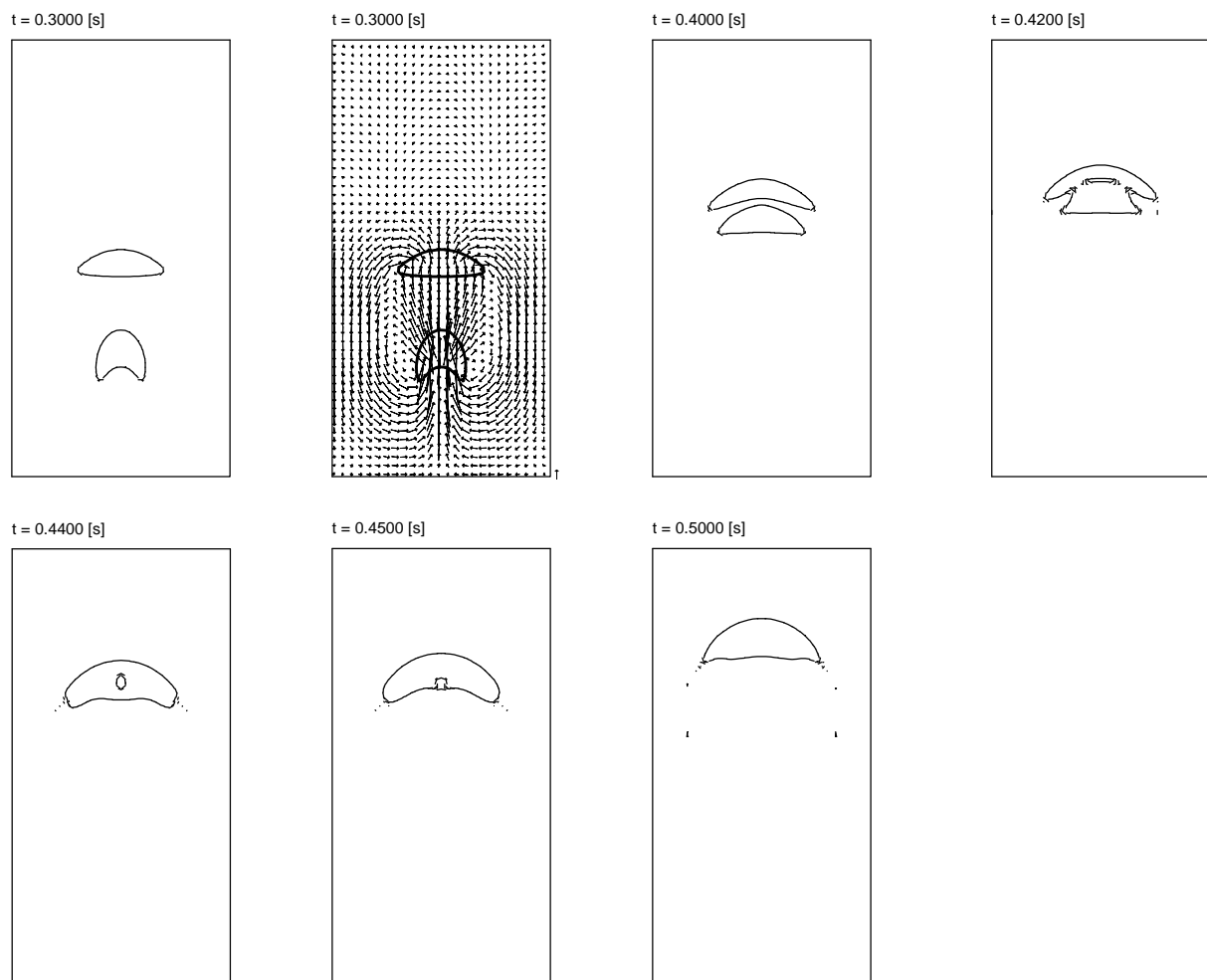


**Figure 8a.** Co – axial coalescence of two bubbles emanating from the same orifice at  $E\ddot{o} \approx 16$  and  $Mo = 2.0 \times 10^{-4}$ . Results obtained with Youngs' VOF model. Height = 0.10m, width = 0.05 m,  $NX = 50$ ,  $NY = 100$ ,  $DT = 5.0 \times 10^{-5}$  s, liquid density =  $1000 \text{ kg m}^{-3}$ , gas density =  $1.2 \text{ kg m}^{-3}$ , liquid viscosity =  $0.05310 \text{ kg m}^{-1} \text{ s}^{-1}$ . The reference vector corresponds to a velocity of  $10 \text{ cm s}^{-1}$ .

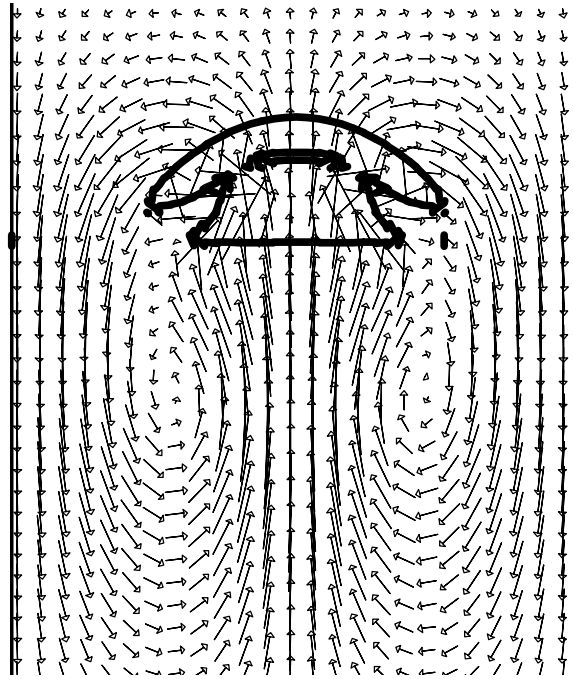


**Figure 8b.** Coalescence of two co-axially rising gas bubbles at  $t = 0.4200$  [s]. Both the gas-liquid interface, as calculated with the Youngs' VOF method, and the velocities of both phases are depicted. Relevant physical properties and numerical parameters are listed in the caption of Figure 8a. Note that one in every two velocity vectors is depicted in this Figure.

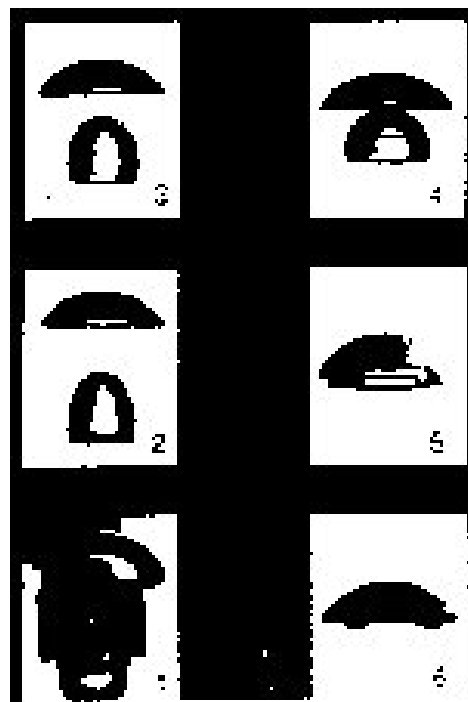


**Figure 8c.** Experimentally observed coalescence between two co-axially rising gas bubbles generated at the same orifice. Experiments by Brereton and Korotney (1991).  $Eö = 16$  and  $M = 2.0 \times 10^{-4}$ .

The co-axial rise and coalescence of two identical gas bubbles is an extremely difficult problem for any volume tracking technique. The flow field is very complex and dominated by the vortex trailing the bubbles. Moreover, as can be seen from Figures 8a and 8b, the topology of the gas-liquid interface changes dramatically during the coalescence of both bubbles (merging of two interfaces!). Level set methods and the older SLIC VOF methods suffer from severe loss of mass (or volume) in these cases. Figure 9 depicts the overall volume fraction of the gas phase as a function of simulation time.

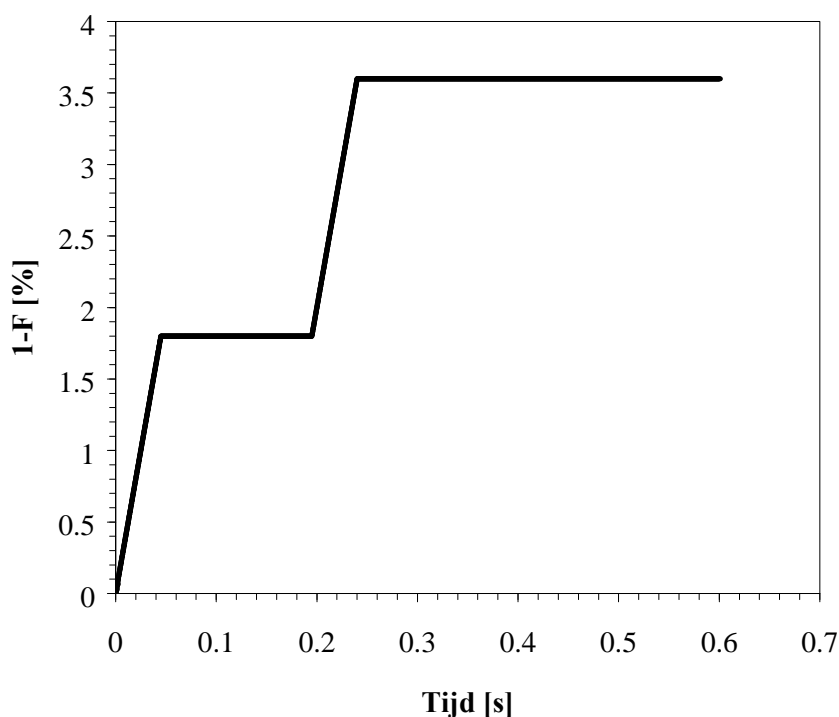


**Figure 9.** Volume fraction of gas [%] versus time for the co-axial coalescence of two identical gas bubbles. The two jumps correspond to the formation of the leading and trailing bubble.

This volume fraction is defined as the total amount of gas in the system versus the total volume of the system under consideration. During the time interval depicted in Figure 9 (0 – 0.6 [s]) the gas-liquid interface is advected in  $1.2 \times 10^3$  separate steps; any loss of volume due to numerical diffusion of the gas-liquid interface will therefore reveal itself within these first 0.6 [s]. In Figure 9, two distinct jumps in the volume fraction can be observed; these correspond to the formation of the leading and the trailing bubble. It can also be seen that after bubble formation the void fraction remains essentially constant, meaning that there is *no*

loss of volume due to numerical diffusion. This is an exceptional result, and we feel confident that the Youngs' VOF model presented in this paper conserves volume to a high degree of accuracy even in cases involving significant deformation (even merging) of the gas-liquid interface.

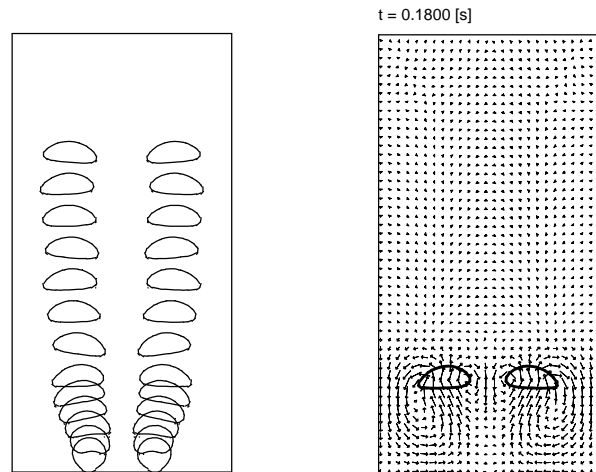


**Figure 10a.** Two bubbles emanating from two adjacent orifices at  $E\ddot{o} \approx 4$  and  $Mo = 2.0 \times 10^{-4}$ . Both instantaneous bubble positions and the flow field at  $t = 0.18$  s are shown. Results obtained with Youngs' VOF model. Height = 0.10 m, width = 0.05 m,  $NX = 50$ ,  $NY = 100$ ,  $DT = 5.0 \times 10^{-5}$  s, liquid density =  $1000 \text{ kg m}^{-3}$ , gas density =  $1.2 \text{ kg m}^{-3}$ , liquid viscosity =  $0.05310 \text{ kg m}^{-1} \text{ s}^{-1}$ . The reference vector corresponds to a velocity of  $10.0 \text{ cm s}^{-1}$ .

#### 4.4 Adjacent bubbles

In the previous section, we studied the co-axial rise and eventual coalescence of two bubbles, as a fourth and final case we will study the formation and rise of two identical gas bubbles emanating from two adjacent orifices. It is interesting to see whether these bubbles will coalesce, as their co-axial counterparts did, or whether they will bounce. Figure 10a depicts the successive positions of both bubbles in a single frame; the associated flow field (one out of every two vectors is shown) of both phases at  $t = 0.18$  [s] is also shown.

It can be seen most clearly from Figure 10a that the two adjacent bubbles do not coalesce; instead, the distance between the bubbles increases. In the early stages of their ascent, both bubbles exhibit a wobbling behavior that appears to diminish as the distance between the bubbles increases. The flow field depicted on the right hand side of Figure 10a clearly reveals

the complex structure of the wake trailing the two bubbles. As can be inferred from this Figure, there is a considerable interaction between the wakes of both bubbles. This can be seen more clearly in Figure 10b, which depicts an enlarged section of the flow field containing the two bubbles. Two asymmetric vortex pairs make up the combined wake of the bubbles. Moreover, there appears to be a significant down flow of liquid in between the bubbles, preventing coalescence.

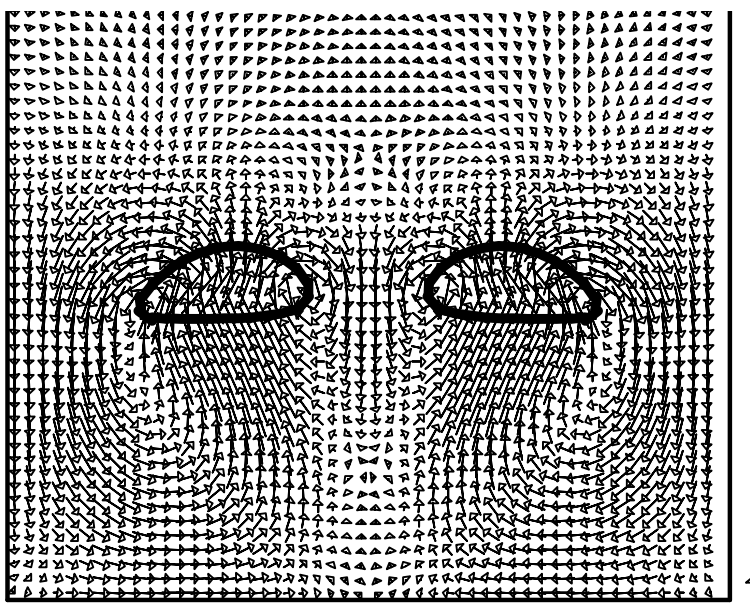


**Figure 10b.** Detailed view of the two bubbles emanating from two adjacent orifices at  $Eö \approx 4$  and  $Mo = 2.0 \times 10^{-4}$ . Both instantaneous bubble positions and the flow field at  $t = 0.18$  s are shown. Relevant physical properties and numerical parameters are listed in the caption of Figure 10a. The reference vector corresponds to a velocity of  $10.0 \text{ cm s}^{-1}$ .

## 5. Conclusions

In this paper, we have presented a volume tracking model developed with the specific objective of studying the behavior of multiple, “large” bubbles rising in an initially quiescent liquid. The model, based on the Volume-Of-Fluid (VOF) concept, solves the incompressible Navier-Stokes equations to obtain the gas and liquid flow fields. In addition, the model tracks the motion of the gas-liquid interface embedded in the overall motion of the flow field, and maintains a compact interface thickness through the use of an advanced interface tracking scheme known as Youngs’ VOF (Youngs, 1982). Interface physics, surface tension in



particular, have been incorporated in the model using the Continuum Surface Force (CSF) model.

Results obtained with this model for four different cases have been discussed: the formation and rise of a skirted bubble and a spherical cap bubble, the co-axial rise and coalescence of two identical gas bubbles and the behavior of two gas bubbles emanating from adjacent orifices. From these results it can be concluded that the volume tracking code, in its present form, is able to accurately track the motion of a gas-liquid interface, subject to appreciable changes in its topology and embedded in a flow field with considerable vorticity. It is therefore that we believe that this volume tracking model offers a promising (perhaps not yet mature) tool for those involved in studying gas-liquid systems.

## 6. Notation

$\beta$	Angle between interface and x-axis [rad]
$\mu_l$	Shear viscosity liquid [ $\text{kg m}^{-1} \text{s}^{-1}$ ]
$\mu_g$	Shear viscosity gas [ $\text{kg m}^{-1} \text{s}^{-1}$ ]
$\delta t$	Time step [s]
$\delta x$	Mesh size in x direction [m]
$\delta y$	Mesh size in y direction [m]
$d_b$	Bubble diameter [m]
$E\ddot{o}$	Dimensionless Eötvös number [-]
$F$	Fractional volume liquid [-]
$F_{\text{right, left, bottom, top}}$	Flux through cell face [ $\text{m}^2$ ]
$\mathbf{F}_{\text{SF}}$	Volumetric surface tension force [N]
$\mathbf{g}$	Acceleration due to gravity [ $\text{m s}^{-2}$ ]
$\kappa$	Surface curvature [ $\text{m}^{-1}$ ]
$Mo$	Dimensionless Morton number [-]
$n^{x, y}$	X or y component of normal [-]
$\mathbf{n}$	Normal of gas-liquid interface [ $\text{m}^{-1}$ ]
$\hat{\mathbf{n}}$	Unit normal of gas-liquid interface [-]
$P$	Pressure [ $\text{N m}^{-2}$ ]
$\rho_g$	Density gas phase [ $\text{kg m}^{-3}$ ]

$\rho_l$	Density liquid phase [kg m <sup>-3</sup> ]
$S_{\text{right, left, bottom, top}}$	Side fraction [-]
$\sigma$	Surface tension coefficient [N m <sup>-1</sup> ]
$t$	Time [s]
$\tau_l$	Stress tensor liquid [N m <sup>-2</sup> ]
$u_{\text{right, left, bottom, top}}$	Velocity through face under consideration [m s <sup>-1</sup> ]
$\mathbf{u}$	Velocity [m s <sup>-1</sup> ]
$\mathbf{x}$	Position vector [m]

## 7. References

Brackbill, J. U., Kothe, D. B. and Zemach, C., 1992, "A continuum method for modeling surface tension", *J. Comp. Physics* **100**, 335.

Brereton, G. and Korotney, D., 1991, "Co-axial and oblique coalescence of two rising bubbles", In: *Dynamics of Bubbles and Vortices near a Free Surface*, 1.

Deckwer, W. D. and Schumpe, A., 1993, "Improved tools for bubble column reactor design and scale up", *Chem. Eng. Sci.* **48**, 889.

Delnoij, E., Kuipers, J. A. M. and van Swaaij, W. P. M., 1997, "Computational fluid dynamics applied to gas-liquid contactors", *Chem. Eng. Sci.* **52** (21 / 22), 3623.

Grace, J.R., 1973, "Shapes and velocities of bubbles rising in infinite liquids", *Trans. Inst. Chem. Eng.* **51**, 116.

Grace, J.R., Wairegi, T. and Nguyen, T.H., 1976, "Shapes and velocities of single drops and bubbles moving freely through immiscible liquids", *Trans. Inst. Chem. Eng.* **54**, 167.

Hirt, C.W. and Nichols, B.D., 1981, "Volume of Fluid (VOF) method for the dynamics of free boundaries", *J. Compt. Phys.* **39**, 201.

Kothe, D. B., Mjolsness, R. C. and Torrey, M. D., 1991, "RIPPLE: a computer program for incompressible flows with free surfaces", Los Alamos National Laboratory, Report LA-12007-MS.

Kothe, D. B. and Rider, W. J., 1995a, “Comments on modeling interfacial flows with volume-of-fluid methods”, Technical Report LA-UR-3384, Los Alamos National Laboratory, Available on World Wide Web at [http://laws.lanl.gov/XHM/personnel/wjr/Web\\_papers/pubs.html](http://laws.lanl.gov/XHM/personnel/wjr/Web_papers/pubs.html).

Kothe, D. B. and Rider, W. J., 1995b, “Practical considerations for interface tracking methods”, Los Alamos National Laboratory, Available on World Wide Web at [http://laws.lanl.gov/XHM/personnel/wjr/Web\\_papers/pubs.html](http://laws.lanl.gov/XHM/personnel/wjr/Web_papers/pubs.html).

Kuipers, J. A. M., van Duin, K. J., van Beckum, F. P. H. and van Swaaij, W. P. M., 1993, “Computer simulation of the hydrodynamics of a two-dimensional gas-fluidized bed”, *Comput. Chem. Engng.* **17**, 839.

Lin, T.J., Reese, J., Hong, T. and Fan, L.S., 1996, “Quantitative analysis and computation of two-dimensional bubble columns”, *AIChE. J.* **42**(2), 301.

Noh, W. F. and Woodward, P. R., 1976, “SLIC (simple line interface calculation method)”, In: *Lecture Notes in Physics*, A. I. Van de Vooren and P. J. Zandbergen (Eds.), 330.

Pilliod Jr., J. E., 1992, “An analysis of piecewise linear interface reconstruction algorithms for volume-of-fluid methods”, Master’s Thesis, University of California at Davis.

Rider, W. J., Kothe, D. B., Jay Mosso, J., Cerutti, J. H. and Hochstein, J. I., 1995, “Accurate solution algorithms for incompressible multiphase flows”, Technical Report AIAA 95-0699, AIAA, also available on World Wide Web at [http://laws.lanl.gov/XHM/personnel/wjr/Web\\_papers/pubs.html](http://laws.lanl.gov/XHM/personnel/wjr/Web_papers/pubs.html).

Rider, W. J. and Kothe, D. B., 1995, “Stretching and tearing interface tracking methods”, Los Alamos National Laboratory, Available on World Wide Web at [http://laws.lanl.gov/XHM/personnel/wjr/Web\\_papers/pubs.html](http://laws.lanl.gov/XHM/personnel/wjr/Web_papers/pubs.html).

Rudman, M., 1997, “Volume-Tracking methods for interfacial flow calculations”, *Int. J. Num. Methods in Fluids* **24**, 671.

Shah, Y. T., Kelkar, B. G., Godbole, S. P. and Deckwer, W. -D., 1982, “Design parameter estimations for bubble column reactors”, *AIChE Journal* **28** (3), 353.

Tomiyama, A., Zun, I., Sou, A. and Sakaguchi, T., 1993, "Numerical Analysis of Bubble Motion with the VOF Method", *Nuclear Engineering and Design* **141**, 69.

Unverdi, S. O. and Tryggvason, G., 1992, "A front tracking method for viscous, incompressible, multi-fluid flows", *J. of Comp. Physics*, **100**, 25.

Youngs, D. L., 1982, "Time-dependent multi-material flow with large fluid distortion", In: *Numerical methods for fluid dynamics*, K. W. Morton and M. J. Baines (Eds.), Academic Press, New York, 273.

## Chapter 3:

### Dynamic simulation of dispersed gas-liquid two-phase flow using a discrete bubble model<sup>1</sup>

#### 0. Abstract

In this paper a detailed hydrodynamic model for the gas-liquid two-phase flow prevailing in a bubble column will be presented. The model is based on a mixed Euler-Lagrange approach and describes the time-dependent two-dimensional motion of small, spherical gas bubbles in a bubble column operating in the homogeneous regime. The motion of these bubbles is calculated from a force balance for each individual bubble, accounting for all relevant forces acting on them (including forces due to hydrodynamic interaction among bubbles). Direct bubble-bubble interactions are accounted for via an interaction model resembling the collision model developed by Hoomans *et al.* (1996). The liquid phase hydrodynamics are described using the volume-averaged, unsteady, Navier-Stokes equations. The results of a preliminary model validation will be reported. We will compare the computational results obtained with our CFD model with experimental observations published in literature. The importance of the various forces acting on the bubbles will be discussed, and it will be shown that the lift force acting on the bubbles significantly affects the lateral distribution of the bubbles. Finally, it will be shown that the hydrodynamic interaction force exerted by the bubbles on each other does not significantly affect the macroscopic flow pattern observed in a bubble column operated in the homogeneous regime at relatively low void fractions (< 5%).

---

<sup>1</sup> Modified version of a previous paper: Delnoij, E., Lammers, F. A., Kuipers, J. A. M. and van Swaaij, W. P. M., 1997, "Dynamic simulation of dispersed gas-liquid two-phase flow using a discrete bubble model", *Chem. Eng. Sci.*, **52** (9), 1429.

## 1. Introduction

Bubble column reactors are frequently employed in the biological, chemical and petrochemical industry. Compared to other multiphase reactors, such as packed towers and trickle bed reactors, bubble columns offer some distinct advantages, among which its simple construction and excellent heat transfer characteristics can be mentioned. The biggest disadvantage, on the other hand, is the limited knowledge about the fluid dynamics of these gas-liquid two-phase systems, despite the significant research efforts that have been made both in academic and industrial research laboratories. Modeling the fluid dynamics of gas-liquid bubble columns is therefore still a challenging problem.

There are two well-known approaches to modeling gas-liquid two-phase flows. One approach is based on the mixture formulation in which effective (transport) properties are used to describe these two-phase flows. This approach is relatively simple to use, but cannot account for any interaction (i.e. slip, mass and heat transfer) between the phases. In the second approach both phases are treated separately where transfer of mass, heat and momentum between the phases can be accounted for. Within the context of this approach one can distinguish Euler-Euler (or two fluid) models which are based on the concept of interpenetrating continua, and Euler-Lagrange models which adopt a continuum description for the liquid phase and additionally track each individual bubble using the Newtonian equations of motion.

In recent years a number of authors (Torvik and Svendsen, 1990; Ranade, 1992; Grienberger and Hofman, 1992; Hjertager and Morud, 1995; Sokolichin and Eigenberger, 1994; Jakobsen *et al.*, 1997 and Van den Akker, 1998) have published interesting results obtained with two-fluid gas-liquid models. Among others, Sokolichin and Eigenberger have contributed to the development of this type of model. Their calculations clearly reveal the inherent unsteadiness of a gas-liquid bubble column, and thus stress the importance of time-dependent CFD models (as opposed to time-averaged models). Long time averaging of their instantaneous velocity distributions leads to the familiar, experimentally observed, liquid velocity profile with liquid up flow in the column center and liquid down flow near the walls of the column.

Due to advances in computer technology Euler-Lagrange models for gas-liquid bubble columns have received increased attention in recent years. Trapp and Mortensen (1993),

Lapin and Lübbert (1994) and Devanathan *et al.* (1995) conducted pioneering work in this field. The models developed by these authors differ in their description of the bubble dynamics, and in the representation of the coupling between the phases. In their paper Lapin and Lübbert developed a two-dimensional Euler-Lagrange model of a bubble column using a simple description of the bubble dynamics. Coupling between the gas and the liquid phase was achieved through the effective density of the mixture. No exchange of momentum between the phases was incorporated in their model.

In this chapter we will present a detailed Euler-Lagrange discrete bubble model for a gas-liquid bubble column operating in the homogeneous regime. The liquid phase will be described using the well-known volume averaged Navier-Stokes equations whereas the dispersed phase will be described by an equation of motion for each individual bubble. The exchange of momentum between the gas and the liquid phase and *vice versa* will be accounted for. In addition bubble dynamics will be described in detail incorporating all relevant forces acting on a bubble rising in a liquid including the force due to hydrodynamic interaction between neighboring bubbles. In order to prevent, physically impossible, bubble-bubble overlap, direct bubble-bubble interactions will be described using a collision model. A preliminary validation of the discrete bubble model will be reported using experimental results obtained from the literature. Finally, the importance of the various forces acting on a bubble will be investigated theoretically.

## 2. Bubble dynamics

Gas-liquid bubble columns can be operated in a number of different regimes. The flow regime encountered in the column depends on one hand on the superficial gas velocity and the physical properties of the phases, and on the other hand on the aspect ratio of the column. One distinguishes the homogeneous or dispersed bubble regime, the heterogeneous or churn turbulent regime and the slug flow regime (Deckwer and Schumpe, 1993). The homogeneous flow regime is characterized by relatively low gas velocities and small, spherical bubbles. In a bubble column operating in the heterogeneous regime, at intermediate gas velocities, a large number of different bubbles with varying size and shape can be observed. Bubble shapes range from spherical to spherical cap. Slug flow occurs at high gas velocities in small diameter bubble columns.

## 2.1 Bubble tracking

As stated in the introduction, the discrete bubble model presented in this paper, models the time-dependent behavior of a bubble column in the homogeneous or dispersed bubble regime. In this operating regime the bubbles are nearly spherical, which significantly simplifies the calculation of the force exerted by the liquid on the bubbles. It is assumed that this force  $\mathbf{F}_{total}$  acting on a non-deformable spherical bubble rising in an unsteady, and non-uniform liquid flow is composed of separate and uncoupled contributions from pressure gradient, drag, virtual or added mass, vorticity, hydrodynamic interaction between neighboring bubbles and gravity (Auton, 1983):

$$\mathbf{F}_{total} = \mathbf{F}_P + \mathbf{F}_D + \mathbf{F}_{VM} + \mathbf{F}_L + \mathbf{F}_{Hydro} + \mathbf{F}_G \quad 1$$

The acceleration of a bubble can then be calculated from a force balance over the bubble under consideration:

$$m_b \frac{d\mathbf{v}}{dt} = \mathbf{F}_{total} \quad 2$$

The new bubble velocity can subsequently be calculated using a simple, explicit integration formula:

$$\mathbf{v}^{n+1} = \mathbf{v}^n + \left( \frac{d\mathbf{v}}{dt} \right)^n DT_{bub} \quad 3$$

Finally, the new time level bubble positions can be obtained from their new time level velocities and their previous time level positions. These three equations and the accompanying description basically summarize the Lagrangian part of the CFD model: the bubble-tracking algorithm. Various important issues however, still have to be discussed. For instance: what expressions for the various forces acting on a bubble and the associated coefficients and parameters should be employed? These expressions are extremely important and can significantly influence the accuracy and reliability of the CFD model. Also: how do we account for hydrodynamic interaction between neighboring bubbles? And which method is used to account for possible direct bubble-bubble interactions (viz. collisions)? These issues will be discussed in more detail in the following sections.



## 2.2 Gravity and far field pressure contribution

The force acting on a bubble due to the pressure gradient in the liquid phase incorporates contributions from the Archimedes displacement force, inertial forces and viscous strain in the liquid. The sum of liquid phase pressure gradient and gravity equals:

$$\mathbf{F}_G + \mathbf{F}_P = \mathbf{r}_g V_b \mathbf{g} - V_b \nabla P \quad 4$$

## 2.3 The drag force

A bubble, moving with a constant velocity through a uniform flow field, experiences a drag force, which consists of a form drag and a friction drag exerted by the liquid on the moving bubble. The drag force acting on a suspended sphere is given by Odar and Hamilton (1964), and is found to be proportional to the relative velocity between the phases as follows:

$$\mathbf{F}_D = -\frac{1}{2} C_D \mathbf{r}_l \rho R_b^2 |\mathbf{v} - \mathbf{u}| (\mathbf{v} - \mathbf{u}) \quad 5$$

The drag coefficient  $C_D$  depends on the (local) flow regime and the liquid properties. For rigid spheres the drag coefficient is usually approximated by the standard drag curve (Clift *et al.*, 1978):

$$C_D = \begin{cases} \text{Re} < 1000 \Rightarrow \frac{24}{\text{Re}} (1 + 0.15 \text{Re}^{0.687}) \\ \text{Re} > 1000 \Rightarrow 0.44 \end{cases} \quad 6$$

However, because of internal gas circulation and deformation, bubbles do not necessarily behave as rigid spheres; their drag coefficient can therefore differ from that predicted by the standard drag curve. According to Clift *et al.* the drag on bubbles in pure water is less than the drag predicted by the standard drag curve. In contaminated systems (tap water for example), on the other hand, the surfactants tend to collect at the rear of the bubble whereby slip along the surface of the bubble is restrained. In contaminated systems, therefore, bubbles behave more like rigid particles (Auton, 1983). As tap water is used in most experiments reported in the literature, we will use the standard drag curve in most simulations as an estimate for the drag coefficient of a spherical bubble.

A different equation for the drag coefficient, also suitable for (spherical) air bubbles rising in unfiltered water, is introduced by Kuo and Wallis (1988) and used by (among others) Boisson and Malin (1996):

$$C_D = \left\{ \begin{array}{l} \text{Re}_b < 0.49 \Rightarrow \frac{16}{\text{Re}_b} \\ 0.49 < \text{Re}_b < 100 \Rightarrow \frac{20.68}{\text{Re}_b^{0.643}} \\ \text{Re}_b \gg 100 \Rightarrow \frac{6.3}{\text{Re}_b^{0.385}} \end{array} \right\} \text{Spherical Bubbles} \quad 7$$

$$\left\{ \begin{array}{l} We > 8 \Rightarrow \frac{8}{3} \\ \text{Re}_b > \frac{2065.1}{We^{2.6}} \Rightarrow \frac{We}{3} \end{array} \right\} \text{Spherical Cap Bubbles (not used)}$$

The two drag coefficients introduced in equations (6) and (7) have both been implemented in our discrete bubble model. Their performance will be assessed in section 5.3.3.

## 2.4 The lift force

A bubble rising in a non-uniform, liquid flow field experiences a lift force due to vorticity or shear in this flow field. Auton (1983) calculated the lift force exerted by an inviscid liquid on a bubble in a vertical, linear shear flow represented by:

$$u_y = (\mathbf{k}x + v_{rise}) \quad 8$$

He derived that the lift force depends on the vector product of the slip velocity and the curl of the liquid velocity. This results in a lift force that acts in a direction perpendicular to both the direction of the slip velocity and the direction of the curl of the liquid velocity field. If the bubble velocity exceeds the liquid velocity the lift force is directed towards a region with a lower liquid velocity. If the bubble moves with a lower velocity the lift force is directed towards the high velocity region:

$$\begin{aligned} \mathbf{F}_L &= -C_L \mathbf{r}_l V_b (\mathbf{v} - \mathbf{u}) \times \boldsymbol{\Omega} \\ \boldsymbol{\Omega} &= \nabla \times \mathbf{u} \end{aligned} \quad 9$$

The expression (9) for the lift force is valid under the assumption of local homogeneity of the flow, or:

$$\frac{R_b \mathbf{k}}{v_{rise}} \ll 1 \quad 10$$

This assumption is satisfied throughout the homogeneous regime where both bubble radius and liquid velocity gradients are rather small; therefore Auton's lift force equation has been implemented in our model. The value of the lift coefficient has been calculated by Auton (1983) and was found to be equal to 0.53.

## 2.5 The virtual mass force

The total force exerted by the liquid on the bubble is in part independent of changes in the slip velocity between the phases and in part dependent on changes in the slip velocity. This latter part can be seen as a resistance to acceleration. This resistance to acceleration is due to an “added mass” of liquid that has to be accelerated when a bubble accelerates. According to Auton (1983) the resulting added or virtual mass force can be modeled using equation (11):

$$\mathbf{F}_{VM} = - \left( \frac{D\mathbf{I}}{Dt} + \mathbf{I} \cdot \nabla \mathbf{u} \right) \quad 11$$

$$\mathbf{I} = C_{VM} \mathbf{r}_l V_b (\mathbf{v} - \mathbf{u})$$

The material derivative in this equation for the virtual mass force should be the derivative pertaining to the gas bubble. In most computations reported in this paper the value for the virtual mass coefficient is considered to be independent of the void fraction and  $C_{VM}$  is taken to equal 0.5.

Van Wijngaarden (1976) argued that neighboring bubbles affect the virtual mass coefficient of the bubble under consideration. This influence can be expressed in terms of the average void fraction in the vicinity of that bubble using:

$$C'_{VM} = C_{VM} (1 + 2.78(1 - \epsilon_l)) \quad 12$$

This dependence of the virtual mass coefficient on the void fraction is considered in our study of the effect of hydrodynamic interaction between bubbles on the macroscopic flow pattern (see also section 2.6).

## 2.6 The hydrodynamic interaction force<sup>2</sup>

Let us now consider the way in which neighboring bubbles affect the total force acting on a specific bubble. This total force acting on a bubble depends, among other things, on the local (at the center of mass position) liquid velocity. This local liquid velocity contains a contribution from the macroscopic liquid flow field (obtained by solving the Navier-Stokes equations discussed in section 3) *and* an additional velocity component induced by neighboring bubbles. This induced velocity contributes to the lift force, the drag force and the

---

<sup>2</sup> The authors wish to thank H. F. Bulthuis for his contribution to this part of our paper. The interested reader is also referred to his thesis for additional details: Bulthuis, H. F., 1997, “Dynamics of bubbly flows”, Twente University, The Netherlands.

virtual mass force acting on the bubble under consideration. In this section, an approximate equation will be derived for this force due to hydrodynamic interaction between neighboring bubbles.

We will assume that the contribution of the induced velocity to the lift force on a bubble is zero because the velocity field induced by the bubbles is assumed to be irrotational. The contribution to the drag force is also neglected or can be implemented by introducing a drag coefficient that depends on the local gas holdup. The force exerted on a bubble by the induced velocity field due to neighboring bubbles can now be written as:

$$\mathbf{F}_{Hydro} = 3 \cdot C_{VM} \mathbf{r}_l V_b \frac{D\mathbf{u}_{induced}}{Dt} = 3 \cdot C_{VM} \mathbf{r}_l V_b \left( \frac{d\mathbf{u}_{induced}}{dt} - (\mathbf{v} - \mathbf{u}) \cdot \nabla \mathbf{u}_{induced} \right) \quad 13$$

This equation can be simplified because the time derivative ( $d\mathbf{u}_{induced}/dt$ ) causes the dependence of the virtual mass coefficient on the local gas holdup; this can be accounted for using equation (11) and the ( $d\mathbf{u}_{induced}/dt$ ) term can therefore be neglected:

$$\mathbf{F}_{Hydro} \approx 3 \cdot C_{VM} \mathbf{r}_l V_b (\mathbf{v} - \mathbf{u}) \cdot \nabla \mathbf{u}_{induced} \quad 14$$

The velocity field induced by a bubble rising with a velocity  $\mathbf{v}_{rise}$  can be calculated using a potential flow approximation (Batchelor, 1967):

$$\mathbf{u}_{induced} = \frac{3}{4\pi r_l} C_{VM} \mathbf{r}_l V_b \mathbf{v}_{rise} \cdot \nabla \nabla \frac{1}{|\mathbf{r}|} \quad 15$$

If we assume that the axial velocity component is the only significant component of the rise velocity, the force acting on bubble  $\alpha$  due to the presence of neighboring bubbles ( $\gamma$ ) can be written as:

$$F_{x,Hydro}^a = \sum_{g \neq a}^{N_{neighbor}} \frac{27}{4\pi r_l} (C_{VM} \mathbf{r}_l V_b^a \cdot \mathbf{v}_{rise}^a) (C_{VM} \mathbf{r}_l V_b^g \cdot \mathbf{v}_{rise}^g) \frac{x_g}{r_g^5} \left( 1 - 5 \frac{y_g^2}{r_g^2} \right) \quad 16$$

$$F_{y,Hydro}^a = \sum_{g \neq a}^{N_{neighbor}} \frac{27}{4\pi r_l} (C_{VM} \mathbf{r}_l V_b^a \cdot \mathbf{v}_{rise}^a) (C_{VM} \mathbf{r}_l V_b^g \cdot \mathbf{v}_{rise}^g) \frac{y_g}{r_g^5} \left( 3 - 5 \frac{y_g^2}{r_g^2} \right) \quad 17$$

From these equations, it can clearly be seen that the force due to hydrodynamic interaction between bubbles decays rapidly ( $\sim r^{-4}$ ) as the distance between the interacting bubbles ( $r$ ) increases. The number of neighboring bubbles ( $N_{neighbor}$ ) is determined using the neighbor list concept also used to resolve the binary collisions between bubbles (see section 2.7).

To resolve the time-dependent motion of the gas and liquid phases, the discrete bubble model employs *three* different time scales (see also Figure 1). The biggest timestep ( $DT_{\text{flow}} = 1.0 \times 10^{-3}$ ) is employed to solve the Navier-Stokes equations to obtain the macroscopic liquid flow field induced by the rising bubbles. The forces acting on a bubble due to pressure, drag, lift, virtual mass, gravity and hydrodynamic interaction are resolved on a smaller time scale ( $DT_{\text{bub}}$ ). This timestep  $DT_{\text{bub}}$  is typically  $1.0 \times 10^{-4}$  [s]. Subsequently, an even smaller timestep  $t_{\text{ab}}$  (calculated using the procedure outlined in section 2.7) is used to displace the bubbles, accounting for possible collisions between these bubbles. During this timestep  $t_{\text{ab}}$ , the relative positions of the bubbles change.

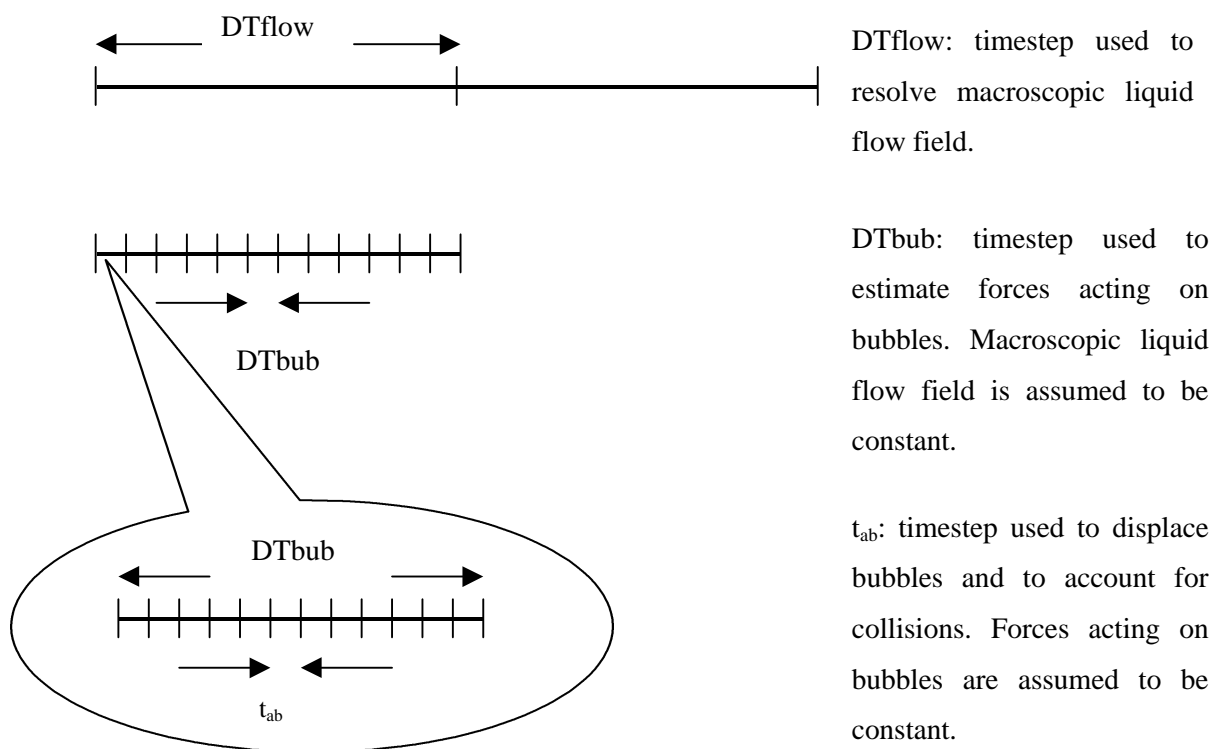


**Figure 1.** Schematic representation of the three timesteps employed by the Euler-Lagrange discrete bubble model.

The force due to hydrodynamic interaction is however assumed to be constant during this timestep. This is a valid assumption and a minor simplification because the temporal resolution employed to update the forces acting on a bubble (corresponding frequency =  $DT_{\text{bub}}^{-1} = 10000$  [Hz]) is sufficient to account for the steep changes in the force due to hydrodynamic interaction between bubbles. For example: two bubbles that approach each other at  $20$  [ $\text{cm s}^{-1}$ ] (a rather high relative velocity) travel  $20$  [ $\mu\text{m}$ ] during each timestep  $DT_{\text{bub}}$ . Bubbles diameters are generally approximately  $1 - 2$  [mm], a displacement of  $20$

[ $\mu\text{m}$ ] therefore constitutes a displacement over 1/50 of the bubble diameter. The corresponding changes in the force due to hydrodynamic interaction acting on these bubbles are therefore small during this timestep  $DT_{\text{bub}}$ .

The effect of these rather detailed hydrodynamic interaction phenomena on the macroscopic flow pattern prevailing in a bubble column will be discussed extensively in section 5.3.4.

## 2.7 Direct bubble-bubble interaction

In a gas-liquid dispersion bubbles have been observed to coalesce, to bounce and subsequently coalesce or to bounce and separate (Duineveld, 1994; Tsao and Koch, 1997). In our model it has been assumed that the bubbles always bounce and separate, which is probably a fair assumption for relatively small bubbles rising in water at high Reynolds numbers. In experiments bouncing and separation of bubbles can be achieved by adding salt to the suspending water (Tsao and Koch, 1994).

There are various approaches to model collisions between bubbles in a gas-liquid dispersion. Sangani *et al.* (1995) employed a soft-core repulsive potential to model the collision process. In the present paper however, a hard sphere collision model resembling the model developed by Hoomans *et al.* (1996) is used to process the sequence of collisions between bubbles in a bubble column. In this method a constant time step  $DT_{\text{bub}}$  is used to account for the forces acting on a bubble. Within this time step, the velocity of the bubbles is assumed to change only due to binary collisions between bubbles. A sequence of collisions is then processed one collision at a time.

Figure 2 graphically depicts the consecutive steps involved in processing the binary collisions between bubbles. The collision sub model initially determines the most likely collision partners using a neighbor list (also depicted in Figure 2). This neighbor list effectively limits the ‘search area’ for possible collision partners to the immediate vicinity of the bubble under consideration. This procedure saves substantial CPU time.

The collision sub-model subsequently determines the collision time  $t_{\text{ab}}$  for the bubble under consideration (a) and its possible collision partners (b) within the neighbor list. This collision partner can be another bubble or one of the walls of the bubble column. This time step  $t_{\text{ab}}$  can

be calculated from the initial position of the bubbles and their velocities. The collision time  $t_{ab}$  is found as the smallest positive root of equation (18):

$$t_{ab} = \frac{-b_{ab} - \sqrt{b_{ab}^2 - |\mathbf{v}_a - \mathbf{v}_b|^2 \left( |\mathbf{r}_a - \mathbf{r}_b|^2 - (R_a + R_b)^2 (1 + C_{VM})^{\frac{2}{3}} \right)}}{|\mathbf{v}_a - \mathbf{v}_b|^2} \quad 18$$

Where:

$$b_{ab} = (r_{ax} - r_{bx})(v_{ax} - v_{bx}) + (r_{ay} - r_{by})(v_{ay} - v_{by}) \quad 19$$

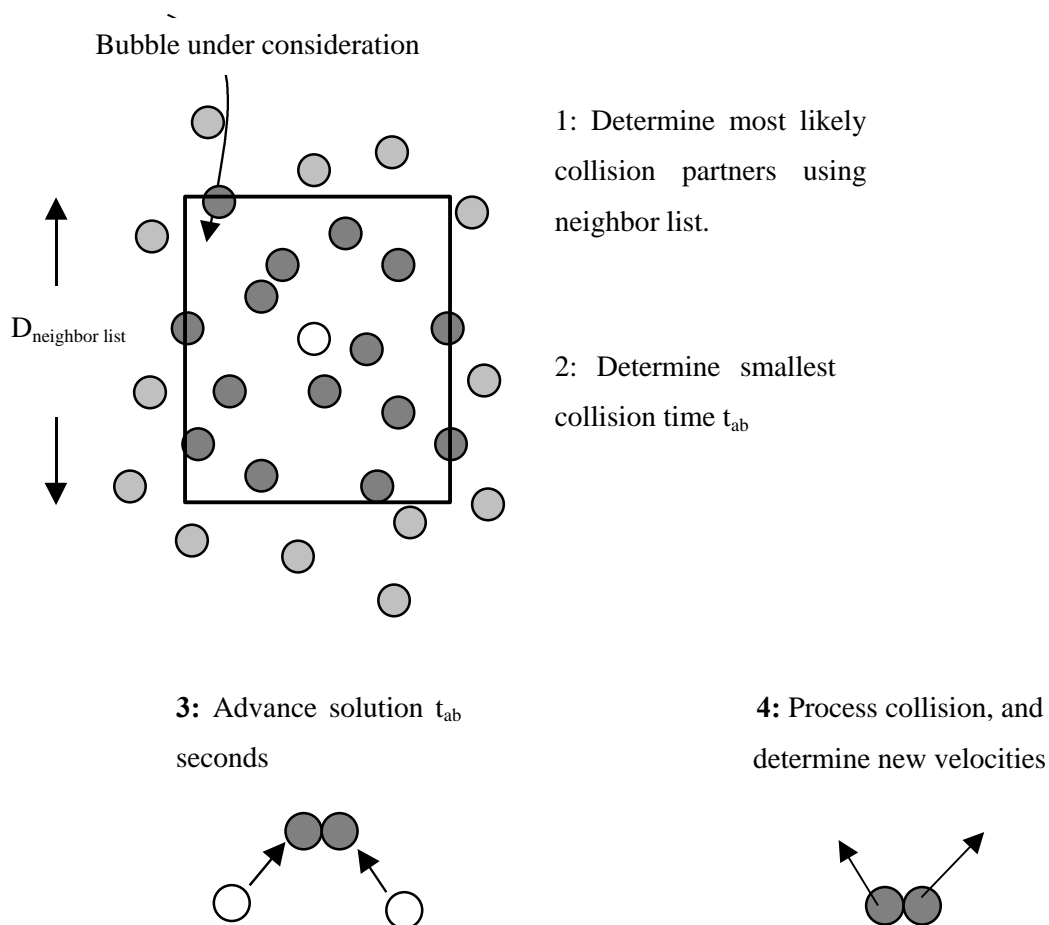


**Figure 2.** Pictorial overview of the consecutive steps taken by the hard sphere collision model incorporated in our discrete bubble model.

Because the time interval to the next collision has been calculated for each individual bubble, the smallest collision time of all bubble pairs contained in the column can now be determined. The bubble positions are subsequently updated using this time interval and the bubble velocities (obtained from equation (3)) as follows:

$$\mathbf{r}_a(t + t_{ab}) = \mathbf{r}_a(t) + \mathbf{v}_a t_{ab} \quad 20$$

Within this time interval  $t_{ab}$  there are at least two bubbles that bounce. Their velocities change due to this collision and these velocities must therefore be updated. This updating can be achieved by splitting the velocities of both bubbles into a component perpendicular to the line connecting the centers of mass of both bubbles and a component parallel to this line. As the component perpendicular to the centerline does not change due to a collision between two bubbles a and b, the other component can be calculated using:

$$(v_{ra})_{aftercollision} = 2 \frac{m_a v_{ra} + m_b v_{rb}}{m_a + m_b} - v_{ra} \quad 21$$

This completes our discussion of the collision procedure; the interested reader is referred to the paper of Hoomans *et al.* (1996) for additional details.

## 2.8 Bubble diameter distribution

Generally, bubbles in a bubble column differ in size and geometry. In our discrete bubble model, it has been assumed that every bubble contained in the column is essentially spherical. This facilitates the closure of the model in terms of the constitutive equations used to calculate the forces acting on a bubble. It has also been assumed that the bubbles do not coalesce or breakup and that the bubble size does not increase as the bubble rises through the bubble column; the bubbles are assumed to be incompressible. In the homogeneous regime, at pressures not exceeding 1.5 MPa, the bubble diameter exhibits a lognormal distribution (Jiang *et al.*, 1995). Because every simulation presented in this paper uses atmospheric pressure as a top-boundary condition, a lognormal distribution of bubble diameters is adopted.

## 3. Liquid phase hydrodynamics

### 3.1 Governing equations

The liquid phase hydrodynamics are described using the volume-averaged mass and momentum conservation equations:

$$\frac{\partial(\mathbf{e}_l \mathbf{r}_l)}{\partial t} + \nabla \cdot \mathbf{e}_l \mathbf{r}_l \mathbf{u} = 0 \quad 22$$

$$\frac{\partial(\mathbf{e}_l \mathbf{r}_l \mathbf{u})}{\partial t} + \nabla \cdot \mathbf{e}_l \mathbf{r}_l \mathbf{u} \mathbf{u} = -\mathbf{e}_l \nabla P - \nabla \cdot \mathbf{e}_l \mathbf{t}_l + \mathbf{e}_l \mathbf{r}_l \mathbf{g} + \Phi \quad 23$$



The spatial resolution with which the liquid velocity field is resolved is small compared to the size of the bubbles; the liquid-bubble interaction is therefore superimposed on the liquid velocity field. This liquid-bubble interaction is modeled using a source term  $\mathbf{F}$  that accounts for the momentum exchange between the bubbles and the surrounding liquid.

In the present study two-dimensional, isothermal motion of both the gas and the liquid phase is assumed. The basic variables that must be calculated by the model are pressure, liquid velocity and the velocity and position of each individual bubble. All other variables in the balance equations must be specified in terms of these basic variables.

### 3.2 Constitutive equations

The liquid phase viscous stress tensor  $\tau_l$  is modeled assuming general Newtonian behavior of the liquid:

$$\mathbf{t}_l = -\left[\left(\mathbf{I}_l - \frac{2}{3}\mathbf{m}_l\right)(\nabla \cdot \mathbf{u})\mathbf{E} + \mathbf{m}_l\left((\nabla \mathbf{u}) + (\nabla \mathbf{u})^T\right)\right] \quad 24$$

The bulk viscosity  $\lambda_l$  is set to zero in all simulations presented in this paper. In most simulations water is used as the liquid phase, which corresponds to a shear viscosity of  $1.0 \times 10^{-3}$  [kg m<sup>-1</sup> s<sup>-1</sup>].

### 3.3 Coupling between bubbles and liquid and vice versa

The two parts that constitute our hydrodynamic model are coupled through the liquid volume fraction  $\varepsilon_l$  and through the source term  $\mathbf{F}$  that accounts for the momentum transfer from the bubbles to the liquid. Both this liquid volume fraction  $\varepsilon_l$  and the source term  $\mathbf{F}$  have to be calculated in accordance with the number of bubbles present in a computational cell. In order to evaluate the reverse momentum transfer rate, i.e. from the liquid to a specific bubble, all quantities pertaining to the liquid phase (i.e. pressure and velocity components) have to be available at the center of mass position of the bubble. These so-called local liquid properties are calculated from the values of the volume-averaged liquid properties at the grid nodes surrounding the bubble under consideration.

The liquid volume fraction  $\varepsilon_l$  of a computational cell is calculated from the volume occupied by the bubbles in the cell under consideration and the volume of the computational cell itself:

$$\mathbf{e}_l = 1 - \frac{\sum_{\forall i \in \text{cell}} V_{bi}}{V_{\text{cell}}} \quad 25$$

In calculating this liquid volume fraction it is very important to account for bubbles overlapping with more than one computational cell. The volume occupied by these bubbles is distributed over the respective computational cells.

The momentum transfer rate from the bubbles to the liquid,  $\mathbf{F} \cdot \mathbf{V}_{\text{cell}}$ , is just the opposite of the momentum transfer rate due to drag, lift and virtual mass forces exerted by the liquid on the bubbles in the computational cell under consideration. Thus  $\mathbf{F} \cdot \mathbf{V}_{\text{cell}}$  can be calculated from:

$$\Phi V_{\text{cell}} = - \sum_{\forall i \in \text{cell}} (\mathbf{F}_{Di} + \mathbf{F}_{VMi} + \mathbf{F}_{Li}) \quad 26$$

In both equation (25) and equation (26) the volume  $V_{\text{cell}}$  represents the volume of a computational cell based on a virtual third dimension, which is due to the two-dimensional nature of our model. This third dimension can be derived from the relation between the 2D gas hold up and the 3D gas hold up assuming similar geometrical arrangement in a two-dimensional and a three-dimensional space (Hoomans *et al.*, 1996). The resulting expression for the volume of a computational cell,  $V_{\text{cell}}$ , is given by:

$$V_{\text{cell}} = dx \cdot dy \cdot 2 \cdot 3^{-0.75} \cdot D_b \quad 27$$

Let us now consider the momentum transfer from the liquid to the bubbles, viz. the force acting on the bubbles. To obtain this force acting on a bubble from equation (1) local values of the pressure, of the liquid velocity, of the partial and substantial derivatives of the pressure and of the partial and substantial derivatives of the liquid velocity have to be available at the center of mass position of the bubble. However, these Eulerian variables and their derivatives are only known at discrete nodes in the computational domain. Therefore an area-weighted averaging technique is used to obtain these local values from the Eulerian variables at the four grid nodes surrounding the bubble. With reference to Figure 3 the local value of a quantity  $f$  can be calculated using:

$$f(\mathbf{r}_i) = \frac{1}{dxdy} \sum_{n=1}^4 A_n f_n \quad 28$$

With  $f_n$  being some Eulerian quantity at node  $n$ , and  $A_n$  representing an area equal to:

$$A_1 = (dx - \mathbf{dx})(dy - \mathbf{dy})$$

$$A_2 = \mathbf{dx}(dy - \mathbf{dy})$$

$$A_3 = (dx - \mathbf{dx})\mathbf{dy}$$

$$A_4 = \mathbf{dx}\mathbf{dy}$$

29

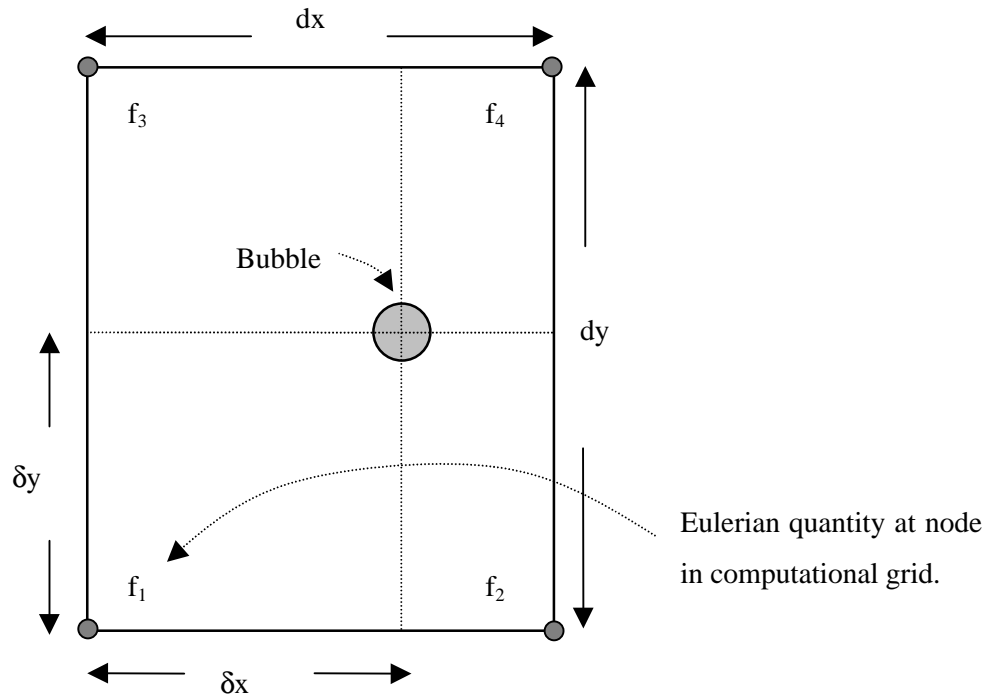


**Figure 3.** Area weighting of four Eulerian quantities ( $f_{1..4}$ ) at the grid nodes surrounding the bubble to obtain the value of that quantity at the center of mass position of the bubble.

**Table 1:** Cell flags and corresponding cell types used in defining boundary conditions

$fl(i,j)$ :	Boundary condition:
1	Interior cell, no boundary conditions specified
2	Impermeable wall, free slip boundary
3	Impermeable wall, no slip boundary
4	Fluid phase influx cell, normal velocity has to be specified
5	Prescribed pressure cell, free slip boundary
6	Continuous outflow cell, free slip boundary
7	Impermeable floor, free slip boundary
8	Impermeable floor, no slip boundary
9	Corner cell, no boundary conditions specified

### 3.4 Boundary conditions

The boundary conditions required to solve the model equations are incorporated in the model using the flag matrix concept. This concept, also used by Kuipers *et al.* (1993), allows boundary conditions to be set for each individual computational cell. Using this flag matrix concept a variety of boundary conditions can be set by specifying the value of the cell flag  $fl(i,j)$ . In table 1 an overview of the various cell flags and the corresponding boundary conditions is given. Figure 4 depicts a typical grid layout used in many of the simulations presented in this paper.

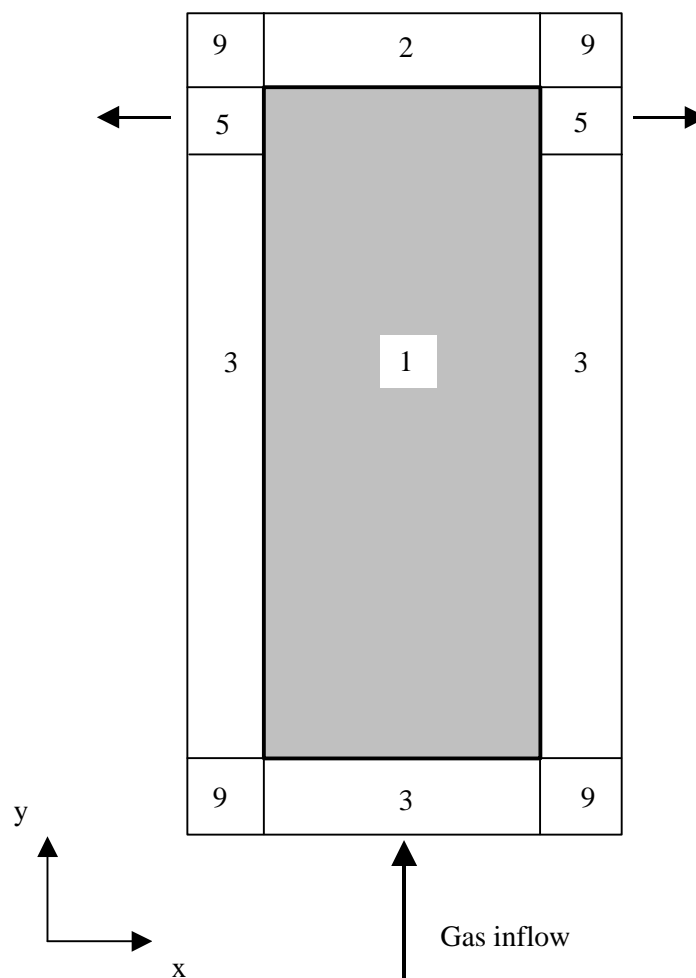


**Figure 4.** Typical grid layout used in a simulation with the discrete bubble model. The cell flags depicted in this Figure are explained in Table 1.

The boundary conditions for the discrete bubble part of the model are essentially specified by the collision routine that accounts for bubble-wall interactions.

#### 4. Numerical solution

In the second and third section of this paper the physics and numerics of our discrete bubble model have been described in detail. This model has been implemented in a computer code written in C. The computer code takes consecutive steps in time, during each of which the code calculates the forces acting on the bubbles in the system, and updates the bubble velocities and the bubble positions, taking into account possible collisions between bubbles. Finally the code calculates the new liquid velocity field using an algorithm also used by Kuipers *et al.* (1993). At the end of each timestep various user-specified data in several file formats can be saved.

On average calculating one minute of the time dependent behavior of a typical bubble column containing several thousand bubbles requires approximately 4 hours dedicated CPU time on a Silicon Graphics Indigo<sup>2</sup> workstation (R4400 MIPS RISC processor). The CPU time depends on the size of the column and the number of bubbles contained by the bubble column. A twofold increase in the number of bubbles in the bubble column (which can be achieved by doubling the superficial gas velocity) roughly doubles the CPU time required to simulate one minute of real-time operation of the bubble column.

#### 5. Results and discussion

In the previous sections we have presented a discrete bubble model for a gas-liquid bubble column. The model incorporates both a bubble-bubble interaction model and a fundamental description of the bubble dynamics. In this section results obtained with our discrete bubble model will be compared to experimental data reported in the literature. Because the model incorporates a detailed description of the bubble dynamics, the relative importance of the various forces acting on a bubble will be studied theoretically.

##### 5.1 Terminal rise velocity of a single bubble

As a first test case for our model the terminal rise velocity of a single bubble, as calculated from a balance of forces, will be compared to the bubble rise velocity predicted by our model. For a bubble rising with a constant velocity through a quiescent liquid the buoyancy force equals the sum of gravity and drag forces. From this balance of forces the bubble's rise velocity can be derived:

$$\mathbf{v}_{rise} = \sqrt{\frac{\frac{8}{3}(\mathbf{r}_g - \mathbf{r}_l)R_b g}{C_D \mathbf{r}_l}} \quad 30$$

The drag coefficient  $C_D$  is calculated using the standard drag curve (equation (6)); including this equation into equation (30) yields an implicit equation in  $\mathbf{v}_{rise}$ , which can be solved numerically. This yields a terminal rise velocity of 20.8 [cm s<sup>-1</sup>] for a 2 [mm] air bubble in water.

**Table 2:** Parameters used to calculate terminal rise velocity of a single air bubble in water using the Euler-Lagrange model.

Bubbles & liquid		Column	
Bubble diameter	2.0 [mm] (uniform)	Height	1.50 [m]
Gas flow rate	-	Width	0.50 [m]
Density gas	1.2 [kg m <sup>-3</sup> ]	Number x-cells	50
Density liquid	1000 [kg m <sup>-3</sup> ]	Number y-cells	100
Liquid shear viscosity	1 x 10 <sup>-3</sup> [Pa s]	DT	5.0 x 10 <sup>-3</sup> [s]
Gas	air		
Liquid	tap water		

Our two-dimensional gas-liquid model was also used to determine the terminal velocity of a single bubble rising in a liquid. We therefore simulated the rise of a single 2 [mm] air bubble in a bubble column of 1.5 [m] in height and 0.50 [m] in width (computational conditions are listed in table 2). At a height of 1m above the gas distributor the bubble appeared to have a steady rise velocity of 20.9 [cm s<sup>-1</sup>], which agrees well with the theoretically calculated bubble rise velocity.

## 5.2 Comparison with experimental data reported by Becker et al. (1995)

Becker *et al.* conducted experiments in a pseudo two-dimensional bubble column. The results of two of their experiments, with a small and a large superficial gas velocity, will be compared with computational results obtained using our model. The experimental setup used by Becker *et al.* (1995) is depicted in Figure 5; it consists of a two-dimensional bubble column (width: 50 [cm], column height: 2 [m], liquid height: 1.5 [m] and depth: 8 [cm]). The column is equipped with a gas distributor consisting of five, individually controllable porous plates.

Becker *et al.* fed gas (air) to the column (containing water) through only one of the five porous plates during their experiments. This plate is located 15 [cm] from the left wall of the column and consists of a 40 [mm] plastic disc with an active pore size of 40 [ $\mu\text{m}$ ]. Becker *et al.* reported data on the liquid velocity field obtained for two different superficial gas velocities. Liquid velocities were measured using Laser Doppler Anemometry (LDA).

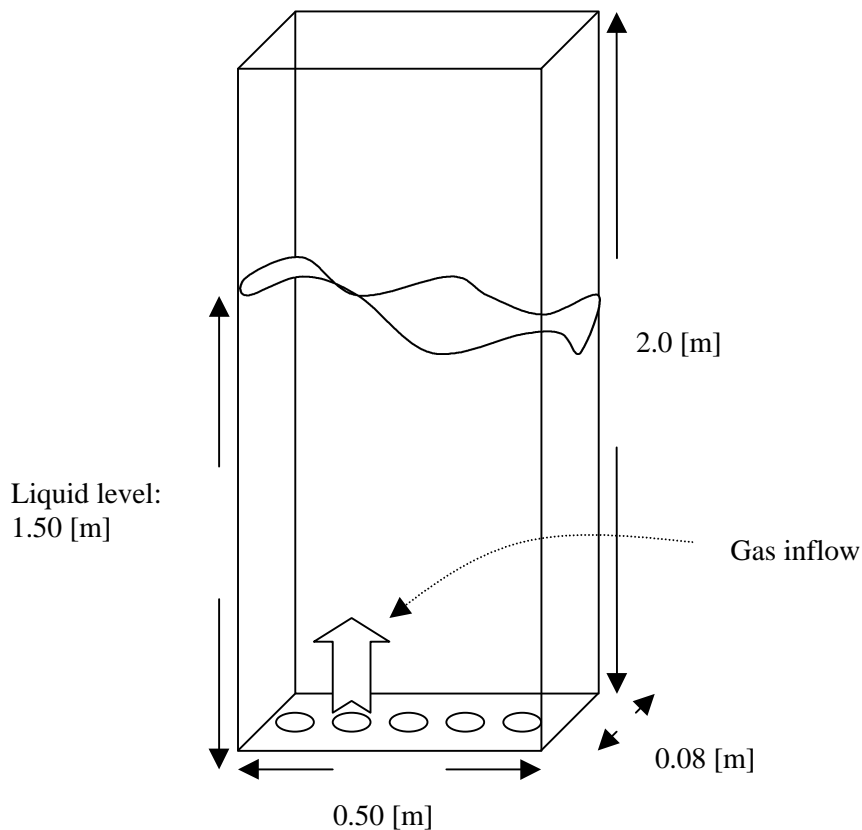


**Figure 5.** Experimental setup used by Becker *et al.* (1995).

Our model was used to simulate a vertical, two dimensional, cross-section of Becker's bubble column, and accounted for drag (according to equation (6)), lift and added mass forces acting on the bubbles. Hydrodynamic interaction between bubbles was however, neglected. The gas bubbles, with a (uniform!) diameter of 3 [mm], were generated in a regular pattern at the gas distributor where the rate of bubble generation was calculated from the specified gas flow rate. Additional experimental conditions and numerical parameters are listed in Table 3.

**Table 3:** Parameters used in model simulation of experiments reported by Becker *et al.* (1995)

Bubbles & liquid		Column	
Bubble diameter	3.0 [mm] (uniform)	Height	2.00 [m]
Gas flow rate (high)	8.0 [l min <sup>-1</sup> ]	Liquid Height	1.50 [m]
Gas flow rate (low)	1.6 [l min <sup>-1</sup> ]	Width	0.50 [m]
Density gas	1.2 [kg m <sup>-3</sup> ]	Number x-cells	50
Density liquid	1000 [kg m <sup>-3</sup> ]	Number y-cells	100
Liquid shear viscosity	1 x 10 <sup>-3</sup> [Pa s]	Orifice width	4.0 x 10 <sup>-2</sup> [m]
Gas	air	DT	5.0 x 10 <sup>-3</sup> [s]
Liquid	water		

### 5.2.1 Comparison between model and experiment for large superficial gas velocity

Becker *et al.* (1995) describe in detail the flow structure observed in their bubble column at a gas flow rate of 8.0 [l min<sup>-1</sup>]. They report a flow dominated by a single circulation cell that covers the entire height of the column. The strong liquid circulation within this circulation cell pushes the bubble swarm firmly against the left wall of the bubble column. As the bubble swarm reaches the free surface it is pushed towards the column's center by a smaller (secondary) vortex at the upper left corner. Due to the strong liquid circulation, with liquid up flow in the vicinity of the bubble swarm and down flow along the right wall of the column, part of the bubble swarm flows downwards near the right wall of the column.

Figure 6 depicts a number of snapshots of the instantaneous bubble positions and the accompanying liquid velocity field in Becker's bubble column as calculated by our discrete bubble model. It can be seen from this Figure that the computed flow structure is similar to that reported by Becker *et al.* Our discrete bubble model predicts a strong liquid circulation that pushes the bubble swarm firmly towards the left wall of the column. This strong liquid circulation is induced by the large amount of bubbles rising through the bubble column. Along the left wall of the bubble column, a secondary vortex develops, which slowly moves up and down the upper part of the left column wall thus causing some unsteadiness. In this respect the results obtained with our model differ from those obtained by Becker *et al.* who reported an essentially steady state flow structure. This difference between model and experiment is most likely due to the two-dimensional nature of our model. It can also be seen



that some bubbles flow downwards near the right wall of the column, as is also reported by Becker *et al.* These bubbles are more or less trapped in the downward liquid flow and form a rotating bubble-cloud, which does not change in size considerably.

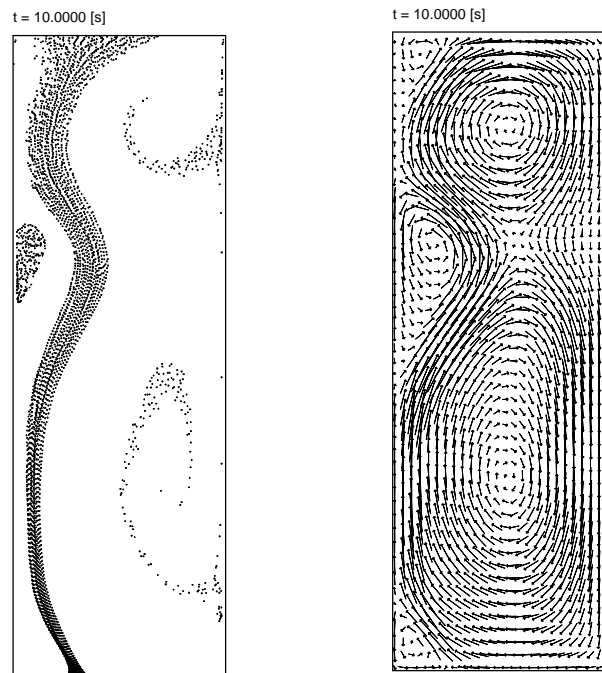


**Figure 6a.** Instantaneous bubble positions and associated liquid velocity field at 10 [s] simulated operation of the bubble column. Simulation of experiment conducted by Becker *et al.* (1995) for high superficial gas velocity. Gas flow rate =  $8.0 \text{ [l min}^{-1}\text{]}$ . Additional conditions are listed in Table 3. The reference vector represents a velocity of  $10 \text{ [cm s}^{-1}\text{]}$ .

The computed time-averaged liquid velocity field is depicted in Figure 7. This Figure clearly reveals a flow pattern that is dominated by a single circulation cell with liquid up flow near the left wall of the column and down flow near the opposite wall of the column. The velocity field depicted in Figure 7 is time-averaged over the first 316 seconds of simulation time.

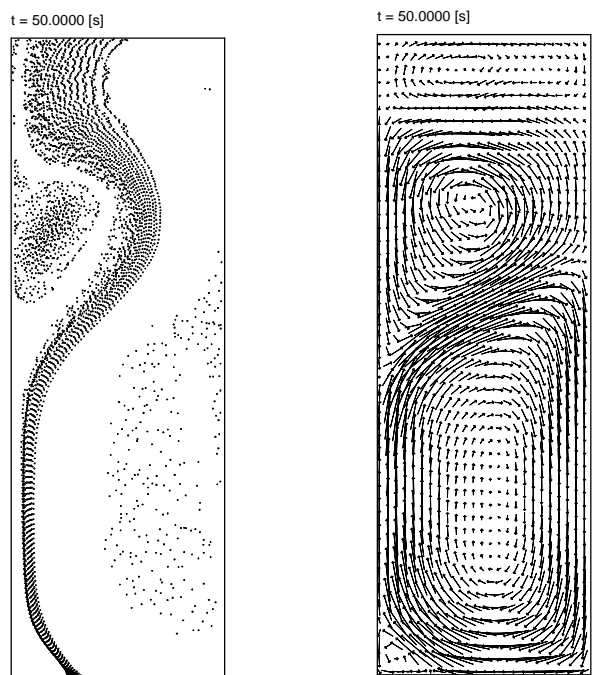


**Figure 6b.** Instantaneous bubble positions and associated liquid velocity field at 50 [s] simulated operation of the bubble column. See Figure 6a.

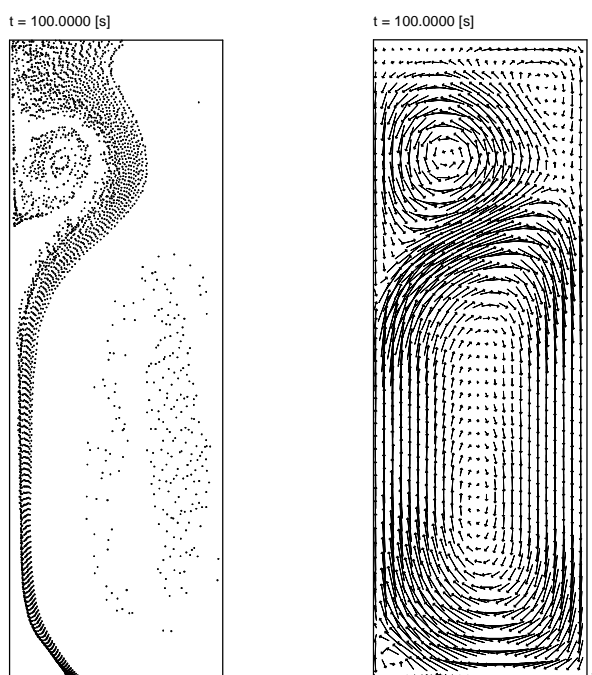


**Figure 6c.** Instantaneous bubble positions and associated liquid velocity field at 100 [s] simulated operation of the bubble column. See Figure 6a.

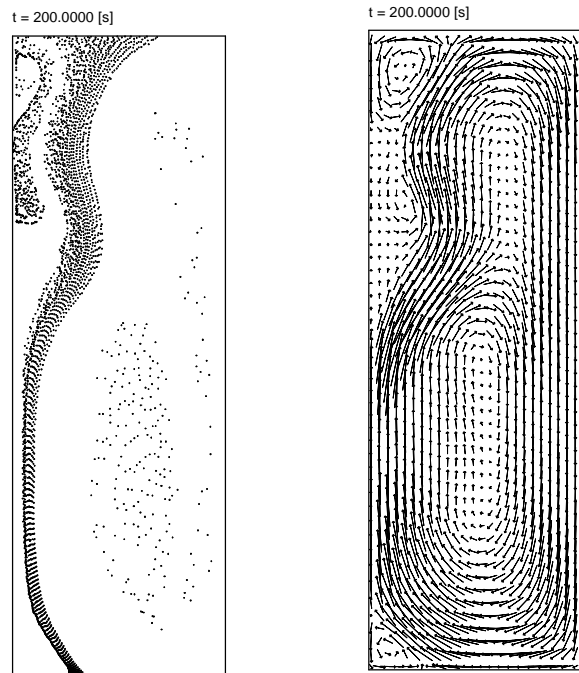


**Figure 6d.** Instantaneous bubble positions and associated liquid velocity field at 200 [s] simulated operation of the bubble column. See Figure 6a.

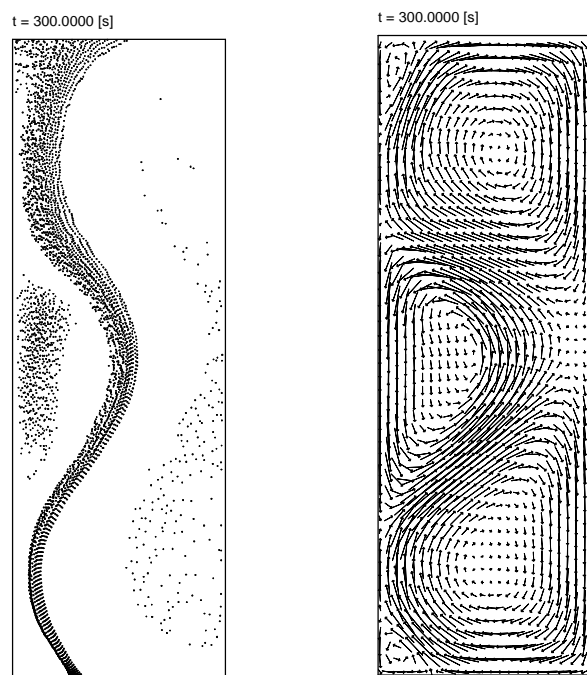


**Figure 6e.** Instantaneous bubble positions and associated liquid velocity field at 300 [s] simulated operation of the bubble column. See Figure 6a.

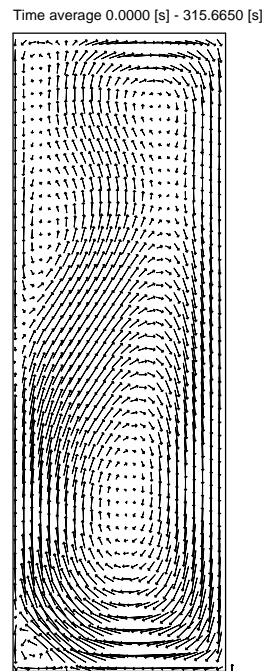


**Figure 7.** Time-averaged liquid velocity field (0 – 316 [s]). Simulation of experiment conducted by Becker *et al.* (1995) for high superficial gas velocity. Gas flow rate =  $8.0 \text{ [l min}^{-1}\text{]}$ . Additional conditions are listed in Table 3. The reference vector represents a velocity of  $10 \text{ [cm s}^{-1}\text{]}$ .

### 5.2.2 Comparison between model and experiment for small superficial gas velocity

At the low superficial gas velocity Becker *et al.* observed a remarkably different flow pattern in their bubble column. The bubble swarm now moves up wards in a meandering manner. Several liquid circulation cells were reported which change their location and size continuously. The flow was observed to be highly dynamic. Time averaged measurements of the vertical liquid velocity at a point  $900 \text{ [mm]}$  above the gas distributor and  $35 \text{ [mm]}$  to the right of the column's left wall, revealed a period of oscillation of the axial liquid velocity of approximately  $40 \text{ [s]}$ ; with axial liquid velocities ranging from  $-20$  to  $+20 \text{ [cm s}^{-1}\text{]}$ .

Figure 8 shows snapshots of the time-dependent behavior of the bubble plume at this lower gas velocity as calculated with our CFD model. It can clearly be seen that our model predicts a meandering behavior similar to that reported by Becker *et al.* Video representation of the computed results unveiled that the meandering behavior of the bubble plume is caused by a vortex that develops at the upper left corner of the column. This vortex subsequently descends along the left wall of the column (pushing the bubbles towards the center of the column) and disappears at the bottom of the column. This process then continues with the

development of a new vortex at the upper left corner of the column. This ongoing process causes the meandering behavior of the bubble plume and the observed inherent unsteadiness of the bubble column.

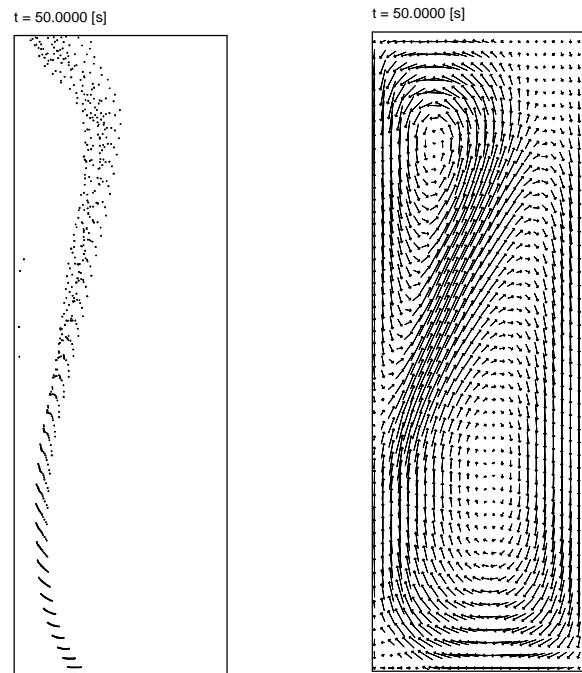


**Figure 8a.** Instantaneous bubble positions and associated liquid velocity field at 50 [s] simulated operation of the bubble column. Simulation of experiment conducted by Becker *et al.* (1995) for low superficial gas velocity. Gas flow rate =  $1.6 \text{ [l min}^{-1}\text{]}$ . Additional conditions are listed in Table 3. The reference vector represents a velocity of  $10 \text{ [cm s}^{-1}\text{]}$ .

Figure 8f depicts the axial liquid velocity as a function of time at the point chosen by Becker *et al.* for their measurements of the axial liquid velocity. The average axial liquid velocity predicted by our discrete bubble model is  $-0.077 \text{ [m s}^{-1}\text{]}$ , which differs from the result obtained by Becker *et al.* who measured an average axial liquid velocity of  $-0.038 \text{ [m s}^{-1}\text{]}$ . From Figure 8f it can also be inferred that the downward liquid velocities predicted by our model (up to  $-50 \text{ [cm s}^{-1}\text{]}$ ) exceed those measured by Becker *et al.* The period of oscillation of the vertical liquid velocity calculated by our model is approximately 30 [s]. This period of oscillation, computed by our model, is smaller than the period measured by Becker *et al.* (40 [s]). These differences are most likely due to the two-dimensional nature of our model which does not account for the front and back wall of the real-life pseudo two-dimensional bubble column used by Becker *et al.*

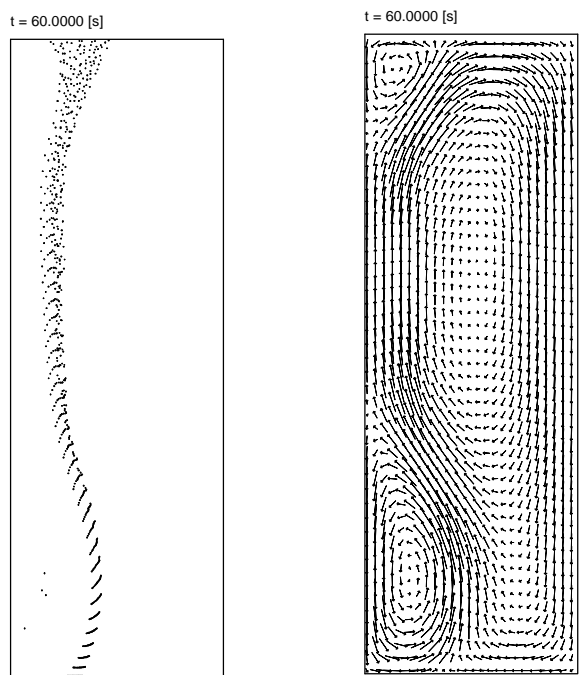


**Figure 8b.** Instantaneous bubble positions and associated liquid velocity field at 60 [s] simulated operation of the bubble column. See Figure 8a.

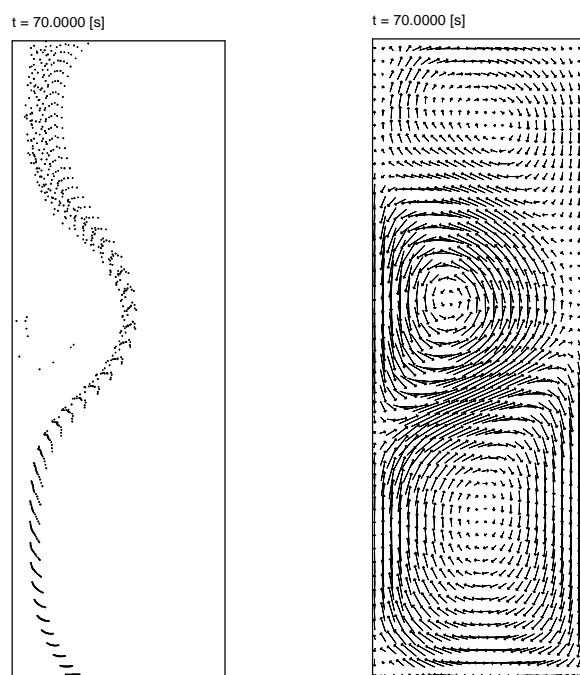


**Figure 8c.** Instantaneous bubble positions and associated liquid velocity field at 70 [s] simulated operation of the bubble column. See Figure 8a.

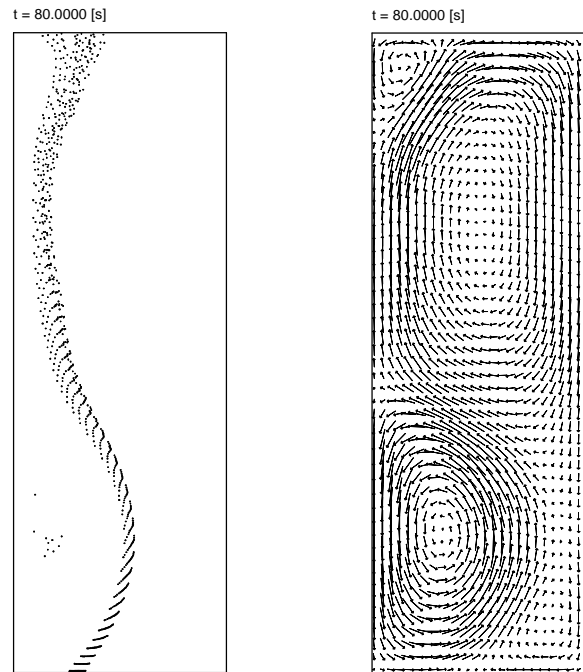


**Figure 8d.** Instantaneous bubble positions and associated liquid velocity field at 80 [s] simulated operation of the bubble column. See Figure 8a.

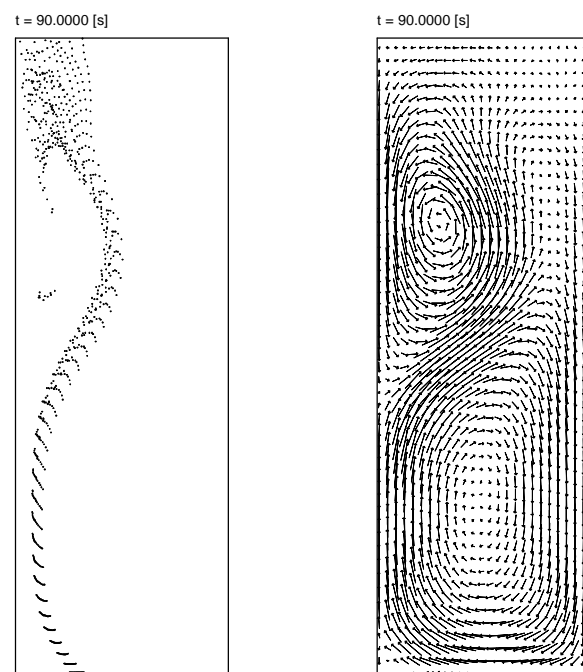


**Figure 8e.** Instantaneous bubble positions and associated liquid velocity field at 90 [s] simulated operation of the bubble column. See Figure 8a.

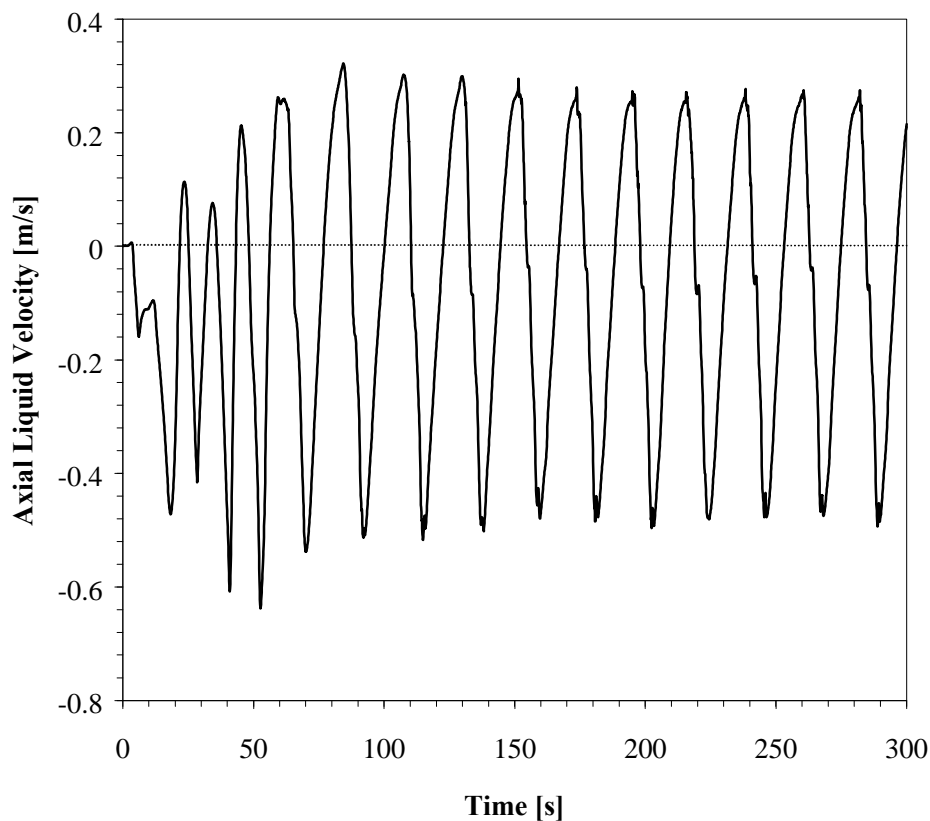


**Figure 8f.** Axial liquid velocity at 900 [mm] above the gas distributor and 35 [mm] from the left wall of the column versus time (0 – 300 [s]). Simulation of experiment conducted by Becker *et al.* (1995) at the low superficial gas velocity. Gas flow rate = 1.6 [l min<sup>-1</sup>]. Additional conditions are listed in Table 3.

### 5.3 The forces acting on the bubbles

One of the key features of the model presented in this Chapter is the detailed description of the bubble dynamics and the forces acting on these bubbles. In section 2 it has been assumed that the force acting on a spherical bubble rising in a liquid is composed of separate and uncoupled contributions from pressure gradient, gravity, drag, added mass, lift and hydrodynamic interaction between adjacent bubbles. This particular section focuses on the impact of the various forces on the flow pattern ultimately obtained in a bubble column. The importance of the added mass force will be discussed. We will compare results obtained with our model *using* the lift force acting on the bubbles with results computed when *neglecting* the lift force. Moreover, we will compare results obtained with either approximation of the drag coefficient, as discussed in section 2. And finally, we will study the way in which



hydrodynamic interaction among bubbles affects the overall flow pattern ultimately obtained in a bubble column.

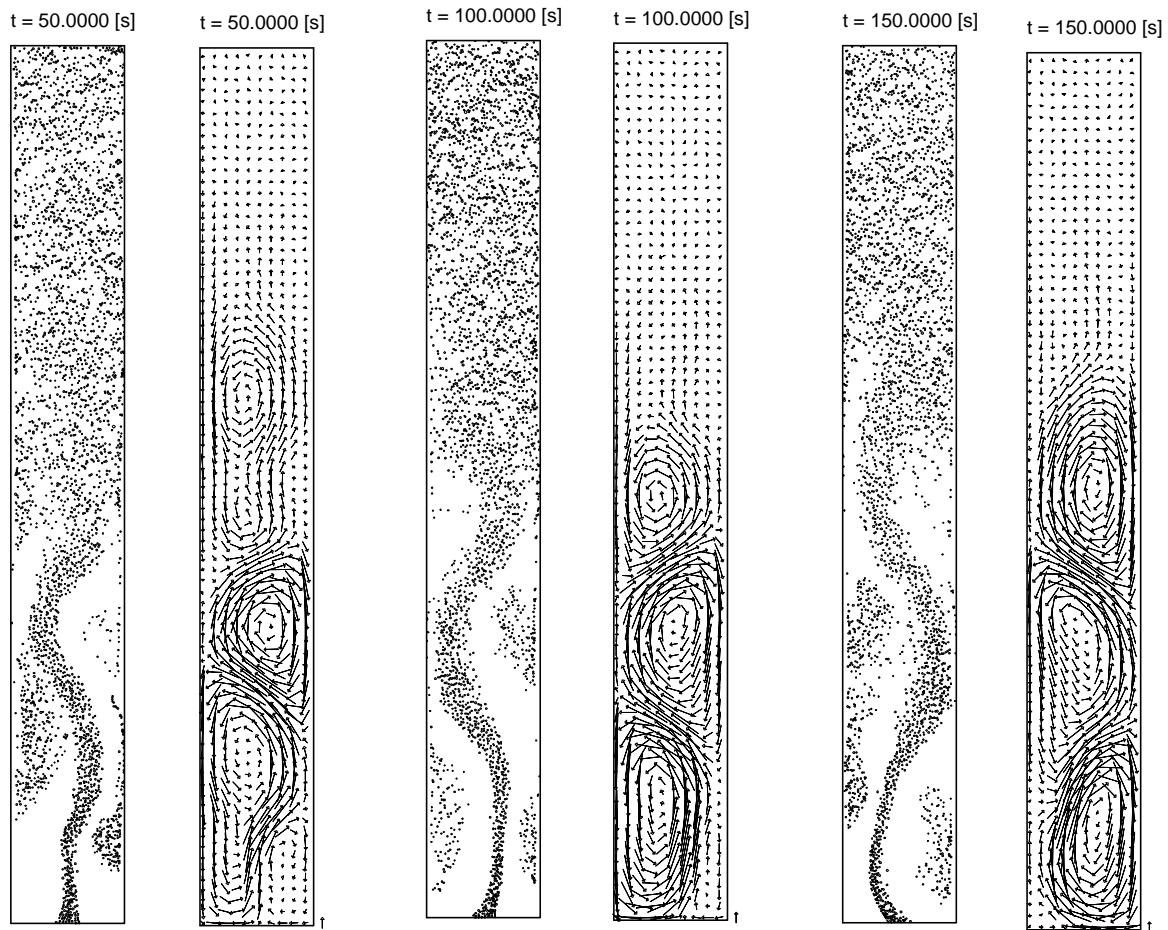


**Figure 9[a-c].** Instantaneous bubble positions and associated liquid velocity field in a bubble column with an aspect ratio of 7.7 at 50 [s], 100 [s] and 150 [s] after start up. The superficial gas velocity is equal to  $35 \text{ [mm s}^{-1}\text{]}$ . Simulation of an experiment conducted by Chen *et al.* (1989). Base case scenario: drag, lift and added mass forces included; hydrodynamic interaction is not accounted for. A log normal bubble size distribution is employed. The reference vector corresponds to a liquid velocity of  $10 \text{ [cm s}^{-1}\text{]}$ .

To study the effects of the various forces acting on a bubble, we have used an experiment by Chen *et al.* (1989) as a test case. Chen *et al.* conducted experiments in a pseudo two-dimensional bubble column and assessed the effect of the column aspect ratio on the flow structure. Their experiment and experimental findings are discussed in detail in Chapter 4, and the interested reader is referred to this Chapter (or the paper by Chen *et al.*) for additional details. Figure 9[a-c] depicts snapshots of the two-phase flow prevailing in a bubble column

with an aspect ratio of 7.7. Table 4 lists the relevant physical properties and numerical parameters used in this computation.

**Table 4.** Parameters used in the computations to assess the effect of the various forces on the flow structure. **Base Case scenario.** Geometry and gas flow rate as used by Chen *et al.* (1989).

Column dimensions	
Width:	0.1750 [m]
Height:	
L/D = 7.7	1.3475 [m]
Superficial gas velocity:	35.0 [mm s <sup>-1</sup> ]
Physical properties	
Density liquid:	1000.0 [kg m <sup>-3</sup> ]
Viscosity liquid:	1.0 x 10 <sup>-3</sup> [Ns m <sup>-2</sup> ]
Density gas:	1.2 [kg m <sup>-3</sup> ]
Bubble diameter:	2.0 [mm] (lognormal distribution)
C <sub>D</sub>	Equation (6)
C <sub>L</sub>	0.53
C <sub>VM</sub>	0.5
Hydrodyn. Int.	Not considered
Computational parameters	
Number of computational cells in lateral direction:	20
Number of computational cells in axial direction:	
L/D = 7.7	154
Time step:	5.0 x 10 <sup>-3</sup> [s]

The case depicted in Figure 9[a-c] is what we call the base case scenario. These results have been obtained using our discrete bubble model, accounting for drag (drag coefficient according to equation (6)), lift and added mass forces acting on the bubbles. Hydrodynamic interaction between adjacent bubbles has however been neglected. Figure 9[a-c] clearly reveals the time-dependent characteristics of the two-phase flow prevailing in the bubble column under consideration. A distinct bubble plume that oscillates from left to right and *vice versa* through the column characterizes the lower section of the bubble column. Whereas in

the upper section of the column, the bubbles have been dispersed over the entire cross section of the column under the action of the lift force. In the upper section of the bubble column, the classical liquid flow field associated with the homogeneous regime prevails (liquid up flow in the wakes of the bubbles and down flow in between the bubbles).

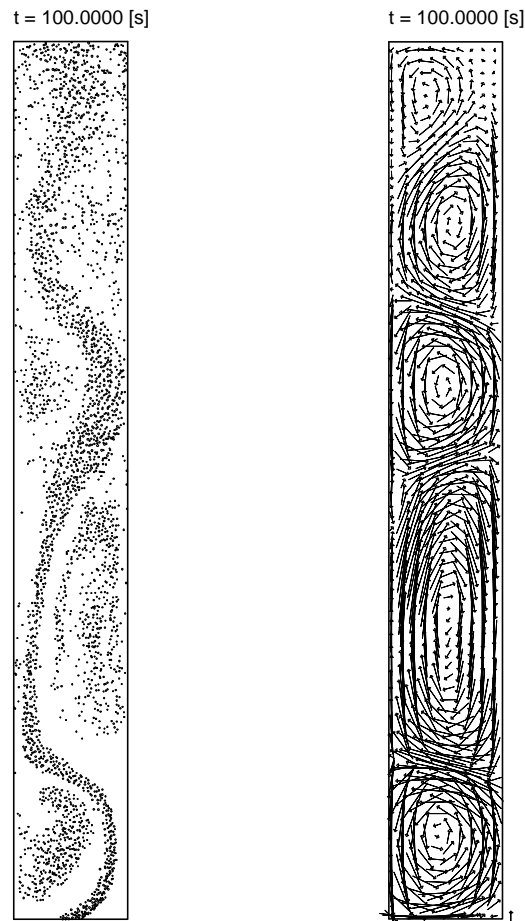


**Figure 10a.** Instantaneous bubble positions and associated liquid velocity field in a bubble column with an aspect ratio of 7.7 at 100 [s] after start up. The superficial gas velocity is equal to 35 [mm s<sup>-1</sup>]. Simulation of an experiment conducted by Chen *et al.* (1989). **No lift scenario:** drag and added mass forces included; lift force and hydrodynamic interaction are not accounted for. A log normal bubble size distribution is employed. The reference vector corresponds to a liquid velocity of 10 [cm s<sup>-1</sup>].

### 5.3.1 The added mass force

The added mass force appears to be extremely important in the vicinity of the gas distributor. In the model presented in this paper, bubbles are assumed to grow at the distributor until a specified radius has been attained; at that point in time the bubbles detach from the

distributor. Near the distributor the bubbles accelerate under the action of the buoyancy force. The only force restraining this acceleration (in the very early stages of a bubble's ascend) is the added mass force; drag forces are not yet significant because the slip velocity is small after the bubble detaches from the gas distributor. Without added mass forces incorporated in the discrete bubble model, the bubble acceleration attains unrealistic values due to the strong buoyancy force and the small mass of the bubble. The omission of the added mass force will therefore cause severe numerical difficulties. From our model simulations and careful analysis of the computed data, we conclude that added mass forces are essential for an accurate description of the behavior of small, spherical gas bubbles in the vicinity of the gas distributor of a bubble column.

### 5.3.2 The lift force

To assess the impact of the lift force acting on the bubbles on the overall flow pattern prevailing in a bubble column we compared the base case results discussed above, with results obtained without accounting for the lift force ( $C_L = 0$ ) acting on the bubbles. Figure 10a depicts the flow pattern predicted by our model when neglecting lift forces acting on the bubbles ( $C_L = 0$ ). The flow pattern clearly differs from the flow pattern depicted in Figure 9[a-c], a distinct bubble plume can be observed in the entire column. Bubbles do not disperse over the cross section of the column, and the associated liquid velocity field also differs considerably from that shown in Figure 9[a-c]. Vortices can now be seen over the entire height of the column.

Figures 10b and 10c compare the time-averaged axial liquid velocity and the time-averaged gas hold up computed with and without lift forces acting on the bubbles. The difference is clear. The axial liquid velocity computed when lift forces are excluded exceeds the axial velocity computed with the model that does account for lift forces. This is due to the distinct bubble plume dominating the flow in the entire column (Figure 10a). This bubble plume gives rise to locally very high gas holdups and therefore to rather large axial liquid velocities. The time averaged gas hold up profiles shown in Figure 10c also clearly differ; in the base case scenario ( $C_L = 0.53$ ) the void fraction clearly exhibits 'wall peaking' generally observed in bubbly up flows (Serizawa *et al.*, 1986). This wall peaking is virtually absent if lift forces are not taken into account.

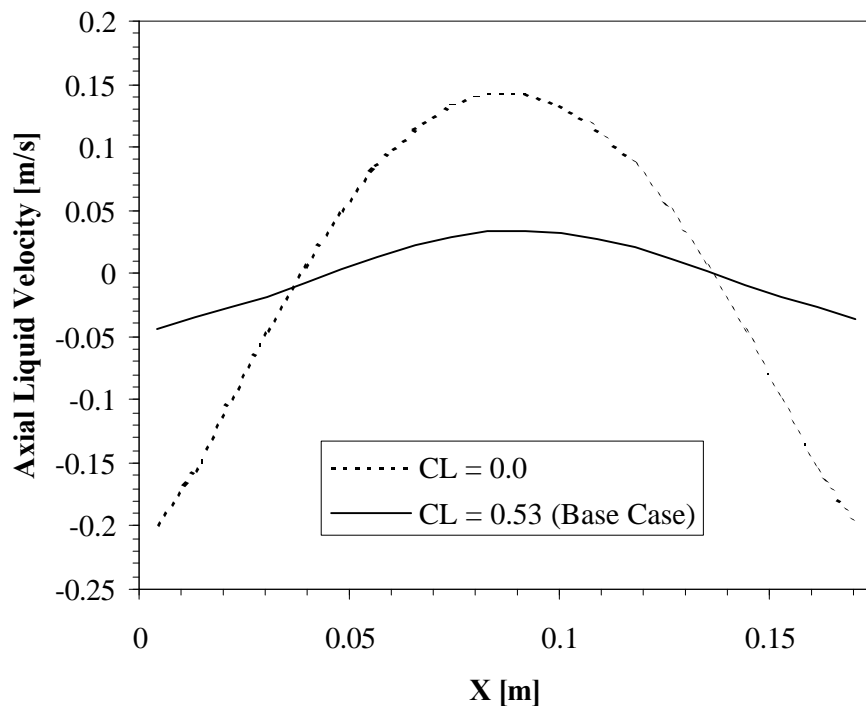


**Figure 10b.** Time averaged (0 – 150 [s]) radial profile of the axial liquid velocity at 1.00 [m] above the gas distributor. Simulation of an experiment conducted by Chen *et al.* (1989). Superficial gas velocity = 35 [mm s<sup>-1</sup>]. This figure compares the velocity profiles calculated **with** and **without** lift forces acting on the bubbles.

Let us explain this ‘wall peaking’ phenomena in some more detail. The radial profile of the axial liquid velocity in a bubble column is (on average) characterized by liquid upflow in the center of the bubble column and liquid downflow along the walls of the column (Figure 10b). The lift force acting on bubbles in the center of the column is directed towards the lower velocity region (i.e. the column wall). The lift force acting on bubbles in the liquid downflow region on the other hand, is directed towards the high velocity region (i.e. the column’s center). The combined effect causes the experimentally observed ‘wall peaking’ of the void fraction. Our findings also seem to be supported by the work of Yang and Thomas (1998) who showed that the lift force acting on bubbles plays a key role in determining the void fraction distribution and causes ‘wall peaking’ of the void fraction in bubbly up flow. We therefore concluded that the lift force acting on bubbles is extremely important in bubble column simulations and can not be omitted or neglected.

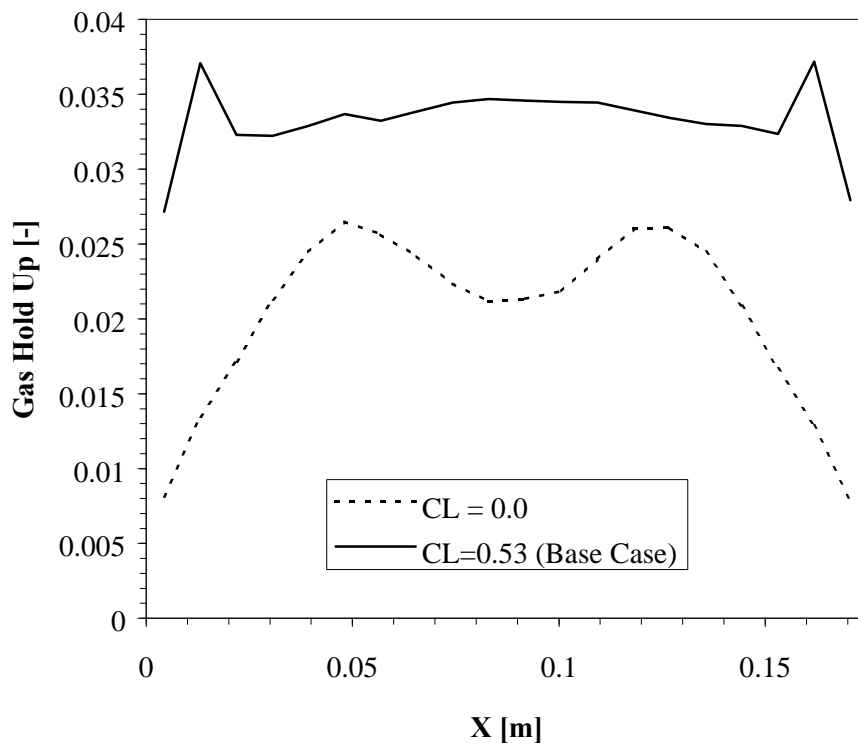


**Figure 10c.** Time averaged (0 – 150 [s]) radial gas holdup profile at 1.00 [m] above the gas distributor. Simulation of an experiment conducted by Chen *et al.* (1989). Superficial gas velocity =  $35 \text{ [mm s}^{-1}\text{]}$ . This figure compares the radial porosity profiles calculated **with** and **without** lift forces acting on the bubbles.

### 5.3.3 The drag force

In section 2 we introduced two different approximations of the drag coefficient for spherical bubbles rising in tap water. Figure 11 compares the time-averaged axial liquid velocity in a bubble column with an aspect ratio of 7.7 computed with both drag coefficients. It can be seen that the profiles differ slightly, this is due to the discrete nature of our model and the finite averaging window. On balance however, the difference (on a time-averaged basis) appears to be extremely small. It is therefore concluded that although the drag force is of crucial importance, and can not be neglected; the particular approximation used does not significantly affect the results ultimately obtained with our CFD model.

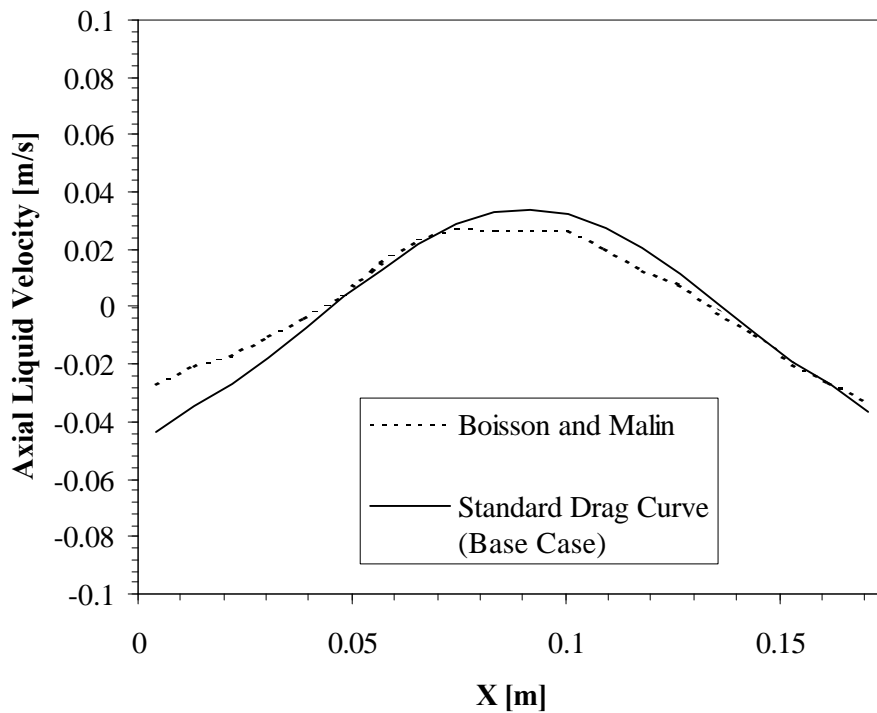


**Figure 11.** Time averaged (0 – 150 [s]) radial profile of the axial liquid velocity at 1.00 [m] above the gas distributor. Simulation of an experiment conducted by Chen *et al.* (1989). Superficial gas velocity = 35 [mm s<sup>-1</sup>]. This figure compares the velocity profiles calculated using two different approximations of the drag coefficient.

#### 5.3.4 Hydrodynamic interaction

Finally, we will study the effect of the hydrodynamic interaction between neighboring bubbles on the macroscopic flow pattern prevailing in our bubble column. Figure 12a depicts the instantaneous position of the bubbles and the associated liquid flow field in the bubble column with an aspect ratio of 7.7. The conditions used for this computation are similar to those used in the base case scenario, except that hydrodynamic interaction between bubbles is now taken into account. On the face of it, the differences between Figure 12a and Figure 9b (without hydrodynamic interaction) are very small. The flow pattern in the lower half of the column is in both cases dominated by a bubble plume that oscillates from left to right (and back) through the column. In the upper half of the column, bubbles have been dispersed over the entire cross section of the column.

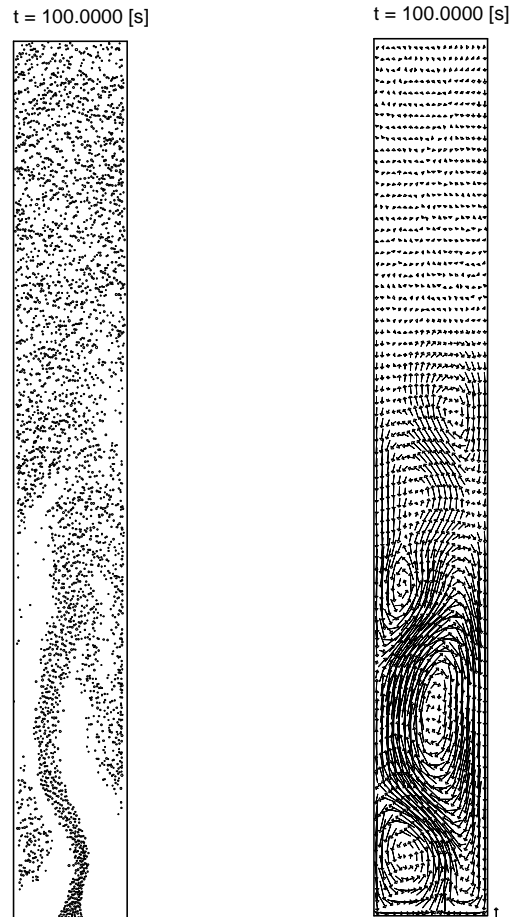


**Figure 12a.** Instantaneous bubble positions and associated liquid velocity field in a bubble column with an aspect ratio of 7.7 at 100 [s] after start up. Simulation of an experiment conducted by Chen *et al.* (1989). Superficial gas velocity = 35 [mm s<sup>-1</sup>]. **Hydrodynamic interaction is taken into account.**

A log normal bubble size distribution is employed. The reference vector corresponds to a liquid velocity of 10 [cm s<sup>-1</sup>].

On a time-averaged basis, the differences are also small, as can be seen most clearly from Figure 12b and Figure 12c. These Figures depict the time-averaged axial liquid velocity and the time-averaged void fraction as calculated by our model. Both scenarios (base case and hydrodynamic interaction) predict wall peaking of the void fraction and a circulating flow with liquid up flow in the column center and liquid down flow along the walls of the column. The small differences that can be inferred from these Figures are most likely due to the discrete nature of our model and the finite averaging window (0 – 150 [s] simulation time) employed.

Based on the results presented in Figures 12[a-c] it can be concluded that the effect of the hydrodynamic interaction between neighboring bubbles on the overall flow pattern observed



in a bubble column is small. This is expected behavior because the bubble column used in this study (Chen's bubble column with an aspect ratio of 7.7) is operated in the homogeneous regime at relatively low void fractions ( $< 5\%$ ). This implies that the average distance between bubbles is relatively large. The force that the bubbles exert on each other due to hydrodynamic interaction will therefore be small, especially in view of the strong decay of this force with increasing distance between the interacting bubbles (see also section 2.6).

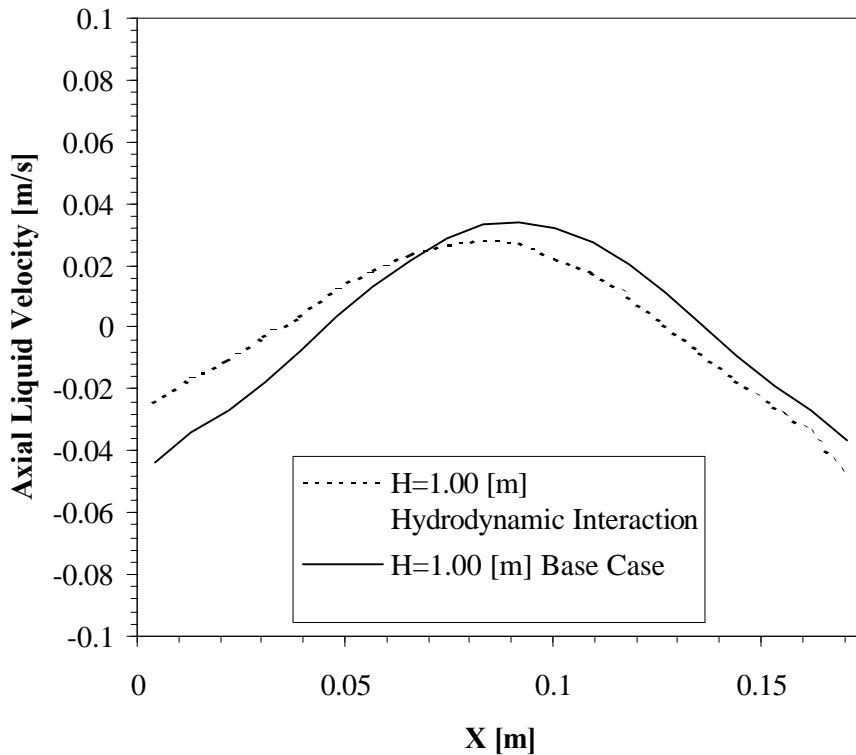


**Figure 12b.** Time averaged (0 – 150 [s]) radial profile of the axial liquid velocity at 1.00 [m] above the gas distributor. Simulation of an experiment conducted by Chen *et al.* (1989). Superficial gas velocity = 35 [mm s<sup>-1</sup>]. This figure compares the velocity profiles calculated **with** and **without** the force due to hydrodynamic interaction between adjacent bubbles acting on the bubbles.

Finally, accounting for hydrodynamic interaction between bubbles has one obvious disadvantage: it requires additional CPU time. It is for this reason and due to the admittedly small macroscopic effect of the hydrodynamic interaction between bubbles, that in future simulations hydrodynamic interaction between bubbles will not be considered.

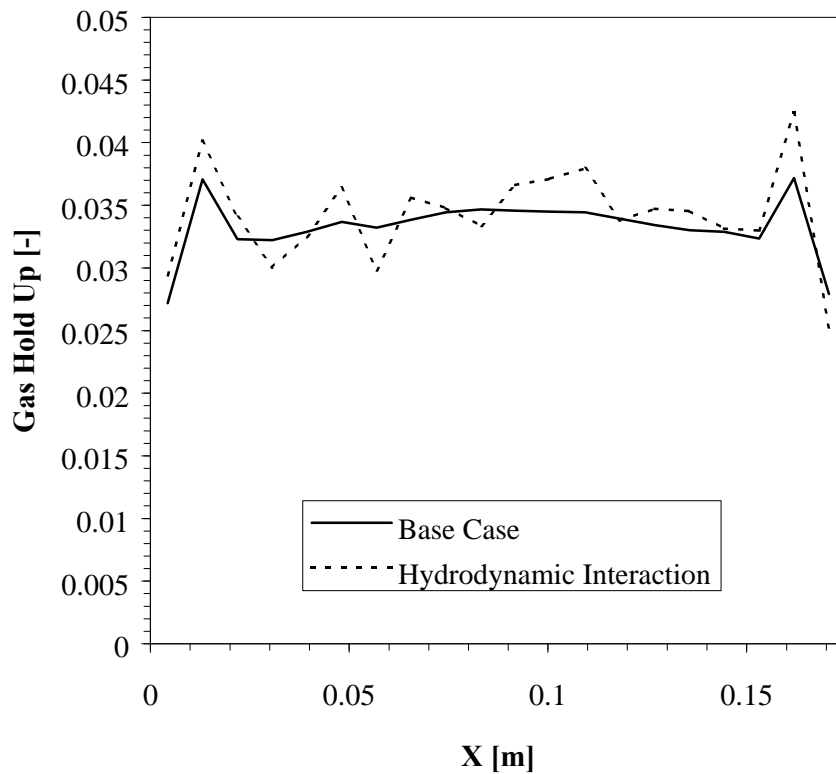


**Figure 12c.** Time averaged (0 – 150 [s]) radial gas holdup profile at 1.00 [m] above the gas distributor. Simulation of an experiment conducted by Chen *et al.* (1989). Superficial gas velocity = 35 [mm s<sup>-1</sup>]. This figure compares the radial porosity profiles calculated **with** and **without** the force due to hydrodynamic interaction between adjacent bubbles acting on the bubbles.

## 6. Conclusions

An Euler-Lagrange model for a gas-liquid bubble column has been developed which resolves the two dimensional, time dependent motion of small spherical gas bubbles in a liquid. The model incorporates all relevant forces acting on a bubble in a liquid, such as contributions from the pressure gradient in the liquid, drag, added or virtual mass, vorticity in the liquid phase, hydrodynamic interaction between bubbles and gravity. A direct bubble-bubble interaction model resembling Hooman's collision model for gas fluidized beds has been incorporated in our model. The liquid phase hydrodynamics are described using the volume averaged Navier-Stokes equations.

Our model has been validated using experimental data from the literature obtained by various workers. The model was shown to compare reasonably well to the experiments conducted by Becker *et al.* The behavior of the bubble plume in Becker's two-dimensional bubble column was predicted for both the high superficial gas velocity and the low superficial gas velocity case. The experimentally observed meandering behavior of the bubble plume at low superficial gas velocities was calculated. The period of oscillation of the bubble plume predicted by the model was found to differ from the one measured by Becker *et al.*

One of the key features of the model presented in this paper is the detailed bubble dynamics incorporated in it. The importance of the added mass force, the lift force, the drag force and the hydrodynamic interaction force acting on the bubbles was investigated theoretically. It was argued that the added mass force is of particular importance near the gas distributor and should be accounted for to realistically predict the behavior of the bubbles in the gas distributor region. The lift force acting on the bubbles disperses the bubbles over the cross section of the column. It was shown that a model that neglects the lift force acting on a bubble could not predict the experimentally determined wall peaking of the void fraction. It was also concluded that the particular approximation (Equation (6) or (7)) for the drag coefficient used in the computations does not significantly affect the flow pattern ultimately predicted by our model. Finally our model was used to study effects of the force due to hydrodynamic interaction between bubbles on the overall flow pattern in the bubble column. It was shown that the hydrodynamic interaction force exerted by the bubbles on each other does not significantly affect the macroscopic flow pattern observed in a bubble column operated in the homogeneous flow regime at relatively low void fractions (< 5%).

## 7. Notation

$\mu_1$	Shear viscosity liquid [ $\text{kg m}^{-1} \text{s}^{-1}$ ]
A	Area [ $\text{m}^2$ ]
$C_D$	Drag coefficient [-]
$C_L$	Lift force coefficient [-]
$C_{VM}$	Virtual mass coefficient [-]
$D_{\text{neighbor list}}$	Size of the neighbor list [m]
DTflow	Time step solver liquid flow field [s]

$DT_{bub}$	Time step used by bubble tracking routine [s]
$E$	Unit tensor [-]
$\epsilon_l$	Volume fraction liquid in computational cell [-]
$f$	Typical Eulerian variable [-]
$F$	Momentum exchange gas to liquid [ $N m^{-3}$ ]
$F_D$	Drag force on a bubble [N]
$F_G$	Force on bubble due to gravity [N]
$F_L$	Lift force on bubble [N]
$F_P$	Force on bubble due to pressure gradient [N]
$F_{total}$	Total force on a bubble [N]
$F_{VM}$	Virtual mass force on bubble [N]
$g$	Acceleration due to gravity [ $m s^{-2}$ ]
$I$	Kelvin impulse deformable body [Ns]
$\kappa$	Velocity gradient in calculating lift force [ $s^{-1}$ ]
$\lambda_l$	Bulk viscosity liquid [ $kg m^{-1} s^{-1}$ ]
$m_b$	Mass of a bubble [kg]
$N_{neighbor}$	Number of neighboring bubbles
$P$	Pressure [ $N m^{-2}$ ]
$r$	Position of bubble [m]
$r_a$	Position of bubble of bubble a [m]
$r_b$	Position of bubble of bubble b [m]
$R_b$	Radius of a bubble [m]
$Re_b$	Reynolds number for flow around a bubble [-]
$\rho_g$	Density gas phase [ $kg m^{-3}$ ]
$\rho_l$	Density liquid phase [ $kg m^{-3}$ ]
$t_l$	Stress tensor liquid [ $N m^{-2}$ ]
$t_{ab}$	time until collision between bubbles a and b [s]
$u$	Liquid velocity [ $m s^{-1}$ ]
$v_{rise}$	Rise velocity of a bubble [ $m s^{-1}$ ]
$v$	Velocity of bubble [ $m s^{-1}$ ]
$V_b$	Volume of a bubble [ $m^3$ ]

We	Weber number [-]
W	Vorticity in liquid phase [ $s^{-1}$ ]
x	X-position of bubble [m]
y	Y-position of bubble [m]

## 8. References

Auton, T. R., 1983, "The dynamics of bubbles, drops and particles in motion in liquids", Ph.D. Thesis, University of Cambridge, Cambridge, United Kingdom.

Batchelor, G. K., 1967, "An introduction to fluid dynamics", Cambridge University Press, Cambridge, United Kingdom.

Becker, S., Sokolichin, A. and Eigenberger, G., 1995, "Gas-liquid flow in bubble columns and loop reactors: part II. Comparison of detailed experiments and flow simulations", *Chem. Eng. Sci.* 49, 5747.

Boisson, N. and Malin, M. R., 1996, "Numerical prediction of two-phase flow in bubble columns", *Int. J. Num. Meth. Fluids* 23, 1289.

Bulthuis, H. F., 1997, "Dynamics of bubbly flows", Ph. D. Thesis, Twente University, Enschede, The Netherlands.

Chen, J. J. J., Jamialahmadi, M. and Li, S. M., 1989, "Effect of liquid depth on circulation in bubble columns: a visual study", *Chem. Eng. Res. Des.* 67, 203.

Clift, R., Grace, J. R. and Weber, M. E., 1978, "Bubbles, drops, and particles", Academic Press, New York.

Deckwer, W. D. and Schumpe, A., 1993, "Improved tools for bubble column reactor design and scale up", *Chem. Eng. Sci.* 48, 889.

Devanathan, N., Dudukovic, M. P., Lapin, A., Lübbert, A., 1995, "Chaotic flow in bubble column reactors", *Chem. Eng. Sci.* 50, 2661.

Duineveld, P. C., 1994, "Bouncing and coalescence of two bubbles in water", Ph.D. Thesis, Twente University, Enschede, The Netherlands.

Freedman W. and Davidson, J. F., 1969, "Holdup and liquid circulation in bubble columns", *Trans. I. Chem. E.* 47, T251.

Grienberger, J. and Hofman, H., 1992, "Investigations and modeling of bubble columns", *Chem. Eng. Sci.* 47, 2215.

Hjertager, B. H. and Morud, K., 1995, "Computational fluid dynamics of bioreactors", *Mod. Ident. and Control* 16, 177.

Hoomans, B. P. B., Kuipers, J. A. M., Briels, W. J. and van Swaaij, W. P. M., 1996, "Discrete particle simulation of bubble and slug formation in a two dimensional gas-fluidised bed: a hard sphere approach", *Chem. Eng. Sci.* 51, 99.

Jakobsen, H. A., Sannaes, B. H., Grevskott, S. and Svendsen, H. F., 1997, "Modeling of vertical bubble-driven flows", *Ind. Eng. Chem. Res.* **36**, 4052.

Jiang, P. Lin, T. J. and Fan, L. -S., 1995, "Flow visualization of a high pressure bubble column: bubble characteristics", *Trans. IChemE* **73A**.

Joshi, J. B. and Sharma, M. M., 1979, "Some design features of radial baffles in sectionalised bubble columns", *Can. J. Chem. Eng.* 57, 375.

Kuipers, J. A. M., van Duin, K. J., van Beckum, F. P. H. and van Swaaij, W. P. M., 1993, "Computer simulation of the hydrodynamics of a two dimensional gas-fluidized bed", *Comput. Chem. Eng.* 17, 839.

Kuo, J. T. and Wallis, G. B., 1988, "Flow of bubbles through nozzles", *Int. J. Multiphase Flow* **14**, 547.

Lapin, A. and Lübbert, A., 1994, "Numerical simulation of the dynamics of two phase gas-liquid flows in bubble columns", *Chem. Eng. Sci.* 49, 3661.

Odar, F. and Hamilton, W. S., 1964, "Forces on a sphere accelerating in a viscous liquid", *J. Fluid Mech.* 18, 302.

Ranade, V. V., 1992, "Flow in bubble column: some numerical experiments", *Chem. Eng. Sci.* 47, 1857.

Sangani, A. S., Kang, S. -Y., Koch, D. L. and Tsao, H. -K., 1995, "Numerical simulation and kinetic theory of simple shear motion of bubbly suspensions", *IUTAM Symposium on waves in liquid/gas and liquid/vapor two-phase systems*, Eds. S. Morioka and L. van Wijngaarden, p. 137, Kluwer Academic Press, Dordrecht.

Serizawa, A., Kataoka, I. and Michiyoshi, I., 1986, "Phase distribution in bubbly flows", *Proceedings of the Second International Workshop on Two-Phase Flow Fundamentals*, Data set No. 24.

Sokolichin, A. and Eigenberger, G., 1994, "Gas-liquid flow in bubble columns and loop reactors: part I. Detailed modeling and numerical simulation", *Chem. Eng. Sci.* 49, 5735.

Svendsen, H. F., Jakobsen, H. A. and Torvik, R., 1992, "Local flow structures in internal loop and bubble column reactors", *Chem. Eng. Sci.* 47, 3297.

Torvik, R. and Svendsen, H. F., 1990, "Modeling of slurry reactors, a fundamental approach", *Chem. Eng. Sci.* 45, 2325.

Trapp, J. A. and Mortensen, G. A., 1993, "A discrete particle model for bubble slug two phase flow", *J. Comp. Physics.* 107, 367.

Tsao, H. -K. and Koch, D. L., 1994, "Collisions of slightly deformable, high Reynolds number bubbles with short-range repulsive forces", *Phys. Fluids* 6, 2591.

Tsao, H. -K. and Koch, D. L., 1997, "Observations of high Reynolds number bubbles interacting with a rigid wall", *Phys. Fluids* 9 (1), 44.

Van den Akker, H. E. A., 1998, "The Euler-Euler approach to dispersed two-phase flows in the turbulent regime", *ERCOFTAC Bulletin* 36, 30.

Wijngaarden, L. van, 1976, "Some problems in the formulation of the equations for gas / liquid flows", *Theoretical and Appl. Mech.* W. T. Koiter (ed.), North Holland Publishing Company.

Yang, X. and Thomas, N. H., 1998, "Prediction of void fraction and velocity profiles of bubbly flows in vertical pipes", *Chem. Eng. Comm.* **163**, 145.



## Chapter 4:

### Dynamic simulation of gas-liquid two-phase flow: effect of column aspect ratio on the flow structure<sup>1</sup>

#### 0. Abstract

In this paper a detailed Euler-Lagrange model for a gas-liquid bubble column is presented and used to study the effect of the aspect ratio of a bubble column on the flow structure. The model, which is described in detail in section 3, resolves the time dependent two-dimensional motion of small, spherical gas bubbles in a Newtonian liquid using the equation of motion. The model incorporates all relevant forces acting on a bubble as it rises through the liquid, and accounts for direct bubble-bubble interactions. The liquid phase hydrodynamics are described using the volume-averaged Navier-Stokes equations. This model is used to study the hydrodynamic behavior of bubble columns with aspect ratios ranging from 1.0 to 11.4. In addition to these theoretical results, experimental observations are presented of the flow structure in a pseudo two-dimensional bubble column with different aspect ratios. A clear transition in the gas-liquid flow pattern could be observed, both experimentally and theoretically, from the well known “cooling tower” mode of circulation ( $L/D = 1.0$ ) to the staggered vortices mode of circulation ( $L/D \geq 2.0$ ). The computational results clearly showed the presence of vortical structures in the liquid phase at aspect ratios exceeding 2.0. These vortical structures in the liquid phase were studied experimentally using neutrally buoyant tracer particles and streak photography. The experimentally observed vortical structures are shown to resemble the computed structures.

---

<sup>1</sup> Delnoij, E., Kuipers, J. A. M. and van Swaij, W. P. M., 1997, “Dynamic simulation of gas-liquid two-phase flow: effect of column aspect ratio on the flow structure”, *Chem. Eng. Sci.* **52** (21/22), 3759.

## 1. Introduction

Bubble column reactors are used throughout the biological, chemical and petrochemical industry. Typical applications are encountered in processes involving absorption, catalytic slurry reactions, bioreactions and coal liquefaction. Bubble column reactors are often used because of their relatively simple construction, low operating costs, excellent heat transfer characteristics to immersed surfaces and the ease with which the liquid residence time can be varied (Shah *et al.*, 1982). Despite their frequent application, knowledge on the fluid mechanical behavior of bubble column reactors is still limited. The structure of the two-phase flow, and its dependence on design parameters such as height and diameter of the column is especially important but fundamental knowledge regarding this topic is lacking. Designers therefore rely on simplified models that neglect many of the important physical aspects of the gas-liquid two-phase flow.

The structure of the two-phase flow has been the subject of both experimental and theoretical investigations for many years. For example: Freedman and Davidson (1969) developed a liquid circulation model known as the “Gulfstream or cooling tower model”. This type of liquid circulation consists of two adjacent vortex cells with liquid flowing upward in the center of the bubble column and downward along the walls of the column. In later years Joshi and Sharma (1979) proposed a model postulating the flow structure in bubble columns to consist of multiple circulation cells which were thought to be located in a regular pattern above each other. Finally, Chen *et al.* (1989) conducted experimental research in two pseudo two-dimensional bubble columns. They investigated the effect of the liquid depth, and thus of the aspect ratio of the bubble column, on the structure of the two-phase flow. Chen *et al.* observed the “cooling tower” mode of circulation cells only when the aspect ratio was less than or equal to 1.0. At liquid depths exceeding this value, the observed flow pattern consists of two rows of staggered circulation cells. In this respect the vortical structures resemble those shed behind a circular cylinder in cross-flow (Batchelor, 1967).

CFD modeling of the gas-liquid two-phase flow prevailing in bubble columns can significantly contribute to our understanding of the (fluid) dynamics of these industrially important systems. In recent years a number of investigators (Lapin and Lübbert, 1994; Sokolichin and Eigenberger, 1994; Sokolichin *et al.*, 1997; Delnoij *et al.*, 1997; Jakobsen *et al.*, 1997 and van den Akker, 1998) have published interesting results obtained with different

types of CFD models. These studies clearly demonstrated that the complex, time-dependent, flow structures observed in gas-liquid bubble columns could be predicted with the aid of these models.

In Chapter 3 we developed a detailed Euler-Lagrange model (also referred to as discrete bubble model) for a gas-liquid bubble column operating in the homogeneous regime. This model describes the time-dependent motion of small, spherical gas bubbles in a Newtonian liquid. It uses the volume-averaged Navier-Stokes equations to describe the liquid phase hydrodynamics and separate equations of motion to track each individual bubble contained in the column. The model incorporates all relevant forces acting on a bubble as it rises through the liquid. Full exchange of momentum between the phases is accounted for, and direct bubble-bubble interactions are described in detail using a collision model. In this chapter we will review the fundamentals of this model and we will use the model to study the structure of the two-phase flow prevailing in a bubble column at various aspect ratios.

In addition to these theoretical results, experimental observations of the flow structure in a pseudo two-dimensional bubble column will be reported. Streak photography and video imaging techniques were used to visualize the structure of the two-phase flow in the bubble column.

## **2. The CFD model**

In this paper we will employ an Euler-Lagrange CFD model to study the way in which the aspect ratio affects the flow structure prevailing in a bubble column. This model has been presented in detail in Chapter 3. In this Chapter, we will therefore only briefly review the fundamentals of this discrete bubble model. There is a slight difference however, between the CFD model used in this paper and the version presented in the previous Chapter. First: we will neglect hydrodynamic interaction between the individual bubbles, which is in agreement with the conclusions presented in the previous Chapter. And also, a new and improved method of accounting for momentum transfer will be introduced.

The Euler-Lagrange CFD model consists of two intimately coupled parts: a part describing the liquid phase hydrodynamics and a part that models the behavior of each individual bubble

using the equation of motion. Both parts, the coupling between these parts and thus the coupling between the gas and the liquid phases will subsequently be discussed in more detail.

## 2.1 Bubble dynamics

As stated previously our model uses an individual equation of motion to calculate each bubble's new position from its previous time level position and its present time level velocity, accounting for possible bubble-bubble collisions. The required new bubble velocity is calculated with a simple, explicit integration formula:

$$\mathbf{v}^{n+1} = \mathbf{v}^n + \left( \frac{d\mathbf{v}}{dt} \right)^n DT \quad 1$$

Each bubble's acceleration is calculated from a force balance over the bubble under consideration:

$$m_b \frac{d\mathbf{v}}{dt} = \mathbf{F}_{total} \quad 2$$

It is assumed that the force  $\mathbf{F}_{total}$  acting on a non-deformable spherical bubble rising in an unsteady, and non-uniform liquid flow field is composed of separate and uncoupled contributions from pressure gradient, drag, virtual or added mass, vorticity and gravity (Auton, 1983):

$$\mathbf{F}_{total} = \mathbf{F}_P + \mathbf{F}_D + \mathbf{F}_{VM} + \mathbf{F}_L + \mathbf{F}_G \quad 3$$

Table 1 summarizes the equations, coefficients and constants used to calculate the various forces acting on a bubble<sup>2</sup>. For a detailed discussion concerning these expressions the interested reader is referred to Delnoij *et al.* (1997) and to Chapter 3 of this thesis. In the present study we do not account for the force acting on a bubble due to hydrodynamic interaction with neighboring bubbles. This is because our study in Chapter 3 revealed that the net effect of this force on the macroscopic flow pattern in a bubble column is effectively non-existent. Moreover, the drag force acting on a bubble is modeled using the standard drag curve approximation to the drag coefficient (Clift *et al.*, 1978). This is also in accordance with our study in Chapter 3, which revealed little difference between the time-averaged axial liquid velocity profiles obtained with different expressions for the drag coefficient.

---

<sup>2</sup> Note that the dependence of the virtual mass coefficient on the local void fraction (equation (11) in Chapter 3) has been omitted because we neglect hydrodynamic interactions between bubbles in this Chapter.

**Table 1:** Forces acting on a non-deformable and spherical gas bubble rising in an unsteady and non-uniform liquid flow field.

Force:	Expression:
Gravity and Far Field Pressure	$\mathbf{F}_G + \mathbf{F}_P = \mathbf{r}_g V_b \mathbf{g} - V_b \nabla P$
Drag Force	$\mathbf{F}_D = -\frac{1}{2} C_D \mathbf{r}_l \rho R_b^2  \mathbf{v} - \mathbf{u}  (\mathbf{v} - \mathbf{u})$ $C_D = \begin{cases} \text{Re}_b \leq 1000 \Rightarrow \frac{24}{\text{Re}} (1 + 0.15 \cdot \text{Re}_b^{0.687}) \\ \text{Re}_b > 1000 \Rightarrow 0.44 \end{cases}$
Lift Force	$\mathbf{F}_L = -C_L \mathbf{r}_l V_b (\mathbf{v} - \mathbf{u}) \times \boldsymbol{\Omega}$ $\boldsymbol{\Omega} = \nabla \times \mathbf{u}$ $C_L = 0.53$
Virtual Mass Force	$\mathbf{F}_{VM} = -\left( \frac{D\mathbf{I}}{Dt} + \mathbf{I} \cdot \nabla \mathbf{u} \right)$ $\mathbf{I} = C_{VM} \mathbf{r}_l V_b (\mathbf{v} - \mathbf{u})$ $C_{VM} = 0.5$

## 2.2 Direct bubble-bubble interaction

In gas-liquid dispersions, bubbles have been observed to coalesce, to bounce and subsequently coalesce or to bounce and separate (Duineveld, 1994 and Tsao and Koch, 1997). In our model it has been assumed that the bubbles always bounce and separate, which is probably a fair assumption for relatively small bubbles rising in water at high Reynolds numbers. In experiments bouncing and separation of bubbles can be achieved by adding salt to the suspending water (Tsao and Koch, 1994).

There are various approaches to modeling collisions between bubbles in a gas-liquid dispersion. Sangani *et al.* (1995) employed a soft-core repulsive potential to model the collision process. In the present paper however, a hard sphere collision model resembling the model developed by Hoomans *et al.* (1996) is used to process the sequence of collisions between bubbles in a bubble column. This algorithm is discussed in detail in Chapter 3.

## 2.3 Liquid phase hydrodynamics

The liquid phase hydrodynamics are described with the volume-averaged mass and

momentum conservation equations given respectively by:

$$\frac{\partial(\mathbf{e}_l \mathbf{r}_l)}{\partial t} + \nabla \cdot \mathbf{e}_l \mathbf{r}_l \mathbf{u} = 0 \quad 4$$

And:

$$\frac{\partial(\mathbf{e}_l \mathbf{r}_l \mathbf{u})}{\partial t} + \nabla \cdot \mathbf{e}_l \mathbf{r}_l \mathbf{u} \mathbf{u} = -\mathbf{e}_l \nabla P - \nabla \cdot \mathbf{e}_l \mathbf{t}_l + \mathbf{e}_l \mathbf{r}_l \mathbf{g} + \Phi \quad 5$$

The spatial resolution with which the liquid velocity field is resolved is small compared to the size of the bubbles; the liquid-bubble interaction is therefore superimposed on the liquid velocity field. This liquid-bubble interaction is modeled with the source term  $\mathbf{F}$  that accounts for the momentum exchange between the bubbles and the liquid.

In the present study two-dimensional, isothermal motion of both the gas and the liquid phase is assumed. The basic variables that are calculated by the model are pressure, liquid velocity and the velocity and position of each individual bubble. All other variables appearing in the balance equations must be specified in terms of these variables.

The liquid phase viscous stress tensor  $\mathbf{t}_l$  is assumed to obey the general form for a Newtonian fluid:

$$\mathbf{t}_l = -\left[ \left( \mathbf{I}_l - \frac{2}{3} \mathbf{m}_l \right) (\nabla \cdot \mathbf{u}) \mathbf{E} + \mathbf{m}_l \left( (\nabla \mathbf{u}) + (\nabla \mathbf{u})^T \right) \right] \quad 6$$

The bulk viscosity  $\lambda_l$  is set to zero in all simulations presented in this paper. In most simulations water is used as the liquid phase which corresponds to a shear viscosity of  $1.0 \times 10^{-3}$  [kg m<sup>-1</sup> s<sup>-1</sup>].

## 2.4 Coupling between the phases

The two parts that constitute our hydrodynamic model are coupled through the liquid volume fraction  $\epsilon_l$  and through the source term  $\mathbf{F}$  that accounts for the momentum transfer from the bubbles to the liquid. Both this liquid volume fraction  $\epsilon_l$  and the source term  $\mathbf{F}$  have to be calculated in accordance with the number of bubbles present in a computational cell. In order to evaluate the reverse momentum transfer rate, i.e. from the liquid to a specific bubble, all quantities pertaining to the liquid phase (i.e. pressure and velocity components) have to be available at the center of mass position of this bubble. These so-called local liquid properties are calculated from the values of the volume-averaged liquid properties at the grid nodes surrounding the bubble under consideration.

This two-way momentum coupling that is included in our model is of crucial importance, as has been shown by Delnoij *et al.* (1997). Delnoij *et al.* showed that a model that neglects two-way momentum coupling could not account for the time-dependent behavior generally observed in pseudo two-dimensional bubble columns.

#### 2.4.1 The liquid volume fraction

The liquid volume fraction in a computational cell is calculated from the volume occupied by the bubbles present in the cell under consideration:

$$\mathbf{e}_l = 1 - \frac{\sum_{\forall i \in \text{cell}} V_{bi}}{V_{\text{cell}}} \quad 7$$

In calculating this liquid volume fraction, it is very important to account for bubbles overlapping with more than one computational cell. In the present code, the volume occupied by these bubbles is distributed over the respective computational cells.

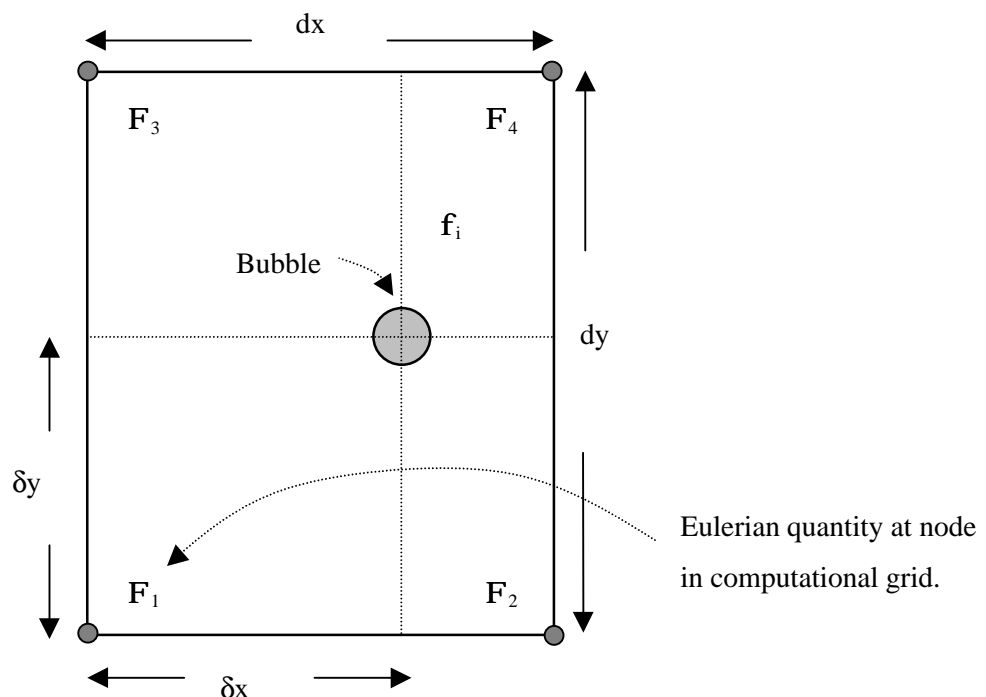


**Figure 1.** Area weighting of the local momentum transfer rate  $f_i$  to obtain the volume-averaged momentum transfer rates  $F$  at the four grid nodes surrounding the bubble.

### 2.4.2 Momentum transfer term $\mathbf{F}$

The momentum transfer rate from the bubbles to the liquid,  $\mathbf{F} \cdot \mathbf{V}_{\text{cell}}$ , is just the opposite of the forces due to drag, lift and virtual mass exerted by the liquid on the bubbles. From these forces, a local (viz. at the center of mass position of the bubble under consideration) momentum transfer rate  $\mathbf{f}_i$  can be calculated using:

$$\mathbf{f}_i = -(\mathbf{F}_{Di} + \mathbf{F}_{VMi} + \mathbf{F}_{Li}) \quad 8$$

Subsequently, an area-weighted averaging technique is used to calculate volume-averaged momentum transfer rates  $\mathbf{F} \cdot \mathbf{V}_{\text{cell}}$  at the four nodes surrounding the bubble, from the local momentum transfer rate  $\mathbf{f}_i$  pertaining to that bubble. Figure 1 illustrates this principle. The volume-averaged momentum transfer rate is calculated from:

$$\begin{aligned} \Phi_1 V_{\text{cell}} &= \frac{A_1}{dxdy} \mathbf{f}_i(\mathbf{r}_i) \\ \Phi_2 V_{\text{cell}} &= \frac{A_2}{dxdy} \mathbf{f}_i(\mathbf{r}_i) \\ \Phi_3 V_{\text{cell}} &= \frac{A_3}{dxdy} \mathbf{f}_i(\mathbf{r}_i) \\ \Phi_4 V_{\text{cell}} &= \frac{A_4}{dxdy} \mathbf{f}_i(\mathbf{r}_i) \end{aligned} \quad 9$$

The area's  $A_{1..4}$  depicted in Figure 1 can be calculated from:

$$\begin{aligned} A_1 &= (dx - \mathbf{dx})(dy - \mathbf{dy}) \\ A_2 &= \mathbf{dx}(dy - \mathbf{dy}) \\ A_3 &= (dx - \mathbf{dx})\mathbf{dy} \\ A_4 &= \mathbf{dx}\mathbf{dy} \end{aligned} \quad 10$$

In both equation (7) and equation (9) the volume  $V_{\text{cell}}$  represents the volume of a computational cell based on a virtual third dimension, which is due to the two-dimensional nature of our model. This third dimension can be derived from the relation between the 2D gas hold up and the 3D gas hold up assuming similar geometrical arrangement in a two-dimensional and a three-dimensional space (Hoomans *et al.*, 1996). The resulting expression for the volume of a computational cell,  $V_{\text{cell}}$ , is given by:

$$V_{\text{cell}} = dx \cdot dy \cdot 2 \cdot 3^{-0.75} \cdot D_b \quad 11$$



### 2.4.3 Local liquid phase properties

In order to calculate the force acting on a bubble with equation (3), local values of the pressure, of the liquid velocity, of the partial and substantial derivatives of the pressure and of the partial and substantial derivatives of the liquid velocity have to be available at the center of mass position ( $\mathbf{r}_i$ ) of the bubble. However, these volume-averaged variables and their derivatives are only available at discrete nodes in the computational domain. Therefore an area-weighted averaging technique, similar to that employed to calculate the momentum transfer rate, is used to obtain local values from the volume-averaged variables at the four nodes surrounding the bubble. This local value of a quantity  $f$  can be calculated using:

$$f(\mathbf{r}_i) = \frac{1}{dxdy} \sum_{n=1}^4 A_n f_n \quad 12$$

Where  $f_n$  represents some volume averaged quantity at node  $n$ , and the areas  $A_n$  are given by equation (10).

The method described here to incorporate momentum transfer between the gas and the liquid phase is slightly different from our previous technique (Delnoij *et al.*, 1997 and Chapter 3). The fundamental difference being that in the algorithm discussed in Chapter 3, the local momentum transfer rate of a bubble was attributed to the volume-averaged momentum transfer rate of the computational cell containing the bubble. In the present method, this local momentum transfer rate is distributed across the four volume-averaged momentum transfer rates surrounding the bubble under consideration. This new method ensures rigorous momentum conservation, as Newton's third law is strictly obeyed (because the reverse procedure is used to derive local values of volume-averaged quantities).

## 2.5 Boundary conditions and numerical solution

The boundary conditions for the Navier-Stokes equations are specified using the flag matrix concept. This concept, also used by Kuipers *et al.* (1993), allows boundary conditions to be set for each individual computational cell. Using this flag matrix concept a variety of boundary conditions can be set by specifying the value of the cell flag  $fl(i,j)$

Bubble-wall interaction is accounted for by the collision sub-model; only instantaneous, hard sphere collisions are assumed to occur. The model treats these collisions similar to bubble-bubble collisions.

The model discussed in this paper has been implemented in a computer code written in C. This code takes consecutive steps in time, during each of which the code calculates the forces acting on the bubbles in the system. It then calculates the new bubble velocities using equations (1) and (2), and the new bubble positions taking into account possible bubble-bubble collisions. Finally, the code solves for the new time level liquid velocity field. For details concerning the solution procedure the interested reader is referred to Kuipers *et al.* (1993) and to Delnoij *et al.* (1997). CPU time requirements depend on the size of the bubble column under consideration, on the number of grid cells used in the computation and on the number of bubbles contained in the bubble column. On average, calculating 1 minute of time-dependent behavior of a typical bubble column (1.0 [m] in height, 0.25 [m] in width and containing  $\approx 4000$  bubbles) requires approximately 4 hours dedicated CPU time on a Silicon Graphics Indigo<sup>2</sup> workstation equipped with a single R4400 processor.

### 3. Experimental set-up

A key issue in computational fluid dynamics, especially in connection with multiphase flows, is the assessment of the validity of the computational results. For this purpose, a sophisticated multiphase flow Particle Image Velocimetry (PIV) technique has been developed at Twente University in collaboration with the Technical University in Delft. This PIV technique can be used for detailed studies of the gas-liquid two-phase flow prevailing in a bubble column and for the quantitative validation of CFD models. This velocimeter will be discussed in Chapters 6 and 7.

In this chapter however, we will present experimental results obtained in a simple pseudo two-dimensional bubble column. This pseudo two-dimensional bubble column is depicted in figure 2. It has a cross section of 250 [mm] x 20 [mm] and is 2000 [mm] in height; the column provides data up to an aspect ratio of 7.0. The bubble column is constructed from clear transparent plexi-glass sheets and is fitted with a gas distributor made from a 6.0 [mm] diameter stainless steel tube. The upward side of this tube has 14 evenly spaced 0.2 [mm] diameter holes in the central part of the tube. The gas flow rate is controlled through a calibrated mass flow controller.

The structure of the two-phase flow was studied using video imaging techniques and streak

photography. Neutrally buoyant tracer particles ( $d_p = 250 \text{ } [\mu\text{m}]$ ) were employed to visualize the vortical structures in the bubble column.

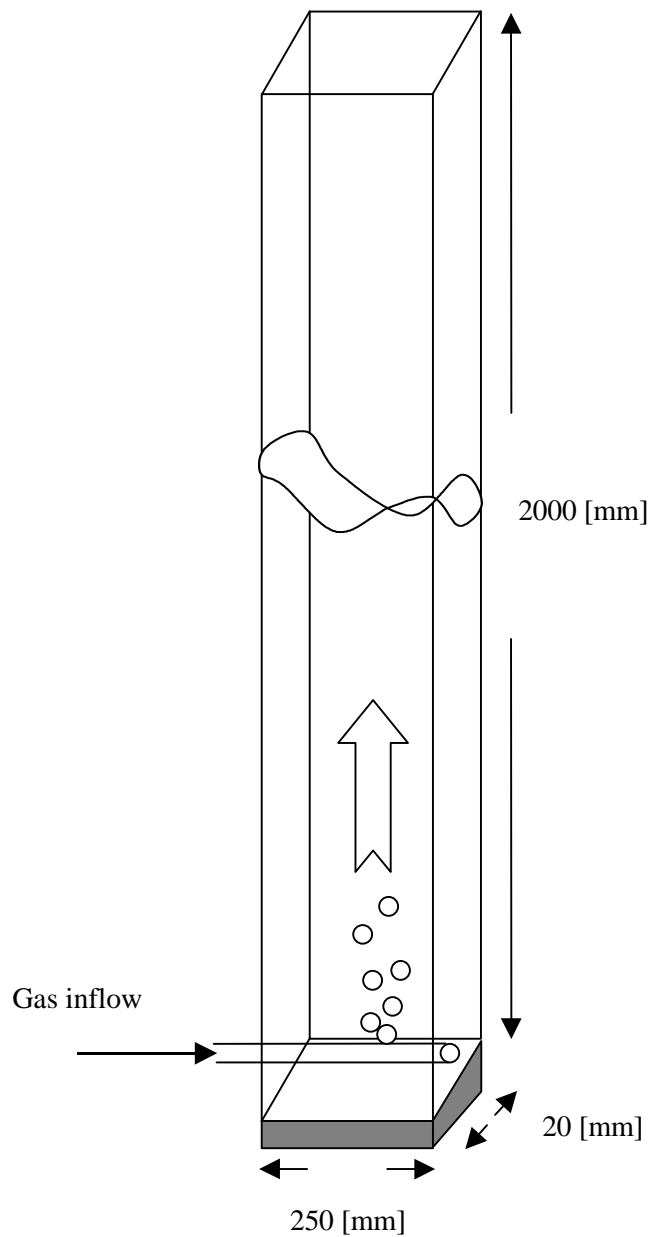


**Figure 2.** Pseudo two-dimensional bubble column used in flow visualisation experiments.

Although simple, these experiments provide valuable qualitative data on the two-phase flow prevailing in a bubble column. These data can be used for preliminary CFD model validation. Moreover, these relatively simple experiments are prerequisite for the design of the complex experiments discussed in Chapters 6 and 7.

## 4. Results and discussion

### 4.1 Effect of column aspect ratio: experiments by Chen *et al.* (1989)

Chen *et al.* studied the liquid circulation in a bubble column with aspect ratios ranging from 0.5 to 11.4. At low liquid depths the “cooling tower” pattern was observed whereas at liquid depths exceeding unity two rows of staggered vortices, resembling the Von Karman Vortex Street were observed. As a validation step, our model was used to simulate the behavior of bubble columns with various aspect ratios. The column considered in our computations was aerated through the center part of its cross section, as opposed to the experimental setup used by Chen *et al.* (1989) that was aerated over the entire cross section. Table 2 lists the numerical values of every important variable used in the simulations.

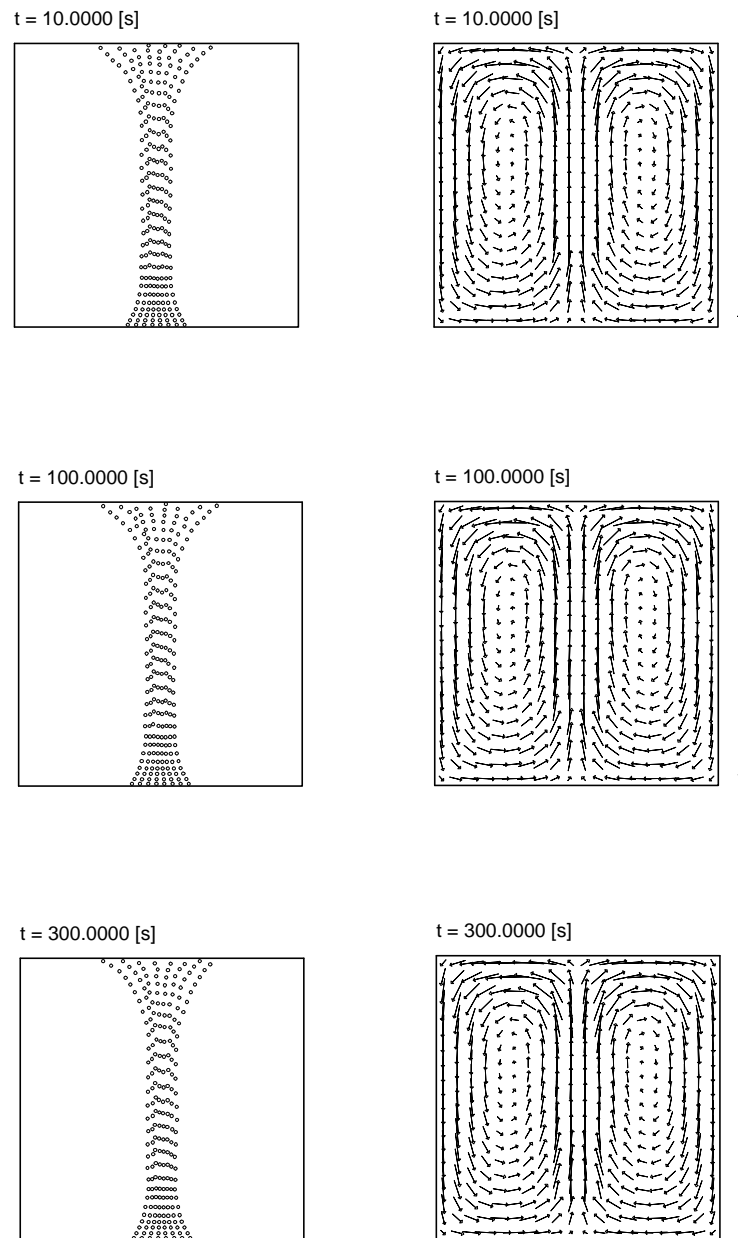
**Table 2.** Parameters used in the computations to assess the effect of the aspect ratio on the flow structure. Geometry and gas flow rate as used by Chen *et al.* (1989).

Column dimensions	
Width:	0.1750 [m]
Height:	
L/D = 1.0	0.1750 [m]
L/D = 2.0	0.3500 [m]
L/D = 4.8	0.8400 [m]
L/D = 7.7	1.3475 [m]
L/D = 11.4	1.9950 [m]
Superficial gas velocity:	35.0 [mm s <sup>-1</sup> ]
Physical properties	
Density liquid:	1000.0 [kg m <sup>-3</sup> ]
Viscosity liquid:	1.0 x 10 <sup>-3</sup> [Ns m <sup>-2</sup> ]
Density gas:	1.2 [kg m <sup>-3</sup> ]
Bubble diameter:	2.0 x 10 <sup>-3</sup> [m]
Computational parameters	
Number of computational cells in lateral direction:	20
Number of computational cells in axial direction:	
L/D = 1.0	20

L/D = 2.0	40
L/D = 4.8	96
L/D = 7.7	154
L/D = 11.0	228
Time step:	$5.0 \times 10^{-3}$ [s]

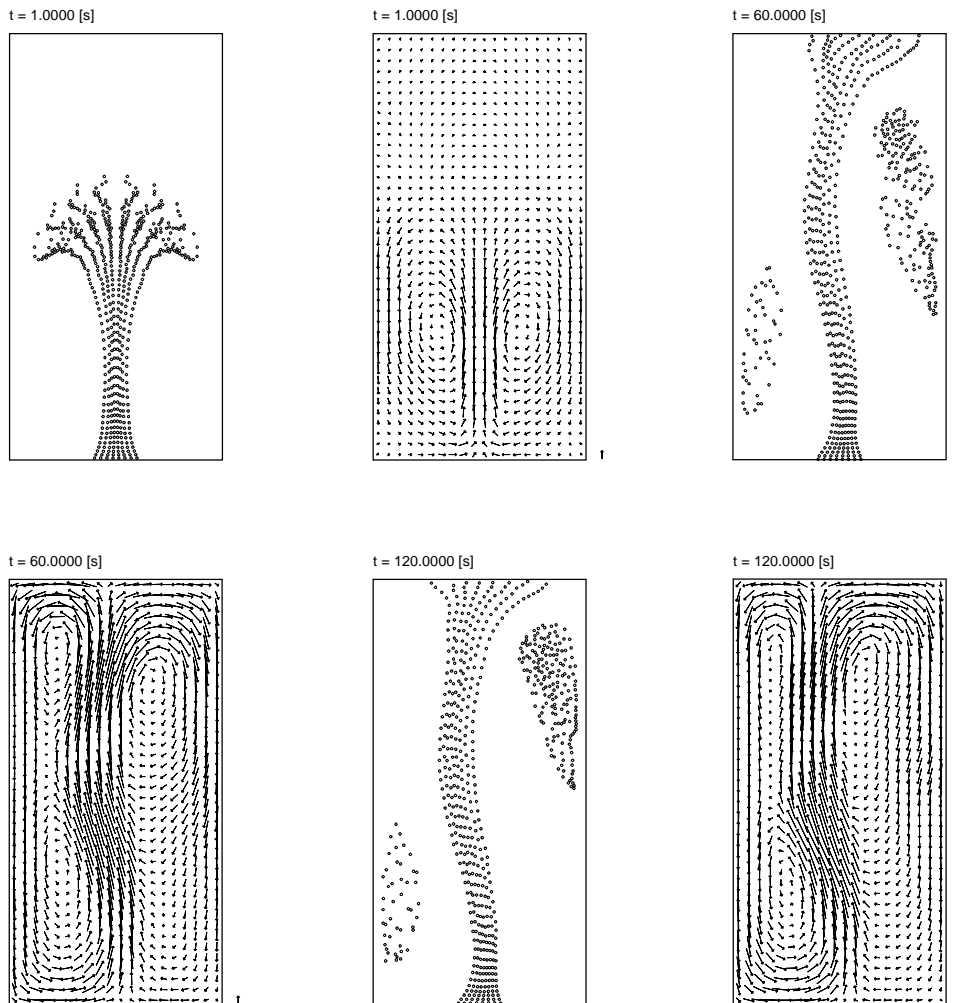
Figure 3 shows a sequence of snapshots that depict the position of the bubbles and the associated instantaneous liquid phase velocity field in a bubble column with an aspect ratio of 1.0. It can be seen that the bubble plume rises along the column's centerline. In this case the computed bubble trajectories change remarkably little over 300 [s] of simulation time. The liquid velocity fields clearly exhibit the same characteristics, with liquid up flow in the column's center (in the wake of the rising bubbles), and liquid down flow along the containing walls. This is the classical "cooling tower" mode of circulation also observed by Chen *et al.* at low column aspect ratios. The two circulation cells that constitute the typical "cooling tower" flow pattern can be seen most clearly from the liquid velocity fields presented in Figure 3.

Figure 4 depicts snapshots of the flow pattern in a bubble column with an aspect ratio of 2.0. Again the instantaneous bubble positions and the corresponding liquid phase velocity fields are shown. Initially the bubble plume rises in a rectilinear fashion along the centerline of the column. A "cooling tower" mode of circulation seems to develop, as is evident from the liquid velocity field at 1.0 second after start up. With increasing operation time however, the flow structure changes to a more complex one with two staggered circulation cells, one cell in the lower left corner and one cell in the upper right corner of the column. These circulation cells influence the bubble plume causing it to rise through the bubble column along an S-shaped path. From Figure 4, and from video representation of the computed results, it could clearly be seen that the flow pattern in the bubble column changed remarkably little during the 120 seconds of simulation time. None of the circulation cells moved through the bubble column and the bubble plume did not change its position considerably.



**Figure 3.** Computed structure of the gas-liquid two-phase flow in a bubble column with an aspect ratio of 1.0. The superficial gas velocity is equal to  $35 \text{ [mm s}^{-1}\text{]}$ . A uniform bubble size distribution is employed. Both the instantaneous bubble positions and the liquid velocity fields are shown at 10 [s], 100 [s] and 300 [s] after start up. The reference vector  $t$  corresponds to a liquid velocity of  $10 \text{ [cm s}^{-1}\text{]}$ .

If the aspect ratio of the bubble column is increased to 4.8 a highly dynamic, time-dependent flow pattern develops. This can be seen most clearly from Figure 5, which depicts the instantaneous position of the bubbles and the liquid phase velocity fields at various times.



**Figure 4.** Computed structure of the gas-liquid two-phase flow prevailing in a bubble column with an aspect ratio of 2.0. The superficial gas velocity is  $35 \text{ [mm s}^{-1}\text{]}$ . A uniform bubble size distribution has been employed. Both the instantaneous bubble positions and the associated liquid flow field are shown at 1 [s], 60 [s] and 90 [s] after start up. The reference vector corresponds to a liquid velocity of  $10.0 \text{ [cm s}^{-1}\text{]}$ .

From this Figure and video representation of the computed results it could be inferred that the bubble plume continuously shifts from left to right and vice versa in the bubble column. The meandering shape and continuous movement of the bubble plume is caused by vortices that develop at the free surface on opposite sides of the column's center and descend along one of the walls of the column. From Figure 5 it can clearly be seen that the flow structure is dominated by rows of staggered vortices, which agrees well with the observations of Chen *et al.* Finally, it can be seen from Figure 5 that the bubbles are dispersed over the column's cross section in the upper section of the bubble column. Delnoij *et al.* (1997) showed that this

is most likely due to the lift force acting on the bubbles in the bubble plume. As a result of this dispersion, bubbles are caught by liquid flowing downwards along the column walls.

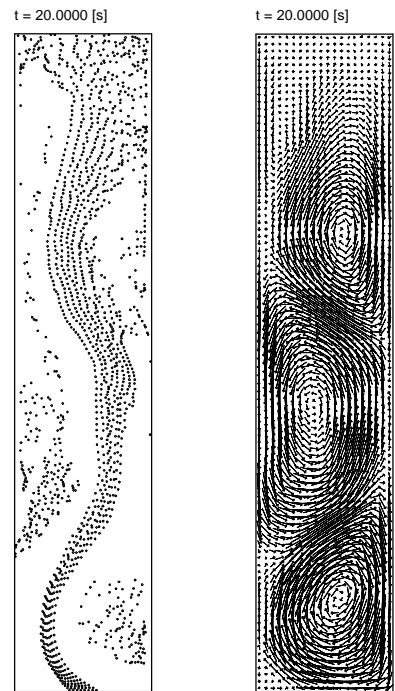


**Figure 5a.** Computed structure of the gas-liquid two-phase flow in a bubble column with an aspect ratio of 4.8, 20 [s] after startup. The superficial gas velocity is equal to  $35 \text{ [mm s}^{-1}\text{]}$ . A uniform bubble size distribution is employed. The reference vector corresponds to a liquid velocity of  $10 \text{ [cm s}^{-1}\text{]}$ .

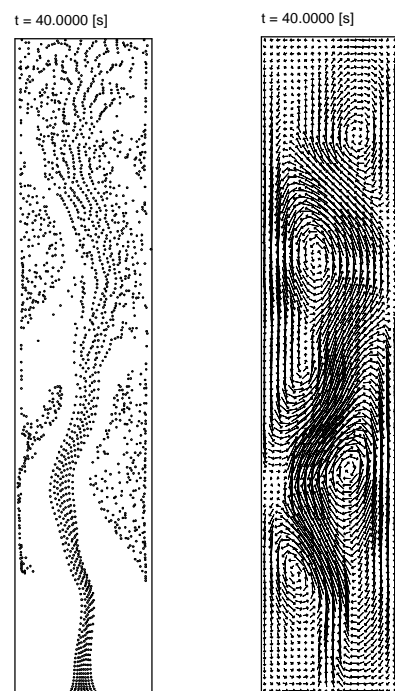


**Figure 5b.** Computed structure of the gas-liquid two-phase flow in a bubble column with an aspect ratio of 4.8, 40 [s] after startup. See Figure 5a.



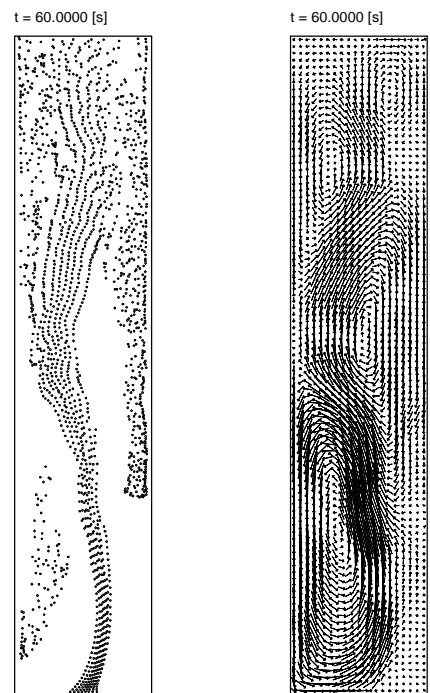


**Figure 5c.** Computed structure of the gas-liquid two-phase flow in a bubble column with an aspect ratio of 4.8, 60 [s] after startup. See Figure 5.

Reconsidering the computed flow structures at aspect ratios of 2.0 and 4.8, reveals that a gradual transition from the “cooling tower” mode of circulation ( $L/D = 1.0$ ) to the fully developed staggered vortices configuration ( $L/D = 4.8$ ) is predicted by our CFD model.

Chen *et al.* also investigated the flow structure in a bubble column with an aspect ratio of 7.7 and in a column with an aspect ratio of 11.4. The computed results for these cases are summarized in Figures 6 and 7. Despite the difference in aspect ratio, the results depicted in Figures 6 and 7 appear quite similar and will therefore be discussed together. Figures 6 and 7 indicate that both bubble columns consist of two distinctly different sections. The flow structure in the first section, or the lower section, of the bubble column resembles that of the multiple staggered vortex mode of operation as was observed in the bubble column with an aspect ratio of 4.8. In the lower section of the bubble column a distinct bubble plume can be observed; its behavior is highly dynamic and is influenced by staggered vortices that develop at the “interface” between the lower and upper section of the bubble column. These vortices move downwards along the walls of the column. In the second section, or the upper section

of the column, the bubbles are dispersed over the entire cross section of the column; the bubble plume has apparently spread out due to lift forces acting on the bubbles and velocity differences in the liquid phase. The liquid velocity field in the upper section of the column is very different from the velocity field in the lower section. Vortices can not be observed, and the flow field resembles the classical flow field thought to prevail in the homogeneous regime, with liquid up flow in the wake of a bubble and liquid down flow in between the bubbles.

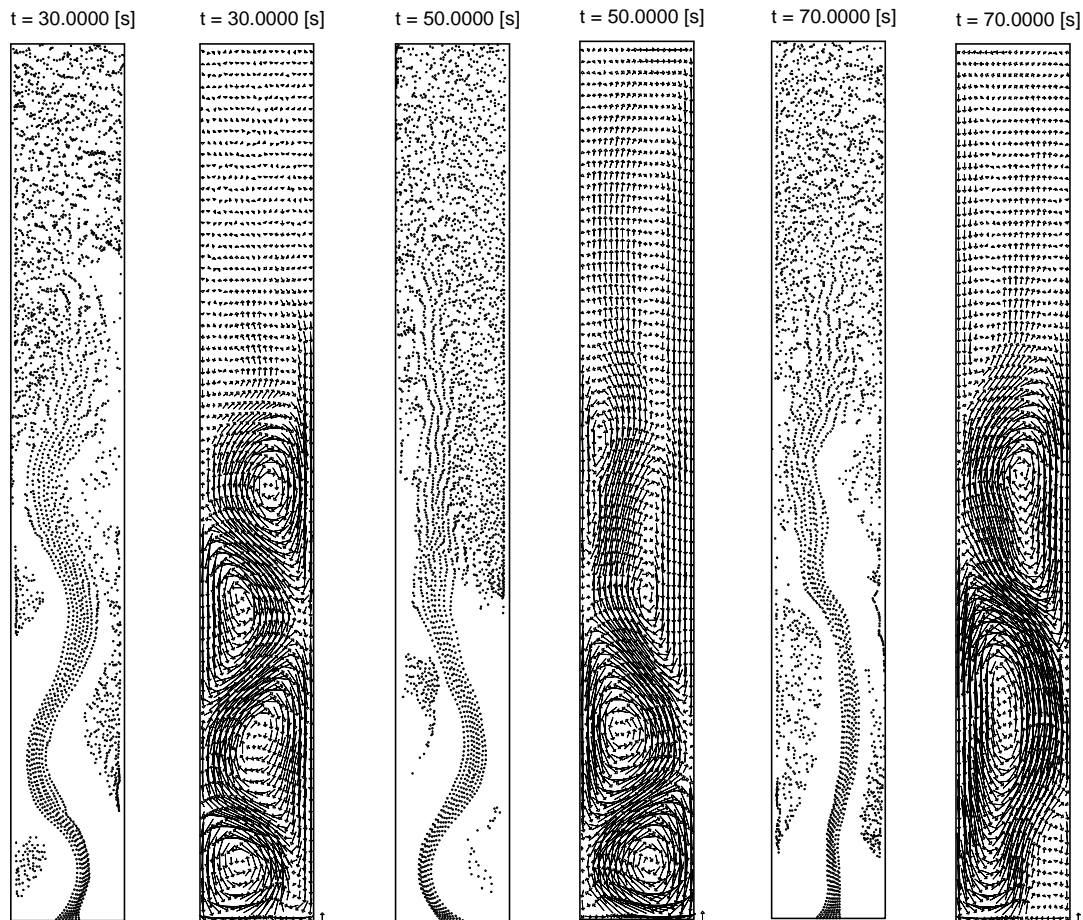


**Figure 6[a-c].** Computed structure of the gas-liquid two-phase flow in a bubble column with an aspect ratio of 7.7; at 30, 50 and 70 [s] after startup. The superficial gas velocity is  $35 \text{ [mm s}^{-1}\text{]}$ . A uniform bubble size distribution is employed. The reference vector corresponds to a liquid velocity of  $10 \text{ [cm s}^{-1}\text{]}$ .

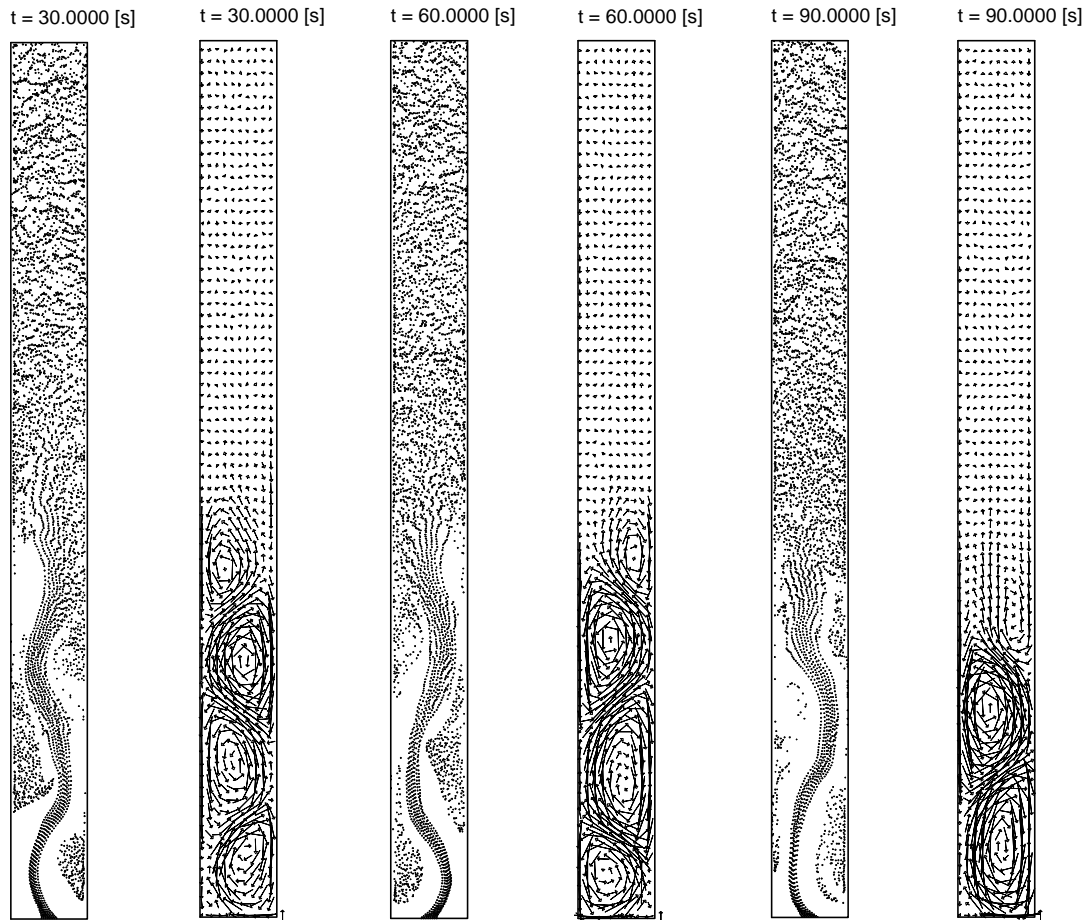


**Figure 7[a-c].** Computed structure of the gas-liquid two-phase flow in a bubble column with an aspect ratio of 11.4; at 30, 60 and 90 [s] after startup. The superficial gas velocity is  $35 \text{ [mm s}^{-1}\text{]}$ . A uniform bubble size distribution is employed. The reference vector corresponds to a liquid velocity of  $10 \text{ [cm s}^{-1}\text{]}$ .

Finally, it has to be noted that Chen *et al.* did not observe the two different sections predicted by our CFD model; instead they observed vortices over the entire height of the column. This point requires further thought. In Chapter 3 we showed that the lift force has a considerable impact on the distribution of bubbles over the cross-section of the bubble column. The precise value of the lift coefficient is a topic of ongoing debate; its value is determined by local flow phenomena (Yang and Thomas, 1998) and may also be influenced by contamination in the liquid phase. Our discrete bubble model does not account for this interplay between local flow phenomena, or contamination of the liquid phase, and the lift coefficient. This may explain the difference between Chen's experimental observations and our numerical predictions.

#### 4.2 Effect of column aspect ratio: comparison with experimental observations

In addition to model simulations, experiments have been conducted in the pseudo two-dimensional bubble column described in section 3. An important theoretical result is the predicted transition of the flow structure from the “cooling tower” flow pattern to the flow pattern with staggered vortices. At an aspect ratio of 1.0 the model predicted a pseudo steady state flow pattern, with the bubble plume rising along the center of the bubble column. This bubble plume did not oscillate. At an aspect ratio of 4.8 however, the model predicted the occurrence of a strongly time-dependent flow structure with an oscillating bubble plume. In order to assess the validity of these computational results the frequency of oscillation of the bubble plume at various aspect ratios was determined experimentally. This frequency of oscillation was obtained from longtime video observation of the bubble plume in columns with aspect ratios ranging from 1.0 to 7.0.

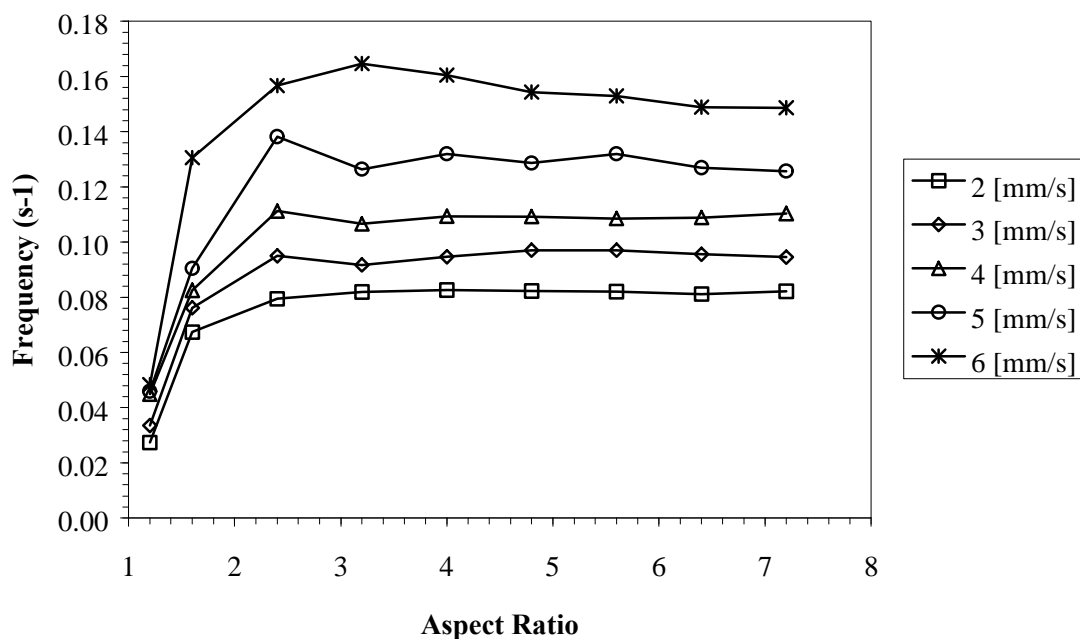


**Figure 8.** Frequency of oscillation of the bubble plume versus the aspect ratio of the bubble column under consideration at various superficial gas velocities. Based on measurements in a pseudo two-dimensional air-water bubble column.

Figure 8 shows the frequency of oscillation of the bubble plume as a function of the aspect

ratio and the superficial gas velocity. It can clearly be seen that the frequency of oscillation of the bubble plume decreases rapidly as the aspect ratio of the bubble column approaches unity. Additionally, the frequency of oscillation is observed to be fairly constant at aspect ratios exceeding 3.0. Based upon these observations there appears to exist a transition region, corresponding to aspect ratios ranging from 1.0 to 3.0, where the frequency of oscillation increases with increasing aspect ratio. This behavior is most likely due to a transition from the “cooling tower” mode of circulation ( $L/D = 1.0$ ) to the staggered vortices flow pattern ( $L/D > 3.0$ ). In this respect, the observations support the results obtained with our model (which predicts a similar transition).

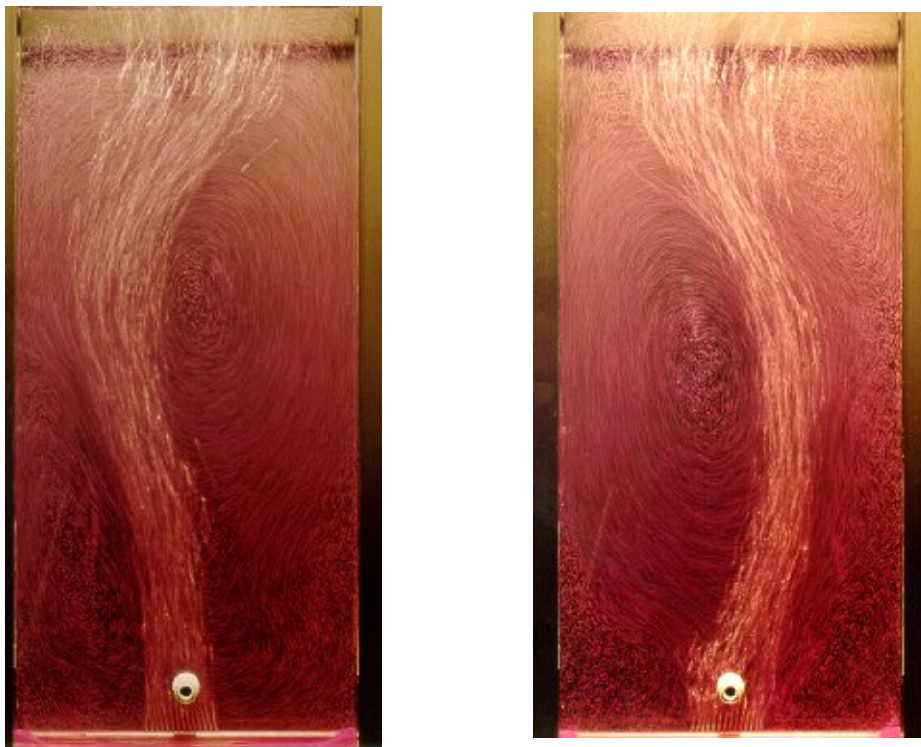


**Figure 9.** Streak photographs depicting the flow structure in a pseudo two-dimensional bubble column with an aspect ratio of 2.2. Neutrally buoyant tracer particles were used to visualize the liquid flow field. Additional parameters are listed in Table 3.

The frequency of oscillation predicted by our model (not shown) however, is 1.5-2 times larger than the experimentally determined frequency of oscillation of the bubble plume. This is most likely due to the two-dimensional nature of our model that does not account for the effect of the front and back walls of the pseudo two-dimensional bubble column.

In a separate experiment, neutrally buoyant tracer particles were added to the two-phase flow in order to visualize the vortical structures dominating the liquid flow field. Figure 9 shows these structures in a bubble column with an aspect ratio of 2.2 (additional parameter values are listed in Table 3). The bubble plume exhibits an oscillatory behavior; Figure 9 shows the two extreme positions of the bubble plume. The vortices determining the structure of the two-phase flow can clearly be seen from these streak photographs. The bubble plume is influenced by a large vortex, pushing it towards the left or towards the right wall of the column. These vortices were observed to develop at the free surface and to descend along the walls of the bubble column, thereby causing the time-dependent, oscillatory behavior of the bubble plume.

**Table 3.** Conditions used in theoretical and experimental study of flow structure prevailing in a pseudo two-dimensional bubble column.

Column dimensions	
Width:	0.2500 [m]
Height:	
L/D = 2.2	0.5500 [m]
Superficial gas velocity	2.0 [mm s <sup>-1</sup> ]
Physical properties	
Density liquid:	1000.0 [kg m <sup>-3</sup> ]
Viscosity liquid:	1.0 x 10 <sup>-3</sup> [Ns m <sup>-2</sup> ]
Density gas:	1.2 [kg m <sup>-3</sup> ]
Bubble diameter:	2.0 x 10 <sup>-3</sup> [m]
Computational parameters	
Number of computational cells in lateral direction:	25
Number of computational cells in axial direction:	
L/D = 2.2	55
Time step:	5.0 x 10 <sup>-3</sup> [s]
Tracer particles	
Type:	XAD-7
Particle size:	250 [μm]
Density:	1070 [kg m <sup>-3</sup> ]
Terminal velocity in water:	2.4 x 10 <sup>-3</sup> [m s <sup>-1</sup> ]

Response time:	3.7 [ms]
Photography	
Exposure time:	0.1250 [s]

The time-dependent behavior of this pseudo two-dimensional bubble column has been investigated with the model presented in this paper. Figure 10 depicts the instantaneous bubble positions and associated liquid velocity field 50 [s] after gas was first supplied to the column. The parameter values used in the computation are listed in Table 3. Comparing Figure 9 to Figure 10 indicates points of difference and points of resemblance between experiment and theory. At first sight, the bubble plumes in Figures 9 and 10 show similar characteristics; the model predicts the S-shaped path followed by the bubbles and it also predicts the large vortex near the left wall of the column. This vortex however, does not move downward along the wall of the column as was observed in the experimental setup. The model also overestimates the amount of bubbles captured by the downward liquid motion along the walls of the column.

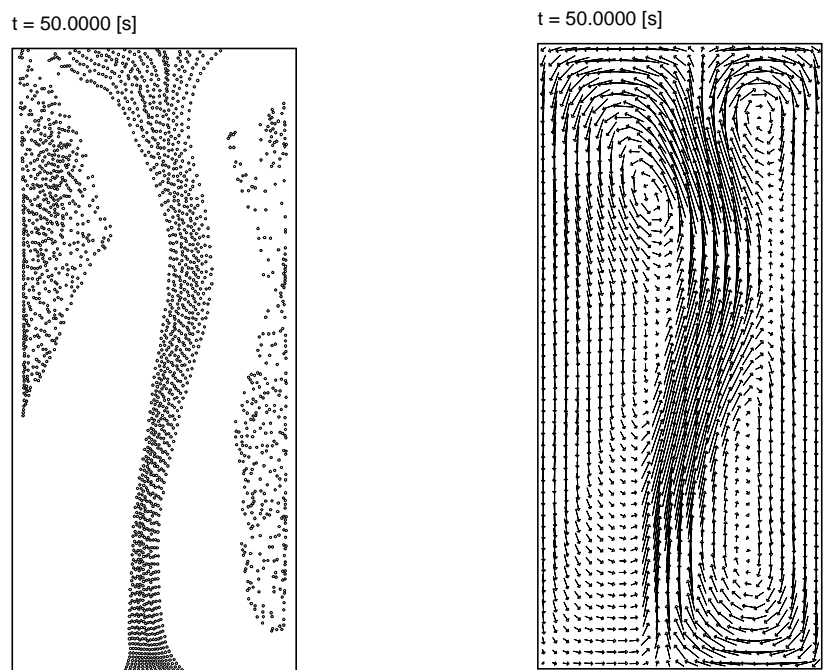


**Figure 10.** Computed structure of the gas-liquid two-phase flow in a bubble column with an aspect ratio of 2.2. The superficial gas velocity is equal to 2 [mm s<sup>-1</sup>]. A uniform bubble size distribution is employed. Both the instantaneous bubble positions and the liquid velocity fields are shown at 50 [s] after start up. The reference vector corresponds to a liquid velocity of 10 [cm s<sup>-1</sup>].

## 5. Conclusions

In the present paper an Euler-Lagrange model for a gas-liquid bubble column has been presented. The model resolves the time-dependent, two-dimensional motion of small, spherical gas bubbles in a liquid. The model incorporates all relevant forces acting on a bubble in a liquid, and additionally accounts for direct bubble-bubble interactions. The liquid phase hydrodynamics are described using the volume-averaged Navier-Stokes equations.

This model has been used to investigate the effect of the aspect ratio of the bubble column on the overall liquid circulation pattern. This effect has been studied experimentally by Chen *et al.* (1989). Computer simulations were performed for bubble columns with aspect ratios of 1.0, 2.0, 4.8, 7.7 and 11.4. A clear transition in the gas-liquid flow pattern could be observed. At an aspect ratio of 1.0 the “cooling tower” flow structure prevailed. Two circulation cells characterize this flow structure with liquid up flow in the center of the column and liquid down flow along the walls of the column. At an aspect ratio of 2.0 the staggered vortices mode of circulation prevailed, although at this aspect ratio the vortices were not observed to move downward along the walls of the column. Increasing the aspect ratio to 4.8 revealed a highly dynamic flow pattern with multiple staggered vortices. These vortices were observed to develop at the free surface, and to subsequently descend along the walls of the column, thereby causing the bubble plume to oscillate. At aspect ratios of 7.7 and higher, the flow structure in the bubble column was found to consist of two different regions. A clear bubble plume and a time-dependent, multiple staggered vortex mode of circulation, characterize the lower region. In the upper region of the bubble column, bubbles are dispersed over the entire cross section of the column and vortices do not appear in this section of the column.

Finally, experimental results obtained in a pseudo two-dimensional bubble column partly support our model findings. The frequency of oscillation of the bubble plume was determined experimentally for several aspect ratios and the data obtained indicate that a clear and distinct transition in flow pattern occurs in case the aspect ratio is changed from 1.0 to 3.0. At  $L/D = 1.0$  the frequency of oscillation approaches zero, indicating the “cooling tower” mode of liquid circulation whereas at  $L/D > 3.0$  the frequency of oscillation approaches a constant value resembling the staggered vortices mode of circulation.

Neutrally buoyant tracer particles were used to visualize the vortices in a pseudo two-



dimensional bubble column with an aspect ratio of 2.2. The computed flow structure resembled the experimentally observed flow pattern although the time-dependent behavior predicted by our model differed from that observed in the real-life bubble column.

## 6. Notation

$\mu_1$	Shear viscosity liquid [ $\text{kg m}^{-1} \text{s}^{-1}$ ]
$A$	Area [ $\text{m}^2$ ]
$C_D$	Drag coefficient [-]
$C_L$	Lift force coefficient [-]
$C_{VM}$	Virtual mass coefficient [-]
$D$	Diameter of the bubble column [m]
$D_b$	Bubble diameter [m]
$DT$	Time step [s]
$dx$	Grid size in x direction [m]
$dy$	Grid size y direction [m]
$E$	Unit tensor [-]
$\varepsilon_1$	Volume fraction liquid in computational cell [-]
$f_i$	Local momentum transfer rate G $\rightarrow$ L bubble i [N]
$F$	Volume aver. momentum transfer rate [ $\text{N m}^{-3}$ ]
$F_D$	Drag force on a bubble [N]
$F_G$	Force on bubble due to gravity [N]
$F_L$	Lift force on bubble [N]
$F_P$	Force on bubble due to pressure gradient [N]
$F_{\text{total}}$	Total force on a bubble [N]
$F_{VM}$	Virtual mass force on bubble [N]
$g$	Acceleration due to gravity [ $\text{m s}^{-2}$ ]
$i$	Bubble index number [-]
$I$	Kelvin impulse deformable body [Ns]
$L$	Height of the bubble column [m]
$\lambda_1$	Bulk viscosity liquid [ $\text{kg m}^{-1} \text{s}^{-1}$ ]

$m_b$	Mass of a bubble [kg]
$P$	Pressure [ $\text{N m}^{-2}$ ]
$\mathbf{r}$	Position of bubble [m]
$R_b$	Radius of a bubble [m]
$Re_b$	Reynolds number for flow around a bubble [-]
$\rho_g$	Density gas phase [ $\text{kg m}^{-3}$ ]
$\rho_l$	Density liquid phase [ $\text{kg m}^{-3}$ ]
$\mathbf{t}_l$	Stress tensor liquid [ $\text{N m}^{-2}$ ]
$\mathbf{u}$	Liquid velocity [ $\text{m s}^{-1}$ ]
$\mathbf{v}$	Velocity of bubble [ $\text{m s}^{-1}$ ]
$V_b$	Volume of a bubble [ $\text{m}^3$ ]
$V_{\text{cell}}$	Volume of a computational cell [ $\text{m}^3$ ]
$\mathbf{W}$	Vorticity in liquid phase [ $\text{s}^{-1}$ ]

## 7. References

Auton, T. R., 1983, The dynamics of bubbles, drops and particles in motion in liquids. Ph.D. Thesis, University of Cambridge, Cambridge.

Batchelor, G. K., 1967, "An introduction to fluid mechanics", Cambridge University Press, Cambridge.

Chen, J. J. J., Jamialahmadi, M. and Li, S. M., 1989, "Effect of liquid depth on circulation in bubble columns: a visual study", *Chem. Eng. Res. Des.* **67**, 203.

Clift, R., Grace, J. R. and Weber, M. E., 1978, "Bubbles, drops and particles", Academic Press, New York, U.S.A.

Delnoij, E., Lammers, F. A., Kuipers, J. A. M. & van Swaaij, W. P. M., 1997, "Dynamic simulation of dispersed gas-liquid two-phase flow using a discrete bubble model", *Chem. Eng. Sci.* **52** (9), 1429. (Chapter 3 of this Thesis).

Duineveld, P. C., 1994, "Bouncing and coalescence of two bubbles in water", Ph.D. Thesis, Twente University, Enschede, The Netherlands.

Freedman W. and Davidson, J. F., 1969, "Holdup and liquid circulation in bubble columns", *Trans. I. Chem. E.* **47**, T251.

Hoomans, B. P. B., Kuipers, J. A. M., Briels, W. J. and van Swaaij, W. P. M., 1996, "Discrete particle simulation of bubble and slug formation in a two dimensional gas-fluidised bed: a hard sphere approach", *Chem. Eng. Sci.* **51**, 99.

Jakobsen, H. A., Sannaes, B. H., Grevskott, S. and Svendsen, H. F., 1997, "Modeling of vertical bubble-driven flows", *Ind. Eng. Chem. Res.* **36**, 4052.

Joshi, J. B. and Sharma, M. M., 1979, "Some design features of radial baffles in sectionalized bubble columns", *Can. J. Chem. Eng.* **57**, 375.

Kuipers, J. A. M., van Duin, K. J., van Beckum, F. P. H. and van Swaaij, W. P. M., 1993, "Computer simulation of the hydrodynamics of a two dimensional gas-fluidized bed", *Comput. Chem. Eng.* **17**, 839.

Lapin, A. and Lübbert, A., 1994, "Numerical simulation of the dynamics of two phase gas-liquid flows in bubble columns", *Chem. Eng. Sci.* **49**, 3661.

Sangani, A. S., Kang, S. -Y., Koch, D. L. and Tsao, H. -K., 1995, "Numerical simulation and kinetic theory for simple shear motion of bubbly suspensions", *IUTAM Symposium on waves in liquid / gas and liquid / vapour two-phase systems*, S.Morioka and L. van Wijngaarden (eds.), Kluwer Academic Press, 137.

Shah, Y. T., Kelkar, B. G., Godbole, S. P. and Deckwer, W. -D., 1982, "Design parameter estimations for bubble column reactors", *AIChE Journal* **28** (3), 353.

Sokolichin, A. and Eigenberger, G., 1994, "Gas-liquid flow in bubble columns and loop reactors: part I. Detailed modelling and numerical simulation", *Chem. Eng. Sci.* **49**, 5735.

Sokolichin, A. and Eigenberger, G., Lapin, A. and Lübbert, A., 1997, "Dynamic numerical simulation of gas-liquid two-phase flows, Euler / Euler versus Euler / Lagrange", *Chem. Eng. Sci.* **52** (4), 611.

Tsao, H. -K. and Koch, D. L., 1997, 'Observations of high Reynolds number bubbles interacting with a rigid wall', *Phys. Fluids* **9**(1), 44.

Tsao, H. -K. and Koch, D. L., 1994, 'Collisions of slightly deformable, high Reynolds number bubbles with short-range repulsive forces', *Phys. Fluids* **6**, 2591.

Van den Akker, H. E. A., 1998, "The Euler-Euler approach to dispersed two-phase flows in the turbulent regime", *ERCRAFTAC Bulletin* **36**, 30.

Yang, X. and Thomas, N. H., 1998, "Prediction of void fraction and velocity profiles of bubbly flows in vertical pipes", *Chem. Eng. Comm.* **163**, 145.

## Chapter 5:

### A three dimensional CFD model for gas-liquid bubble columns<sup>1</sup>

#### 0. Abstract

This paper discusses the development of a three-dimensional Euler-Lagrange CFD model for a gas - liquid bubble column. The model resolves the time-dependent, three-dimensional motion of small, spherical gas bubbles in a liquid. Our model incorporates all relevant forces acting on a bubble rising in a liquid, and accounts for two-way momentum coupling between the phases. The liquid phase hydrodynamics are described using the volume - averaged Navier -Stokes equations. This three-dimensional CFD model is used to study the effect of the aspect ratio of the bubble column on the overall liquid circulation pattern. Computer simulations were performed for bubble columns with aspect ratios of 1.0, 2.0, 4.8 and 7.7. A clear transition in the gas - liquid flow pattern could be observed. At an aspect ratio of 1.0 and 2.0 the “cooling tower” flow pattern prevailed. Increasing the aspect ratio to 4.8 and 7.7 revealed a highly complex and dynamic flow pattern with multiple staggered vortices. The results computed with this three-dimensional discrete bubble model reveal a considerably more complex flow structure than that predicted by our two-dimensional discrete bubble model (Delnoij *et al.*, 1997c).

---

<sup>1</sup> Delnoij, E., Kuipers, J. A. M. and van Swaaij, W. P. M., 1998, “A three dimensional CFD model for gas-liquid bubble columns”, *Accepted for presentation at ISCRE 15 and publication in Chem. Eng. Sci.*

## 1. Introduction

Gas-liquid bubble columns are of considerable importance to the biological, chemical and petrochemical industries. They are typically employed in applications involving gas-liquid mass transfer and (exothermal) chemical reactions such as hydrogenation reactions, oxidation reactions, catalytic slurry reactions, bioreactions and coal liquefaction. This widespread application stems from the fact that bubble columns offer some distinct advantages over other multiphase reactors, among which its excellent heat transfer characteristics, its simple construction and its low operating costs should be mentioned (Shah *et al.*, 1982). Despite their frequent application in industry however, our knowledge of the fluid dynamic phenomena prevailing in bubble columns is limited. These phenomena include bubble coalescence and breakup, the transition between the flow regimes, and the vortical structures dominating the liquid flow field in the bubble column.

In recent years, computational fluid dynamics (CFD) has emerged as a powerful tool for engineers and scientists alike, providing valuable information on the temporal and spatial distribution of key variables in a flow field. CFD can be applied with confidence to solve a variety of single-phase flow problems. However, a considerable research effort still has to be made before CFD can be applied to the study of gas-liquid two-phase flows with the same level of confidence. Several problems have yet to be solved, for instance, there seems to be no general agreement on the definite form of the governing equations (Stewart and Wendroff, 1984 and Jakobsen *et al.*, 1997). There is also an ongoing debate about which modeling approach (Euler-Euler or Euler-Lagrange) is most suited for the study of these gas-liquid two-phase flows (Delnoij *et al.*, 1997b and Van den Akker, 1998). Finally, CFD modeling of gas-liquid two-phase flows is complicated by considerable ambiguity about the correct description of bubble dynamics and of the interplay between bubbles and turbulent eddies.

Nevertheless, CFD modeling of dispersed gas-liquid two-phase flows has shown remarkable progress over the last decade. The two most common approaches to modeling bubble columns are the Euler-Euler or Two-Fluid approach and the Euler-Lagrange or discrete bubble approach. In the Euler-Euler approach, both phases (the continuous liquid phase and the dispersed gas phase) are modeled as two interpenetrating continua. In the Euler-Lagrange approach, on the other hand, the volume averaged Navier-Stokes equations are used to

describe the motion of the liquid phase and each bubble is tracked on basis of a balance of forces acting upon the bubble and an equation of motion<sup>2</sup>.

In recent years, a number of authors (Torvik and Svendsen, 1990; Ranade, 1992; Grienberger and Hofman, 1992; Hjertager and Morud, 1995; Sokolichin and Eigenberger, 1994 and Van den Akker, 1998) have published interesting results obtained with Euler-Euler CFD models for bubble columns. The results obtained by Sokolichin and Eigenberger (1994) clearly reveal the time-dependent behavior of a gas-liquid bubble column. Only long time averaging of the instantaneous results showed the familiar experimentally observed ‘cooling tower’ liquid circulation with liquid up flow along the centerline of the column and liquid down flow along the containing walls.

Trapp and Mortensen (1993), Lapin and Lübbert (1994), Devanathan *et al.* (1995) and Delnoij *et al.* (1997[a-c]) conducted pioneering work on Euler-Lagrange modeling of the dispersed gas-liquid two-phase flow encountered in bubble columns operated in the homogeneous regime. The models developed differ in their description of the bubble dynamics and the coupling between the phases. Delnoij *et al.* (1997c) used their two-dimensional Euler-Lagrange CFD model to study a/o the effect of the column aspect ratio on the flow structure prevailing in a bubble column. The computed results revealed vortical structures in the liquid flow field at aspect ratios exceeding two. In reality however, these vortical structures exhibit three-dimensional features (all three components of velocity are significant in oscillating and circulating flows); the computational results obtained with the two-dimensional model therefore prompted the development of a three-dimensional Euler-Lagrange discrete bubble model for a bubble column operated in the homogeneous regime. The essential features of this CFD model, and the results obtained with this model will be discussed in this paper.

---

<sup>2</sup> Recently, fully resolved Navier-Stokes simulations have been employed in LES / DNS studies of bubbly flows. These extremely detailed models use the instantaneous Navier-Stokes equation to obtain the flow field surrounding the individual bubbles. In this paper however, the term Euler-Lagrange refers to the less detailed CFD models that use the volume-averaged Navier-Stokes equations to obtain the macroscopic flow field.

## 2. Model equations

The three-dimensional discrete bubble model presented in this paper describes the homogeneous or dispersed bubble regime. Relatively low gas velocities and small, spherical bubbles characterize this regime. The discrete bubble model consists of two intimately coupled parts: the first part describes the liquid phase hydrodynamics and the second part models the behavior of each individual bubble using the Newtonian equation of motion and appropriate expressions for the relevant forces acting on a bubble. In section 2 these parts will be discussed in more detail whereas in section 3 the two-way coupling and the numerical aspects of the model are addressed.

### 2.1 Bubble dynamics

Our model employs an equation of motion for each individual bubble to calculate that bubble's new position from its previous time level position and present time level velocity. The required new bubble velocity is calculated with a simple, explicit integration formula:

$$\mathbf{v}^{n+1} = \mathbf{v}^n + \left( \frac{d\mathbf{v}}{dt} \right)^n DT \quad 1$$

Each bubble's acceleration is calculated from a force balance for the bubble under consideration:

$$m_b \frac{d\mathbf{v}}{dt} = \mathbf{F}_{total} \quad 2$$

It is assumed that the force  $\mathbf{F}_{total}$  acting on a non-deformable and spherical gas bubble rising in an unsteady, and non-uniform liquid flow field is composed of separate and uncoupled contributions from pressure gradient, drag, virtual or added mass, vorticity and gravity (Auton, 1983):

$$\mathbf{F}_{total} = \mathbf{F}_P + \mathbf{F}_D + \mathbf{F}_{VM} + \mathbf{F}_L + \mathbf{F}_G \quad 3$$

Table 1 summarizes the equations and constants used to calculate the various forces acting on a bubble. For a more elaborate discussion of these expressions, the interested reader is referred to Delnoij *et al.* (1997a). The two-dimensional discrete bubble model developed by Delnoij *et al.* (1997[a-c]) accounted for direct bubble-bubble interaction using a collision. The three-dimensional discrete bubble model presented in this paper does not account for these direct bubble-bubble interactions. The model does however, account for collisions between bubbles and the walls of the bubble column.



**Table 1:** Forces acting on a non-deformable and spherical gas bubble rising in an unsteady and non-uniform liquid flow field.

Force:	Expression:
Gravity and Far Field Pressure	$\mathbf{F}_G + \mathbf{F}_P = \mathbf{r}_g V_b \mathbf{g} - V_b \nabla P$
Drag Force	$\mathbf{F}_D = -\frac{1}{2} C_D \mathbf{r}_l \rho R_b^2  \mathbf{v} - \mathbf{u}  (\mathbf{v} - \mathbf{u})$ $C_D = \begin{cases} \text{Re}_b \leq 1000 \Rightarrow \frac{24}{\text{Re}} (1 + 0.15 \cdot \text{Re}_b^{0.687}) \\ \text{Re}_b > 1000 \Rightarrow 0.44 \end{cases}$
Lift Force	$\mathbf{F}_L = -C_L \mathbf{r}_l V_b (\mathbf{v} - \mathbf{u}) \times \boldsymbol{\Omega}$ $\boldsymbol{\Omega} = \nabla \times \mathbf{u}$ $C_L = 0.53$
Virtual Mass Force	$\mathbf{F}_{VM} = -\left( \frac{D\mathbf{I}}{Dt} + \mathbf{I} \cdot \nabla \mathbf{u} \right)$ $\mathbf{I} = C_{VM} \mathbf{r}_l V_b (\mathbf{v} - \mathbf{u})$ $C_{VM} = 0.5$

## 2.2 Liquid phase hydrodynamics

The liquid phase hydrodynamics are described with the volume-averaged mass and momentum conservation equations given respectively by:

$$\frac{\partial(\mathbf{e}_l \mathbf{r}_l)}{\partial t} + \nabla \cdot \mathbf{e}_l \mathbf{r}_l \mathbf{u} = 0 \quad 4$$

And:

$$\frac{\partial(\mathbf{e}_l \mathbf{r}_l \mathbf{u})}{\partial t} + \nabla \cdot \mathbf{e}_l \mathbf{r}_l \mathbf{u} \mathbf{u} = -\mathbf{e}_l \nabla P - \nabla \cdot \mathbf{e}_l \mathbf{t}_l + \mathbf{e}_l \mathbf{r}_l \mathbf{g} + \Phi \quad 5$$

The liquid flow field is solved using a finite difference technique; details of this particular method can be found in Kuipers *et al.* (1993). The spatial resolution employed to solve the liquid velocity field is small compared to the size of the bubbles; the liquid-bubble interaction can therefore be superimposed on the liquid velocity field in a straightforward fashion. This liquid-bubble interaction is modeled with the source term  $\mathbf{F}$  that accounts for the momentum exchange between the bubbles and the liquid.

In the present study three-dimensional, isothermal motion of both the gas and the liquid phase is assumed. The basic variables that are calculated by the model are pressure, the three

components of the liquid velocity and the velocity and position of each individual bubble. All other variables appearing in the balance equations must be specified in terms of these variables.

The liquid phase viscous stress tensor  $\mathbf{t}_l$  is assumed to obey the general form for a Newtonian fluid:

$$\mathbf{t}_l = -\left[\left(\mathbf{I}_l - \frac{2}{3}\mathbf{m}_l\right)(\nabla \cdot \mathbf{u})\mathbf{E} + \mathbf{m}_l\left((\nabla \mathbf{u}) + (\nabla \mathbf{u})^T\right)\right] \quad 6$$

The bulk viscosity  $\lambda_l$  is set to zero in all simulations presented in this paper. In most simulations water is used as the liquid phase with a shear viscosity of  $1.0 \cdot 10^{-3} \text{ kg m}^{-1} \text{ s}^{-1}$ .

### 3. Coupling between the phases

The two parts that constitute our CFD model are coupled through the liquid volume fraction  $\varepsilon_l$  and through the source term  $\mathbf{F}$  that accounts for the momentum transfer from the bubbles to the liquid. Both this liquid volume fraction  $\varepsilon_l$  and the source term  $\mathbf{F}$  have to be calculated in accordance with the number of bubbles present in a computational cell. In order to evaluate the reverse momentum transfer rate, i.e. from the liquid to a specific bubble, all quantities pertaining to the liquid phase (i.e. pressure and velocity components) have to be available at the center of mass position of this bubble. These so-called local liquid properties are derived from the values of the volume-averaged liquid properties at the grid nodes surrounding the bubble under consideration.

The two-way momentum coupling included in our model is of crucial importance, as has been shown by Delnoij *et al.* (1997a). Delnoij *et al.* showed that a model not using two-way momentum coupling could not account for the time-dependent behavior generally observed in pseudo two-dimensional gas-liquid bubble columns.

#### 3.1 The liquid volume fraction

The liquid volume fraction in a computational cell is derived from the volume occupied by the bubbles in that cell and the total volume of that cell:

$$\mathbf{e}_l = 1 - \frac{\sum_{\forall i \in \text{cell}} V_{bi}}{V_{\text{cell}}} \quad 7$$

In determining the liquid volume fraction according to equation (7), it is important to account for gas bubbles that overlap with more than one computational cell. Figure 1 depicts such a bubble; its center of mass position is well within a particular computational cell, but the bubble nevertheless overlaps with adjacent cells. The volume occupied by this gas bubble has to be distributed over the computational cells concerned. Exact calculation of the fractional gas volume proves CPU time consuming, especially if two or more cell faces cut the bubble under consideration. In these cases, the fractional volume of a bubble attributable to a particular computational cell is estimated using the fractional bubble volume defined by each face separately. This particular approach significantly reduces the CPU time required to determine the liquid volume fraction without compromising the accuracy of the computer code.

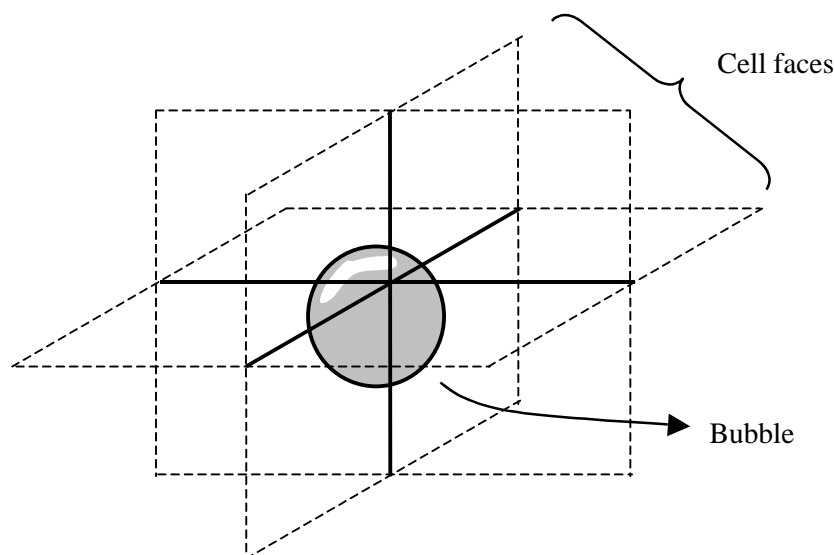


**Figure 1.** Schematic representation of the overlap between a gas bubble and multiple computational cells. In this case, the volume of the gas bubble has to be distributed proportionally over the computational cells concerned.

### 3.2 Momentum transfer from bubbles to liquid

The momentum transfer from the bubbles to the surrounding liquid ( $\mathbf{F} \cdot \mathbf{V}_{\text{cell}}$ ) is just the opposite of the drag, lift and virtual mass forces exerted by the liquid on the bubbles. These forces can be used to determine the local (at the center of mass position of the bubble under consideration) momentum transfer rate  $\mathbf{f}_i$  for an individual bubble:

$$\mathbf{f}_i = -(\mathbf{F}_{Di} + \mathbf{F}_{VMi} + \mathbf{F}_{Li}) \quad 8$$

A volume-weighted averaging technique (similar to the area-weighted averaging technique developed for the two-dimensional discrete bubble model (Delnoij *et al.*, 1997[a-c])) is

employed to determine the volume-averaged momentum transfer rate ( $\mathbf{F} \cdot \mathbf{V}_{\text{cell}}$ ) at the eight grid nodes surrounding a particular bubble from the local momentum transfer rate pertaining to that bubble (see also Figure 2).

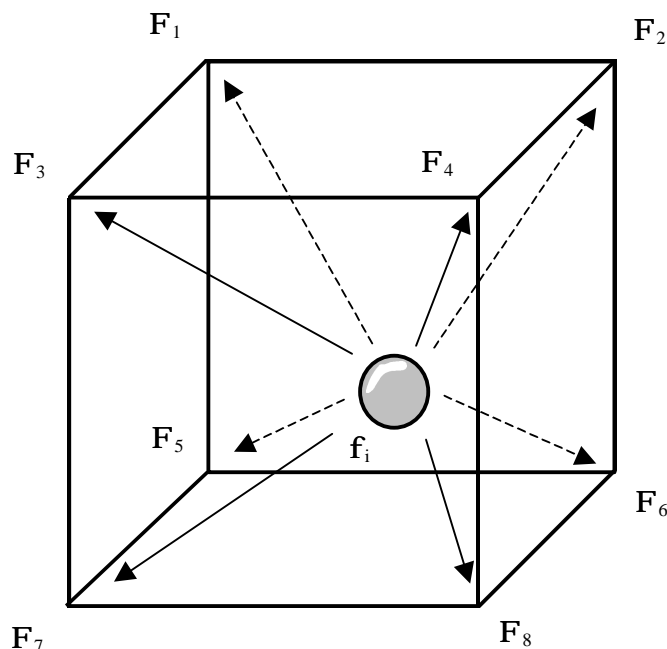


**Figure 2.** Volume weighting of local momentum transfer rate  $f_i$  to obtain the volume-averaged momentum transfer rate  $\mathbf{F}$  at the eight grid nodes surrounding the bubble.

### 3.3 Local liquid phase properties

The forces acting on a bubble can be calculated using the equations listed in Table 1. To determine these forces, local averaged values of the continuum variables (notably: pressure and the three components of velocity) and their respective spatial and substantial derivatives, are required at the center of mass position ( $\mathbf{r}_i$ ) of the bubble under consideration. However, these volume-averaged properties are only available at discrete nodes in the computational domain. Therefore, a volume-weighted averaging technique, similar to the technique employed to calculate the momentum transfer rate, is applied to obtain local values of the volume-averaged variables from their values at the eight grid nodes surrounding the bubble.

The method described in this paper employs a volume-averaging technique to obtain the volume-averaged momentum transfer rate and employs a similar averaging procedure to obtain the reverse momentum transfer rate (from the liquid to the bubbles). This ensures

rigorous momentum conservation because Newton's third law is strictly obeyed, even at the level of the individual bubbles.

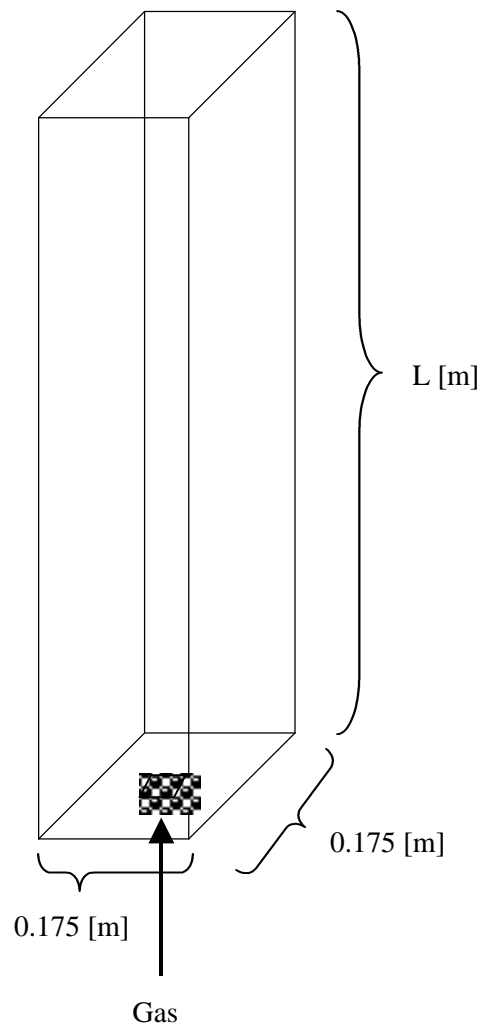


**Figure 3.** Schematic representation of the rectangular bubble column used in the simulations presented in this paper. A single gas-distributor (3.2 [cm] x 3.2[cm]) is mounted in the bottom of the column.

### 3.4 Numerical solution

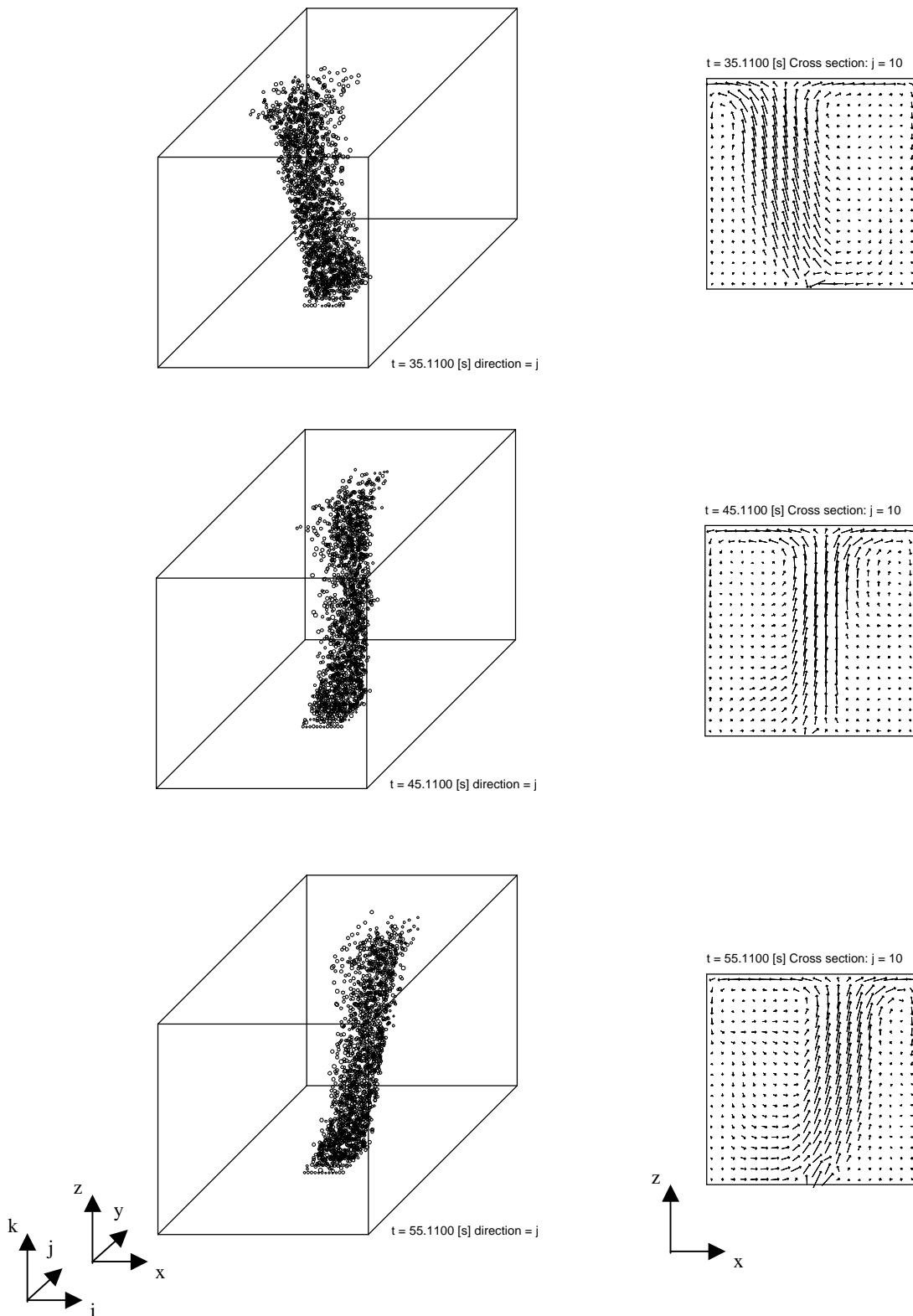
The three-dimensional discrete bubble model presented in this paper has been implemented in a computer code written in C, that solves the incompressible Navier-Stokes equations and tracks the motion of each individual bubble through the bubble column. The liquid flow field is computed using a technique also used by Kuipers *et al.* (1993); the system of equations resulting from the finite difference approximation of the Pressure-Poisson Equation (PPE) is solved using an iterative Conjugate Gradient Squared STABILized (CGSTAB) matrix solver (Ferziger and Peric, 1996). This particular method is exceptionally stable and robust and in

speed second only to the multigrid methods. Boundary conditions for the Navier-Stokes equations are specified using the flag matrix concept. CPU time requirements differ and depend on the number of nodes used to resolve the liquid flow field, and the number of bubbles contained in the bubble column. One of the larger problems, a bubble column of 0.175 m in width, 0.175 m in depth, 1.3475 m in height,  $6.16 \times 10^4$  nodes and  $7.0 \times 10^4$  bubbles requires approximately 300 hours dedicated CPU time on a Silicon Graphics Origin200 workstation equipped with a MIPS R10K RISC processor.

#### 4. Results

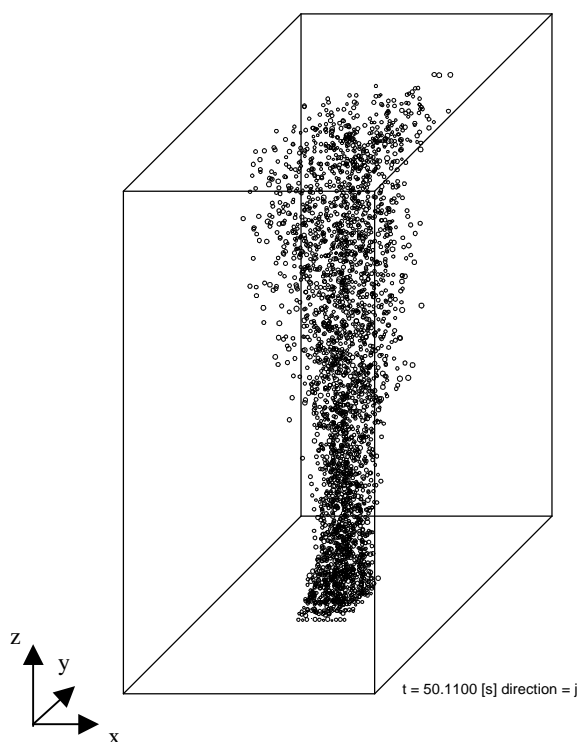
Delnoij *et al.* (1997c) studied the effect of the column aspect ratio on the flow structure prevailing in a bubble column. This work was inspired by experimental observations reported by Chen *et al.* (1989). Chen *et al.* studied the liquid circulation in bubble columns with aspect ratios ranging from 0.5 to 11.4 and they concluded that at low liquid depths ( $L/D < 1$ ) the ‘cooling tower’ flow pattern prevailed, whereas at liquid depths exceeding unity two rows of staggered vortices dominated the flow field. Delnoij *et al.* demonstrated that their two-dimensional model could predict this remarkable transition in flow pattern. Moreover, the computed results revealed the presence of vortical structures in the liquid phase at aspect ratios exceeding two. In this paper, the effect of the column aspect ratio on the flow structure will be studied with the three-dimensional version of the discrete bubble model as outlined in the previous sections. The three-dimensional CFD model simulates the operation of a rectangular bubble column (depicted in Figure 3) for a specified period of time, starting at  $t = 0.0$  [s] with an initially bubble free and quiescent liquid.

Figure 4 depicts the instantaneous position of the bubbles in a bubble column with an aspect ratio of 1.0 at three different times (relevant conditions listed in the caption of Figure 4). Also shown are the associated liquid velocity fields in a vertical cross section through the center of the bubble column (the x-z plane,  $y = 8.75$  [cm]). The velocity vectors depicted in Figure 4 are projections of the three dimensional velocity onto the plane of the cross section. It should be mentioned that the geometry of the bubble column used in this particular simulation differs from the column geometry employed by Chen *et al.*



**Figure 4.** Instantaneous position of the individual bubbles and the associated liquid velocity field ( $y = 8.750$  [cm]) at three different times in a bubble column with aspect ratio 1.0.  $NX = 20$ ;  $NY = 20$ ;  $NZ = 20$ ; Width = 0.175 [m]; Depth = 0.175 [m]; Height = 0.175 [m]; liquid: water; gas: air; gas flow rate =  $9.2 \times 10^{-5}$  [ $\text{m}^3 \text{s}^{-1}$ ];  $DT = 5.0 \times 10^{-3}$  [s].

From Figure 4, it can clearly be seen that the bubble plume, although on average rising along the column's centerline, slightly oscillates about this mean trajectory. This behavior can also be inferred from the associated liquid velocity field in a cross section of the bubble column. From these flow fields, two adjacent circulation cells can be seen to dominate the flow pattern observed in this particular configuration. The movement of the bubble plume is also clearly reflected in the liquid phase velocity field. Staggered vortices could not be observed in any cross section of the flow. Therefore, the flow pattern observed in the column still resembles the 'cooling tower' mode of circulation, despite the dynamic behavior of the bubble plume. This 'cooling tower' flow pattern still prevails at an aspect ratio of 2.0, as can be derived from Figure 5. This Figure depicts the instantaneous position of the bubbles in the bubble column after 50 [s] of simulated behavior of this column. Video animation of the computed results revealed that the bubble plume oscillated slightly around the centerline of the column. In this case, ( $L/D = 2.0$ ) the liquid flow field is likewise composed of two separate circulation cells that do not move through the bubble column.



**Figure 5.** Instantaneous position of the individual bubbles in a bubble column after 50 [s] of simulated operation of the column. Aspect ratio = 2.0.  $NX = 20$ ;  $NY = 20$ ;  $NZ = 40$ ; Width = 0.175 [m]; Depth = 0.175 [m]; Height = 0.350 [m]; liquid: water; gas: air; gas flow rate =  $9.2 \times 10^{-5}$  [m<sup>3</sup> s<sup>-1</sup>];  $DT = 5.0 \times 10^{-3}$  [s].



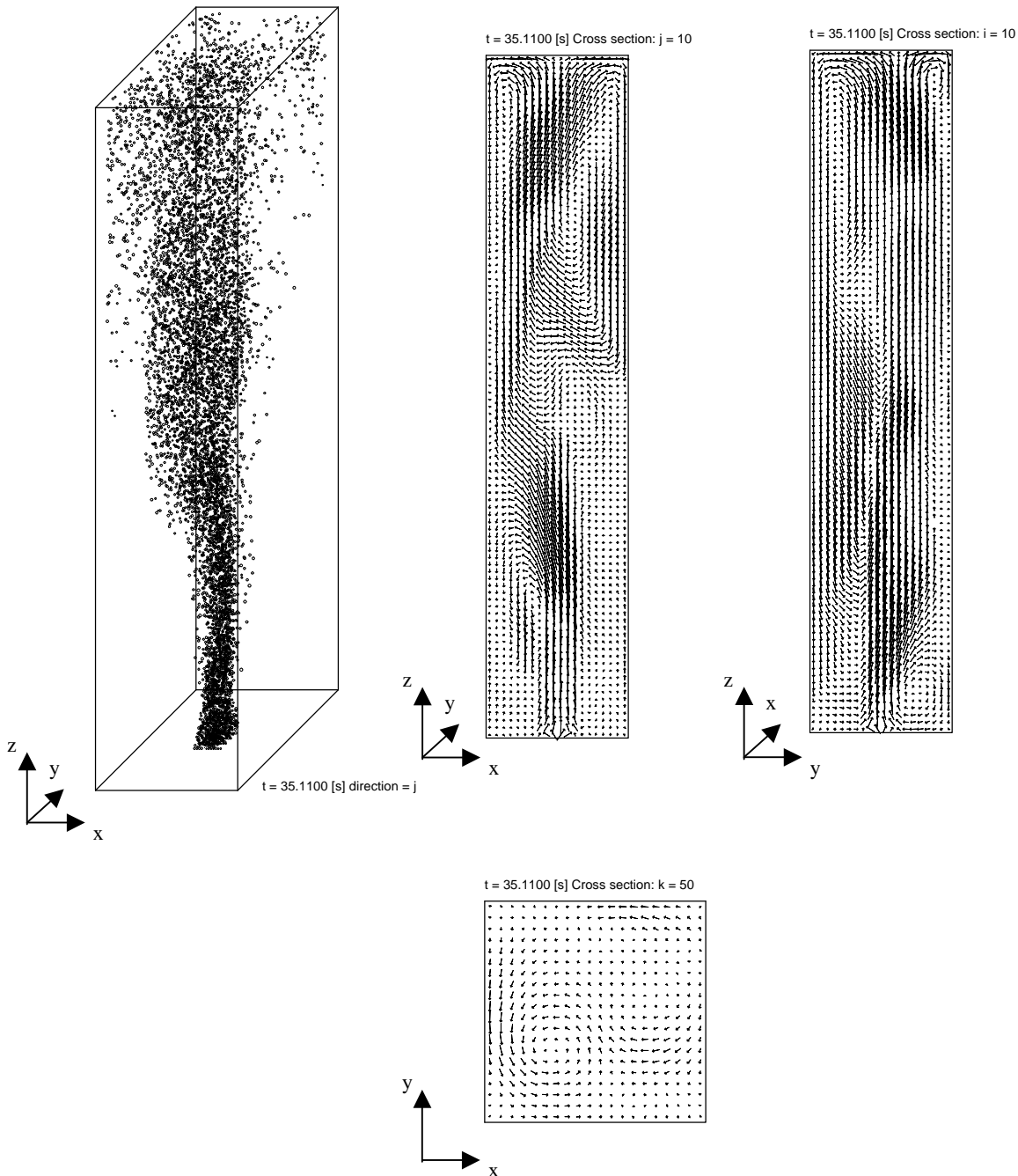


**Figure 6.** Instantaneous position of the individual bubbles and associated liquid velocity field in three perpendicular cross sections (at  $y = 8.750$  [cm],  $x = 8.750$  [cm] and  $z = 43.750$  [cm]) of a bubble column after 35 [s] of simulated operation of the column. Aspect ratio = 4.8.  $NX = 20$ ;  $NY = 20$ ;  $NZ = 96$ ; Width = 0.175 [m]; Depth = 0.175 [m]; Height = 0.840 [m]; liquid: water; gas: air; gas flow rate =  $9.2 \times 10^{-5}$  [ $\text{m}^3 \text{s}^{-1}$ ];  $DT = 5.0 \times 10^{-3}$  [s].

Time-dependent behavior can be observed in a bubble column with an aspect ratio of 4.8. Figure 6 shows the instantaneous position of the bubbles and the associated liquid flow field

in three perpendicular cross-sections through the bubble column after approximately 35 [s] of simulation time. The flow pattern depicted in Figure 6 changes continuously; the bubble plume moves through the column in a meandering and swirling fashion. The two-phase flow pattern observed at this aspect ratio is very complex, and is dominated by vortical structures in the liquid phase (the so-called ‘staggered vortex’ mode of circulation). Throughout the column, regions with liquid up flow and regions with liquid down flow can be observed. Liquid velocities also differ remarkably throughout the column; there are regions with high liquid velocities and regions with low liquid velocities.

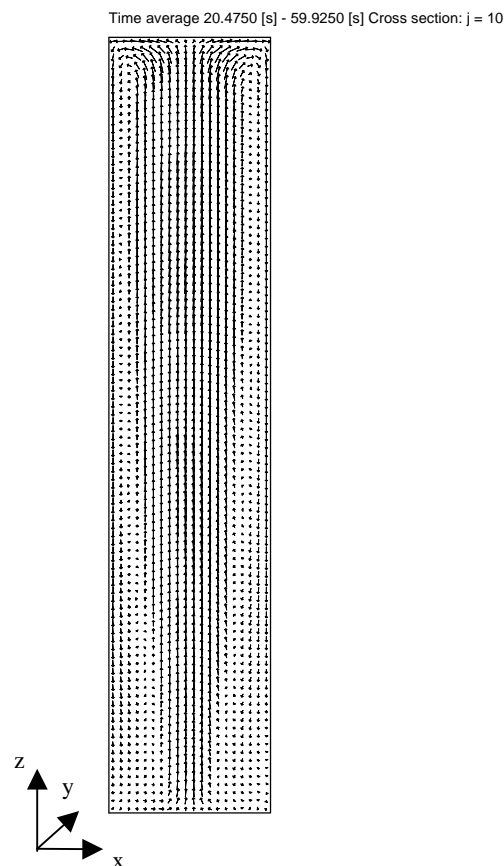


**Figure 7.** Time averaged liquid velocity field in a cross section ( $y = 8.750$  [cm]) of the bubble column. Time interval: 20 – 60 [s]. Aspect ratio = 4.8.  $NX = 20$ ;  $NY = 20$ ;  $NZ = 96$ ; Width = 0.175 [m]; Depth = 0.175 [m]; Height = 0.840 [m]; liquid: water; gas: air; gas flow rate =  $9.2 \times 10^{-5}$  [m<sup>3</sup> s<sup>-1</sup>];  
 $DT = 5.0 \times 10^{-3}$  [s].

With reference to previous work (Delnoij *et al.*, 1997c) it can be concluded that the flow pattern prevailing in this bubble column is considerably more complex than the pattern predicted with the two-dimensional discrete bubble model developed previously. Moreover,

there appears to be a transition in flow pattern from the ‘cooling tower’ mode of circulation to the staggered vortex mode of circulation as the aspect ratio of the bubble column is increased from 1.0 to 4.8. This result is in accordance with the observations reported by Chen *et al.* (1989) who described a similar transition in flow pattern.

Time averaging of the computed results reveals an entirely different flow pattern. This time averaged liquid velocity field (again in a cross section of the bubble column) can be seen in Figure 7. This time averaged flow pattern resembles the classical ‘cooling tower’ flow pattern with liquid up flow in the center of the column and liquid down flow near the walls of the column. Comparing Figures 6 and 7 clearly shows that the time averaged liquid flow field does not resemble the flow field prevailing in a bubble column. Therefore, experiments in gas-liquid bubble columns should be conducted using pseudo instantaneous, whole field measurement techniques rather than techniques yielding time averaged data.

Finally, the structure of the two-phase flow in a bubble column with an aspect ratio of 7.7 has been studied using our discrete bubble model. Figure 8a depicts the instantaneous position of the bubbles and Figure 8b shows the associated liquid flow field in three parallel cross sections of the bubble column. From video animation of the computed results, the bubble plume could be observed to oscillate vigorously through the bubble column. The bubble plume also spreads significantly under the action of lift forces acting on the gas bubbles. As a result of this dispersion, bubbles are caught by liquid flowing downward along the walls of the column. Again, it can clearly be seen that the flow structure in the bubble column at this aspect ratio is extremely complex and dominated by vortical structures in the liquid phase. These vortical structures develop at the free surface on opposite sites of the column center and subsequently descend along the walls of the bubble column. In this case, the flow structure computed by our three-dimensional discrete bubble model is considerably more complex than that predicted by our two-dimensional discrete bubble model (Delnoij *et al.*, 1997c).

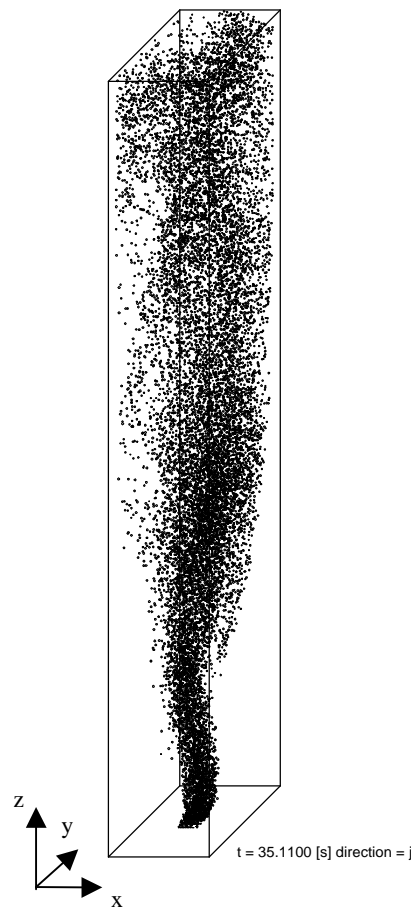


**Figure 8a.** Instantaneous position of the individual bubbles in a bubble column with an aspect ratio of 7.7.  $NX = 20$ ;  $NY = 20$ ;  $NZ = 154$ ; Width = 0.175 [m]; Depth = 0.175 [m]; Height = 1.3475 [m]; liquid: water; gas: air; gas flow rate =  $9.2 \times 10^{-5}$  [m<sup>3</sup> s<sup>-1</sup>];  $DT = 5.0 \times 10^{-3}$  [s].

## 5. Discussion and conclusions

In this paper, a three-dimensional Euler-Lagrange CFD model for a gas - liquid bubble column has been presented. The model resolves the time-dependent, three-dimensional motion of small, spherical gas bubbles in a liquid. The model incorporates all relevant forces acting on a bubble rising in a liquid, and accounts for two-way momentum coupling between the phases. The liquid phase hydrodynamics are described using the volume - averaged Navier - Stokes equations. The equations constituting our model, as well as details concerning the coupling between the phases have been discussed.

Our three-dimensional CFD model has been used to study the effect of the aspect ratio of the bubble column on the overall liquid circulation pattern. Computer simulations were performed for bubble columns with aspect ratios of 1.0, 2.0, 4.8 and 7.7. A clear transition in

the gas - liquid flow pattern could be observed. At an aspect ratio of 1.0 and 2.0 the “cooling tower” flow pattern prevailed. Two circulation cells characterize this flow structure with liquid up flow in the center of the column and liquid down flow along the walls of the column. Increasing the aspect ratio to 4.8 and 7.7 revealed a highly dynamic flow pattern with multiple staggered vortices. These vortices were observed to develop at the free surface, and to subsequently descend along the walls of the column, thereby causing the bubble plume to oscillate. The time-averaged liquid velocity fields however, still resembled the classical ‘cooling tower’ mode of circulation. This result therefore underlines the importance of dynamic modeling and it further strengthens the case for the development of two-phase (pseudo) instantaneous, whole field (preferably three-dimensional) measurement techniques, rather than measurement techniques that produce time-averaged data.

Generally, the flow structures computed by our three-dimensional discrete bubble model are considerably more complex than those predicted by our two-dimensional discrete bubble model (Delnoij *et al.*, 1997c). This is expected behavior due to the complex nature of the dispersed gas-liquid two-phase flow encountered in a bubble column and the inherently three-dimensional characteristics of this flow.

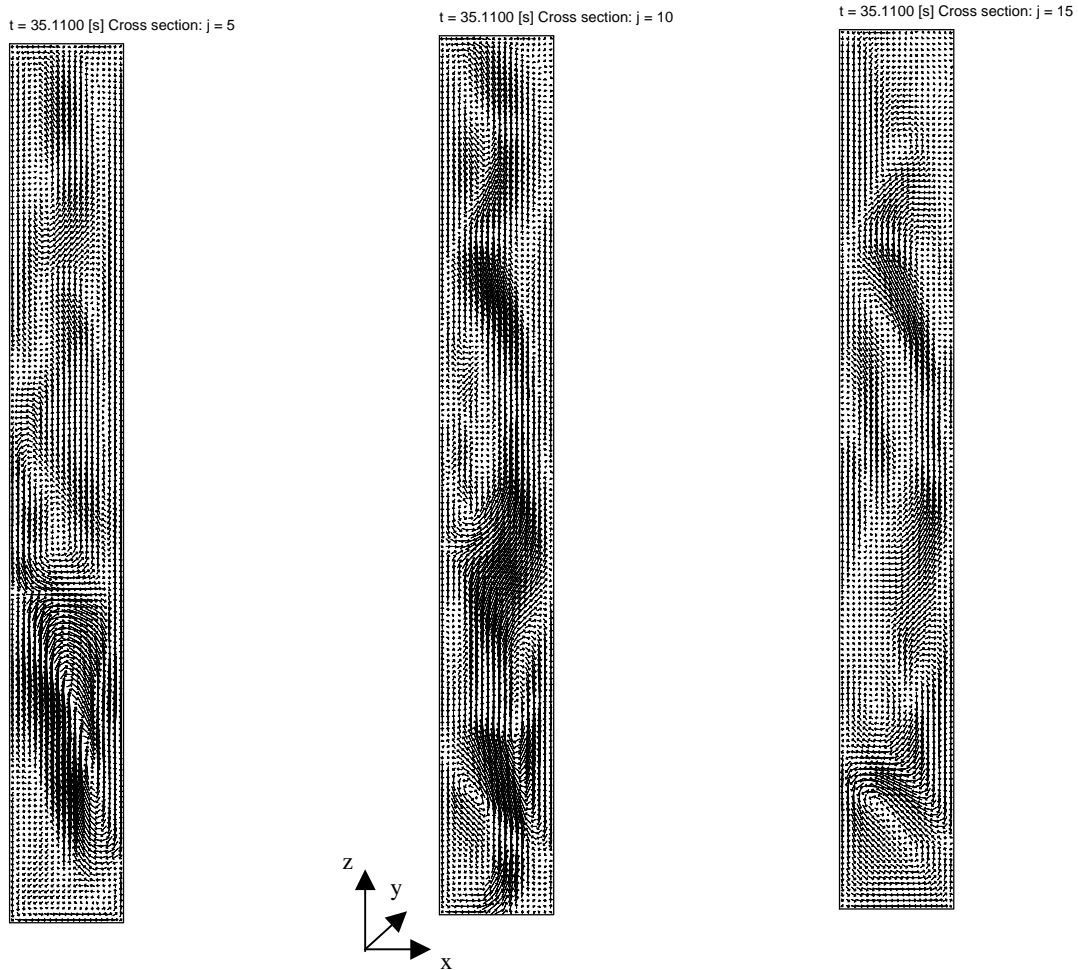


**Figure 8b.** Liquid velocity field in three parallel cross-sections through a bubble column with an aspect ratio of 7.7. Cross sections at  $y = 4.375$  [cm],  $y = 8.750$  [cm] and  $y = 13.125$  [cm].  $NX = 20$ ;  $NY = 20$ ;  $NZ = 154$ ; Width = 0.175 [m]; Depth = 0.175 [m]; Height = 1.3475 [m]; liquid: water; gas: air; gas flow rate =  $9.2 \times 10^{-5}$  [m<sup>3</sup> s<sup>-1</sup>];  $DT = 5.0 \times 10^{-3}$  [s].

## 6. Notation

$\mu_l$	Shear viscosity liquid [kg m <sup>-1</sup> s <sup>-1</sup> ]
$C_D$	Drag coefficient [-]
$C_L$	Lift force coefficient [-]
$C_{VM}$	Virtual mass coefficient [-]
$D$	Diameter of the bubble column [m]
$DT$	Time step [s]
$E$	Unit tensor [-]

$\varepsilon_l$	Volume fraction liquid in computational cell [-]
$f$	Local momentum transfer gas to liquid [N]
$F$	Volume averaged momentum transfer [ $\text{N m}^{-3}$ ]
$F_D$	Drag force on a bubble [N]
$F_G$	Force on bubble due to gravity [N]
$F_L$	Lift force on bubble [N]
$F_P$	Force on bubble due to pressure gradient [N]
$F_{\text{total}}$	Total force on a bubble [N]
$F_{\text{VM}}$	Virtual mass force on bubble [N]
$g$	Acceleration due to gravity [ $\text{m s}^{-2}$ ]
$i$	Bubble index number [-]
$I$	Kelvin impulse deformable body [Ns]
$L$	Height of the bubble column [m]
$\lambda_l$	Bulk viscosity liquid [ $\text{kg m}^{-1} \text{s}^{-1}$ ]
$m_b$	Mass of a bubble [kg]
$P$	Pressure [ $\text{N m}^{-2}$ ]
$r$	Position of bubble [m]
$R_b$	Radius of a bubble [m]
$Re_b$	Reynolds number for flow around a bubble [-]
$\rho_g$	Density gas phase [ $\text{kg m}^{-3}$ ]
$\rho_l$	Density liquid phase [ $\text{kg m}^{-3}$ ]
$t_l$	Stress tensor liquid [ $\text{N m}^{-2}$ ]
$u$	Liquid velocity [ $\text{m s}^{-1}$ ]
$v$	Velocity of bubble [ $\text{m s}^{-1}$ ]
$V_b$	Volume of a bubble [ $\text{m}^3$ ]
$V_{\text{cell}}$	Volume of a computational cell [ $\text{m}^3$ ]
$W$	Vorticity in liquid phase [ $\text{s}^{-1}$ ]

## 7. References

Auton, T. R., 1983, The dynamics of bubbles, drops and particles in motion in liquids, *Ph. D. Thesis*, University of Cambridge, Cambridge, United Kingdom.

Chen, J. J. J., Jamialahmadi, M. and Li, S. M., 1989, "Effect of liquid depth on circulation in bubble columns: a visual study", *Chem. Eng. Res. Des.* **67**, 203.

Delnoij, E., Lammers, F. A., Kuipers, J. A. M. and van Swaaij W. P. M., 1997a, Dynamic simulation of dispersed gas-liquid flow using a discrete bubble model, *Chem. Eng. Sci.* **52** (9), 1429. (Chapter 3 of this Thesis).

Delnoij, E., Kuipers, J. A. M. and van Swaaij, W. P. M., 1997b, Computational fluid dynamics applied to gas-liquid contactors, *Chem. Eng. Sci.* **52** (21/22), 3623.

Delnoij, E., Kuipers, J. A. M. and van Swaaij, W. P. M., 1997c, Dynamic simulation of gas-liquid two-phase flow: effect of column aspect ratio on the flow structure, *Chem. Eng. Sci.* **52** (21/22), 3759. (Chapter 4 of this Thesis).

Devanathan, N., Dudukovic, M. P., Lapin, A. and Lübbert, A., 1995, "Chaotic flow in bubble column reactors", *Chem. Eng. Sci.* **50**, 2661.

Ferziger, J. H. and Peric, M., 1996, Computational methods for fluid dynamics, Springer Verlag, Berlin.

Grienberger, J. and Hofman, H., 1992, "Investigations and modeling of bubble columns", *Chem. Eng. Sci.* **47**, 2215.

Hjertager, B. H. and Morud, K., 1995, "Computational fluid dynamics of bioreactors", *Mod. Ident. and Control* **16**, 177.

Jakobsen, H. A., Sannaes, B. H., Grevskott, S. and Svendsen, H. F., 1997, "Modeling of vertical bubble-driven flows", *Ind. Eng. Chem. Res.* **36**, 4052.



Kuipers, J. A. M., van Duin, K. J., van Beckum, F. P. H. and van Swaaij, W. P. M., 1993, Computer simulation of the hydrodynamics of a two-dimensional gas-fluidized bed, *Comput. Chem. Engng.* **17**, 839.

Lapin, A. and Lübbert, A., 1994, "Numerical simulation of the dynamics of two phase gas - liquid flows in bubble columns", *Chem. Eng. Sci.* **49**, 3661.

Ranade, V. V., 1992, "Flow in bubble column: some numerical experiments", *Chem. Eng. Sci.* **47**, 1857.

Shah, Y. T., Kelkar, B. G., Godbole, S. P. and Deckwer, W. -D., 1982, Design parameter estimations for bubble column reactors, *A.I.Ch.E. J.* **28** (3), 353.

Sokolichin, A. and Eigenberger, G., 1994, "Gas - liquid flow in bubble columns and loop reactors: part I. Detailed modeling and numerical simulation", *Chem. Eng. Sci.* **49**, 5735.

Stewart, H. B. and Wendroff B., 1984, Two-phase flow: Models and methods, *J. Compt. Phys.* **56**, 363.

Torvik, R. and Svendsen, H. F., 1990, "Modeling of slurry reactors, a fundamental approach", *Chem. Eng. Sci.* **45**, 2325.

Trapp, J. A. and Mortensen, G. A., 1993, "A discrete particle model for bubble slug two phase flow", *J. Comp. Physics.* **107**, 367.

Van den Akker, H., 1998, The Euler-Euler approach to dispersed two-phase flows in the turbulent regime, *ERCOFTAC Bulletin* **36**, 30.



# Chapter 6:

## Measurement of gas-liquid two-phase flow in bubble columns using ensemble correlation PIV<sup>1</sup>

### 0. Abstract

This paper highlights the development of a new ensemble correlation, multiphase flow PIV technique. The particular approach discussed in this paper is a straightforward extension of single-phase PIV and one of the major advantages of the technique is that it employs a single CCD camera. This velocimeter measures the motion of the liquid-phase and the bubbles using an ensemble correlation procedure of successive recordings of bubble-tracer patterns. Moreover, the ensemble correlation technique enables the simultaneous measurement of the concentration of tracer particles and bubbles. The performance of the PIV technique is studied using synthetic bubble-tracer patterns. The performance is gauged in terms of the amplitude of the displacement correlation peak pertaining to the bubbles and in terms of the valid detection probability of that same peak. Finally, the newly developed PIV technique is tested by studying experimentally the two-phase flow in a pseudo two-dimensional bubble column.

---

<sup>1</sup> Delnoij, E., Kuipers, J. A. M. and van Swaaij, W. P. M. and Westerweel, J., 1998, "Measurement of gas-liquid two-phase flow in bubble columns using ensemble correlation PIV", *Submitted to Int. J. Multiphase Flow*.

## 1. Introduction

Gas-liquid bubble columns are employed throughout the chemical, biochemical and petrochemical industries. Typical applications usually involve gas-liquid mass transfer and (exothermal) chemical reactions. The gas-liquid two-phase flow prevailing in these bubble columns has a profound impact on the performance of the bubble column as a chemical reactor. Yet, many important fluid dynamical aspects of this two-phase flow are still poorly understood. This explains to some extent the considerable effort made by various researchers to develop sophisticated CFD models for gas-liquid bubble columns (see for instance Lapin and Lübbert, 1994, Devanathan *et al.*, 1995, Delnoij *et al.*, 1997[a-c] and Jakobsen *et al.*, 1997). From these numerical studies, mainly devoted to the behavior of a bubble column operated in the homogeneous regime, the gas-liquid flow is known to be highly time-dependent and dominated by a rich variety of coherent structures.

To accurately assess the validity of these CFD models, quantitative experimental data are required on the instantaneous flow phenomena observed in bubble columns and on the coherent structures dominating the flow. In other words, there is a need for accurate data regarding the instantaneous velocities of both phases and regarding the time-dependent, local volume fraction of gas in the bubble column. Precisely in this area however, reliable experimental data are scarcely available in the open literature. In recent years a considerable amount of work has been devoted to (qualitative) experimental observations of the flow structure in pseudo two-dimensional and three-dimensional bubble columns (Chen *et al.*, 1989, Chen *et al.*, 1994 and Becker *et al.*, 1995). These studies provide insight into the time-dependent behavior of bubble columns and the flow regimes prevailing in them, but fail to provide adequate quantitative data suitable for detailed model validation. Also various experimental techniques are available that provide point information on the two-phase flow and hence time-averaged information regarding flow structures. Arguably the most well known among these techniques are radioactive particle tracking (Devanathan *et al.*, 1990) and laser doppler velocimetry (Becker *et al.*, 1995 and Groen *et al.*, 1996). These techniques do not however provide instantaneous, whole field data on the velocity and hold up of both phases.

Clearly there is a need for more comprehensive, quantitative data on the instantaneous, whole field characteristics of the two-phase flow in a bubble column. In recent years, two

experimental techniques have emerged with the potential to yield these data: Digital Particle Image Velocimetry (PIV) and Particle Tracking Velocimetry (PTV). Basically, PIV and PTV are two different modes of a technique that visualizes fluid motion by adding small tracer particles to the fluid and that infers the velocity field from the position of these tracer particles at two instances of time, viz. from the particle displacement. Particle Tracking refers to the mode of operation where the number density of tracer particles is low and the velocity field is obtained from the displacement of individual tracer particles. Reese and Fan (1994), Murai and Matsumoto (1995), Lin *et al.* (1996) and Mudde *et al.* (1997) used Particle Tracking Velocimetry (PTV) to study the flow in bubble columns. In PIV on the other hand, the density of tracer particles is increased with respect to PTV, and hence PIV determines the velocity field by estimating the mean displacement of groups of tracer particles. For a more detailed discussion on the differences between PTV and PIV, the interested reader is referred to Adrian (1991) and Westerweel (1993).

The application of PIV to two-phase bubbly flows was pioneered by Oakley *et al.* (1995) who employed cinematic PIV to solve for the liquid flow field and used a tracking technique to resolve the motion of individual gas bubbles. Typically, two-phase PIV velocimeters separate the images of the tracers from the images of the bubbles. This can be achieved through the use of fluorescent tracer particles or sophisticated image processing techniques. The two-phase PIV techniques that employ fluorescent tracer particles require a two-camera set-up, as images of tracer particles and bubbles have to be separated optically on basis of the wavelength of the scattered or emitted light. However, the complicated alignment of the two CCD cameras and the significant amount of ultraviolet light scattered by the bubbles, hamper this particular approach. It is for these reasons that we have developed a simplified single camera PIV technique for use in dispersed gas-liquid two-phase flows (i.e. bubble columns operated in the homogeneous regime). This paper discusses this PIV technique. It will be shown that the implementation chosen is capable of measuring simultaneously the pseudo-instantaneous velocity field and concentration field of both the gas and the liquid phase. The operating envelope of this particular PIV technique will be studied theoretically using synthetic PIV images. Finally, sample results obtained in a pseudo two-dimensional bubble column, for the gas and the liquid flow field as well as for the concentration of tracers and bubbles, will be discussed.

## 2. Theory

### 2.1 Single-phase flow PIV

Let us first examine ‘single phase’ Particle Image Velocimetry before extending the technique to gas-liquid two-phase flows. In single phase PIV, the fluid is seeded with small tracer particles and a cross section of the flow is illuminated using a laser light sheet. Successive positions of the tracer particles are recorded, usually by means of a CCD camera. The local fluid velocity is then inferred from the mean displacement between two successive exposures of the flow, of the tracer particles in a small interrogation window. It has been shown (Adrian, 1988 and Westerweel, 1997) that for an incompressible fluid, seeded homogeneously with ‘ideal’ tracer particles, the displacement of the tracers in a small interrogation window can be inferred from the cross-correlation of two successive exposures of the flow field. Figure 1 depicts the different stages involved in the analysis of PIV images, such as the various Fast Fourier Transforms that are used to compute the cross-correlation function efficiently.

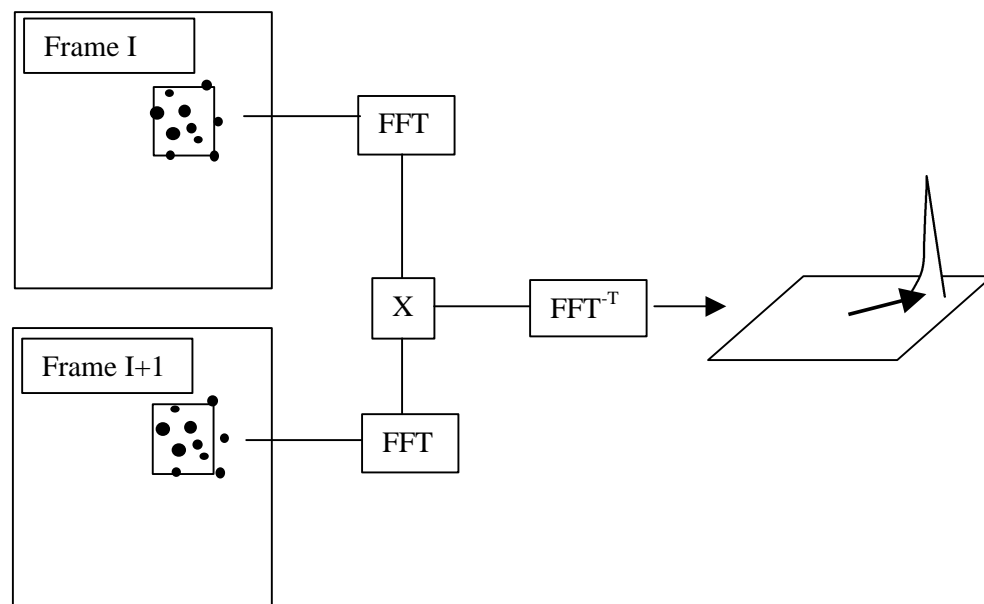


**Figure 1.** Schematic representation of the subsequent stages of the analysis of PIV images.

In the following theoretical analysis we study this cross-correlation function in more detail, employing techniques similar to those used by Keane and Adrian (1993). First, let us assume that the local intensity of the recorded PIV images can be written as the sum of a mean and a fluctuating component:

$$I = \langle I \rangle + I' \quad 1$$

This allows the instantaneous cross-correlation function to be written as (using notation also employed by Keane and Adrian, 1993):

$$R(\mathbf{s}) = R_D(\mathbf{s}) + R_C(\mathbf{s}) + R_F(\mathbf{s}) \quad 2$$

In this equation,  $R_D$  represents the cross-correlation of the fluctuating image intensity of the first frame with the fluctuating image intensity of the second frame. This contribution ( $R_D$ ) is generally referred to as the ‘displacement’ component of the cross-correlation function.  $R_C$  is the cross-correlation of the mean image intensity; and  $R_F$  represents the cross-correlation of the mean image intensity with the fluctuating image intensity. See also Figure 2, which depicts a typical instantaneous cross-correlation function with its various components.

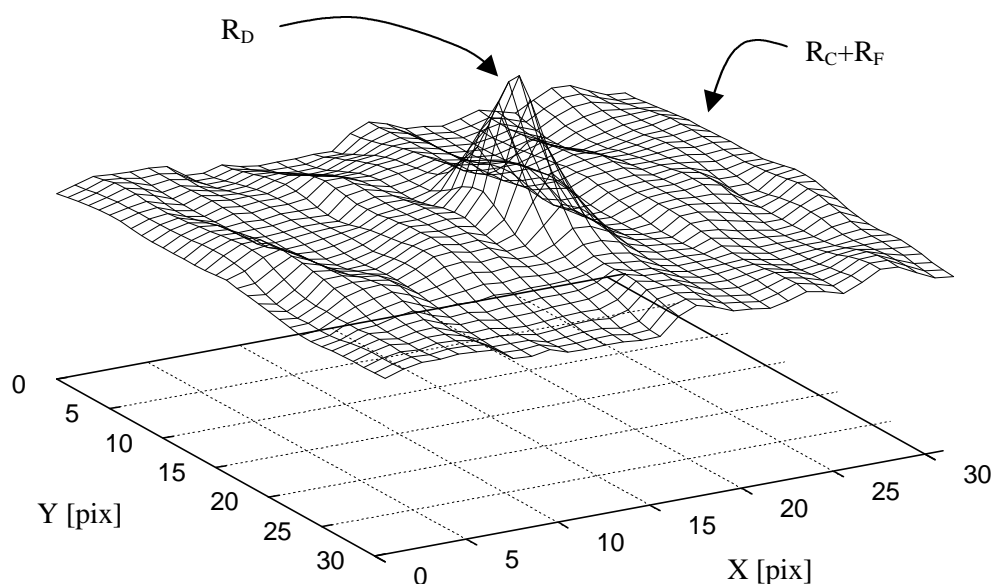


**Figure 2.** Typical cross-correlation function (32 x 32 [pix] interrogation window) encountered in single phase, single exposure, double frame PIV.

Subtracting the mean image intensity from the local intensity of the recorded PIV images ( $I - \langle I \rangle = I'$ ), before determining the cross-correlation function, eliminates the two contributions associated with the mean image intensity (i.e.  $R_C(\mathbf{s})$  and  $R_F(\mathbf{s})$ ):

$$R(\mathbf{s}) = R_D(\mathbf{s}) \quad 3$$

Now, consider an ensemble of PIV images of identical velocity fields in which each realization contains different sets of randomly dispersed tracer particles. The mean behavior

of the cross-correlation function can subsequently be studied by determining the conditional average of the displacement component of the cross-correlation function:

$$\langle R_D(\mathbf{s})|\mathbf{u} \rangle \sim N_I F_I F_O F_t(\mathbf{s} - \mathbf{s}_D) \quad 4$$

where  $N_I$  is the mean number of particle images within the interrogation area,  $F_I$  and  $F_O$  are the loss-of-correlation due to in-plane and out-of-plane motion of the tracer particles respectively, and  $F_t$  represents the self-correlation of the particle images (see also Keane and Adrian 1993).

The amplitude of this displacement component depends on the velocity field in the interrogation window under consideration. The function has a distinct maximum at  $\mathbf{s} = \mathbf{s}_D = \mathbf{M}\mathbf{u}\Delta t$ , the local mean in-plane displacement of the tracer particles. This maximum is generally referred to as the displacement correlation peak. The strength (or the amplitude) of this displacement correlation peak is determined by the mean effective number of particle image pairs or  $N_I F_I F_O$  (see equation 4). The width of the displacement correlation peak can be approximated assuming that the particle image intensity is essentially a Gaussian curve centered at the particle image center with particle image ( $e^{-2}$ ) diameter ( $d_t/d_r$ ) pixels. In this approximation, it can be shown that the width of the displacement correlation is equal to  $(d_t/d_r)\sqrt{2}$  pixels.

Success or failure of the PIV analysis is determined by the velocimeter's ability to detect the displacement correlation peak  $\langle R_D(\mathbf{s}_D)|\mathbf{u} \rangle$  among neighboring random noise peaks. Improving this detectability implies maximizing the amplitude (or strength) of  $\langle R_D(\mathbf{s}_D)|\mathbf{u} \rangle$ . Keane and Adrian (1993) studied this problem extensively using Monte-Carlo simulations. For single-exposure double-frame PIV, they recommended design rules that, when used, optimize the performance of the velocimeter:

1. The mean effective number of particle images per interrogation area, based on the leading frame, should exceed 7, i.e.  $N_I F_I F_O > 7$
2. The local mean gradient of the velocity field should be negligible:  $M|\Delta\mathbf{u}|\Delta t/D_I < d_t/D_I \approx 0.03-0.05$ .

These rules basically govern the design of the Particle Image Velocimeter.



## 2.2 Two-phase flow PIV

In the previous section, we reviewed the fundamentals of single-phase flow PIV; this section focuses entirely on the newly developed two-phase flow velocimeter. In our two-phase PIV implementation, the liquid is also seeded with small tracer particles, and a laser light sheet is used to illuminate a cross section of the flow. In this case both the tracers and the bubbles scatter light. Provided we can distinguish tracers from bubbles, this implies that the local displacement of both the gas and the liquid phase can be estimated from the displacement of bubbles and tracers between two successive exposures of the flow.

In analogy with equation (1) the local intensity of the two-phase PIV image can be written as the sum of mean and fluctuating intensities associated with the tracer particles and the bubbles:

$$I = \langle I^{(T)} \rangle + I'^{(T)} + \langle I^{(B)} \rangle + I'^{(B)} \quad 5$$

Subtracting the mean image intensities ( $\langle I^{(T)} \rangle + \langle I^{(B)} \rangle$ ) from the local image intensity given by equation (5) yields a cross-correlation function that depends entirely on the correlation of the fluctuating intensities:

$$R(\mathbf{s}) = R_D^{(TT)}(\mathbf{s}) + R_D^{(BB)}(\mathbf{s}) + R_D^{(TB)}(\mathbf{s}) + R_D^{(BT)}(\mathbf{s}) \quad 6$$

The components of the cross-correlation function resulting from the mutual convolution of the fluctuating intensities of the tracers and the bubbles (the terms  $R_D^{(TB)}$  and  $R_D^{(BT)}$  in equation 6) are expected to exhibit more or less random characteristics. These terms can thus be regarded as ‘noise’ in the sense that due to their presence the detectability of the displacement components of the cross-correlation (the terms  $R_D^{(TT)}$  and  $R_D^{(BB)}$ ) deteriorates.

The detectability of the displacement components of the cross-correlation function associated with the motion of the tracers and with the motion of the bubbles ( $R_D^{(TT)}$  and  $R_D^{(BB)}$ ) can be improved considerably by determining the cross-correlation of an ensemble of PIV images. The ensemble average of the cross-correlation function shown in equation (6) contains just two distinct contributions (see also Figure 3):

$$\langle R(\mathbf{s}) \rangle = \langle R_D^{(TT)}(\mathbf{s}) \rangle + \langle R_D^{(BB)}(\mathbf{s}) \rangle \quad 7$$

In other words: the ensemble cross-correlation function contains two distinct peaks; one associated with the displacement of the bubbles and the other with the displacement of the

tracer particles. The disturbing influence of the random correlation between tracers and bubbles is avoided due to the mutual extinction of these contributions to the cross-correlation function.

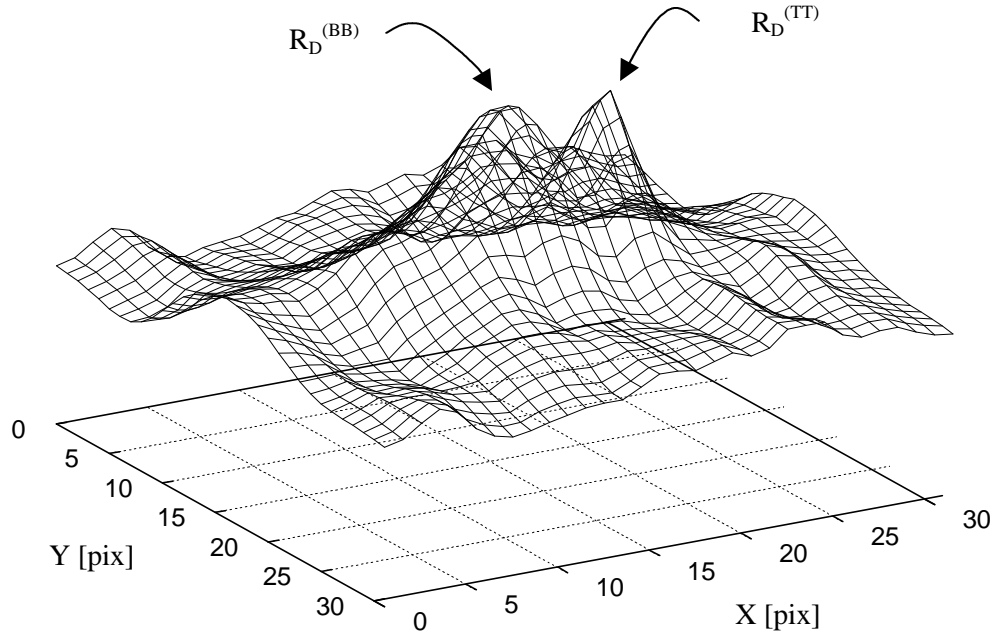


**Figure 3.** Typical cross-correlation function (32 x 32 [pix] interrogation window) in two-phase single exposure, double frame PIV.

The displacement component pertaining to the bubbles is given by the conditional average of the cross-correlation of the fluctuating intensity of the bubble-image pattern:

$$\left\langle R_B^{(BB)}(\mathbf{s}) \mid \mathbf{u}^{(B)} \right\rangle \sim N_I^{(B)} F_I^{(B)} F_O^{(B)} F_t^{(B)} (\mathbf{s} - \mathbf{s}_D^{(B)}) \quad 8$$

It can be seen that the amplitude of this bubble displacement component is proportional to the mean effective number of bubble image pairs in the interrogation window. This implies that the ensemble correlation two-phase PIV procedure discussed above also enables the measurement of the concentration of bubbles (defined as the ensemble mean number of bubbles that reside within a particular interrogation window) from the amplitude of the bubble displacement correlation peak.

In summary, the two-phase gas-liquid PIV technique proposed in this paper consists of stages similar to those outlined for single-phase PIV. The difference is that ultimately the

displacement of both bubbles and tracers is determined by taking the ensemble correlation of a set of PIV images.

### 3. Two-phase flow PIV: performance

The interrogation performance of single phase Particle Image Velocimeters has been studied extensively by Keane and Adrian (1990, 1991 & 1993). They used synthetic PIV images to study the performance of multiple exposure, single-frame PIV systems and of single exposure, double-frame PIV systems. In this section, we will study the performance of our two-phase single exposure double-frame velocimeter, also using synthetic PIV images. The interrogation performance is gauged in terms of the amplitude and the valid detection probability of the displacement correlation peak pertaining to the bubbles.

#### 3.1 Monte-Carlo simulations

To assess the performance of the PIV technique under two-phase flow conditions, a Monte-Carlo procedure was used to generate pairs of images of bubble-tracer patterns. A set of 200 realizations is generated for each particular velocity field in which bubbles and tracers are scattered randomly with a particular number density. Special care is taken to ensure that each interrogation window contains exactly the specified number of tracers or bubbles. Each realization is processed separately using the PIV software developed by Westerweel (1993) that determines the ensemble cross-correlation function for a set of interrogation areas. Because a uniform displacement is applied throughout the image, and because the seeding is assumed to be ‘ideal<sup>2</sup>’, this procedure resembles taking the ensemble correlation of a set of PIV images. In the following, the loss of correlation due to out-of-plane motion is set to zero in line with the experiment discussed in section 4 that was conducted in a pseudo two-dimensional bubble column which eliminates out-of-plane motion altogether. The image density of the tracers and their velocity is assumed to be constant and the image density of the bubbles is varied from 1 to 10. The particle image diameter and the bubble image diameter are set to 2 pixels; which is the optimal particle image diameter as discussed by Westerweel (1993). The displacement of the bubbles as well as the number of ensembles used to determine the cross-correlation function is varied.

---

<sup>2</sup> ‘Ideal’ tracer particles are assumed to perfectly follow the fluid motion.

### 3.2 Performance: number of realizations

The two-phase PIV technique described in this paper determines the ensemble correlation of a set of PIV images to measure the local displacement of tracers and bubbles. So how big should this set of PIV images be? On the one hand, it should be small to accurately capture the small time-scale characteristics of the flow; on the other hand, it should be large enough to ensure valid detection of the bubble displacement correlation peak. Figure 4 depicts the valid detection probability versus the bubble image density and the size of the set of PIV images used in the ensemble correlation procedure. In this case, and all others presented in this paper, the valid detection probability is defined as the probability that a single interrogation spot produces a bubble velocity measurement that is within 0.5 pixel of the bubble velocity specified as an input parameter for the Monte-Carlo simulation. The bubbles are displaced in a direction perpendicular to the displacement of the tracer particles; this allows us to study *sec* the effect of the size of the set of PIV images on the valid detection probability.

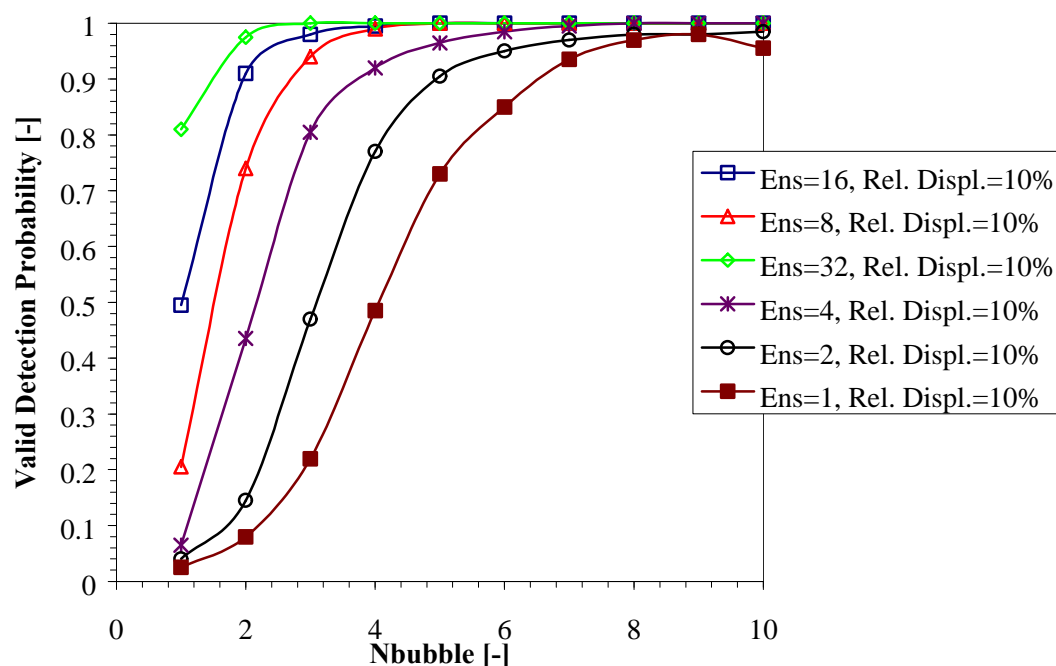


**Figure 4.** Valid Detection Probability versus bubble image density and number of realizations constituting the ensemble correlation set. Relative displacement of the bubbles is 10 % of the width of the interrogation area. Displacement of the tracer particles is 6 pixels. Interrogation area: 32 x 32 pixels.

Figure 4 reveals a clear and distinct effect of the number of realizations used in the ensemble correlation analysis on the valid detection probability. The valid detection probability increases as the number of images in the ensemble correlation set increases because the bubble displacement correlation peak is amplified and the overall noise level is diminished due to mutual extinction of random noise peaks. At a typical bubble number density (typical meaning also encountered in our experiments) of two, the number of realizations should be 16 or 32 to yield a valid detection probability exceeding 90 %. This number of images corresponds to one or two seconds of bubble column operation for a PIV setup that employs a 15 [Hz] camera.

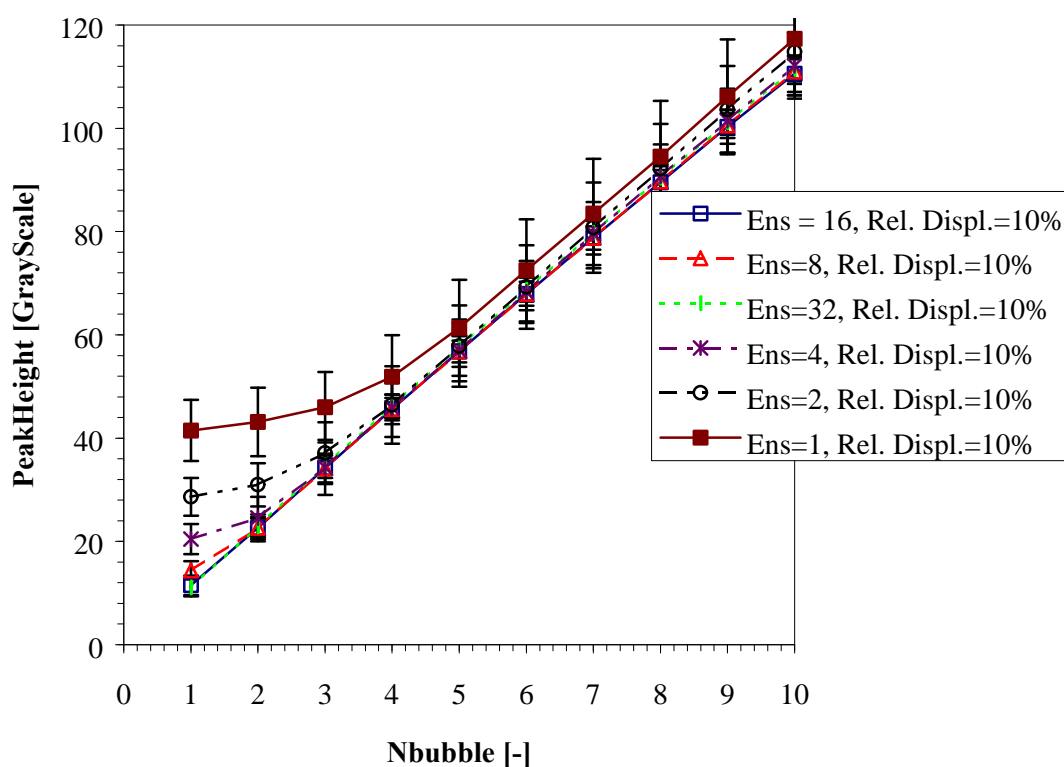


**Figure 5.** Amplitude of the bubble displacement correlation peak versus bubble image density at different sizes of the set of images used in the ensemble correlation procedure. Relative displacement of the bubbles is 10 % of the width of the interrogation area. Interrogation area 32 x 32 pixels. Bubbles displaced in a direction perpendicular to the shift-direction of the tracer particles.

Figure 5 depicts the amplitude of the bubble displacement correlation peak versus the bubble image density and the size of the set of PIV images used in determining the ensemble

correlation. At high bubble image densities ( $N_{IB} > 4-5$ ), the peak amplitude can be seen to increase linearly with the bubble image density, as is predicted by PIV theory (see also equation 8). Moreover, it can be seen that at high bubble image densities the peak amplitude does not depend on the size of the ensemble correlation set. At low bubble image densities ( $N_{IB} < 4$ ) however, the peak amplitude no longer depends on the bubble image density in a linear fashion, and the size of the ensemble correlation set clearly affects the peak amplitude. There appears to be an offset in the amplitude of the bubble displacement correlation peak. This offset represents the random noise level because at low bubble image densities and small sizes of the ensemble correlation set, the valid detection probability is also small (see also Figure 4). Random noise peaks exceeding the bubble displacement correlation peak thus cause this small valid detection probability and impose a lower limit on the measurable bubble image density. The random noise level (the offset in Figure 5) decreases by a factor  $\sqrt{2}$  as the size of the ensemble correlation set is increased by a factor of 2. This is expected behavior due to the white random field characteristics of the background noise. Note that the peak amplitude no longer decreases with increasing size of the ensemble correlation set at sufficiently large sizes of the ensemble correlation set (16 or 32 images). In these cases, the peak amplitude (in Figure 5) no longer represents the random noise level, but the actual amplitude of the bubble displacement correlation peak. See also Figure 4, which clearly reveals that at these sizes of the correlation set the valid detection probability is high.

### 3.3 Performance: effect of bubble image displacement

Previous results (Keane and Adrian, 1990, 1991 & 1993 and Westerweel, 1993) indicate that the valid detection probability can be related to the mean effective number of particle image pairs (or in this case the mean effective number of bubble image pairs) remaining in an interrogation area. Figure 6 shows the relationship between the valid detection probability and the mean effective number of bubble image pairs in the interrogation area for single-exposure double-frame ensemble correlation PIV. It can be seen that to ensure a 95 % valid detection probability, the mean effective number of bubble image pairs should exceed 2.5 ( $N_{IB}F_{IB}F_{OB} > 2.5$ ).

Also shown in Figure 6 are lines indicating the probability of finding at least one, at least two and at least three bubble image pairs in an interrogation spot at a given mean effective number of bubble image pairs. The number of bubbles in an interrogation window is governed by Poisson statistics. So, for the case of finding at least one bubble image pair in an

interrogation area, the corresponding probability, or valid data yield  $\Gamma$ , is given by (Westerweel, 1993):

$$\Gamma \approx 1 - e^{-N_I^{(B)} F_I^{(B)} F_I^{(B)}} \quad 9$$

In general, it can be inferred from Figure 6 that the valid detection probability resembles the probability of finding between two and three bubble image pairs in each ensemble of 16 interrogation areas. The number of bubble images is not a design parameter, as the number of tracer particles ( $N_{IT}$ ) is, however the size of the ensemble correlation set can be chosen to ensure that the valid detection probability exceeds 95 % for the gas-liquid system under consideration.

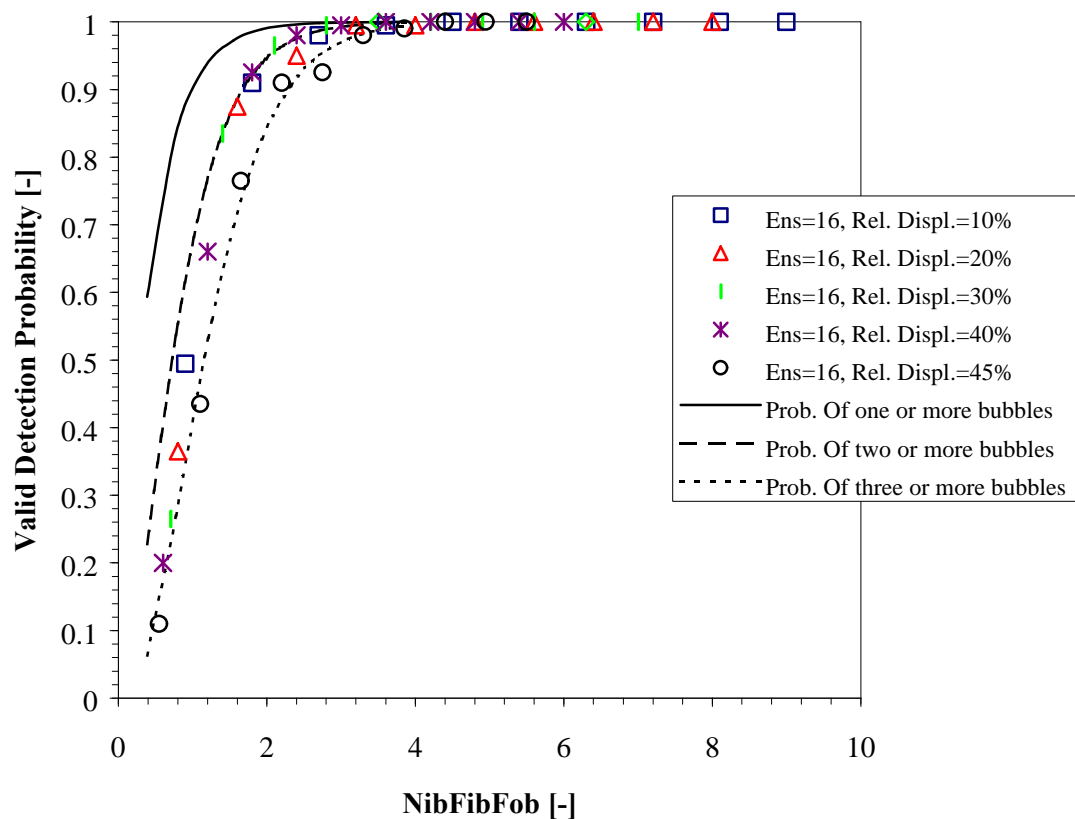


**Figure 6.** Valid Detection Probability versus mean effective number of bubble image pairs at various values for the relative displacement of the bubbles. Number of realizations = 16. Interrogation area 32 x 32 pixels. The lines represent the probability that an interrogation area contains at least one, at least two or at least three bubble image pairs. Bubbles displaced in a direction perpendicular to the shift-direction of the tracer particles.

### 3.4 Performance: parallel shift

In the previous sections, we studied the performance of ensemble correlation PIV using Monte-Carlo simulations, whereby the bubbles were shifted in a direction perpendicular to the shift-direction of the tracer particles. Obviously, bubbles and tracer particles move more or less in a parallel direction in a real-life bubble column. This section assesses to what extent bubbles, moving in a direction identical to that of the tracers, affect the performance of the two-phase flow velocimeter.

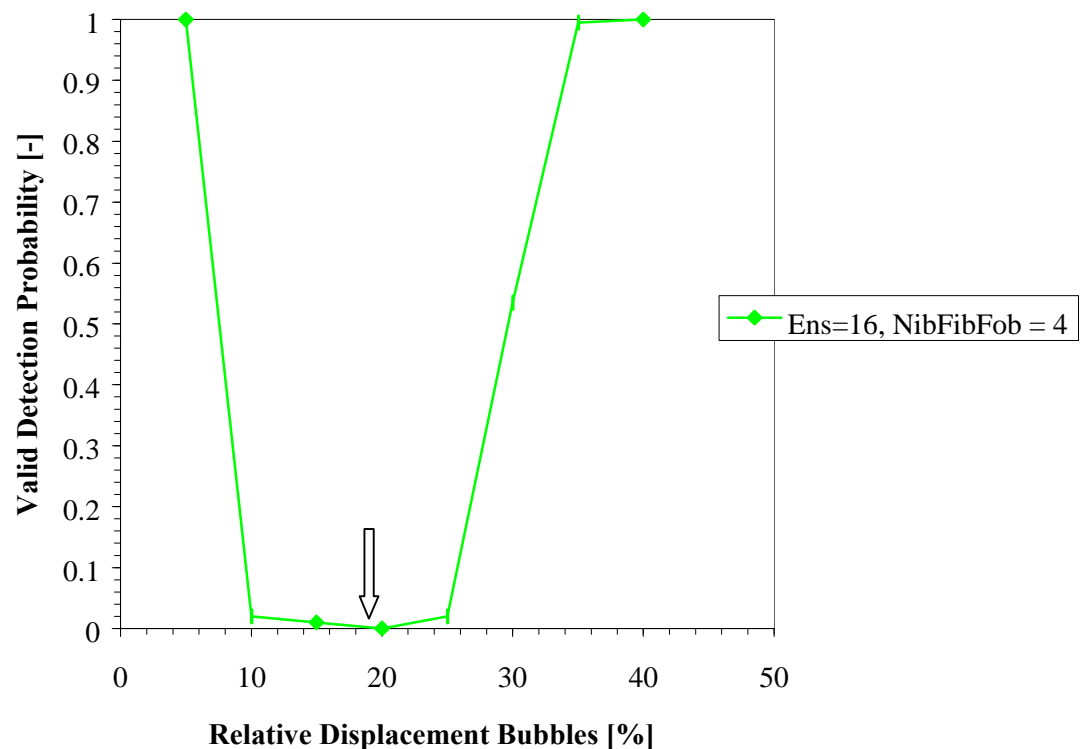


**Figure 7.** Valid Detection Probability as a function of the relative displacement of the bubbles (relative to the size of the interrogation area). Number of realizations = 16. Interrogation area: 32 x 32 pixels. The mean effective number of bubble image pairs is 4.

Figure 7 shows the valid detection probability as a function of the relative displacement of the bubbles in the interrogation window. Both bubbles and tracer particles are displaced in the x-direction, and the relative displacement of the tracers is approximately 18.8 % of the width of the interrogation area, as indicated by the block arrow in Figure 7. The valid detection probability decreases sharply as the displacement of the bubbles (viz. their velocity) approaches the displacement of the tracer particles. This is expected behavior due to the



overlap between the two displacement correlation peaks (one associated with the bubbles, the other with the tracer particles) in these cases.

From Figure 7, it can also be inferred that the valid detection probability approaches unity as the difference in displacement between the bubbles and the tracers exceeds approximately 10 % of the width of the interrogation area, equivalent to 3 [pix]. This result is in broad agreement with theory. In the case discussed in this section the width of the displacement correlation peak (in the Gaussian approximation), for both bubbles and tracers, is equal to  $(d_b/d_p)\sqrt{2} \approx 3$  pixels. Generally, two overlapping Gaussian peaks can be detected as their relative distance exceeds approximately half their width, which resembles 1.5 pixels for the case discussed in this section.

## 4. Experimental

In the preceding sections, we discussed the underlying principle of our ensemble correlation, two-phase PIV implementation and we used artificially generated bubble-tracer patterns to assess certain aspects of its performance. To verify the analytical and numerical results obtained thus far, test experiments were conducted in a pseudo two-dimensional bubble column. This section discusses the experimental results obtained in this set-up.

### 4.1 Experimental set-up

The pseudo two-dimensional bubble column used in the test experiments is shown schematically in Figure 8. The viewing section of the column is constructed from ordinary glass; this section is 200 [mm] wide, 500 [mm] high and 8 [mm] deep. Gas can be injected through any of five gas distributors (porous stainless steel plates, pore size 10 [ $\mu\text{m}$ ]) flush mounted with the bottom of the column. The gas flow rate through each of these orifices is controlled individually through a mass flow controller (MFC).

In the experiment discussed in this paper, de-mineralized water (liquid height 260 [mm]) is used as the liquid phase whereas compressed air is used as the gas phase. Polystyrene particles with a sauter mean diameter of 250 [ $\mu\text{m}$ ], a density of 1070 [ $\text{kg m}^{-3}$ ] and a particle response time of 3.7 [ms] (Elghobashi, 1994) are used as tracer particles. Gas is fed to one orifice as indicated by the arrow in Figure 8. This particular configuration forces the bubble

plume to rise along the right sidewall of the column thus inducing a circulation cell to the left of the bubble plume. The gas flow rate equals  $2.5 \text{ [ml s}^{-1}\text{]}$ ; at this gas flow rate and at the porosity of the orifices mentioned, bubble sizes are approximately  $0.6\text{-}1.0 \text{ [mm]}$ .

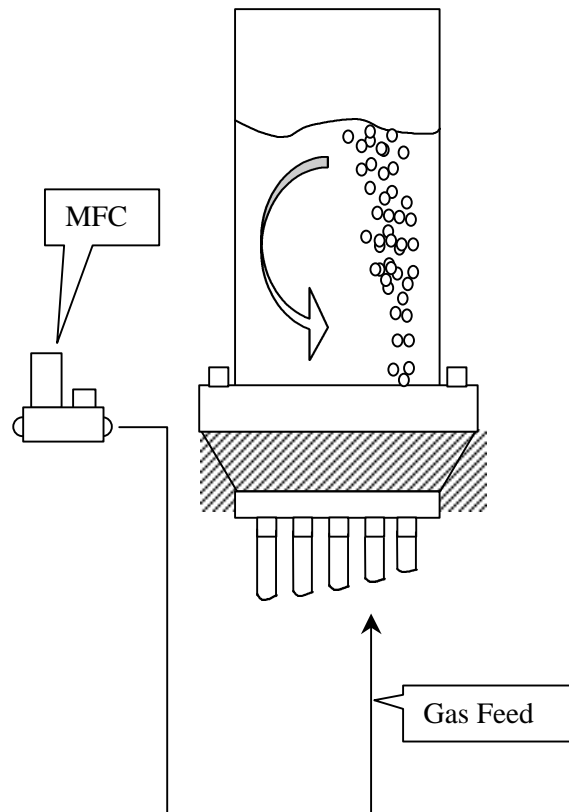
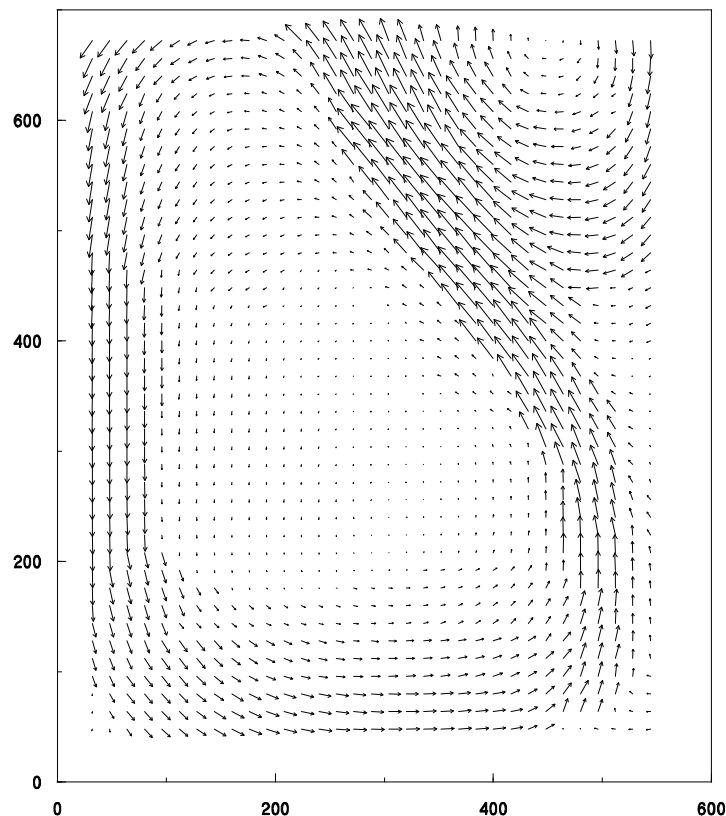


**Figure 8.** Schematic representation of the pseudo two – dimensional bubble column used in the test experiments.

A  $25 \text{ [Hz]}$  interlaced CCD camera ( $720 \times 576$  non-square pixels) equipped with a variable electronic shutter is used to record successive images of the flow in the bubble column. These images are recorded directly onto the hard disk of a PC (Pentium 120 MHz) using a 'Perception Video Recorder' frame grabber (Digital Processing Systems Inc.). Ordinary white light sources are used to illuminate the flow field. In total 19 frames are used in the ensemble correlation PIV analysis. The video images are analyzed with the PIV software developed by Westerweel (1993).

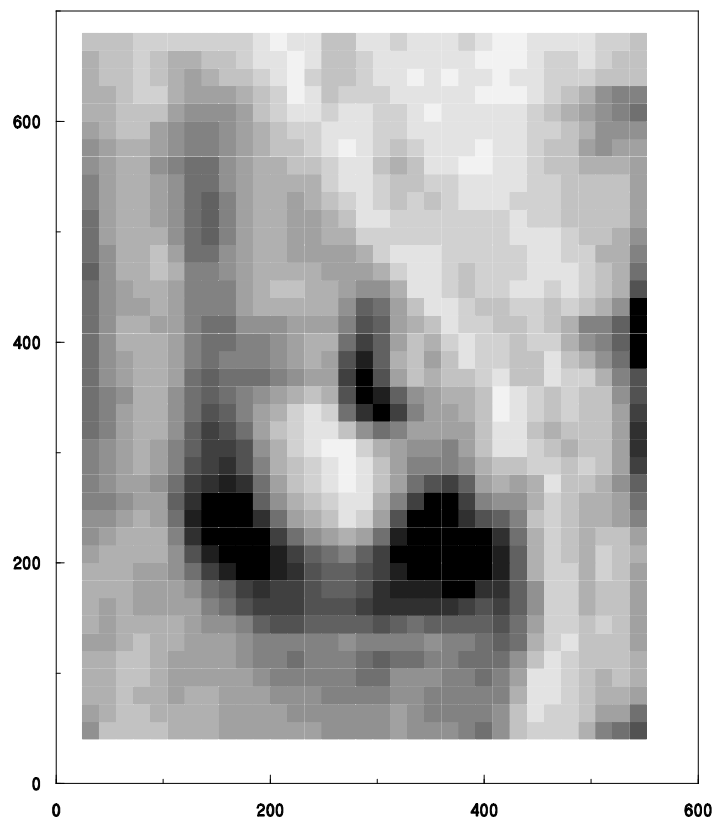
## 4.2 Results

Figure 9 depicts the liquid flow field as measured by our ensemble correlation two-phase PIV technique. The liquid is seen to rise along the right sidewall of the column and can be seen to descend along the opposite wall. Intuitively, this kind of behavior is expected and in accordance with results obtained using our gas-liquid CFD model (Delnoij *et al.*, 1997[a-c]). It is caused by the gas that is fed to a gas distributor positioned to right of the column's center; the bubbles therefore tend to rise along the right sidewall of the bubble column with liquid rising in their wakes. In the upper right corner of Figure 9, a smaller circulation cell can be seen to develop that is typical of the types of coherent structures that dominate the gas-liquid two-phase flow prevailing in bubble columns. This circulating cell forces the bubble plume away from the right sidewall.



**Figure 9.** Vector map of the liquid velocity in the pseudo two – dimensional bubble column. Measured with the two – phase implementation of the DPIV technique. Gas flow rate =  $2.5 \text{ ml s}^{-1}$ . Size of ensemble correlation set: 19 frames. The x-axis and y-axis depict the position in pixels.

The implementation of ensemble correlation PIV discussed in this paper allows us to measure the concentration of both tracers and bubbles from the amplitude of the respective displacement correlation peaks. Figure 10 shows a gray scale plot of the relative concentration of the tracer particles in the flow. It can clearly be seen that the concentration of tracer particles is not uniform; areas of high and low concentration can be distinguished. This is particularly striking near the bubble plume because the bubbles exclude the tracer particles. On the other hand, there are also distinct regions with a high concentration of tracer particles. This implies that, apparently, the tracer particles can not be considered to behave ‘ideal’ and they cannot remain distributed homogeneously over the flow. One of the basic rules underlying the PIV technique is therefore violated in this experiment. Nevertheless it is expected that the influence of the non-uniform distribution of tracer particles on the flow structure is negligible compared to the liquid motion induced by the bubbles.



**Figure 10.** Grayscale plot of the relative concentration of tracer particles in the gas – liquid two – phase flow prevailing in the bubble column. The concentration is derived from the amplitude of the displacement correlation peak associated with the motion of the tracers. Size of ensemble correlation set: 19 frames. The x-axis and y-axis depict the position in pixels.

In Figure 11, the ensemble averaged velocity field of the bubbles is shown, it is superimposed on the liquid flow field. Clearly, the PIV algorithm only yields bubble velocities to the right of the column's center, in the bubble plume. The bubbles can be seen to rise with a velocity that considerably exceeds the liquid velocity. Careful analysis of the experimental results revealed a slip velocity of approximately  $22 \text{ [cm s}^{-1}\text{]}$ , which resembles the terminal rise velocity of a spherical bubble with a diameter of 1 mm in a quiescent liquid. It can also be seen in Figure 11 that the PIV algorithm does not resolve the bubble velocity in the area of the flow where the small circulation cell (upper right corner) interacts with the rising bubble plume. This is most likely due to peak splitting caused by strong velocity gradients. Finally, Figure 12 depicts the gas hold up as measured by our ensemble correlation PIV technique. The shape of the bubble plume clearly emerges and is in broad agreement with video representation of the recorded images themselves. The gas hold up appears to be high near the gas distributor and diminishes as the bubbles rise through the column and the bubble plume spreads out.

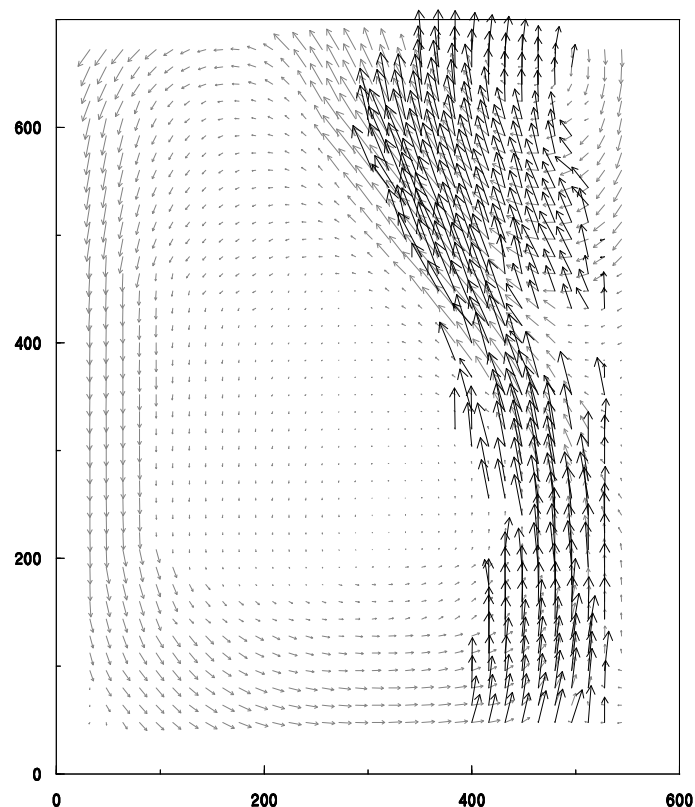


**Figure 11.** Vector map of the bubble velocity in the pseudo two – dimensional bubble column superimposed on the flow field of the liquid phase. Gas flow rate =  $2.5 \text{ ml s}^{-1}$ . Size of ensemble correlation set: 19 frames. The x-axis and y-axis depict the position in pixels.

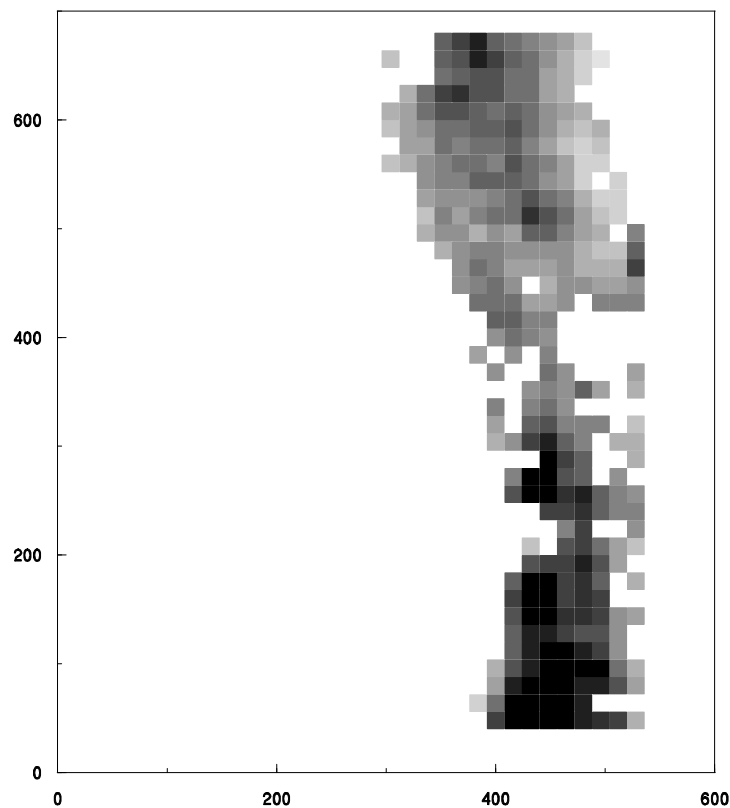


**Figure 12.** Grayscale plot depicting the relative concentration of the bubbles in the pseudo two – dimensional bubble column. This concentration is derived from the amplitude of the displacement correlation peak pertaining to the gas phase. Size of the ensemble correlation set: 19 frames. The x-axis and y-axis depict the position in pixels.

## 5. Discussion and conclusions

The need for more comprehensive quantitative data on the instantaneous, whole field characteristics of the two-phase flow in a bubble column prompted the development of a new ensemble correlation, multiphase flow, PIV technique. The measurement principle underlying this particular approach has been discussed. The motion of both the liquid phase and the bubbles is determined from ensemble correlation of successive recordings of bubble-tracer patterns. The ensemble correlation PIV technique also enables the simultaneous measurement of the concentration of tracer particles and bubbles.

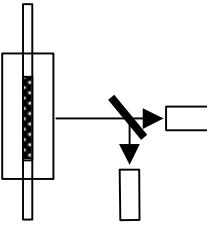
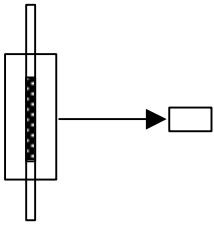
The performance of the PIV technique developed and discussed in this paper was studied using synthetic bubble-tracer patterns. The performance was gauged in terms of the

amplitude of the displacement correlation peak pertaining to the bubbles and in terms of the valid detection probability of that same peak. It was found that to ensure a valid detection probability of at least 90 % the number of realizations that constitute the ensemble correlation set should be 16 or more and that the mean effective number of bubble image pairs ( $N_{IB}F_{IB}F_{OB}$ ) should exceed 2.5. Moreover, from the Monte-Carlo simulations, it is found that at high bubble image densities or sufficiently large sizes of the ensemble correlation set, the amplitude of the bubble displacement correlation peak is proportional to the bubble image density; thus enabling gas phase hold up measurements. Finally, the theoretical studies revealed that the velocity difference between liquid and gas (viz. tracers and bubbles) should be sufficiently large to avoid overlap between the two displacement correlation peaks. This is generally the case in gas-liquid two-phase flows due to the considerable slip velocity between bubbles and the surrounding liquid.

We also tested the newly developed PIV technique by using it to study experimentally the two-phase flow in a pseudo two-dimensional bubble column. The experimental results clearly revealed the capability of the PIV technique to measure simultaneously the whole field characteristics (velocity field and concentration field of both phases) of the gas-liquid two-phase flow. One important remark regarding this experiment is that it has been conducted in a pseudo two-dimensional bubble column. Thereby eliminating the problems associated with out-of-plane motion. This out-of-plane motion can be significant in bubble columns because of the highly time-dependent flow structure that is dominated by (inherently three-dimensional) vortical structures. This out-of-plane component can be resolved using stereo PIV or dual-plane PIV.

The two-phase PIV technique discussed in this paper uses an ensemble of PIV images to determine the velocity field and concentration field of the gas and the liquid phase. Whether the use of an ensemble of PIV images compromises the measurement accuracy is a topic of further study. It is estimated however, that the error introduced by using the ensemble correlation of a set of PIV images is small. Generally, the time that is required to record a sufficient amount of PIV images is significantly smaller than the time-scales associated with the larger coherent structures encountered in bubble columns. These latter time-scales are generally assumed to be of the order of 30-60 [s] (Becker *et al.*, 1995 and Delnoij *et al.*, 1997).

**Table 1.** Ensemble correlation two-phase PIV versus a two camera two-phase PIV system.

	Advantages	Disadvantages
<b>Two camera system</b> 	<ul style="list-style-type: none"> <li>• Data separated at source</li> <li>• No ambiguity in tracer / bubble identification</li> </ul>	<ul style="list-style-type: none"> <li>• PTV for low density phase</li> <li>• Two camera alignment</li> <li>• Fluorescent tracer particles needed</li> <li>• Two CCD cameras needed</li> <li>• Bubbles scatter UV-light</li> </ul>
<b>Ensemble correlation PIV</b> 	<ul style="list-style-type: none"> <li>• Single CCD camera</li> <li>• Any type of tracer particles</li> <li>• No additional PTV algorithm needed</li> <li>• Straightforward extension to three-phase flow</li> <li>• Stereo PIV requires only one extra CCD camera</li> </ul>	<ul style="list-style-type: none"> <li>• Increased noise</li> <li>• Ambiguity problem</li> <li>• Limited to dispersed two (or three) phase flow</li> </ul>

We conclude this paper with a discussion of the relative advantages and disadvantages of the ensemble correlation PIV technique. Table 1 compares our ensemble correlation, multiphase flow PIV technique to a two-phase flow PIV technique that employs fluorescent tracer particles and a two-camera setup. Both systems have their respective advantages and disadvantages. However, in dispersed gas-liquid two-phase flows the ensemble correlation PIV technique has some particularly favorable properties. Chief among these is the ease with which the technique can be implemented, due to the use of a single camera, the simple optical alignment and the use of standard PIV software. Another advantage is the absence of a limitation regarding the bubble image density. Whereas ordinary PIV is limited to image densities exceeding 1 ( $N_I \gg 1$ ) and PTV is limited to image densities smaller than 1 ( $N_I \ll 1$ ), ensemble correlation PIV can also be applied to systems with image densities of approximately unity. Remember: bubble image densities of approximately 1 or 2 are typical for the image densities encountered during experiments in bubble columns at moderate gas



holdups. Finally, in the stereo PIV mode of operation, ensemble correlation PIV uses two CCD cameras as opposed to four cameras in case of the fluorescent particle PIV technique.

## 6. Acknowledgement

The authors want to thank M. J. S. Ytsma for his study of the performance of the ensemble correlation two-phase PIV technique and the J. M. Burgers Center for Fluid Dynamics for its financial contribution to this project.

## 7. Notation

$\Gamma$	Valid data yield
$\rho(\mathbf{s})$	Displacement distribution function
$\Delta t$	Exposure time delay
$D_I$	Diameter interrogation window
$d_r$	Diameter of a pixel
$d_t$	Diameter of a particle image
$F_I$	In-plane loss of correlation
$F_O$	Out-of-plane loss of correlation
$F_t$	Structure function of tracer particles or bubbles
$F_I^{(B)}$	In-plane loss of correlation bubbles
$F_O^{(B)}$	Out-of-plane loss of correlation bubbles
$I_Z$	Maximum intensity in light sheet
$I$	Local image intensity
$\langle I \rangle$	Mean image intensity
$I'$	Fluctuating image intensity
$M$	Magnification
$N_I$	Image density
$N_I^{(B)}$	Bubble image density
$R_D$	Displacement correlation peak single phase PIV
$R_D^{(BB)}$	Displacement correlation peak bubbles
$R_D^{(BT)}$	Random correlation between bubbles and tracers
$R_C$	Convolution of the mean image intensity

$R_D^{(TT)}$	Displacement correlation peak tracers
$R_F$	Convolution mean and fluctuating intensity
$R_D^{(TB)}$	Random correlation between tracers and bubbles
$\mathbf{s}$	Vector
$\mathbf{s}_D$	In-plane displacement of tracers or bubbles
$t_0$	Integrated intensity
$\mathbf{u}$	Velocity

## 8. References

Adrian, R. J., 1988, “Statistical properties of particle image velocimetry measurements in turbulent flow”, *Laser Anemometry in Fluid Mechanics – III* (Ed. R. J. Adrian *et al.*), LADOAN Instituto Superior Tecnico, Lisbon.

Adrian, R. J., 1991, “Particle-imaging techniques for experimental fluid mechanics”, *Ann. Rev. Fluid Mech.* **23**, 261.

Becker, S., Sokolichin, A and Eigenberger, G., 1995, “Gas-liquid in bubble columns and loop reactors: part II. Comparison of detailed experiments and flow simulations”, *Chem. Eng. Sci.* **49**, 5747.

Chen, J. J. J., Jamialahmadi, M. and Li, S. M., 1989, “Effect of liquid depth on circulation in bubble column: a visual study”, *Chem. Engng. Res. Des.* **67**, 203.

Chen, R. C., Reese, J. and Fan, L. –S., 1994, “Flow structure in a three-dimensional bubble column and three-phase fluidized bed”, *AIChE Journal* **40**(7), 1093.

Delnoij, E., Lammers, F. A., Kuipers, J. A. M. and van Swaaij W. P. M., 1997a, “Dynamic simulation of dispersed gas-liquid two-phase flow using a discrete bubble model”, *Chem. Eng. Sci.* **52**(9), 1429. (Chapter 3 of this Thesis).

Delnoij, E., Kuipers, J. A. M., and van Swaaij, W. P. M., 1997b, “Computational fluid dynamics applied to gas-liquid contactors”, *Chem. Eng. Sci.* **52**(21/22), 3623.

Delnoij, E., Kuipers, J. A. M., and van Swaaij, W. P. M., 1997c, "Dynamic simulation of gas-liquid two-phase flow: effect of column aspect ratio on the flow structure", *Chem. Eng. Sci.* **52**(21/22), 3759. (Chapter 4 of this Thesis).

Devanathan, N., Moslemian, D. and Dudukovic, M. P., 1990, "Flow mapping in bubble columns using CARPT", *Chem. Eng. Sci.* **45**(8), 2285.

Devanathan, N., Dudukovic, M. P., Lapin, A. and Lübbert, A., 1995, "Chaotic flow in bubble column reactors", *Chem. Eng. Sci.* **50**(16), 2661.

Elghobashi, S., 1994, "On predicting particle-laden turbulent flows", *Appl. Sci. Res.* **52**, 309.

Groen, J. S., Oldeman, R. G. C., Mudde, R. F. and van den Akker, H. E. A., 1996, "Coherent structures and axial dispersion in bubble column reactors", *Chem. Eng. Sci.* **51**, 1703.

Jakobsen, H. A., Sannaes, B. H., Grevskott, S. and Svendsen, H. F., 1997, "Modeling of vertical bubble-driven flows", *Ind. Eng. Chem. Res.* **36**, 4052.

Keane, D. K. and Adrian, R. J., 1990, "Optimization of particle image velocimeters. Part I: Double pulsed systems", *Meas. Sci. Technol.* **1**, 1202.

Keane, D. K. and Adrian, R. J., 1991, "Optimization of particle image velocimeters: II. Multiple pulsed systems", *Meas. Sci. Technol.* **2**, 963.

Keane, D. K. and Adrian, R. J., 1993, "Theory of cross-correlation analysis of PIV images", *Flow Visualization and Image Analysis (Ed.: F. T. M. Nieuwstadt)*, Kluwer Academic Publishers, 1.

Lapin, A. and Lübbert, A., 1994, "Numerical simulation of the dynamics of two-phase gas-liquid flows in bubble columns", *Chem. Eng. Sci.* **49**(21), 3661.

Lin, T. -J., Reese, J., Hong, T. and Fan, L. -S., 1996, "Quantitative analysis and computation of two-dimensional bubble columns", *AIChE Journal* **42**(2), 301.

Mudde, R. F., Lee, D. J., Reese, J. and Fan, L. -S., 1997, "Role of coherent structures on Reynolds stresses in a 2-D bubble column", *AIChE Journal* **43**(4), 913.

Mura, Y. and Matsumoto, Y., 1995, "Three-dimensional structure of a bubble plume-measurement of the three dimensional velocity", *ASME FED-VOL.209, Flow visualization and image processing of multiphase systems*, 187.

Oakley, T. R., Loth, E. and Adrian, R. J., 1995, "Cinematic two-phase PIV for bubbly flows", *ASME FED-VOL.209, Flow visualization and image processing of multiphase systems*, 123.

Reese, J. and Fan, L. -S., 1994, "Transient flow structure in the entrance region of a bubble column using particle image velocimetry", *Chem. Eng. Sci.* **49**(24B), 5623.

Westerweel, J., 1993, "Digital particle image velocimetry-Theory and application", *PhD Thesis Delft University of Technology*, The Netherlands.

Westerweel, J., 1997, "Fundamentals of digital particle image velocimetry", *Meas. Sci. Technol.* **8**, 1379.

# Chapter 7:

## Ensemble correlation PIV applied to bubble plumes rising in a bubble column<sup>1</sup>

### 0. Abstract

This Chapter discusses an ensemble correlation, double-exposure single-frame, Particle Image Velocimetry (PIV) technique that can be applied to study dispersed gas-liquid two-phase flows. The essentials of this technique will be reviewed and several important issues concerning the implementation of the PIV technique will be discussed. These issues include the need to employ an image shift and a window offset to resolve the directional ambiguity problem common to double-exposure single-frame PIV recordings. The capabilities of the newly developed PIV technique will be demonstrated by examining the liquid flow field induced by a bubble plume rising in a rectangular bubble column. The effect of the size of the ensemble correlation set on the flow field determined with our PIV technique will be illustrated. Ensemble correlation PIV furthermore enables the measurement of the local gas velocity and of the local void fraction. Figures depicting sample results will be presented and discussed.

---

<sup>1</sup> Delnoij, E., Westerweel, J., Deen, N. G., Kuipers, J. A. M. and van Swaaij, W. P. M., 1999, "Ensemble correlation PIV applied to bubble plumes rising in a bubble column", *Accepted for publication at the fourth conference on Gas-Liquid and Gas-Liquid-Solid Reactor Engineering GLS'99*, August 23 –25, Delft, The Netherlands.

## 1. Introduction

Gas-liquid bubble columns are used extensively in the process industries for applications that require a large liquid bulk, i.e. applications involving a chemical reaction that is slow with respect to gas-liquid mass transfer or a chemical reaction that produces excessive amounts of heat. The gas-liquid two-phase flow prevailing in a bubble column is extremely complex, is dominated by a rich variety of coherent structures and exhibits inherent unsteadiness. In recent years, a considerable effort has been made by various researchers to develop Computational Fluid Dynamics (CFD) models for these gas-liquid two-phase flows (see for instance: Lapin and Lübbert, 1994, Devanathan *et al.*, 1995, Delnoij *et al.*, 1997[a-c], Jakobsen *et al.*, 1997, Van den Akker, 1998 and Delnoij *et al.*, 1998a). Experimental validation of these CFD models is a prerequisite for the widespread acceptance of CFD models as a reliable design tool in the engineering community and indeed for the development of more sophisticated models. Contemporary CFD models predict the spatial and temporal distribution of key hydrodynamic variables associated with the two-phase flow in a bubble column. Accurate assessment of the validity of CFD results therefore requires an experimental technique that provides time-dependent and two- or three-dimensional information regarding these key hydrodynamic variables (i.e. velocity of both phases and void fraction).

Particle Image Velocimetry (PIV) is a non-intrusive, pseudo-instantaneous and whole field experimental technique that can be used to obtain the required information. PIV has been used successfully by various investigators (Oakley *et al.*, 1997, Brücker, 1998 and Kiger, 1998), to study dispersed two-phase flows at low volume fractions of the dispersed phase (applications were usually limited to several bubbles or solid particles). Oakley *et al.* for instance, used a tracking technique to resolve the time-dependent motion of individual bubbles in a turbulent planar free shear layer and a PIV technique to obtain the associated liquid flow field. Each two-phase PIV implementation however, requires an algorithm to discriminate between tracer particles and dispersed phase particles. This algorithm is the principal point of difference between the approaches adopted by the authors mentioned previously. Brücker (1998) employs an edge detection algorithm to separate the images of the tracer particles from those of the gas bubbles. Kiger (1998) uses a particle pattern correlation algorithm and Oakley's (Oakley *et al.*, 1997) technique requires the user to identify individual bubbles.

In the previous Chapter, we have introduced an ensemble correlation PIV technique that can be applied to the study of bubble plumes rising in liquids or bubble columns operated in the homogeneous regime at void fractions up to 3 – 5 %. This particular two-phase flow PIV technique is a straightforward extension of single-phase flow PIV. The velocimeter employs a single CCD camera and determines the local displacement (viz. the local velocity) of the liquid and the bubbles using an ensemble correlation procedure of successive recordings of bubble-tracer patterns. Contrary to the two-phase PIV techniques discussed earlier, our PIV technique discriminates between bubbles and tracers on basis of the slip velocity between the bubbles and the surrounding liquid.

In this Chapter, we will demonstrate the capabilities of our ensemble correlation PIV technique by using it to study a bubble plume rising in a small scale, rectangular, bubble column. First, we will present the essentials of ensemble correlation two-phase flow PIV and we will discuss several important details concerning its implementation. The experimental setup will be discussed thereafter. Finally, results obtained with our PIV implementation will be presented; the experimentally determined velocity field of both phases will be shown and the effect of the size of the ensemble correlation set on the flow field ultimately obtained, will be studied.

## **2. Theory of two-phase PIV**

Ensemble correlation PIV is an experimental technique that visualizes the two-phase flow prevailing in a bubble column by seeding the liquid with small tracer particles and by subsequently illuminating a planar cross section of the flow with a scanning laser beam. The instantaneous positions of the bubbles and the tracer particles are recorded by means of a CCD camera (see Figure 1). The velocimeter then uses the video images recorded by the CCD camera to estimate the local displacement of groups of tracers and bubbles from their respective positions at two instances of time (i.e. two successive exposures). A first order estimate of the velocity field of both phases can be obtained by dividing the measured displacements by the exposure time-delay  $\Delta t$ .

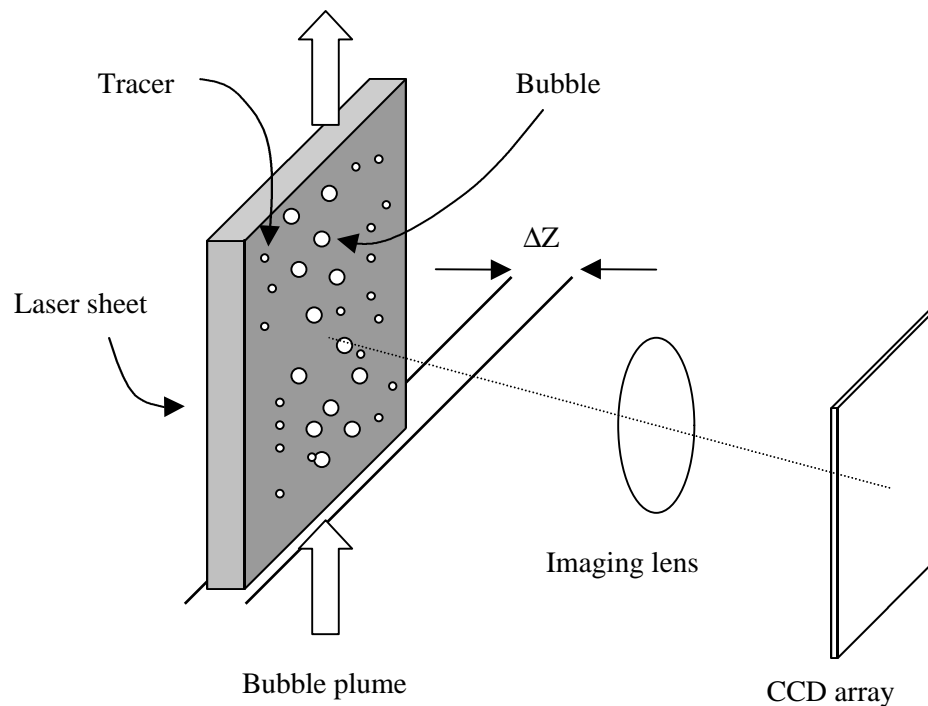


**Figure 1.** Schematic representation of a PIV imaging system (after Westerweel, 1997). The cross section of the flow illuminated by the laser sheet (constructed using a scanning laser beam), the tracers and bubbles residing in this cross section, the imaging lens and the CCD array are shown.

The current implementation of our PIV technique records two successive exposures of the flow (i.e. two scan-cycles of the laser beam) on a single frame captured by the CCD camera. This mode of operation is referred to as *double-exposure single-frame* PIV and is preferred here because of the small exposure time-delay  $\Delta t$  imposed by the (estimated) mean flow velocity. In double-exposure single-frame PIV the local displacement of sets of tracers and bubbles is determined using a correlation between two interrogation windows that reside in the same frame and may overlap only partially (see also Keane and Adrian, 1992 and Willert, 1996). Our two-phase PIV method improves its signal-to-noise ratio (SNR) considerably by taking the ensemble mean of the local cross-correlation function of sequentially recorded PIV images.

Two issues that arise in the evaluation of double-exposure single-frame PIV recordings, directional ambiguity and the use of a (discrete) window offset will be discussed in the following sections. These issues will be clarified using examples of single-phase flow correlation functions for reasons of simplicity.



## 2.1 Directional ambiguity and image shifting

As indicated previously, PIV involves determination of the correlation between two interrogation windows to obtain the local displacement of sets of tracer particles. Let us first consider a single-phase flow correlation function in more detail. Figure 2 depicts a typical correlation function determined using two completely overlapping interrogation windows of  $32 \times 32$  [pix<sup>2</sup>]. It can clearly be seen that this correlation function is identical to the well-known auto-correlation function. The function is symmetric with respect to its origin and contains three distinct peaks: the so-called self-correlation peak ( $R_P$ ) and the positive and negative displacement correlation peak ( $R_D^+$  and  $R_D^-$  respectively). The correlation function depicted in Figure 2 is generally written as (Keane and Adrian, 1990):

$$R(\mathbf{s}) = R_C(\mathbf{s}) + R_F(\mathbf{s}) + R_P(\mathbf{s}) + R_D^-(\mathbf{s}) + R_D^+(\mathbf{s}) \quad 1$$

$R_F$  and  $R_C$  represent the correlation of particle images with the wrong partners and the correlation of the mean intensity.

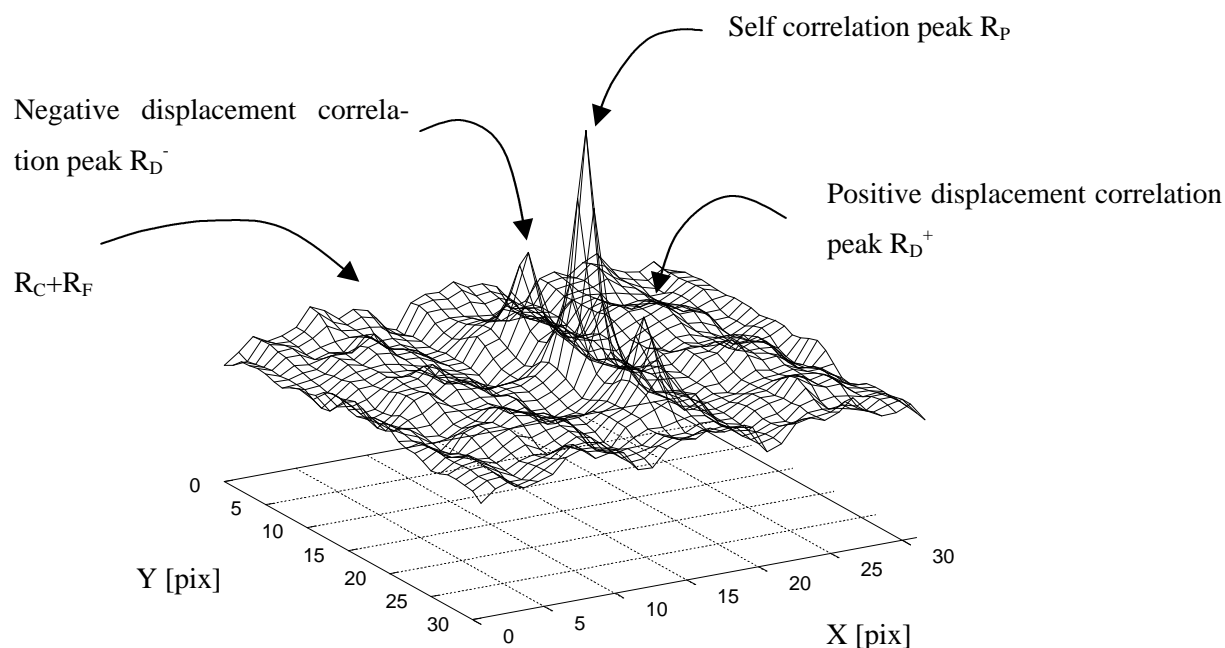


**Figure 2.** Typical correlation function encountered in a single-phase double-exposure single-frame PIV experiment. No interrogation window offset was used in the analysis of the PIV image. Size of the interrogation area:  $32 \times 32$  [pix<sup>2</sup>].

The mean displacement of the tracer particles in the interrogation window is represented by the vector from the center of the cross-correlation function to one of the displacement correlation peaks. Clearly, the direction of the displacement is ambiguous because it is

impossible to decide which displacement correlation peak ( $R_D^-$  or  $R_D^+$ ) represents the actual displacement in the object plane, unless the first and second images of the tracer particles can be identified. This directional ambiguity issue is only a problem in flows that are not unidirectional.

In this Chapter, our objective is to apply PIV to study the gas-liquid two-phase flow prevailing in a bubble column. This two-phase flow is dominated by coherent structures (i.e. vortices) in the liquid phase, and hence both positive and negative velocities can be expected. This implies that the problem of directional ambiguity common to double-exposure single-frame PIV recordings has to be resolved. This in turn means that we have to come up with a method to distinguish the first exposure from the second exposure. Various techniques are available to achieve this. Adrian (1986) discusses several methods to mark the first and second images (in the low image density limit, viz. in PTV) using for instance unequal intensities of the laser beam, multiple colors or multiple pulse sequences with a coded spacing.

Our PIV technique uses a different approach referred to as *image shifting* (also discussed by Adrian, 1986). In image shifting, the second image of each tracer particle is translated with respect to the first image such that every image displacement is negative (or positive) even though the actual displacement in the object plane may be positive (or negative, depending on the direction of the image shift employed). Our two-phase velocimeter achieves this image shifting using the line transfer of the CCD camera. Illuminating the CCD chip during its read-out period effectively shifts the image plane downward (with respect to the object plane) between two successive exposures. The technique is illustrated graphically in Figure 3. Obviously, the measured displacement has to be corrected for the effective displacement associated with the image shift, to obtain the actual displacement of the tracer particles.



## 2.2 Window offset

In section 2.1, we discussed an image shifting technique to resolve the directional ambiguity issue arising in the interrogation of double-exposure single-frame PIV recordings. This basically implies that a known uniform particle image shift with a magnitude equal to the image shift can be found in each PIV image. This uniform image shift can be used as an offset between the two interrogation windows used by the correlation procedure to determine the mean in-plane displacement of the tracer particles in the interrogation window under consideration. This window offset has two effects: the self-correlation peak will shift away from the center of the correlation plane by an amount equal to the offset employed. Moreover, the amplitude of the negative displacement correlation peak (or the positive one depending on the offset used) will increase whereas the amplitudes of the opposite displacement correlation peak and the self-correlation peak will decrease. Willert (1996) discusses the use of a uniform window offset in the evaluation of double-exposure single-frame PIV images, whereas Westerweel *et al.* (1997) discuss the effect of a local discrete window offset on the accuracy of the velocimeter.

In the experiments presented in this paper, the image shift generally exceeds the width of the interrogation windows (Typical image shift: 43 [pix]. Typical interrogation window:  $32^2$  [pix<sup>2</sup>]). Figure 4 depicts the effect of a window offset that exceeds the width of the interrogation window on the correlation function. It can be seen that in this case, the correlation function resembles the classical cross-correlation function with a single displacement correlation peak. The local displacement of the tracer particles associated with the correlation function depicted in Figure 4 is given by the location of the displacement correlation peak with respect to the center of the correlation plane. A Gaussian curve fit (Westerweel, 1993) is used to locate the peak's centroid with sub-pixel accuracy.

Let us summarize the preceding two sections. The two-phase PIV technique discussed in this paper uses an image shift (the line transfer of the CCD camera) and a discrete (integer number of pixels) window offset. This combination of an image shift and a window offset resolves the directional ambiguity issue related to double-exposure single-frame PIV recordings and improves the strength of the displacement correlation peak.

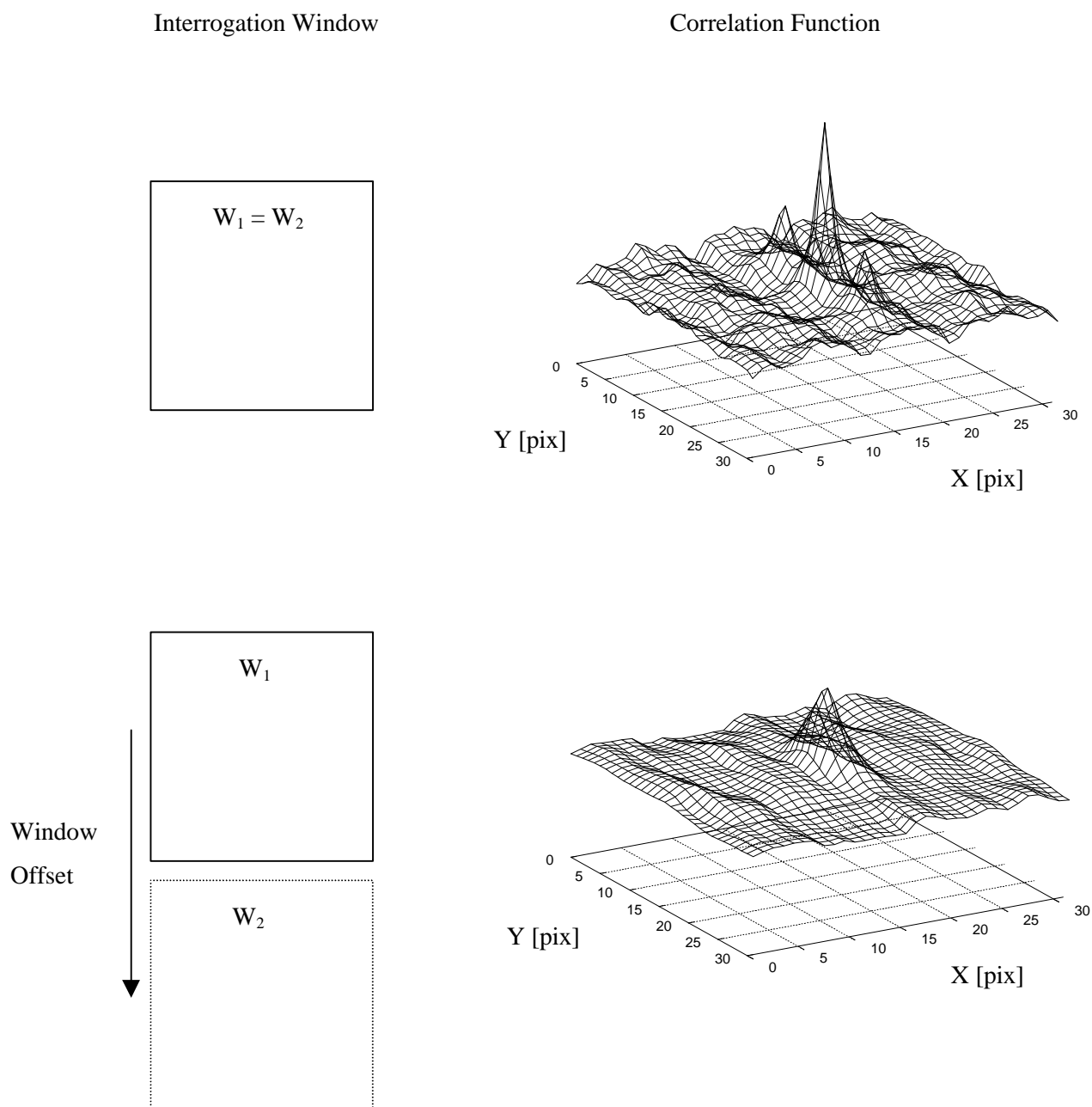


**Figure 4.** Description of the effect of an interrogation window offset on the cross-correlation function. The size of the interrogation window is  $32 \times 32$  [pix<sup>2</sup>].  $W_1$  represents the first interrogation window and  $W_2$  represents the second window.

### 2.3 From single-phase to two-phase PIV

In our two-phase particle image velocimeter, the liquid is also seeded with tracer particles and a cross-section of the flow is illuminated using a scanning laser beam. The plane of illuminated particles and bubbles is imaged onto the CCD sensor of a video camera. The recorded video frames therefore contain images of both tracers and bubbles. A correlation procedure similar to that employed in single-phase PIV is used to estimate the displacement

of sets of tracer particles and bubbles. It is expected that the cross-correlation function contains contributions from both tracers and bubbles, i.e. the cross-correlation function contains two displacement correlation peaks: one associated with the tracer particles and one associated with the bubbles (see also Delnoij *et al.*, 1998). These two displacement correlation peaks do not overlap significantly due to the velocity difference between the bubbles and the surrounding liquid.

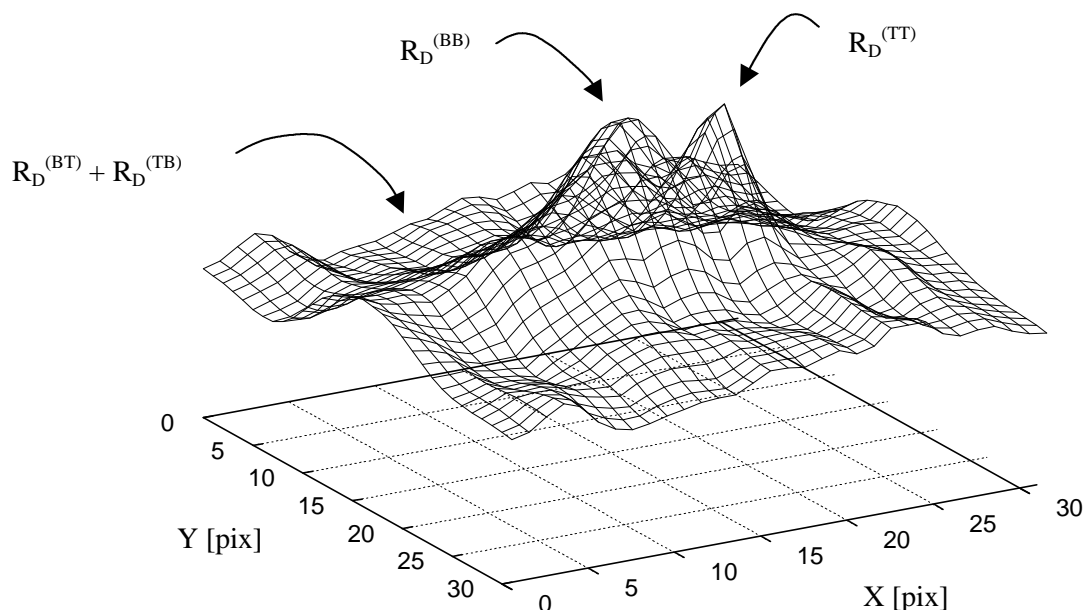


**Figure 5.** Typical correlation plane observed in two-phase ensemble correlation PIV. This particular correlation function has been determined by cross-correlating two interrogation windows from a double-exposure single-frame PIV image with a window offset of 36 [pix]. The size of the interrogation window is 32 x 32 [pix<sup>2</sup>].

Figure 5 depicts a typical correlation function obtained with a double-exposure single-frame PIV technique in a dispersed gas-liquid two-phase flow. From this Figure, the two displacement correlation peaks can clearly be seen. In the previous Chapter, it was postulated that the cross-correlation function could be written as (after subtracting the mean image intensity from the PIV image, to eliminate noise associated with correlations between the mean image intensity and the fluctuating intensity, i.e. the tracer and bubble images):

$$R(\mathbf{s}) = R_D^{(TT)}(\mathbf{s}) + R_D^{(BB)}(\mathbf{s}) + R_D^{(TB)}(\mathbf{s}) + R_D^{(BT)}(\mathbf{s}) \quad 2$$

The terms  $R_D^{(TB)}$  and  $R_D^{(BT)}$  in this equation represent the random correlation between tracers and bubbles and *vice versa*.

Equation (2) clearly reflects that the cross-correlation function contains two displacement correlation peaks. One is associated with the motion of the tracer particles ( $R_D^{(TT)}$ ); the other is associated with the motion of the bubbles ( $R_D^{(BB)}$ ). The performance of the velocimeter depends on its success in detecting these two displacement correlation peaks among neighboring noise peaks. The detectability of the two displacement correlation peaks depends, in turn, on their amplitude with respect to the strength of neighboring noise peaks. Several theoretical studies have been devoted to this detectability issue. Keane and Adrian (1990) used synthetic PIV images to study this problem, and they presented design rules for PIV experiments that, when employed, optimize the performance of a double-exposure, single-frame velocimeter. The performance, under dispersed two-phase flow conditions, of the PIV technique presented in this paper was studied in the previous Chapter. The interested reader is therefore referred to that Chapter and the references cited therein for additional details.

## 2.4 Ensemble correlation to improve SNR

The signal-to-noise ratio (SNR) of the displacement correlation peak associated with the bubbles is generally rather poor due to the limited number of bubbles in the interrogation window. Therefore, the ensemble mean of the correlation function for several sequentially recorded PIV images is calculated using:

$$R_{Ensemble}(\mathbf{s}) = \sum_{i=1}^{N_{Ensembles}} R_i(\mathbf{s}) \quad 3$$

Delnoij *et al.* (1998) studied the statistical properties of this ensemble correlation PIV technique and revealed that approximately 16 PIV images were required to obtain a 90 % valid detection probability for the bubble displacement. Figure 6 clearly illustrates the improvement of the SNR with increasing size of the ensemble correlation set. It can clearly be seen that the amplitude of the two displacement correlation peaks increases dramatically as the number of PIV images in the ensemble correlation set increases. The overall noise level, on the other hand, changes remarkably little, as more PIV recordings are included in the ensemble correlation set<sup>2</sup>. These are promising results. However, the size of the ensemble correlation set and its associated time-scale (the time needed to acquire all these PIV images)

---

<sup>2</sup> In this case, the ensemble correlation function is not normalized with respect to the height of the displacement correlation peak.

has to be small compared to the time-scale of the flow phenomenon of interest. The way in which the size of the ensemble correlation set affects the flow field ultimately obtained with our PIV technique will be discussed in section 4.

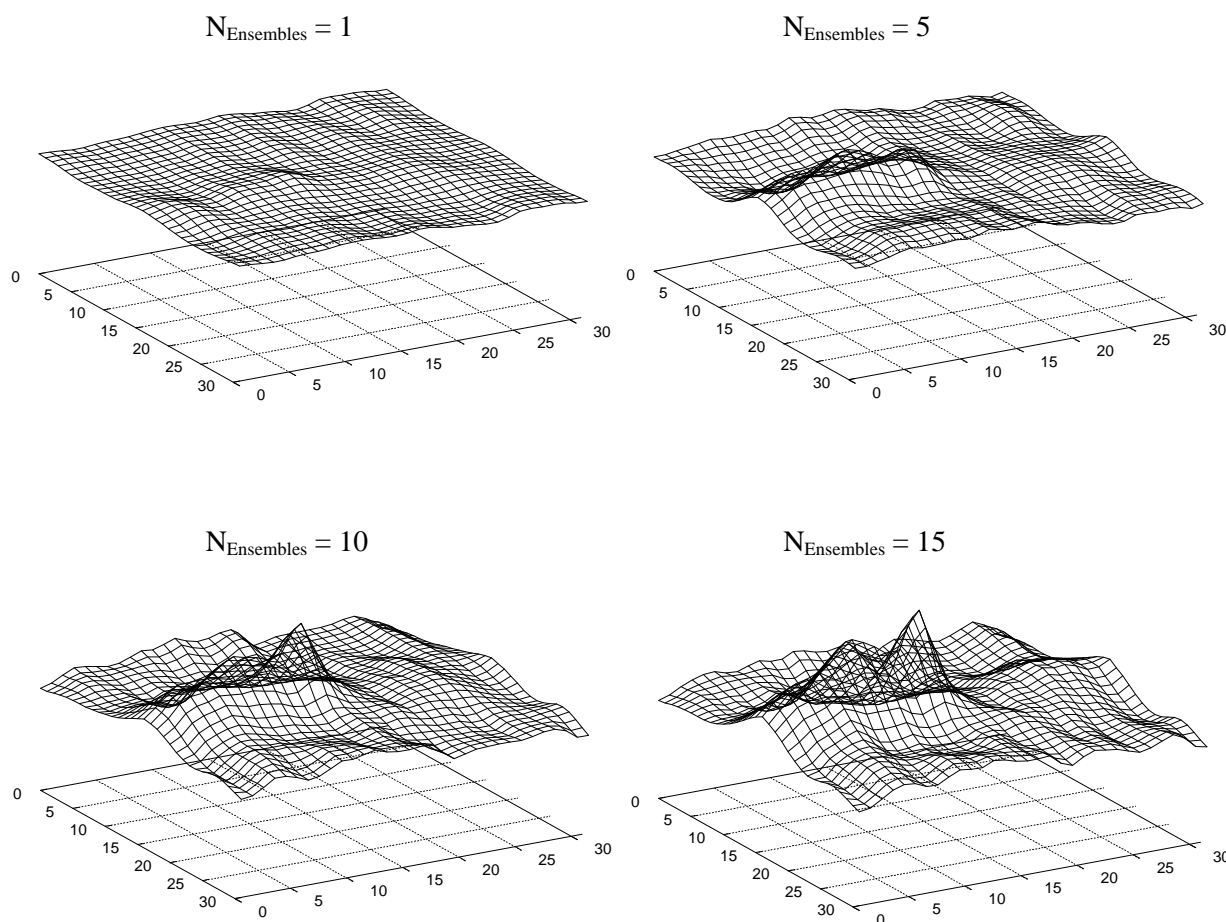


**Figure 6.** Effect of the size of the ensemble correlation set on the correlation plane. Two-phase flow, double-exposure, single-frame PIV. A uniform window offset of 43 [pix] is employed in the interrogation of the PIV images. The size of the interrogation window is 32 x 32 [pix<sup>2</sup>].

In the previous Chapter, we discussed a graph depicting the linear dependence of the amplitude of the displacement correlation peak associated with the motion of the bubbles on the mean effective number of bubble image pairs. It was concluded that the strength of the displacement correlation peak pertaining to the bubbles can be used as a first estimate of the local void fraction (i.e. the ensemble mean number of bubbles). Two-phase ensemble correlation PIV should therefore allow us to gauge (qualitatively) the local void fraction. This issue will also be addressed in section 4.



## 2.5 Discriminating between gas and liquid

From Figures 5 and 6 it can clearly be seen that in case PIV is applied to dispersed gas-liquid two-phase flows, both the tracer particles and the bubbles generate a signal in the correlation plane. Obviously, we need some practical method to discriminate the signal from the tracer particles from that of the bubbles. In the present implementation, some prior knowledge of the gas-liquid flow field is required to achieve this. The user of the PIV system has to specify a single interrogation window known to contain only tracer particles. The highest displacement correlation peak in this window then evidently pertains to the liquid phase. The displacement associated with this assigned<sup>3</sup> peak is subsequently compared to the displacements associated with both<sup>4</sup> displacement correlation peaks in neighboring interrogation windows. A residual displacement test is used to determine, for each of these unassigned displacements, whether it belongs to the liquid phase. If so, the displacement is said to represent the local motion of the liquid. However, in case the displacement correlation peak can not be contributed to the motion of the tracer particles (i.e. the liquid phase), it either represents the motion of the gas phase or it should be marked as a spurious result. The algorithm distinguishes between displacements associated with the motion of the bubbles and erroneous results on basis of the strength of the corresponding displacement correlation peak with respect to the overall noise level. The strength of the bubble displacement correlation peak (if present) generally significantly exceeds the amplitude of the noise peaks. If successful, this procedure generates two more so-called ‘assigned’ displacements, one associated with the motion of the tracer particles and one associated with the motion of the bubbles. A computer algorithm has been implemented that applies this procedure to every interrogation window in the PIV image.

---

<sup>3</sup> Assigned displacement meaning: this displacement is most likely due to the motion of that particular phase.

<sup>4</sup> The cross-correlation function can also contain one displacement correlation peak in the absence of gas bubbles in this particular part of the flow field. In this case, the algorithm acts as a filter rejecting any spurious vectors.

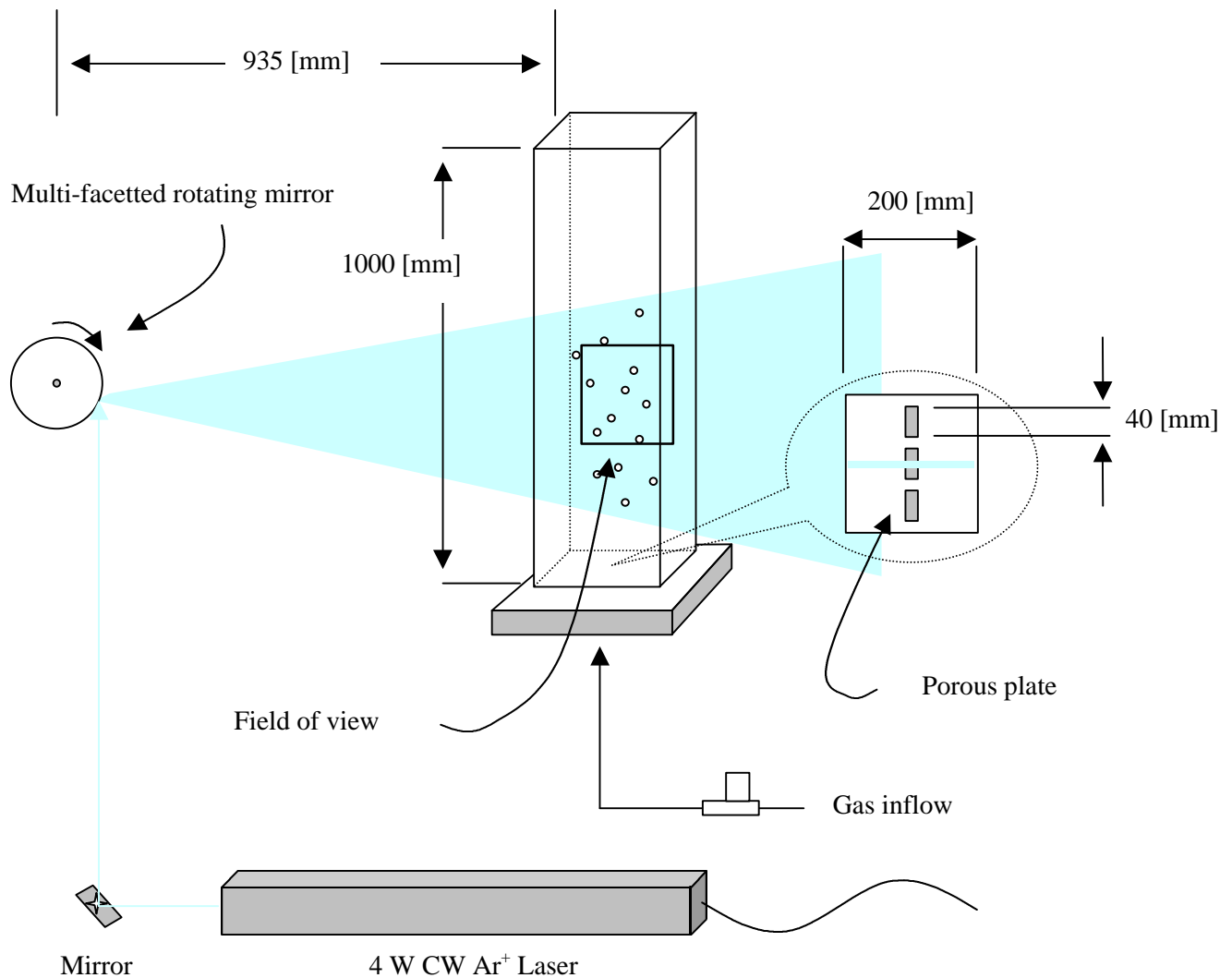


**Figure 7.** Schematic representation of the experimental setup. The rectangular bubble column, the rotating mirror and the  $\text{Ar}^+$  laser are shown. The CCD camera and associated hardware are not shown.

### 3. Experimental set-up

The experimental set-up is depicted in Figure 7. It consists of a bubble column, an  $\text{Ar}^+$  laser, optics used to illuminate a cross section of the flow, a CCD camera and an image acquisition system (not shown). The rectangular bubble column (200 [mm] x 200 [mm] x 1000 [mm]) is constructed from ordinary glass and fitted with three porous plates (40 [mm] x 20 [mm]; active pore size: 10 [ $\mu\text{m}$ ]) that act as gas distributors. Three mass flow controllers (MFC) are used to control the gas flow rate through each of these gas distributors. Bubble sizes are approximately 2 [mm]. In the experiments discussed in this Chapter, gas is fed to the porous plate in the center of the bubble column; this results in a bubble plume rising along the

columns' centerline. Compressed air is used as the gas phase and de-mineralized water is used as the liquid phase. The liquid flow is seeded with polyamid particles (Dantec measurement technology). These particles are approximately spherical, have a diameter of  $50 \pm 20$  [ $\mu\text{m}$ ] and a density of  $1030$  [ $\text{kg m}^{-3}$ ]. Experiments revealed that these tracer particles did not noticeably affect bubble sizes. Some of the important dynamic properties of these particles are listed in Table 1.

**Table 1.** Characteristics of the polyamid tracer particles.

Diameter	$50 \pm 20$ [ $\mu\text{m}$ ]
Density	$1030$ [ $\text{kg m}^{-3}$ ]
Particle response time	$0.6$ [ms]
Sedimentation velocity	$0.3$ [ $\text{mm s}^{-1}$ ]

A 4 W continuous wave (CW) Argon-ion laser (Spectra Physics, Stabilite 2017) is used to illuminate a vertical cross section of the bubble column. The laser is operated in the multi-line mode (with its most significant lines at  $488$  [nm] and  $514.5$  [nm]) with the aperture set to ensure an approximately Gaussian laser beam. The diameter of the laser beam is  $3.8$  [mm]. The laser beam is deflected onto a rotating multi-faceted mirror (72 facets, scan angle:  $10^\circ$ ) which in turn deflects the laser beam through the bubble column. Each facet of the mirror corresponds to a single scan of the laser beam through the bubble column. The frequency of rotation of the multi-faceted mirror is derived from the exposure time delay  $\Delta t$  (the time between two successive exposures of the flow). This exposure time delay is determined using the expected mean velocity of the tracer particles and the bubbles. The exposure time delay is usually set to ensure that the displacement of both tracers and bubbles *including* image shift exceeds the width of an interrogation window (based on a  $32^2$  [ $\text{pix}^2$ ] interrogation window). The design rule laid down by Keane and Adrian (1990), that limits the displacement of tracer particles to 25 % of the width of an interrogation window, is strictly obeyed due to the window offset that is employed during PIV image interrogation.

Two successive exposures of the flow to the laser light are recorded using a CCD camera. This camera (Texas Instruments MC-1000WU-20) employs the TI-TC215 full-frame CCD sensor, which features 1017000 active pixels (1017 active lines with 1000 active pixels each). The CCD sensor measures  $17.2$  [mm] diagonally and has  $12$  [ $\mu\text{m}$ ] square pixels with a fill

factor equaling 100 %. It is a black and white, non-interlaced camera with a frame rate of 15.46 [Hz]. A separate liquid crystal display (LCD) shutter is employed, which is synchronized to the rotating multi-faceted mirror to ensure that exactly two sweeps of the laser beam are captured by the CCD camera. These two sweeps are recorded during the read-out period of the CCD array. Image read-out is accomplished by transferring the charge, accumulated by the CCD sensor during its illumination, one line at a time into two serial registers. This procedure (i.e. the so-called line transfer) effectively results in an image shift of 16.233 [lines per millisecond exposure time-delay]. This image shift can also be determined from careful analysis of the recorded PIV images. The camera is connected to a MaxVideo 200 data acquisition system and a Sun Sparc station is used to control the image acquisition process and store the acquired data on hard disk or DAT tape. The memory capacity of the MaxVideo 200 data acquisition system limits the total amount of frames that can be recorded to 15.

The recorded PIV images are analyzed using PIV software originally developed by Westerweel (1993), which has been adapted for use in dispersed gas-liquid two-phase flows. This software package features efficient FFT routines, which are used to determine the correlation between two interrogation windows. Particle and bubble displacements can be estimated at sub-pixel level using a Gaussian peak fit. Nevertheless, a limited number of spurious vectors may emerge. These spurious results can be detected based on their deviation with respect to the local median of the displacements (Westerweel, 1993). The algorithm subsequently replaces the spurious vector by a new vector, which is the mean value of the eight surrounding vectors.

#### **4. Results**

The ensemble correlation PIV technique presented in this Chapter has been used to study the gas-liquid two-phase flow prevailing in our lab-scale bubble column. We therefore conducted an experiment in which gas was fed to the center orifice of the bubble column at a flow rate of 0.203 [dm<sup>3</sup> min<sup>-1</sup>]. This caused a bubble plume to rise along the centerline of the bubble column. Table 2 lists the relevant experimental conditions used in this experiment. This section discusses the results of these experiments. We will study the liquid flow field induced by the bubble plume rising in the bubble column and we will discuss the local mean gas velocity and local mean void fraction as measured with our velocimeter. Moreover, the effect

of the size of the ensemble correlation set and the size of the interrogation window on the flow field ultimately obtained with our technique will be highlighted.

**Table 2.** Relevant experimental conditions pertaining to the experiments discussed in section 4.

General properties:	
System	De-mineralized water / Air
Liquid density	$1.0 \times 10^3$ [kg m <sup>-3</sup> ]
Liquid kinematic viscosity	$1.0$ [mm <sup>2</sup> s <sup>-1</sup> ]
Liquid Height	$0.425$ [m]
Bubble diameter	$\approx 2.0 \times 10^{-3}$ [m]
Gas flow rate	$0.0122$ [m <sup>3</sup> h <sup>-1</sup> ]
Interrogation:	
View area	$152 \times 154$ [mm <sup>2</sup> ]
Interrogation resolution (typical)	$32$ [pix]
Interrogation increment (typical)	$16$ [pix]
Number of vectors/frame	$3782$ [vectors frame <sup>-1</sup> ]
Image recording:	
Exposure time delay (typical)	$2.5 \times 10^{-3}$ [s]
Number of exposures/frame	$2.0$ [-]
Image shift	$43$ [pix]
Optics:	
Lens focal length	$50$ [mm]
Numerical aperture	$1.8$ [-]
Object distance	$700$ [mm]
Image distance	$54$ [mm]
Magnification	$0.079$ [-]
Focal depth	$1.2$ [mm]
Seeding:	
Volume fraction tracer particles	$3.5 \times 10^{-5}$ [-]
Amount of tracer particles	$0.62 \times 10^{-3}$ [kg]
Image density <sup>5</sup>	$14$ [-]
Laser:	
Sheet thickness	$3.8$ [mm]
Output power laser (typical, all-lines)	$1.0$ [W]

<sup>5</sup> Based on a  $32 \times 32$  [pix<sup>2</sup>] interrogation window.

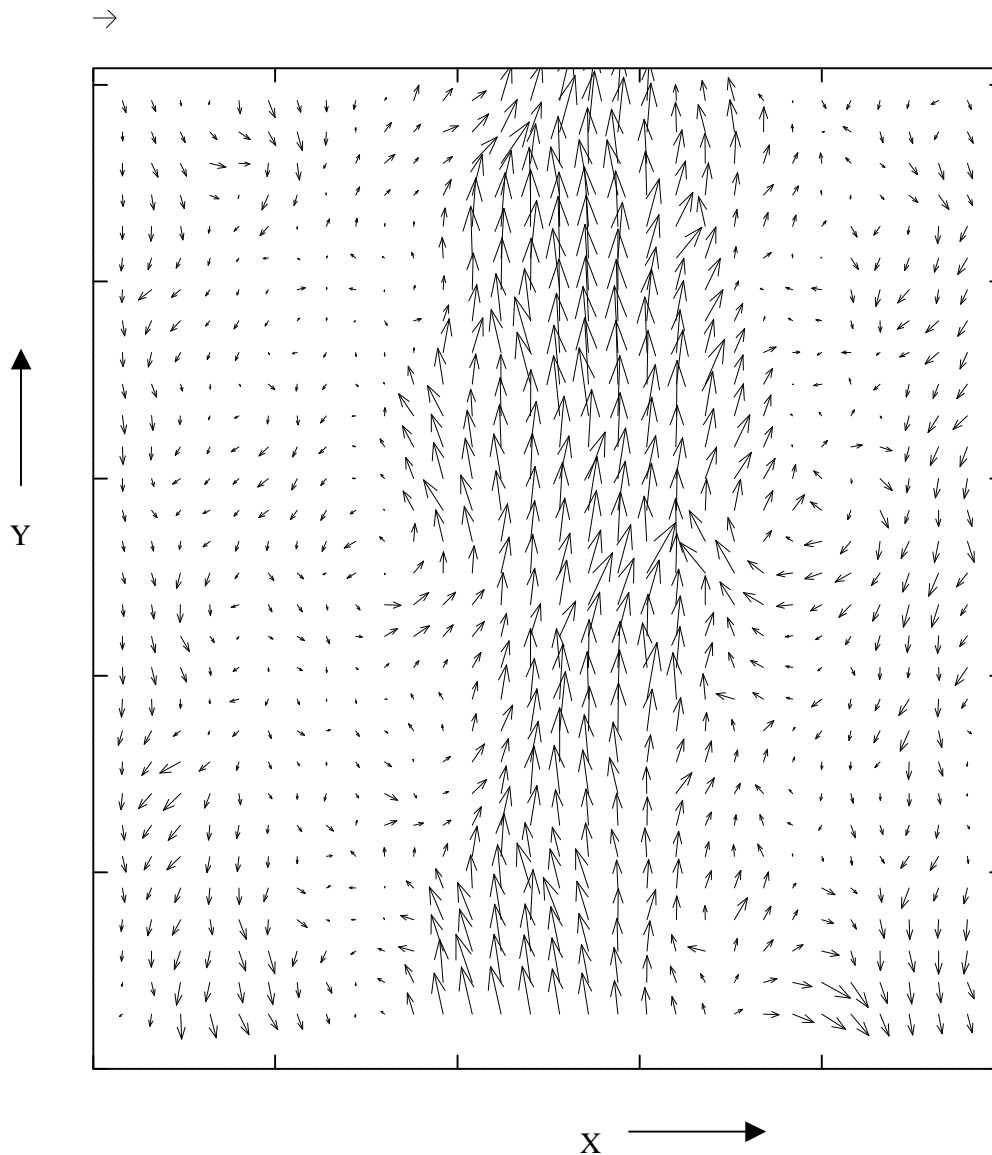


**Figure 8a.** Instantaneous liquid flow field induced by a bubble plume rising in water. PIV image number 5. The size of the interrogation windows is  $64 \times 64$  [pix<sup>2</sup>]. A uniform window offset of 43 [pix] is used in the interrogation of the PIV images. The reference vector corresponds to a velocity of  $6$  [cm s<sup>-1</sup>].

#### 4.1 Instantaneous liquid flow field

Let us first consider the instantaneous liquid flow field induced by the bubble plume rising through the liquid. Figures 8a and 8b depict this instantaneous liquid flow field in a vertical cross-section halfway through the column, obtained from two different double-exposed PIV images. Figure 8b was recorded approximately 0.4 [s] after Figure 8a. The local median test (discussed in section 3) was used to remove erroneous results. The word ‘instantaneous’ is used here because the flow field is obtained by interrogating a single double-exposure PIV

image (i.e. no ensemble averaging has been applied). Remember that in section 2.4, we discussed the use of the ensemble mean of the cross-correlation function to improve the SNR of the bubble displacement correlation peak. The SNR of the displacement correlation peak associated with the motion of the tracers is generally reasonably good. This implies that it is possible to use a small set of PIV images (or just one image as in Figure 8[a, b]) to determine the ensemble mean of the correlation function in order to obtain meaningful results for the liquid flow field.

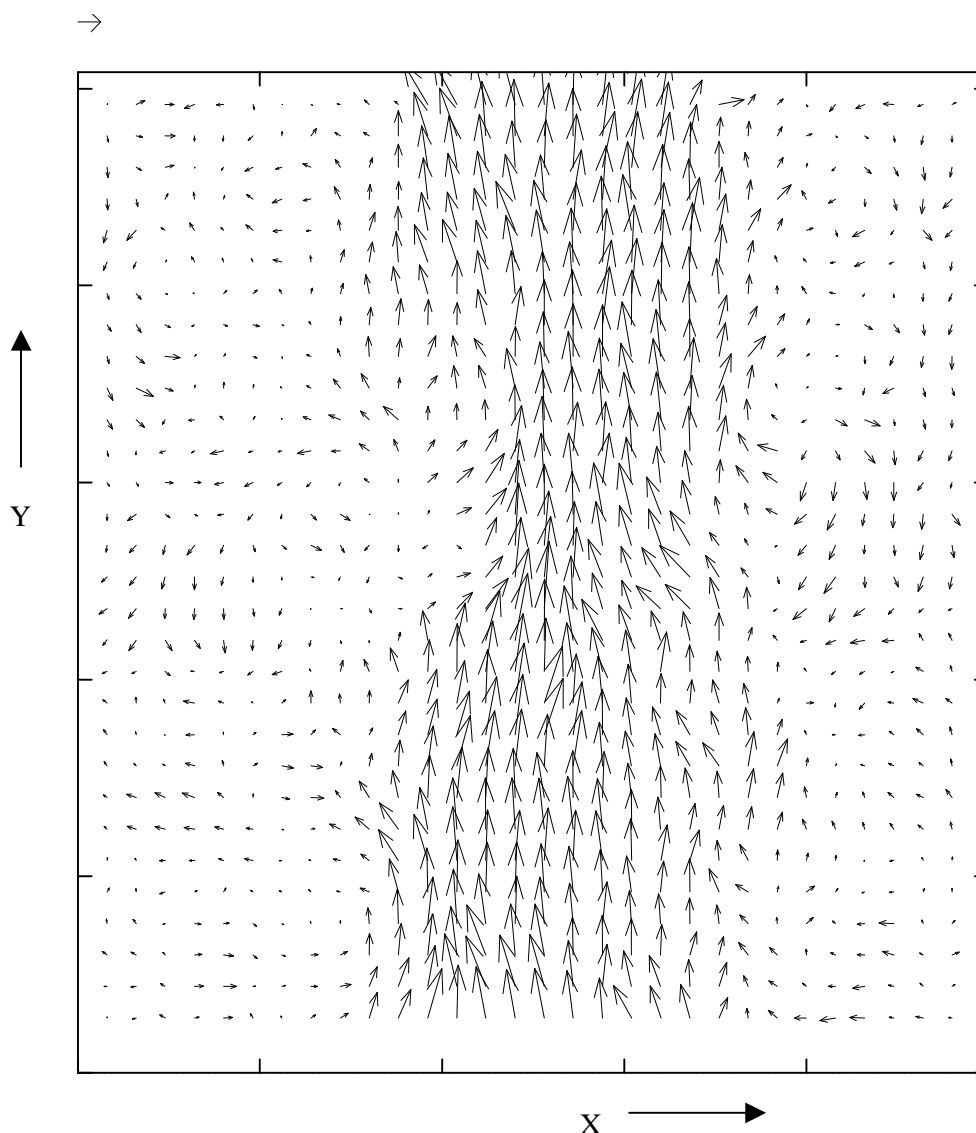


**Figure 8b.** Instantaneous liquid flow field induced by a bubble plume rising in water. PIV image number 11. The size of the interrogation windows is  $64 \times 64$  [pix<sup>2</sup>]. A uniform window offset of 43 [pix] is used in the interrogation of the PIV images. The reference vector corresponds to a velocity of  $6$  [cm s<sup>-1</sup>].

From Figures 8a and 8b, the complex nature of the gas-liquid two-phase flow encountered in a bubble column can clearly be seen. It can also be seen that the flow structure changes significantly with time. The rather large axial liquid velocities in the center of the vector map are due to the bubbles that ascent through the liquid in this region of the flow (close to the column's center). Visual observation of the two-phase flow in the bubble column revealed that the bubble plume is largely confined to this region. To the left and right of this high velocity region, vortical structures can be observed. Near the walls of the bubble column (2.5 [cm] separates the boundaries of the vector map depicted in Figure 8 from the walls of the column) liquid down flow is detected.

Figure 9 shows the instantaneous liquid flow field obtained from the same double-exposed PIV recording as that used to obtain Figure 8a. Figure 9 however, has been determined using smaller interrogation windows of  $32 \times 32$  [pix<sup>2</sup>]. Again, the bubble plume region can be clearly distinguished. The complex nature of the liquid flow field observed in the bubble column is even more apparent than could be inferred from Figure 8a. It can be seen that, owing to the smaller interrogation windows, smaller structures in the liquid flow field can be resolved. The liquid flow is clearly turbulent, which is in accordance with visual observations of the liquid flow prevailing in the bubble column. Moreover, the liquid flow field in the bubble column seems to be inherently three-dimensional because it would appear that the two-dimensional flow field depicted in Figure 9 is not always divergence free.

It has to be noted that the number of spurious results also increases as the size of the interrogation windows is reduced from  $64^2$  [pix<sup>2</sup>] to  $32^2$  [pix<sup>2</sup>]. This is due to a low particle image density in the latter case, which is caused by two concurrent effects. The amount of tracer particles that was added to the bubble column was carefully determined to ensure that a sufficiently large image density could be obtained. In this experiment, the particle image density is 14 (in a  $32^2$  [pix<sup>2</sup>] interrogation window), which is in accordance with the design rules presented by Keane and Adrian (1990). However, the tracer particles were found to accumulate slightly at the free surface, thereby effectively reducing the true number of tracer particles in the liquid bulk and thus the particle image density. Moreover, reducing the size of the interrogation window as indicated, reduces the effective particle image density in an interrogation window ( $N_I F_I F_O$ , see previous Chapter) by a factor of 4. This in turn, reduces



the amplitude of the displacement correlation peak and increases the number of spurious results (see also Keane and Adrian, 1990).

→

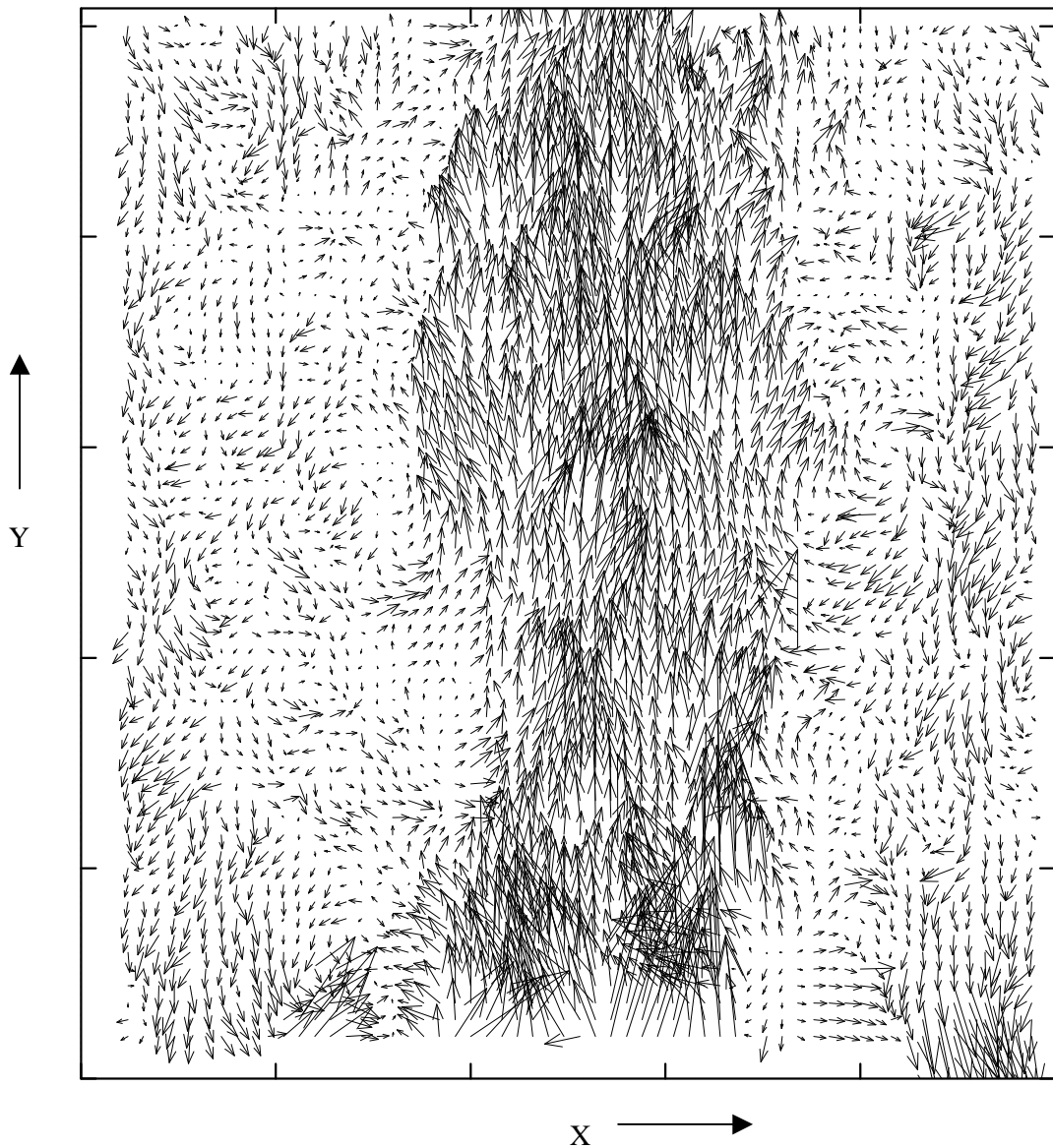


**Figure 9.** Instantaneous liquid flow field induced by a bubble plume rising in water. The size of the interrogation windows is  $32 \times 32$  [pix<sup>2</sup>]. A uniform window offset of 43 [pix] is used in the interrogation of the PIV images. The reference vector corresponds to a velocity of  $6$  [cm s<sup>-1</sup>].

#### 4.2 Size of the ensemble correlation set

The SNR of the displacement correlation peaks pertaining to the liquid phase and to the gas phase can be improved considerably by taking the ensemble-mean of the correlation function

for several sequentially recorded PIV images. Figures 10[a-e] depict the liquid flow field induced by the bubble plume rising through our bubble column. The various flow fields were determined using different sizes of the ensemble correlation set<sup>6</sup>.

→

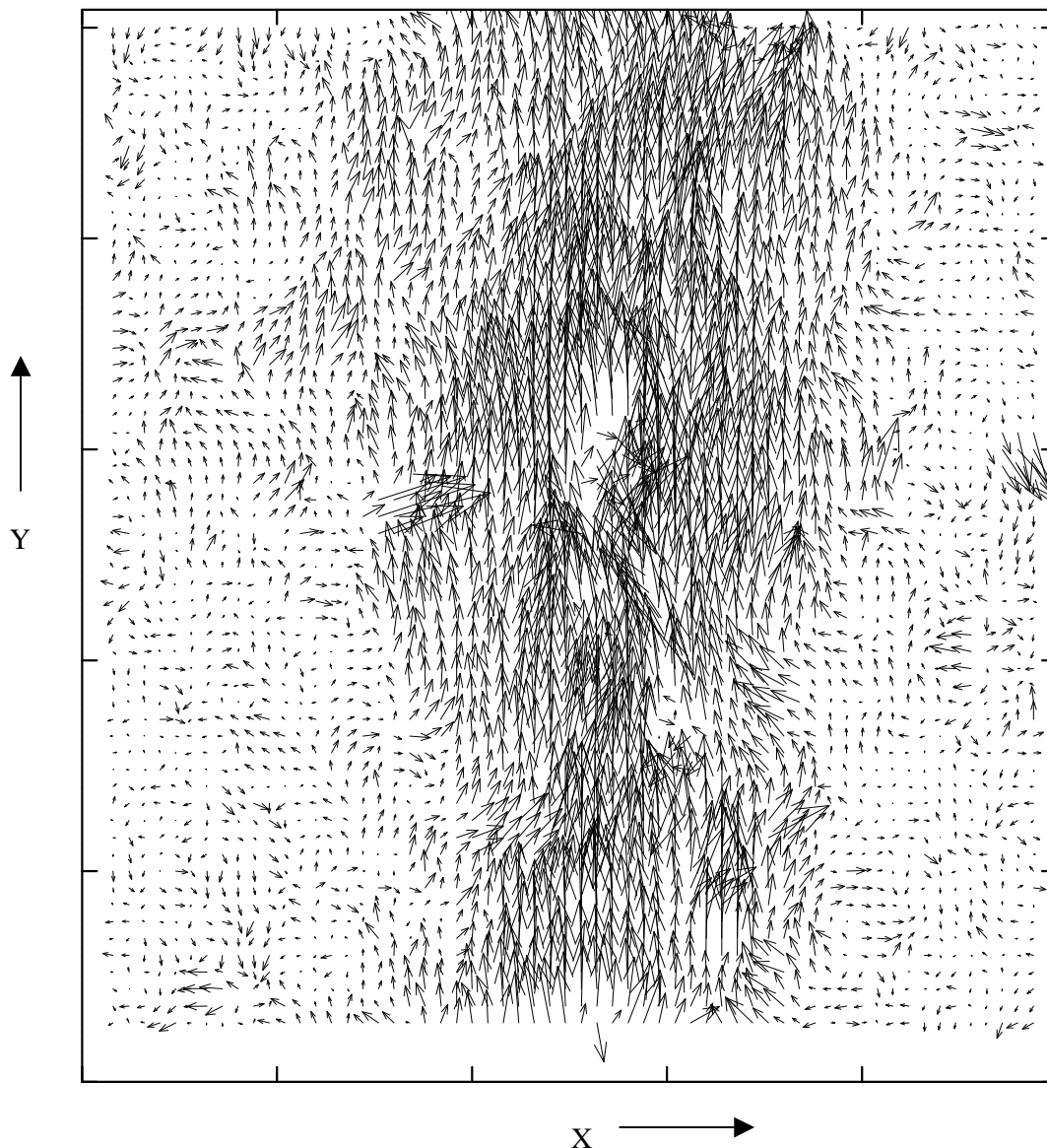


**Figure 10a.** Liquid velocity field determined using the ensemble-mean of the correlation function of 1 double-exposed PIV image. The size of the interrogation windows is  $32 \times 32$  [pix<sup>2</sup>]. A uniform window offset of 43 [pix] is employed in the interrogation of the PIV images. The reference vector corresponds to a velocity of  $6$  [cm s<sup>-1</sup>].

<sup>6</sup> The ensemble correlation set comprises the PIV images used to determine the ensemble-mean of the correlation function.

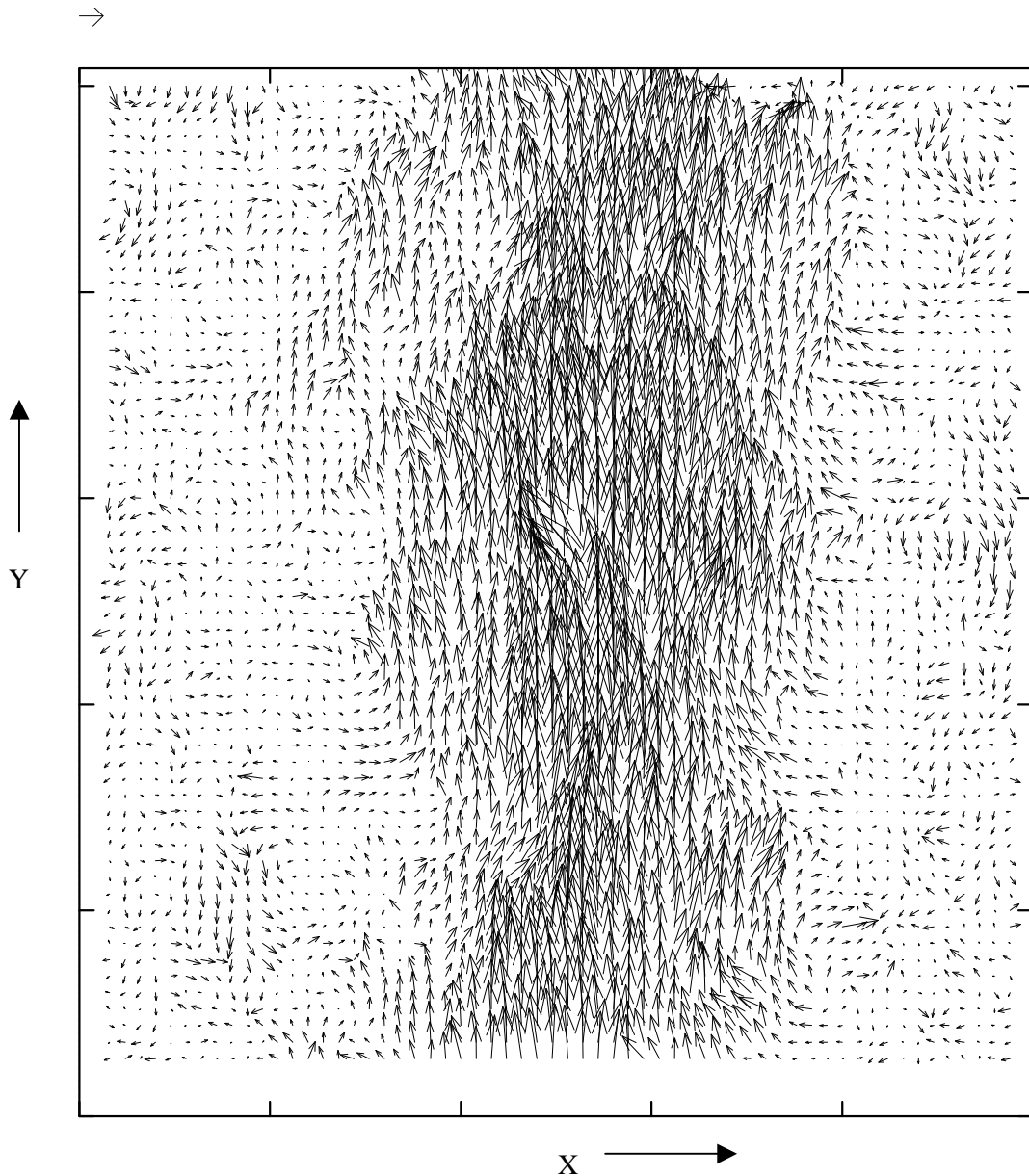


**Figure 10b.** Liquid velocity field determined using the ensemble-mean of the correlation function of 2 double-exposed PIV images. The size of the interrogation windows is  $32 \times 32$  [pix<sup>2</sup>]. A uniform window offset of 43 [pix] is employed in the interrogation of the PIV images. The reference vector corresponds to a velocity of  $6$  [cm s<sup>-1</sup>].

From these Figures, it can be inferred that as the size of the ensemble correlation set increases (i.e. as we time-average the flow field over an extended period of time), the liquid flow field, as determined with the PIV technique, changes. The small-scale structures in the liquid flow field, whose presence is ubiquitous in the instantaneous flow field, disappear step-by-step as the size of the ensemble correlation set increases from 1 PIV image to 15 PIV images. This is expected behavior because using the ensemble-mean correlation function of 15 PIV images

effectively corresponds to determining a 1 [s] time-average of the liquid flow field (frame rate CCD camera: 15 [Hz]). The time-scales associated with the small-scale structures in the liquid flow field are generally significantly smaller than 1 [s], causing these small-scale structures to disappear.

→

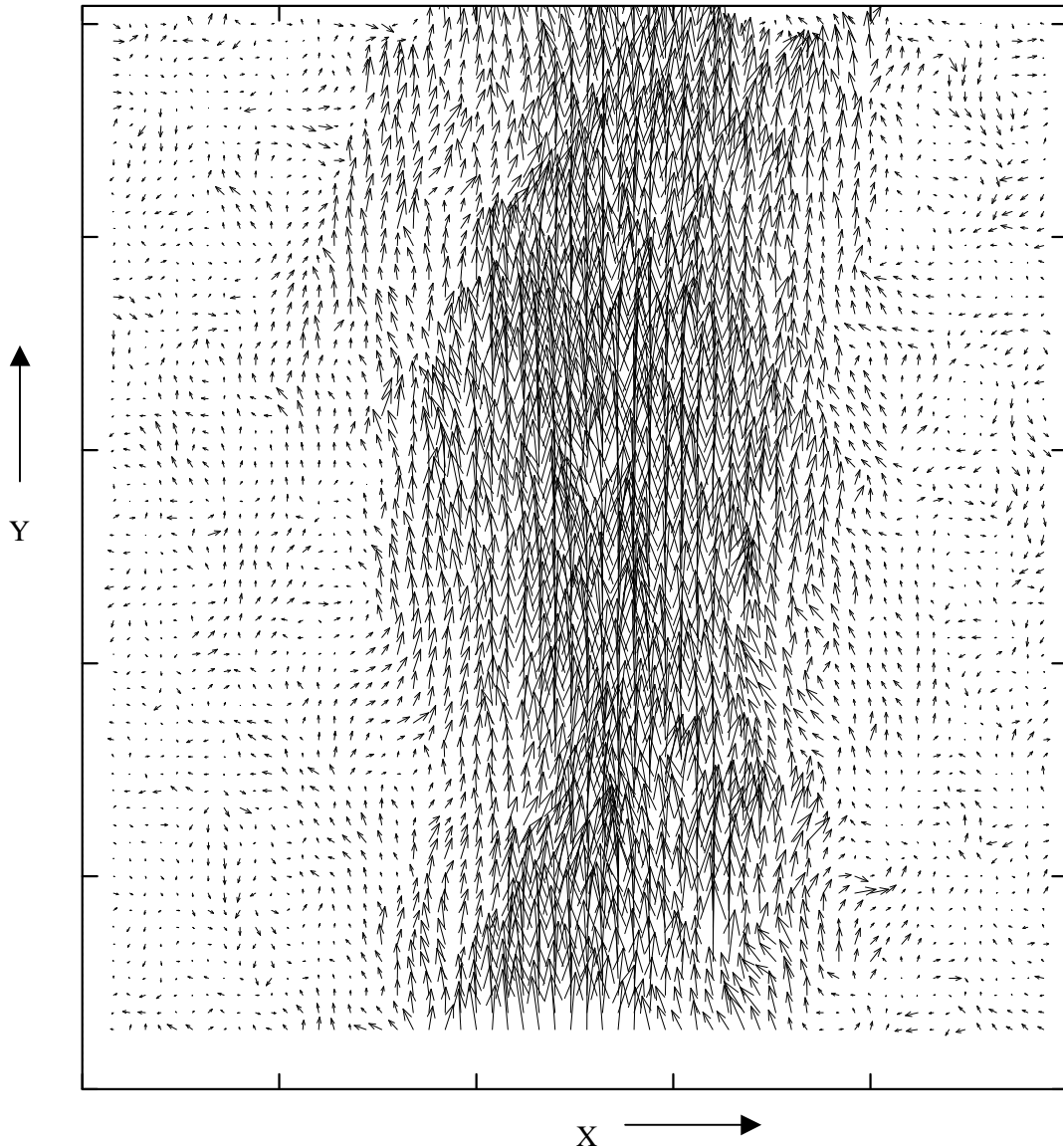


**Figure 10c.** Liquid velocity field determined using the ensemble-mean of the correlation function of 4 double-exposed PIV images. The size of the interrogation windows is  $32 \times 32$  [pix<sup>2</sup>]. A uniform window offset of 43 [pix] is employed in the interrogation of the PIV images. The reference vector corresponds to a velocity of  $6$  [cm s<sup>-1</sup>].

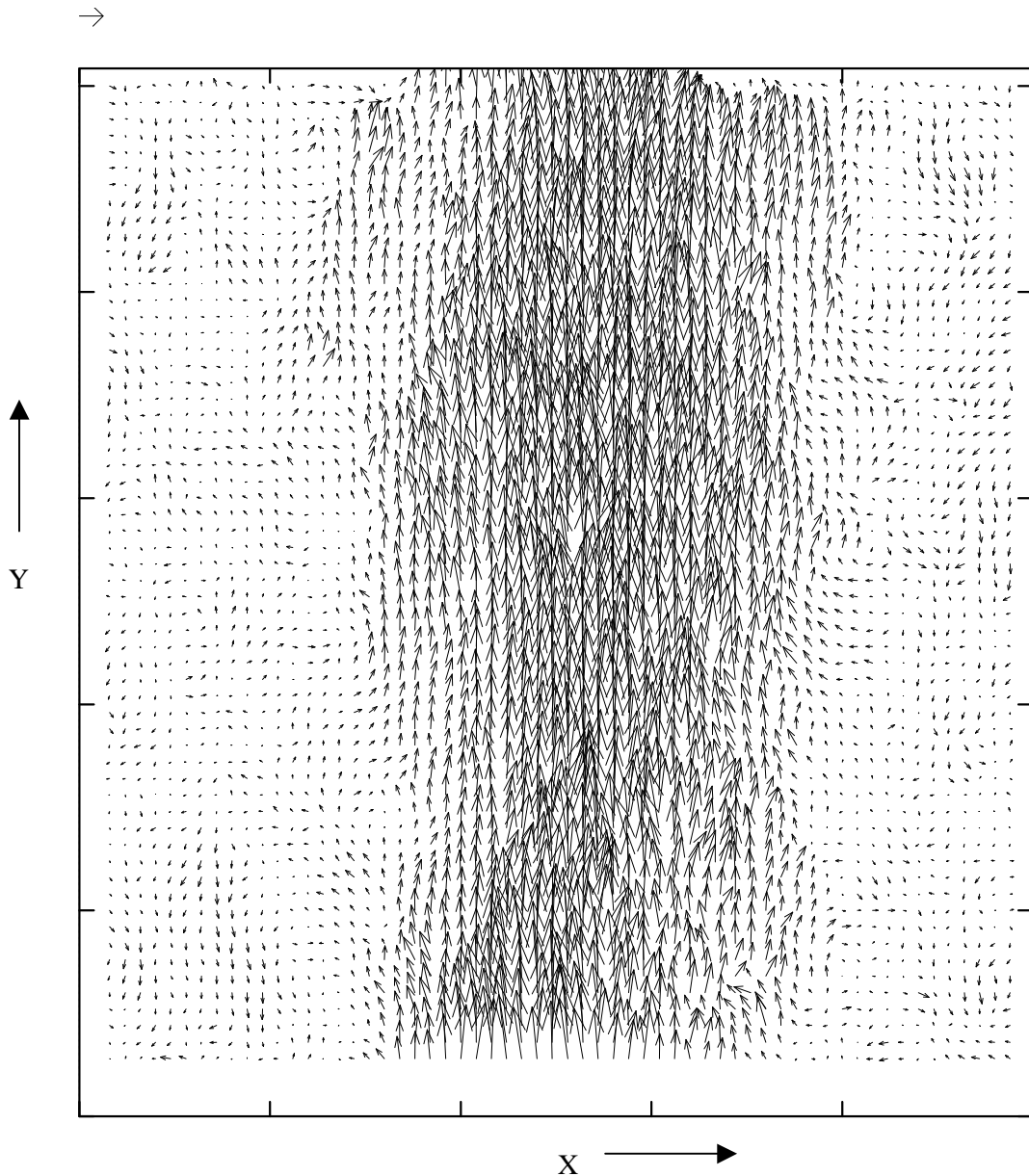


**Figure 10d.** Liquid velocity field determined using the ensemble-mean of the correlation function of 8 double-exposed PIV images. The size of the interrogation windows is  $32 \times 32$  [pix<sup>2</sup>]. A uniform window offset of 43 [pix] is employed in the interrogation of the PIV images. The reference vector corresponds to a velocity of  $6$  [cm s<sup>-1</sup>].

This loss of temporal resolution is compensated for by the enhanced detectability of the displacement correlation peaks associated with the motion of both tracer particles and bubbles. The number of spurious results decreases from approximately 25 % of the total amount of vectors as the ensemble set consists of 1 image, to 0.25 % of the total number of vectors as the ensemble correlation set is made up of 15 images. This implies that the larger flow structures (with their correspondingly larger time-scales) can be resolved more

accurately and more reliably. This can clearly be seen in Figure 10e, where the liquid upflow in the wake of the bubbles is clearly depicted, as well as the region immediately surrounding the bubble plume with its low velocity and coherent structures.

→

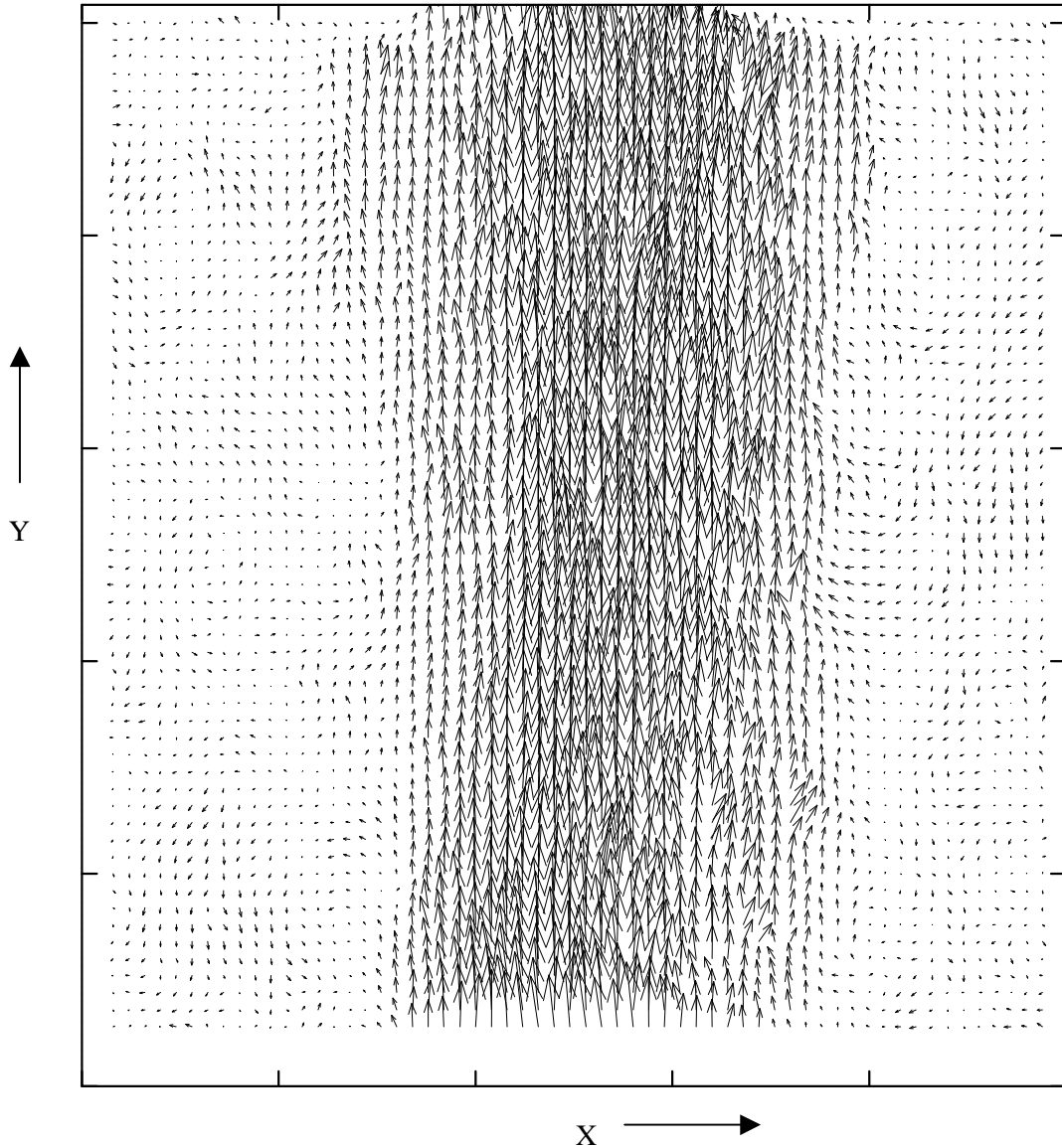


**Figure 10e.** Liquid velocity field determined using the ensemble-mean of the correlation function of 15 double-exposed PIV images. The size of the interrogation windows is  $32 \times 32$  [pix<sup>2</sup>]. A uniform window offset of 43 [pix] is employed in the interrogation of the PIV images. The reference vector corresponds to a velocity of  $6$  [cm s<sup>-1</sup>].

### 4.3 Bubble velocity and local void fraction

The local (albeit time-averaged) gas velocity can also be determined with the aid of the ensemble-mean correlation PIV technique. Due to the low bubble image density (typically 1 – 2 bubbles per interrogation window), this would be almost impossible to achieve with the instantaneous cross-correlation function.

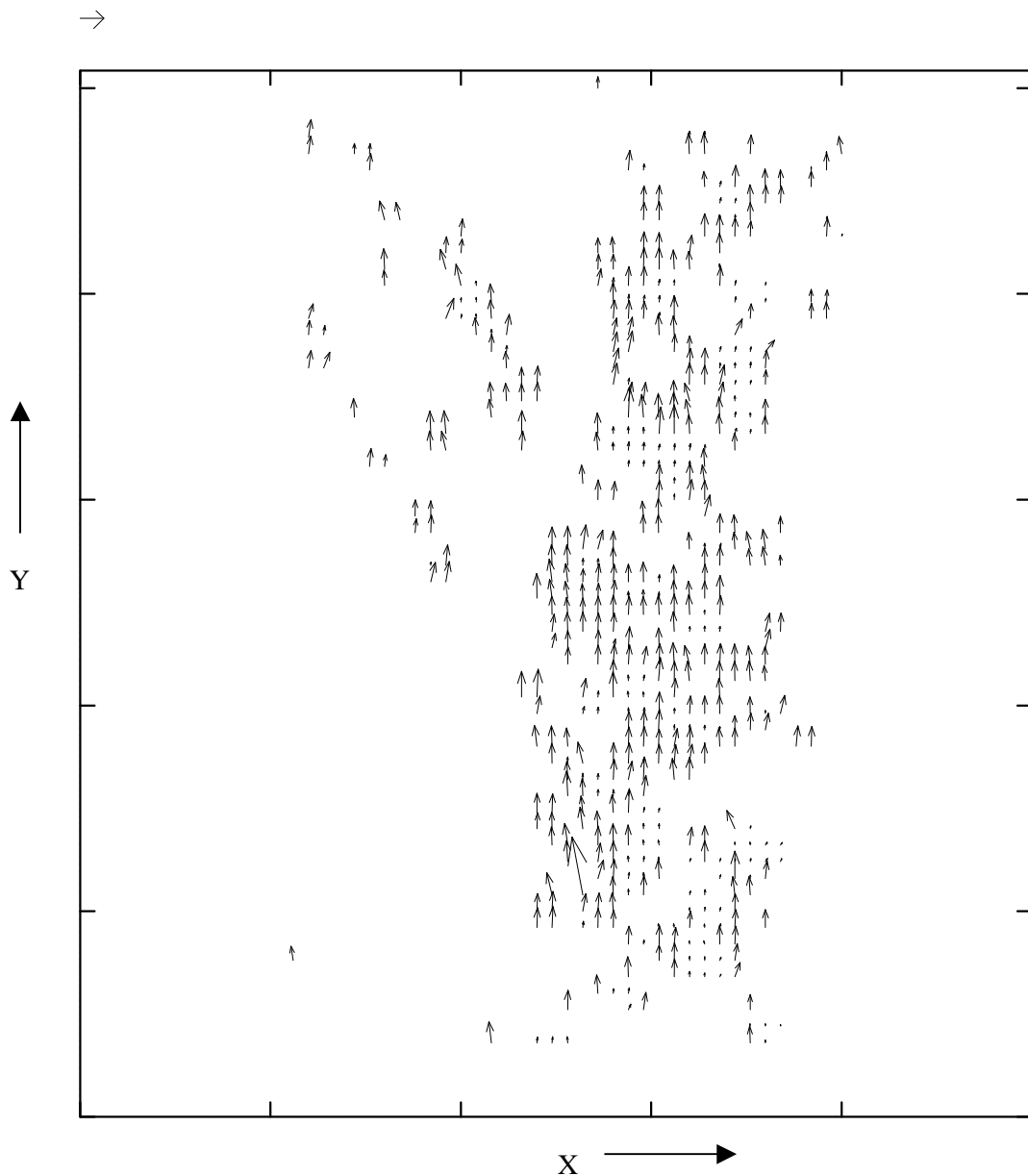


**Figure 11.** Local bubble velocities in our bubble column determined using the ensemble-mean of the correlation function of 15 double-exposed PIV images. The size of the interrogation windows is  $32 \times 32$  [pix<sup>2</sup>]. A uniform window offset of 36 [pix] is employed in the interrogation of the PIV images.

The reference vector corresponds to a velocity of  $60$  [cm s<sup>-1</sup>].

Figure 11 depicts the local gas velocity prevailing in the bubble column. Because the bubble plume is largely confined to the center of the bubble column, very few bubbles can be observed near the walls of the bubble column. This implies that bubble velocities can only be obtained for the interrogation windows in the center of the bubble column, because in the absence of bubbles a bubble velocity can obviously not be determined. From Figure 11, it can be seen that the bubbles evidently rise through the bubble column in a more or less rectilinear fashion. Due to the ensemble correlation procedure, the majority of the small time-scale oscillations that bubbles generally exhibit are not resolved. However, the ‘time-averaged’ bubble velocities depicted in Figure 11 provide valuable information in connection to the liquid flow field depicted in Figure 10e. Both can be used to estimate, for instance, the drag force acting on a bubble rising in a liquid. For example: typical bubble velocities, inferred from Figure 11, are approximately  $42 \text{ [cm s}^{-1}\text{]}$ . The local (ensemble mean) liquid velocity inside the bubble plume, as obtained from Figure 10e, is approximately  $20 \text{ [cm s}^{-1}\text{]}$ . The slip velocity between the gas and the liquid phase is therefore  $22 \text{ [cm s}^{-1}\text{]}$ , which resembles the steady rise velocity of a  $2 \text{ [mm]}$  air bubble in quiescent water.

From PIV theory, it can be derived that, for constant in-plane displacements, the amplitude of the displacement correlation peak pertaining to the bubbles is proportional to the number of bubble image pairs in the interrogation window under consideration (Delnoij *et al.*, 1998). However, the strength of the bubble displacement correlation peak also depends on the local in-plane displacement because of the so-called loss-of-correlation due to in-plane displacement  $F_1$  (see Westerweel, 1993). Provided that we correct for this loss-of-correlation, we can use the strength of the bubble displacement correlation peak as an estimate of the local void fraction. Figure 12 shows the local void fraction (or better: the local amplitude of the displacement correlation peak pertaining to the bubbles corrected for loss-of-correlation due to in-plane displacement) for the interrogation windows that generated a valid bubble velocity vector. The structure of the bubble plume can clearly be inferred from this Figure. Visual observation of the bubble plume rising through the bubble column revealed a similar structure of the bubble plume. In the interpretation of Figure 12, it should be noted however, that the strength of the displacement correlation peak is only a qualitative measure for the local void fraction. This implies that a calibration of the ensemble correlation PIV technique, with respect to the estimation of the local void fraction, is required. This calibration procedure will be a topic of future studies.



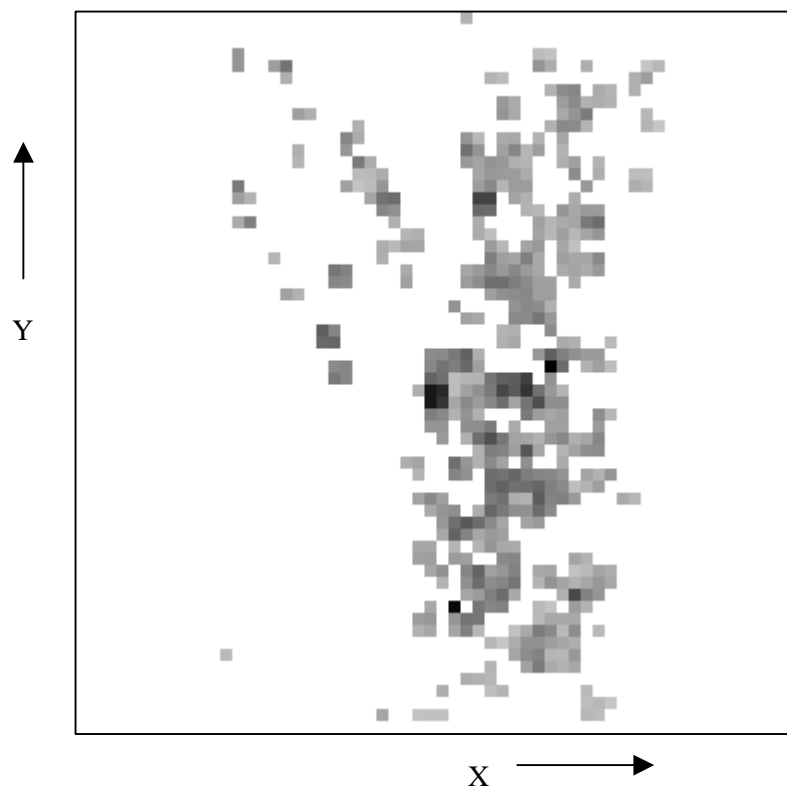


**Figure 12.** The strength of the displacement correlation peak associated with the motion of the bubbles as a measure for the local mean void fraction. The size of the ensemble correlation set is 15 double-exposed PIV images. The size of the interrogation windows is  $32 \times 32$  [pix<sup>2</sup>].

## 5. Conclusions

This Chapter highlighted the need for more accurate time-dependent and full field data on the flow structure prevailing in gas-liquid bubble columns. To meet this objective we developed an ensemble correlation Particle Image Velocimetry (PIV) technique that can be applied to the study of dispersed gas-liquid two-phase flows. The essentials of this technique were reviewed and it was concluded that the so-called double-exposure single-frame mode of operation was to be preferred due to the small exposure time-delay imposed by the (expected) mean flow velocity.

Next, several important issues concerning the implementation of the double-exposure single-frame PIV technique were discussed. These issues included the need to employ an image shift and a corresponding window offset to resolve the directional ambiguity problem common to double-exposure single-frame PIV systems. The image shift is ultimately

achieved through the use of the line transfer of the CCD camera. The effect of a window offset on the correlation plane was also discussed and the favorable properties of this window offset (improved SNR of the displacement correlation peak) were highlighted.

The PIV technique was subsequently used to examine the liquid flow field induced by a bubble plume rising in a rectangular bubble column. The complex nature of the liquid flow field prevailing in this bubble column could clearly be inferred from the experimental results. It could also be seen that the flow in a bubble column is dominated by small-scale coherent (i.e. turbulent) structures. The effect of the size of the ensemble correlation set on the flow field determined with our PIV technique was illustrated. It could be concluded that as the size of the correlation set increases, some data on the small-scale turbulent structures are lost. This is however offset by the substantial improvement of the detectability of the displacement correlation peaks pertaining to both the gas and the liquid phase. This improved detectability implies that the larger flow structures observed in a bubble column can be resolved more accurately and reliably. Ensemble correlation PIV furthermore enables the measurement of the local gas velocity and of the local void fraction. Figures depicting sample results were shown and discussed.

Finally, we feel that it can be concluded that the ensemble correlation PIV technique, as discussed in the preceding two Chapters, is a powerful and viable experimental technique that can be used to study the liquid flow field prevailing in gas-liquid bubble columns. Future work should also enhance the reliability of the ensemble correlation PIV technique as a tool to gauge the local gas velocity and the local void fraction.

## 6. Acknowledgement

The authors would like to thank the J. M. Burgers Center for Fluid Dynamics for its financial contribution to the project.

## 7. Notation

$\Delta t$	Exposure time delay
$D_I$	Diameter interrogation window

$F_I$	In-plane loss of correlation
$F_O$	Out-of-plane loss of correlation
$M$	Magnification
$N_I$	Image density
$N_I^{(B)}$	Bubble image density
$N_{\text{Ensembles}}$ set	Number of PIV images in ensemble correlation
$R_D^+$	Positive displacement correlation peak
$R_D^-$	Negative displacement correlation peak
$R_D^{(BB)}$	Displacement correlation peak bubbles
$R_D^{(BT)}$	Random correlation between bubbles and tracers
$R_C$	Convolution of the mean image intensity
$R_D^{(TT)}$	Displacement correlation peak tracers
$R_F$	Convolution mean and fluctuating intensity
$R_D^{(TB)}$	Random correlation between tracers and bubbles
$R_P$	Self correlation peak
$s$	Vector

## 8. References

Adrian, R. J., 1986, "Image shifting technique to resolve directional ambiguity in double-pulsed velocimetry", *Applied Optics* **25** (21), 3855.

Brücker, Ch., 1998, "Bubble interaction in swarms: a study of the wake structures with 3-D scanning particle image velocimetry (3-D SPIV)", *Int. Conf. Multiphase Flow 1998*, 8 – 12 June, Lyon, France.

Delnoij, E., Lammers, F. A., Kuipers, J. A. M. and van Swaaij, W. P. M., 1997a, "Dynamic simulation of dispersed gas-liquid two-phase flow using a discrete bubble model", *Chem. Eng. Sci.* **52**(9), 1429. (Chapter 3 of this Thesis).

Delnoij, E., Kuipers, J. A. M., and van Swaaij, W. P. M., 1997b, "Computational fluid dynamics applied to gas-liquid contactors", *Chem. Eng. Sci.* **52**(21/22), 3623.

Delnoij, E., Kuipers, J. A. M., and van Swaaij, W. P. M., 1997c, “Dynamic simulation of gas-liquid two-phase flow: effect of column aspect ratio on the flow structure”, *Chem. Eng. Sci.* **52**(21/22), 3759. (Chapter 4 of this Thesis).

Delnoij, E., Kuipers, J. A. M. and van Swaaij, W. P. M., 1998a, “A three-dimensional dimensional CFD model for gas-liquid bubble columns”, *Accepted for publication at ISCRE15*, 13 – 17 September, Newport Beach CA, USA. (Chapter 5 of this Thesis).

Delnoij, E., Kuipers, J. A. M. and van Swaaij, W. P. M. and Westerweel, J., 1998b, “Measurement of gas-liquid two-phase flow in bubble columns using ensemble correlation PIV”, *Submitted to Int. J. Multiphase Flow*.

Devanathan, N., Dudukovic, M. P., Lapin, A. and Lübbert, A., 1995, “Chaotic flow in bubble column reactors”, *Chem. Eng. Sci.* **50**(16), 2661.

Jakobsen, H. A., Sannaes, B. H., Grevskott, S. and Svendsen, H. F., 1997, “Modeling of vertical bubble-driven flows”, *Ind. Eng. Chem. Res.* **36**, 4052.

Keane, R. D. and Adrian, R. J., 1990, “Optimization of particle image velocimeters: I. Double pulsed systems”, *Meas. Sci. Technol.* **1**, 1202.

Keane, R. D. and Adrian, R. J., 1992, “Theory of cross-correlation analysis of PIV images”, *Appl. Sci. Res.* **49**, 191.

Kiger, K. T., 1998, “Scanning PIV technique to resolve dispersed two-phase flow”, *Int. Conf. Multiphase Flow 1998*, 8 – 12 June, Lyon, France.

Lapin, A. and Lübbert, A., 1994, “Numerical simulation of the dynamics of two-phase gas-liquid flows in bubble columns”, *Chem. Eng. Sci.* **49**(21), 3661.

Oakley, T. R., Loth, E. and Adrian, R. J., 1997, “A two-phase cinematic PIV method for bubbly flows”, *J. of Fluids Eng.* **119**, 707.

Van den Akker, H. E. A., 1998, “The Euler-Euler approach to dispersed two-phase flows in the turbulent regime”, *ERCOFTAC Bulletin* **36**, 30.

Westerweel, J., 1993, "Digital particle image velocimetry-Theory and application", *PhD Thesis Delft University of Technology*, The Netherlands.

Westerweel, J., Dabiri, D. and Graham, M., 1997, "The effect of a discrete window offset on the accuracy of cross-correlation analysis of digital PIV recordings", *Exp. In Fluids* **23**, 20.

Westerweel, J., 1997, "Fundamentals of digital particle image velocimetry", *Meas. Sci. Technol.* **8**, 1379.

Willert, C., 1996, "The fully digital evaluation of photographic PIV recordings", *Appl. Sci. Res.* **56**, 79.



## Publications

### This Thesis

Delnoij, E., Lammers, F. A., Kuipers, J. A. M. and van Swaaij, W. P. M., 1997, "Dynamic simulation of dispersed gas-liquid two-phase flow using a discrete bubble model", *Chem. Eng. Sci.*, **52** (9), 1429-1458.

Delnoij, E., Kuipers, J. A. M. and van Swaaij W. P. M., 1997, "Dynamic simulation of gas-liquid two-phase flow: effect of column aspect ratio on the flow structure", *Chem. Eng. Sci.*, **52** (21/22), 3759-3772.

Delnoij, E., Kuipers, J. A. M. and van Swaaij, W. P. M., 1997, "Computational fluid dynamics applied to gas-liquid contactors", *Chem. Eng. Sci.*, **52** (21/22), 3623-3638.

Delnoij, E., Kuipers, J. A. M. and van Swaaij, W. P. M., 1998, "Numerical simulation of bubble coalescence using a Volume-Of-Fluid (VOF) model", *Int. Conf. on Multiphase Flows 1998*, June 8-12, Lyon, France.

Delnoij, E., Kuipers, J. A. M. and van Swaaij, W. P. M., 1998, "Computational fluid dynamics applied to dispersed gas-liquid two-phase flows", *ECCOMAS Computational Fluid Dynamics Conference*, September 7-11, Athens, Greece.

Delnoij, E., Kuipers, J. A. M. and van Swaaij, W. P. M., 1998, "A three dimensional CFD model for gas-liquid bubble columns", *Accepted for presentation at ISCRE 15 and accepted for publication in Chem. Eng. Sci.*, September 13-16, Newport Beach, USA.

Delnoij, E., Kuipers, J. A. M. and van Swaaij, W. P. M. and Westerweel, J., 1998, "Measurement of gas-liquid two-phase flow in bubble columns using ensemble correlation PIV", *Submitted for publication to Int. Journal of Multiphase Flow*.

Delnoij, E., Westerweel, J., Deen, N. G., Kuipers, J. A. M. and van Swaaij, W. P. M., 1999, "Ensemble correlation PIV applied to bubble plumes rising in a bubble column", *Accepted*

*for presentation at the fourth conference on gas-liquid and gas-liquid-solid reactor engineering GLS'99, August 23 – 25, Delft, The Netherlands.*

**M. Sc. work**

Nieuwland J. J., Delnoij E., Kuipers J. A. M. and van Swaaij W. P. M., 1997, “An engineering model for dilute riser flow”, *Powder Technology*, **90**, 115-123.



## Dankwoord

Het schrijven van dankwoorden is dankbaar werk. Dit zijn immers, naar alle waarschijnlijkheid, de meest gelezen bladzijden van dit proefschrift. En terecht. Een proefschrift, en daarmee een promotie, is niet het werk van één persoon. Het is het resultaat van de inspanning van velen. Bij de bijdrage van een aantal personen aan deze promotie wil ik in dit dankwoord expliciet stil staan. Een promotie is bij definitie niet mogelijk zonder de inzet en ondersteuning van een promotor, in dit geval Prof. Wim van Swaaij. Bedankt!

Veel dank ben ik verschuldigd aan mijn assistent promotor Hans Kuipers. Zijn stimulerende begeleiding, grote kennis van alles wat samenhangt met CFD en enorme inzet hebben een significante bijdrage geleverd aan het slagen van dit promotieproject. Hans: ik heb de vier jaar dat ik met jou heb mogen werken enorm gewaardeerd! Dat laatste geldt zeker ook voor het clubje CFD AIO's dat Hans de afgelopen jaren om zich heen heeft verzameld, met mannen als Bob Hoomans en (wat later) Mathijs Goldschmidt. Door de combinatie van sterk verweven CFD projecten op het gebied van gas-vast en gas-vloeistof systemen konden 'synergie' effecten tussen de verschillende promotieprojecten maximaal worden uitgebuit. Een garantie voor succes.

Op het experimentele vlak heeft zich de afgelopen jaren in het kader van het Burgerscentrum een interessante en misschien wel ietwat ongebruikelijke samenwerking ontwikkeld tussen de groep Proceskunde en de vakgroep stromingsleer van de Technische Universiteit Delft. Het begon als een ongemakkelijk verstandshuwelijk tussen drie Burgerscentrum groepen met grote plannen en weinig geld. Maar gaande weg is hier denk ik toch iets heel aardigs uit voort gekomen. Dit is vooral te danken aan de persoonlijke inzet van Jerry Westerweel, die veel geïnvesteerd heeft in de samenwerking met de groep Proceskunde. Het resultaat mag er zijn: een geslaagde toepassing van Particle Image Velocimetry op gas-vloeistof bellenkolommen en een tweetal mooie papers (de hoofdstukken 6 en 7 van dit proefschrift).

Dit proefschrift was misschien een stuk minder dik geweest als DSM ons niet financieel ondersteund had. De vele discussie, die ik in dit kader met Mevr. Eiman Abu Bakr en Peter de Wit heb gevoerd, heb ik als erg nuttig ervaren. Bedankt voor jullie inbreng en succes met jullie werk.

Iedereen die het proefschrift heeft gelezen heeft kunnen constateren dat er binnen mijn promotieproject nogal wat geprogrammeerd is. Programmeren is handwerk en veel van dat handwerk is verricht door studenten in het kader van hun afstudeeropdracht. Het begon allemaal met Bart Lammers en Marcel Eigelaar. Mijn eerste studenten, vijf maanden na mijn begin als AIO stonden ze al op mijn stoep. Ik wist zelf nauwelijks wat ik moest gaan doen! Terugkijkend op mijn promotie denk ik dat Bart een heel cruciale eerste stap heeft gezet met de ontwikkeling van het twee-dimensionaal discreet bellenmodel. Marcel heeft een begin gemaakt met de andere belangrijke maar extreem moeilijke modelleerlijn: het VOF werk. Later hebben Michiel Gunsing (3D discreet bellenmodel), Hans Hoff (Hirt & Nichols VOF), Sander Metzner (PIV), Mattijs Ytsma (discreet bellenmodel en PIV), Marcel Giesen (2D Euler-Euler model) en Niels Deen (weer PIV) ook afstudeeropdrachten in het kader van mijn promotieproject verricht. Annemarie Kempers en Marcel Meijnen hebben als HTS afstudeerders oriënterend experimenteel werk op hun schouders genomen. Voor allemaal geldt: bedankt!

Experimenteren is opstellingen bouwen. Daar komen de bekwame handen van mijn technicus Gerrit Schorfhaar om de hoek kijken. Gerrit: soms dacht ik dat je de oren van mijn hoofd af zou kletsen, maar bellenkolommen maken dat kun je als geen ander! Je werk was zondermeer van topkwaliteit. Zelfs voor lasers en andere voor de vakgroep volstrekt nieuwe technologie draaide jij je hand niet om. Je hebt enorm geholpen bij al het constructiewerk dat we samen hebben verricht of hebben laten verrichten. En als het IMC er weer eens naast kleunde (eerder regel dan uitzondering) dan wist jij gelukkig altijd wel een oplossing.

Dit is ook een mooi moment om een aantal mensen met name te noemen die indirect bij mijn promotie betrokken zijn geweest. Met veel plezier denk ik terug aan discussies met Martijn Letzel over de rentabiliteit en toekomst strategie van de vaderlandse private sector. Veel steun heb ik gekregen van mijn ouders en van een aantal zeer goede vrienden: Saskia & Patrick, Mirjam en Harriët. Zonder deze bijzondere mensen was het in ieder geval een stuk minder leuk geweest!

Belangrijke zaken tot slot: Odette heeft zonder enige twijfel de belangrijkste vinger in de pap gehad bij het slagen van dit promotieproject. Zij heeft mij door dik en dun gesteund. Met veel geduld heeft ze al mijn verhalen over de promotie aangehoord. Ze heeft een hoop tijd en

moeite gestoken in het minutieus uitkammen van het proefschrift op zoek naar de laatste (spel)fout. Bedankt, voor alles.

Erik.



## Levensloop

Erik Delnoij werd op 29 november 1969 geboren te Geleen. Lager onderwijs werd gevolgd in Waalwijk en Zutphen. In die laatste plaats bezocht hij vanaf 1982 het Stedelijk Lyceum. In het voorjaar van 1988 werd het VWO diploma in ontvangst genomen.

In augustus 1988 begon hij met de studie Chemische Technologie aan de Universiteit Twente te Enschede. In het kader van deze ingenieursopleiding liep hij in de zomer van 1993 drie maanden stage bij het Energie Onderzoek Centrum Nederland (ECN) te Petten. In augustus 1994 studeerde hij af bij de vakgroep Proceskunde op het onderwerp: “Experimenteel en modelmatig onderzoek aan circulerend fluid bedden”. In september van datzelfde jaar werd het ingenieursdiploma in ontvangst genomen.

Na afloop van zijn studie trad hij (in november 1994) in dienst bij de vakgroep Proceskunde om als assistent in opleiding (AIO) een promotie onderzoek te verrichten naar de hydrodynamica van gas-vloeistof bellenkolommen. Dit proefschrift is de weerslag van dat werk. In aanvulling op zijn promotie werk heeft hij tevens de ontwerpersopleiding tot Procesontwikkelaar gevolgd.

Sinds 1 oktober 1998 is hij werkzaam bij Akzo Nobel NV waar hij zich als medewerker research onder meer bezighoudt met Computational Fluid Dynamics.





